UNIVERSITAT DE BARCELONA

University of Barcelona

Faculty of Chemistry

Department of Materials Science and Metallurgical Engineering

Materials Technology
Doctorial program 2005-2007

"MECHANICAL PROPERTIES OF HTSC AT MICRO/NANOMETRIC SCALE"

Memory presented by
D. JOAN JOSEP ROA ROVIRA
In partial fulfilment for the degree of
Doctor by the University of Barcelona.

Supervissor: MERCÈ SEGARRA RUBÍ
Co-supervissor: XAVIER GARCIA CAPDEVILA

FEBRUARY 2010

Mercè Segarra i Rubí, Associate Professor at the Department of Materials Science and Metallurgical Engineering in the University of Barcelona and *Xavier Garcia Capdevila*, Post-doctoral researcher at the Centre of Design and Optimization of Processes and Materials in the Parc Científic of Barcelona.

CERTIFY:

The present work entitled: "**Mechanical properties of HTSC at Micro/Nanometric scale**" has been carried out at the Department of Materials Science and Metallurgical Engineering in the University of Barcelona, by Joan Josep Roa Rovira, and constitutes his Doctoral Thesis report.

Barcelona, February 2010.

Supervissor:
Dra. Mercè Segarra Rubí
Department of Materials Science and Metallurgical Engineering
University of Barcelona

Co-Supervissor:
Dr. Xavier Garcia Capdevila
Centre of Design and Optimization of Processes and Materials
Parc Científic of Barcelona

AGRADECIMIENTOS-ACKNOWLEDGEMENTS

Had I but served my God with
half the zeal I served my King,
He would not in mine age have
left me naked to mine enemies

William Shakespeare (1564-1616)
British poet and playwright

Antes de nada, no quisiera olvidarme de nadie, que me haya ayudado de manera directa o indirecta durante estos cuatro años de investigación. En tal caso os pido disculpas de antemano.

En primer lugar quiero agradecer a la gente del grupo de BIOPOLÍMEROS VEGETALES de la “Universitat Rovira i Virgili” donde me introduje al mundo de la ciencia bajo la supervisión de la Dra. Vanesa Fierro y de la Sra. Vanessa Torné. Muchas gracias.

También me gustaría dar mi sincero agradecimiento a los directores de tesis, la Dra. Mercè Segarra i el Dr. Xavier Garcia, por tantas horas de plácida discusión sobre como realizar los experimentos, por aguantar el bombardeo de preguntas durante estos años, y sobretodo durante estos últimos meses. Gracias Mercè por enseñarme lo que son las preguntas retóricas y por las clases improvisadas de moda en el Zara o en el H&M de San Sebastián, o en el Corte Ingles de Albacete. Gracias especialmente a mi compañero de ajedrez, antiajedrez o Worms. No tengo palabras para agradecerte lo mucho que has hecho por mí. Sólo tienes un único defecto, que eres del Español.

Al Prof. Ferran Espiell, por sus continuas lecciones de la vida. Gracias, por las magistrales clases de Materiales Plásticos y por querer compartir un poco de tu conocimiento conmigo. También me gustaría agradecer a los demás doctores i docentes del grupo DIOPMA (Miki, Inés i Txema) i por supuesto a Núria (Bon profit, Núria. ;P).

No querría olvidarme de la gente del grupo de Fractura de la ETSEIB, a Carlos, Jordi, Gemma y Álvaro. Muchas gracias por tan buenos momentos, tanto dentro de la Universidad, como en el bar Tomás de Sarriá o en el congreso de Fractura celebrado en Santander, en el 2009. También, a Yves Gaillard, una persona realmente fascinante y un amante de su trabajo. En especial, quiero agradecer al Dr. Emilio Jiménez por tantas tardes en tu despacho o en la cafetería de la ETSEIB, discutiendo y debatiendo resultados. Por tus interesantes clases sobre la cerveza y el lúpulo en la Cerveteca; espero que lo podamos repetir más a menudo.

Je ne voudrais pas m'oublier d'un personne très spéciale, Christophe, qui m'a beaucoup aidé pendant les derniers mois de ma thèse. Je me souviendrai toujours du jour où je suis arrivé à la Gare de Poitiers pour passer quelques mois avec une personne magnifique tant au niveau personnel que professionnel, avec une telle énergie et sagesse. Merci beaucoup pour tous ces mois à ton côté. Vraiment, je n'avais jamais rencontré quelqu'un qui aimait le travail autant que toi. Je rappellerai toujours ton visage le jour où tu as vu la grande chambre de la résidence, jejeje. Merci beaucoup à J. Rabier pour ses conseils sur les mécanismes de déformation plastique du YBCO.

Tampoco quiero olvidar a toda la gente que ha confiado en mí y me ha enviado sus muestras para que se las estudie: Fabio (Brasil), Edi (Parma), Miguel (Zaragoza), Juan Carlos (La Laguna), José Canales (Albacete). A todos vosotros, muchas gracias por confiar en mí. En especial a José Ignacio Pastor y a Konstantina (Universidad Politécnica de Madrid), por su incondicional apoyo y consejo en el campo de la fractura de materiales cerámicos a baja temperatura.

No puedo olvidarme de los chicos del curso de Postgrado de Sevilla; fue una semana fantástica. Sobretodo, me gustaría agradecer a los del ICMA de Zaragoza (Raquel, Elena y Daniel). Espero que ya veáis la luz al final del túnel y podamos celebrarlo este mes de Junio en vuestra ciudad.

Sobretodo, agradecer y destacar a los del Servicios Científico Técnicos de la Universidad de Barcelona (SCT), a Jordi, Gerard y Marc de "técnicas nanométricas", a Eva de SEM y EBSD. Quim, Aranzazu, Jordi, Félix y Josep de TEM.

A Albert Calleja, Xavier Granados, Xavier Obradors, Bernat y Roberto del ICMAB, por tan buenos momentos vividos y cada uno de ellos, mejor que el anterior. Un especial agradecimiento a la Dra. Elena Bartolomé, desde el primer EUCAS (en Bruselas) hasta el día de hoy, has sido una buena compañera y asesora en temas científicos. Gracias por tus consejos y por esas reuniones maratonianas en el nanoindentador o en la EUSS.

Bueno, y como no a la gente de DIOPMA, con quienes tantos buenos ratos he compartido. A los nuevos Doctores, Elena (la persona más alegre y más habladora del grupo), Mónica (una persona de calidad, una amiga, sobretodo cuando estás de congreso. Gracias por dejarme dormir en tú magnífico sofá, me lo tendrás que regalar) y al Dr. Llamaradas (amigo y compañero de congresos, que tan buenos momentos hemos pasado. Además, de un esplendido guía y una agenda ambulante). No quiero olvidarme de los compañeros de despacho, Padi (el correcaminos) y a nuestra Indurain del grupo (H). Tampoco a los del zulito, Sergio, Esther y Ferranet. A los compañeros del café de la mañana, Joan (una enciclopedia andante del fútbol y un buen portero). A Maria (vigila con la cafetera, espero que en Zaragoza no te quemes) y como no, Judit. No tengo palabras para deciros lo mucho que me habéis ayudado durante estos años. A los más nuevos del grupo, Ricardo, Eliany, Anna, Camila y Jéssica (nuestra Messi). Muchas gracias a todos vosotros y como no, a EDU, aunque no lo conozca, me hago una leve idea de cómo es. Un fuerte abrazo para los ex-DIOPMA: Laia, Maria José (Cádiz), Montse, Annita, Oscar y como no, los ex-Florensos, Carlos (el rastas) y Anna Magrasó. Qué puedo decir que no sepáis.

Thanks to the organizers of lovely summer schools on superconductors: SCENET School 2006 in Camerino (Edi and Andrea). Big hugs to the friends I made there: Cesar, Nuria, Tristan, Jose. I'll always bring you with me.

Another big big thank you goes to Futuroscope (Poitiers). At the PHYMAT group (University of Poitiers). Special thanks also to Vivek, Ciril, Alex and all the PhD Students. Thanks for the several months that I spent in the Institute.

Also, I would like to give a big big THANKS all to the people of the SCY MY BEECY residence 2009. The Belgium's women (Sara madre, Sara GB, Lotte, Sophie peluche, Inge and Ann). Of course, Ben, Allice, and Anna. Also, an Indian's man, Ginu (I taste the spicy food, wonderful, amazing, and main blowing, no?). And of course, Ozren, our salsa teacher in the residence. Also a good person of Croacia. During this time in the residence, I made a close close friends like Doro (or Ideafix), Fran (chez de village o el padrino), Elena (one of my salsa's partner), Benedetta (la mama and also my salsa partner), Anastasia, Miko (his way to drive is very curious, no. We can ask to "K") and Kirsten (at the end, she loves Pa amb Tomaquet). Ups!!! I forgot Tom (Asterix) ;P. Very thanks for all the time we spent together in a small and beautiful Village in Poitier. I wear all of us in my heart.

En el ámbito personal, primero de todo quiero agradecer a todos mis amigos de Ingeniería Química (Cefe, Gerard, Esther y sobretodo a Gemma). También a sus parejas y amigos de Reus: Mónica, Montse, Lluís, Sergi, Sonia, Gustavo, Gosha y Marcos. Quiero agradecer esta tesis a una compañera de viaje, Roser; compañera de tren y una amiga con la que puedes confiar, sobretodo para criticar a RENFE.

Por supuesto, también quiero agradecer al Maestro (por sus sabios consejos de albañilería, eso si, él te da los consejos y tú pones la mano de obra), a su mujer Dori (que tiene mucha paciencia). Como no, Pere y Marina por tantos momentos inolvidables que hemos pasado juntos (sobretodo camino de Bienvenida, un viaje casi eterno), o saltando dentro del ascensor de Austria,…

Como no, a mis padres, Juan y Antonia, que siempre me han dado la suficiente libertad para hacer lo que me gustaba. Así como por su especial paciencia desde el pasado mes de septiembre, donde los nervios ya empezaban a estar a flor de piel. Un fuerte abrazo a mis tíos, mi prima y su marido (Joan, Justa, Montse y Javi), y un beso muy especial a mi ahijado y mi primita, Marc y Marta. Quiero agradecer de forma especial a unos seres muy queridos que aunque ahora ya no están, siempre los llevaré en mi corazón; mis abuelos (Josep y Montserrat) por ayudarme en todo y por los largos paseos por los caminos del pueblo. Sin vuestros consejos, no hubiese llegado donde estoy. Muchas gracias por todo, siempre estaréis en mi corazón.

Muchas gracias a todas las personas que me han ayudado a llevar a buen puerto esta tesis. Muchas gracias a toda la gente que me ha apoyado y ha confiado en mí. Muchas gracias a todos por haber contribuido con vuestro granito de arena. Pero realmente, quiero agradecer a una persona que ha estado a mi lado en lo bueno y en lo malo durante estos años, sin ella no habría tenido suficiente fuerza para poder acabar esta tesis. Muchas gracias VANESSA.

LIST OF ACRONYMS AND SYMBOLS

> ***A gem cannot be polished***
> ***without friction, nor a man***
> ***perfected without trials***
>
> *Chinese Proverb*

a:	Radius of circle of contact, constant for linear fit
$A, A_c, A(h_c)$:	Projected contact area, constant for *P* vs. *h* relationship
A_f:	Portion of contact area carried by the film
AFM:	Atomic Force Microscopy
A_s:	Portion of contact area carried by substrate
B:	Dimensionless factor
BCS:	Bardeen, Cooper, and Schrieffer theory
C_o:	Size of plastic zone
C_i:	Load frame compliance, concentration in the growth interface
C_{LY-123}:	Concentration in the liquid
cc:	Coated conductors
CSM:	Continuous Stiffness Measurement
dP/dh:	Slope of the initial portion of the unloading curve
E:	Young’s modulus, elastic modulus
E_{Bec}:	Young’s modulus obtained using the Bec model

EELS:	Electron Energy Loss Spectroscopy
E_c**:**	Composite Young's modulus
E_{eff}**:**	Effective Young's modulus
E_f**:**	Film Young's modulus
E_i**:**	Indenter Young's modulus
E_r**:**	Reduced Young's modulus
E_{Rar}**:**	Young's modulus obtained using the Rar model
$E_{Y\text{-}123}$**:**	Matrix Young's modulus
$E_{Y\text{-}211}$**:**	Inclusions Young's modulus
$E_{Y\text{-}123/Y\text{-}211}$**:**	Interphase Young's modulus
E_s**:**	Substrate Young's modulus
FEM:	Finite Element Method
FE-SEM:	Field Emission Scanning Electron Microscopy
FIB:	Focused Ion Beam
FS:	Force Spectroscopy
H**:**	Hardness
h**:**	Penetration depth
HAADF:	High Angular Annular Dark Field
h_c**:**	Contact depth
H_c**:**	Composite hardness
H_{c1}**:**	Minimum critical field
H_{c2}**:**	Maximum critical field
h_e**:**	Elastic penetration depth
HEP:	High Energy Physics
h_f**:**	Final penetration depth
H_f**:**	Film hardness
H^{GB}**:**	Grain boundary hardness
H^{G}**:**	Grain hardness
h_{max}, h_t**:**	Total depth or maximum penetration depth
h_s**:**	Penetration depth at unloading force P_s, depth at which spherical indenter tip meets conical support measured from indenter tip
H_s**:**	Substrate hardness
H_v**:**	Vickers hardness
$H_{Y\text{-}123}$**:**	Matrix hardness
$H_{Y\text{-}211}$**:**	Inclusions hardness
$H_{Y\text{-}123/Y\text{-}211}$**:**	Interphase hardness
HR-TEM:	High Resolution Transmission Electron Microscopy
HTSC:	High Temperature SuperConductors
ITT:	Indentation Testing Technique
J_c^{GB}**:**	Grain boundary critical current density
J_c^{G}**:**	Grain critical current density
K**:**	Constant for determining inicial penetration depth

K_{IC}:	Fracture toughness
m:	Nanoindentation coefficient
MEG:	Magnetoencephalography
MRI:	Magnetic Resonance Imaging
MTG:	Melt Texture Growth
NDE:	Non-Destructive Evaluation
NMR:	Nuclear Magnetic Resonance
OM:	Optical Microscopy
P:	Applied load
PED:	Pulsed Electron Deposition
PLD:	Pulsed Laser Deposition
p_m, p_o:	Mean contact pressure
P_{max}:	Maximum applied load
PVA:	Polyvinyl Alcohol
R:	Radius of the indenter
R^*:	Critical radius
S:	Stiffness
SC:	Superconducting/Superconductor
SEM:	Scanning Electron Microscopy
SMES:	Superconducting Magnetic Energy Storage
SQUID:	Superconducting Quantum Interferometric Device
SRLCP:	Solute Rich Liquid-Crystal Pulling
STEM:	Scanning Transmission Electron Microscopy
STM:	Scanning Tunnelling Microscopy
t:	Film thickness
T_c:	Critical temperature
$t_{coating}$:	Coating thickness
TEM:	Transmission Electron Microscopy
T_{max}:	Maximum temperature
T_p:	Peritectic temperature
TSMG:	Top-Seeded Melt Growth
W_p:	Plastic work
W_{tot}:	Total work of indentation
W_u:	Work recovered during unloading
x, δ:	Oxygen content approaches
Y_f:	Yield stress of film
Y_s:	Yield stress of substrate
α:	Cone semi-angle, thin film hardness parameter, buckling parameter
β:	Indenter geometry shape factor
ε:	Strain
Θ:	Face angle, phase angle between force and depth in oscillatory indentation test, misorientation angle between

	two different YBCO blocks
λ:	Penetration depth
ξ:	Coherence length
ν:	Poisson’s ratio
ν_i:	Indenter Poisson’s ratio
ΔG_v:	Volumetric driving forces
ΔG_s:	Increasing solid energy
σ:	Stress
σ_{max}:	Maximum yield stregth
σ_{ys}:	Yield strength
τ:	Shear stress

ABSTRACT

Chose a job you love, and you will never have to work a day in your life

Confucius (BC 551-BC 479)
Chinese philosopher

The nanoindentation or indenter testing technique (ITT) is a functional and fast technique that can give us a lot of information about the mechanical properties of different materials at nanometric scale, from soft to brittle materials. The principle of the technique is the evaluation of the response of a material to an applied load. In a composite material, if the size of the residual imprint resulting from a certain load is lower than the size of the studied phase, then it is possible to determine its mechanical properties, and therefore its contribution to the global mechanical properties of the composite. Depending on the tipped indenter used, different equations should be applied to study the response of the material, and thus calculate stress-strain curves, and parameters such as hardness, Young's modulus, toughness, yield strength and shear stress. These equations are related to the different deformation mechanisms (elastic and elasto-to-plastic) that the material undergoes.

In the case of most of the ceramic composites, when a spherical tipped nanoindenter is used, elastic deformation takes place, and Hertz equations can be used to calculate the yield strength, shear stress and the strain-stress curves. On the other hand, when a Berckovich indenter is used, plastic deformation takes place, then Oliver and Pahrr equations must be applied to evaluate the hardness, Young's modulus and toughness. Nevertheless, in the hardness study, Indentation Size Effect (ISE) must be considered.

The mechanical properties of a ceramic superconductor material have been studied. $YBa_2Cu_3O_{7-\delta}$ (YBCO or Y-123) samples textured by Bridgman and Top Seeding Melt Growth (TSMG) techniques have been obtained, and their mechanical properties studied by nanoindentation. This material presents a phase transition from tetragonal to orthorhombic that promotes a change in its electrical properties, from insulating to superconductor, and that can be achieved by partially oxygenating the material. On the other hand, the structure of the textured material is heterogeneous, and two different phases are present: Y-123 as a matrix and Y_2BaCuO_5 (Y-211) spherical or quasi-spherical inclusions. Moreover, the texture process induces an anisotropic structure, thus being the *ab*-planes the ones that transport the superconductor properties while the *c*-axis remains insulating. Nowadays, efforts are focused on the production of long length Superconductor Materials. Silver welding is a technique that allows us to join several TSMG samples thus trying to obtaining larger samples. Nevertheless, one important factor to be accounted for is the mechanical stability across the welding zone, which has been studied in this Thesis.

Another attempt to produce long length superconductor materials is to shape thus as wires or plates. In this case, a metallic sheet, covered with different buffer layers is used as substrate on which YBCO layers can be deposited by PED for example. These structures have been also studied in the present Thesis.

TABLE OF CONTENTS

Nothing is more terrible than to see ignorance in action

Johann Wolfgang Von Goethe (1749 –1832)
German poet, novelist and dramatist

Acknowledgments (Agraïments)………………………………………………………………… v
List of acronyms and symbols……………………………………………………………. xi
Abstract………………………………………………………………………………………... xv

CHAPTER 1. Introduction to mechanical properties……………………………………….. 1
1.1. Mechanical properties………………………………………………………………… 1
1.1.1. Testing equipment-Instrumentation…………………………………………………….. 4
1.1.2. Contact mechanisms……………………………………………………………………. 8
1.1.2.1. Elastic regime………………………………………………………………… 8
1.1.2.2. Elastic-to-Plastic regime……………………………………………………… 12
1.1.3. Considerations to be account during the indentation process………………………. 19
1.1.3.1. Effective Indenter Shape……………………………………………………... 19
1.1.3.2. Errors due to pile-up and sink-in…………………………………………….. 20
1.1.4. Thin solid films characterization……………………………………………………….. 23
1.1.4.1. Testing of thin films………………………………………………………... 23
1.1.4.2. Film thickness…….………………………………………………………….. 25

1.1.4.3. Film hardness, H_f……………………………………………………………. 25
1.1.4.4. Elastic modulus of films, E_f………………………………………………….. 27
1.2. Superconductor materials……………………………………………………………. 29
1.2.1. Aplications……………………………………………………………………………… 31
1.2.2. $YBa_2Cu_3O_{7-\delta}$ materials………………………………………………………. 33
1.2.2.1. Crystallographic structure…………………………………………………. 34
1.2.2.2. Structural blocks………………………………………………………………… 35
1.2.3. Growth of $YBa_2Cu_3O_{7-\delta}$ single crystals……………………………………………. 36
1.2.3.1. Phase diagram……………………………………………………………………… 38
1.2.3.2. Solidification process……………………………………………………………….. 41
1.2.3.3. Manufacturing process…………………………………………………………... 44
1.2.3.4. Oxygenation process…………………………………………………………... 49
1.2.3.5. Microstructural defects generated during the texture process………………. 50
1.2.3.6. Microstructural defects generated during the oxygenation process…………. 54
1.3. Mechanical properties of YBCO samples…………………………………….. 57
1.4. Plastic deformation mechanism of YBCO samples…………………………………… 59
1.5. References……………………………………………………………………………….. 59

CHAPTER 2. Objectives…………………………………………………………………….. 67

CHAPTER 3. Experimental procedure……………………………………………………….. 69
3.1. Synthesis, texture and oxygenation process…………………………………………… 69
3.1.1. Synthesis of YBCO powders………………………………………………………. 69
3.1.2. Texture and oxygenation process…………………………………………………. 71
3.1.2.1. TSMG samples……………………………………………………………………… 71
3.1.2.2. Bridgman samples…………………………………………………………….. 73
3.1.2.3. YBCO coated conductors, YBCO-cc………………………………………….. 76
3.2. Specimen preparation……………………………………………………………………... 76
3.3. Mechanical characterization…………………………………………………………… 77
3.3.1. H and E measurements…………………………………………………………………. 77
3.3.2. σ–ε curves……………………………………………………………………………… 78
3.4. Residual imprint characterization……………………………………………………... 79
3.4.1. Field Emission Scanning Electron Microscopy, FE-SEM…………………………... 79
3.4.2. Atomic Force Miroscopy, AFM……………………………………………………… 81
3.4.3. Focused Ion Beam, FIB……………………………………………………………… 81
3.5. Microstructural characterization……………………………………………………. 82
3.5.1. Transmission electron microscopy, TEM, and High Resolution TEM, HR-TEM…… 82
3.5.2. Tomography with TEM…………………………………………………………………. 83
3.6. References……………………………………………………………………………….. 84

CHAPTER 4. Measurement of nanohardness and Young's modulus………………………. 87
- **4.1. YBCO samples textured by Bridgman technique**……………………………………... 87
- **4.2. YBCO samples textured by TSMG technique**………………………………………… 97
- **4.3. Conclusions**………………………………………………………………………… 101
- **4.4. References**………………………………………………………………………….. 101

CHAPTER 5. Measurement of the Stress-Strain curves…………………………………….. 103
- **5.1. YBCO textured by Bridgman technique**………………………………………………. 103
- **5.2. YBCO textured by TSMG technique**…………………………………………………... 111
- **5.3. Conclusions**…………………………………………………………………………. 114
- **5.4. References**…………………………………………………………………………... 115

CHAPTER 6. Study of the different plastic mechanisms……………………………………. 117
- **6.1. Bridgman poly-crystaline samples**…………………………………………………….. 119
  - *6.1.1. Deformation induced by a Berkovich indenter*………………………………………. 119
  - *6.1.2. Deformation induced by a Spherical indenter*……………………………………….. 122
- **6.2. TSMG single crystal samples**………………………………………………………... 123
  - *6.2.1. Deformation induced by a Berkovich indenter*………………………………………. 123
  - *6.2.2. Deformation induced by a Spherical indenter*……………………………………….. 125
- **6.3. Conclusions**…..…………………………………………………………………….. 126
- **6.4. References**………………………………………………………………………….. 126

CHAPTER 7. Correlation between mechanical versus electrical properties………………. 129

CHAPTER 8. Nanoindentation of multilayers employed as coated conductors…………… 137

CHAPTER 9. Discussion………………………………………………………………………. 145
- **9.1. Elastic contact**………..…………….……………………………………………… 146
- **9.2. Elasto-Plastic contact**……………………….…………………………………………... 150
  - *9.2.1. Hardness value*…………………………………………………………………… 150
  - *9.2.2. Young's modulus value*…………………………………………………………… 152
- **9.3. Fracture mechanisms** ……………………………………………………………… 154
- **9.4. Coated conductors**…………………………………………………………………. 157
- **9.5. References**………………………………………………………………………….. 159

CHAPTER 10. Conclusions……………………………………………………………………. 161

CHAPTER 11. Future work…………………………………………………………………… 165

APPENDIX SECTION………………………………………………………………………… 167
APPENDIX A. Resum en Català…………………………………………………………... 169
APPENDIX B. Publications and meetings……………………………………………………. 195

From error to error,
one discovers the entire truth

Sigmund Freud

A mis padres,
y en especial a
Vanessa

1

INTRODUCTION TO MECHANICAL PROPERTIES

One thing only know, and that is
that I know nothing

Socrates (BC 469-BC 399)
Greek philosopher

1.1. Mechanical properties

Indentation or hardness (*H*) testing has long been used for characterization and quality control of materials, but the results are not absolute and depend on the test method. In general, traditional hardness test consist of the application of a single static force and corresponding dwell time with a specified tip shape and material, resulting in a residual impression whose dimensions depends on the applied load (*P*). The output of these *H* tests is typically a single *H* value, which is a measure of the relative penetration depth of the indentation tip into the sample. Nowadays, there are a lot of durometers which are used to characterize the mechanical resistance of materials, which have different spring constants, and either a flat conical, a sharp conical, or a spherical tip, is used as specified in ASTM D2240, Standard Test Method for Rubber Property-Durometer Hardness.

The methods used for local mechanical testing of materials have often been formally divided into macroindentation, microindentation, nanoindentation, and even picoindentation, according to the characteristic indentation sizes that fall into a particular size range. However, these methods can be classified in a physically more justified manner. An increase in the applied load, *P*, leads to a change not only in the characteristic size of a locally deformed region, but also in the ratio between the contributions of the elastic and plastic deformations (see *Fig. 1.1*), and in the atomic mechanisms of deformation.

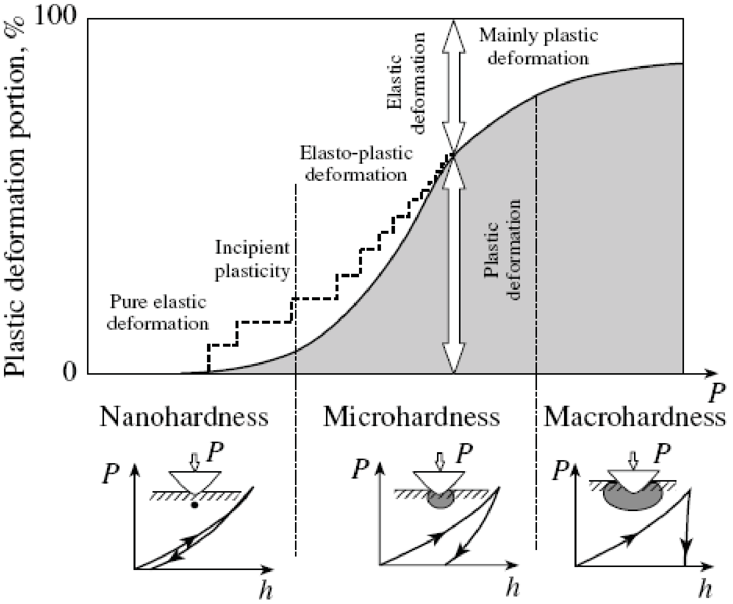

Fig. 1.1. Schematic diagram illustrating the change in the relative contribution of the plastic deformation to the formation of an indentation with an increase in the indentation load, *P*, and a change in the corresponding stage of the penetration of an indenter into the material[1].

The deformation of materials takes place via two different processes: *elastic* (reversible) and *plastic* (irreversible). Since elastic deformation is a reversible process, and is governed by angstrom scale (10^{-10} m), it exhibits virtually no size dependence unless a large population of pre-existing defects is involved[2]. The plastic deformation response, which takes place as a result of the generation, annihilation, and motion of defects such as dislocations, displays marked size effects when those defect dimensions are in the range of microns or below.

During the last years, Instrumented indentation testing (IIT) has been widely employed. Also known as depth-sensing indentation, continuous-recording indentation, ultra-low-load indentation or nanoindentation, IIT is a relatively new form of mechanical testing, which significantly expands the capabilities of traditional hardness testing. It employs high-resolution instrumentation to continuously control and monitor the loads and displacements of an indenter. The method was introduced in 1992 for measuring *hardness* and *elastic modulus*, has been widely adopted and used in the characterization of mechanical behaviour at nanometric scales[3,4]. This technique has several advantages: Firstly, it is a local probe that can evaluate the properties of a material in different areas. Secondly, it is depth-sensing, so it can characterize a material at different depths, unlike most scanning probe techniques, which usually only work at a given depth. Moreover, it can also measure the Young's modulus (E) of the material. Also, the nanoindentation technique is especially well suited for the characterization of small volumes of material, such as single grains or phases in a composite[5], dislocation dynamics[6], small structures[7] or thin films and coatings[8,9]. Finally, it eliminates the need to visualize the imprint produced during the test for homogeneous materials, which makes the extraction of mechanical properties easier. Due to all these advantages, nanoindentation could be a good and versatile technique for characterizing the mechanical properties of a given component. For these reasons, this method has become a primary technique for the determination of the mechanical properties of thin films and small structural features[10, 11, 12, 13]. During the past decade, IIT has introduced several changes to the method that have improved its accuracy and extended its fields of application. These modifications have been developed through experience in testing a large number of materials, and by improvements to testing equipment and techniques. Some of these changes are[13]:

- *i)* *new methods for calibrating indenter area functions and load frame compliance, and*
- *ii)* *dynamic techniques allowing continuous measurement of properties as a function of depth.*

A nanoindenter is an equipment, which measures load (P) and total depth (h_{max} or h_t) of penetration as function of time during loading and unloading, and displays load-displacement data (P-h). Depending on the details of the specific testing systems, loads as small as 1 nN can be applied, and displacements of 0.1 nm (1 Å) can be measured.

Mechanical properties, such as hardness (H), elastic or Young's modulus (E), toughness fracture (K_{IC}), yield strength (σ_{ys}), shear stress (τ), or stress (σ)-strain (ε) curve, can be obtained from the P-h data and with the corresponding tip indenter.

The most frequently employed technique measures the H and E [3,14]. This technique, also allows to evaluate the σ_{ys} and to obtain strain-hardening curves of metals [15], characteristic parameters of damping and internal friction in polymers, such as the storage and loss modulus and the activation energy and stress exponent for creep[16,17].

Mechanical properties are usually measured from submicron indentations, and with careful adjustments, properties have even been determined from indentating only a few nanometers deep. Many IIT testing systems are equipped with automated specimen manipulation stages. In these systems, the spatial distribution of the near-surface mechanical properties can be mapped on a point-to-point basis along the surface in a fully automated way.

1.1.1. Testing equipment-Instrumentation

Many instrumented indentation systems can be generalized in terms of the schematic illustration shown in *Fig. 1.2*[3].

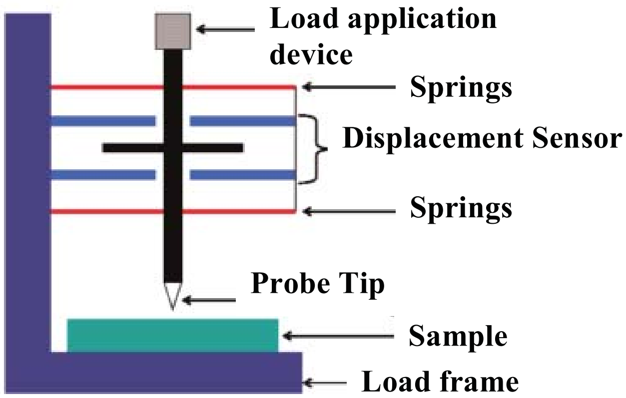

Fig. 1.2. Schematic illustration of an instrumented indentation system[3].

As shown in *Fig. 1.2*, the equipment for performing instrumented indentation test consists of three components:

- *i)* *an indenter of specific geometry, usually assembled to a rigid column through which the force is transmitted,* *ii) an actuator for applying the force, and*

iii) a sensor for measuring the indenter displacement.

However, to date, most IIT development has been performed using instruments specially designed for small-scale work. Advances in instrumentation have been driven by technologies that demand accurate mechanical properties at the micron and submicron levels, such as the microelectronic and magnetic storage industries.

One of the most important parts of the instrumented indentation system is the probe tip. Nowadays, several indenters are made of a variety of materials. Diamond is probably the most frequently used material because its high H and E minimize the indenter deformation. Indenters can be made of other less-stiff materials, such as sapphire, tungsten carbide, or hardened steel.

Attending to their shape, indenters can be classified in four different groups:

- ***Pyramidal indenters:*** The most used sharp indenter in nanoindentation technique is the Berkovich indenter. It is a three-sided pyramid with the same depth-to-area relation as the four-sided Vickers pyramid commonly used in microhardness work. This indenter allows to obtain the H and E. The toughness (K_{IC}) of brittle materials can also be determined with a Berkovich tip indenter.

- ***Spherical indenters:*** For spherical indenters, the contact stress is initially small and produces only elastic deformation. As the spherical indenter is driven into the surface, a transition from elastic-to-plastic deformation occurs, which can theoretically be used to examine yielding and work hardening, and to recreate the entire uniaxial stress(σ)-strain(ε) curve[18,19]. The spherical indenter can be used when one wishes to take advantages of the continuously changing strain. In principle, elastic modulus, yield stress, and strain-hardening behaviour of a material can be determined all in one test.

- ***Cube-corner indenters:*** A three-sided pyramid with mutually perpendicular faces arranged in geometry like the corner of a cube. The center-line-to-face angle for this indenter is 34.3° whereas for the Berkovich indenter is 65.3°. The sharper cube corner, produces much higher σ and ε in the vicinity of the contact, which is useful, for example, in producing very small, well defined cracks around residual impression in brittle materials; such cracks can be used to estimate the K_{IC} at small scales[20].

- ***Conical indenters:*** The conical indenter is interesting due the unexistance of σ concentrations at the sharp edges of the indenter. It is difficult to manufacture conical diamonds with sharp tips, making them of little use in nanoindentation technique[21].

The indenters most frequently used in nanoindentation technique are the Berkovich and Spherical tip indenters. Both allows to characterize the plastic, the elastic, and the elasto-to-plastic deformation range. A typical tip employed for this purpose is shown in *Fig. 1.3*.

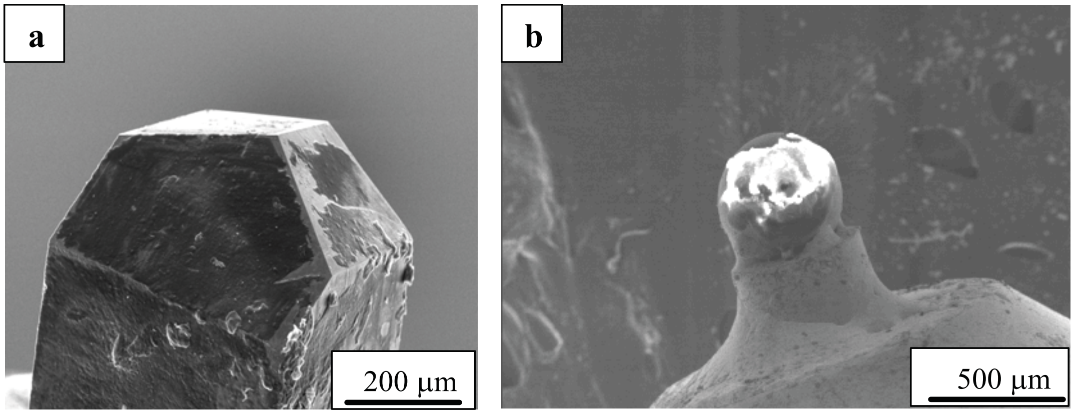

Fig. 1.3. SEM image of, *a)* Berkovich diamond indenter and *b)* Spherical sapphire indenter.

The success of the nanoindentation technique can be summarized in two simple questions: What study do we want to carry out on this sample?, and Which is the best indenter that I have to do that? In other words, as in any experimental work, accurate measurements can be obtained only with good experimental techniques and practices. The most important factors that can be controlled in a nanoindentation test are shown below:

- ***Choosing an appropriate indenter:*** this step requires consideration of a number of factors. One consideration is the strain the tip imposes on the test materials. Although the indentation process produces a complex strain field beneath the indenter, it has been proven to be useful to quantify this field with a single quantity, often termed the characteristic strain. There are problems, however, in obtaining accurate measurements of H and E with cube-corner indenter[22]. Although not entirely understood, the problems appear to have two separate origins: first, as the angle of the indenter decreases, friction in the specimen-indenter interface and its influence on the contact mechanics becomes increasingly important; on the other hand, to obtain the relation between contact stiffness (S), contact area ($A(h_c)$) and effective or reduced Young's modulus (E_{eff} or E_r), corrections are required, and the magnitude of the correction factor depends on the angle of the indenter.

- ***Environmental control:*** to take full advantage of the fine displacement resolution available in most IIT systems, several precautions must be taken when choosing and preparing the testing environment. Uncertainties and mistakes in measured displacement arise from two separate environmental sources: *vibration and variation in temperature.* To minimize vibration, testing system should be located on quite, solid foundation and mounted on vibration-isolation system. Thermal stability can be provided by enclosing the testing apparatus in a thermally buffer cabin and controlling room temperature to within ± 0.5 ºC.

- ***Surface preparation:*** control of the surface roughness of the samples is extremely important during the nanoindentation test because the contact areas, from which mechanical properties are obtained, and calculated from the contact depth and area function, on the presumption that the surface roughness depends on the anticipated magnitude of the measured displacements, and the tolerance for uncertainty in the contact area. The main problems are found when the characteristic wavelength of the roughness is comparable to the contact diameter.

- ***Testing procedure:*** to avoid interference from previous assays, and ensure the independence of the measurement, successive indentations should be separated up to 20 to 30 times the maximum penetration depth (h_{max}) when Berkovich or Vickers indenters are employed. For other geometries, the rule is to perform indentation separated from 7 to 10 times the maximum contact radius.

- ***Detecting the surface:*** the most important part of any good nanoindentation test procedure is to accurate identification of the location of the specimen's surface. For hard and stiff materials, such as hardened metals and ceramics, the load and/or contact stiffness, both of which increase upon contact, are often employed. However, for soft compliant materials (such as polymers and biological tissue), the rate of increase in load and contact stiffness is often too small to allow for accurate surface identification. In these situations, a better method is sometimes offered by dynamic stiffness measurement[23,24].

1.1.2. Contact mechanisms

1.1.2.1. Elastic regime

Hertz formulated elastic equations of contact for spherical surfaces in the latter part of the 19th century[25]. The model described here is essentially to study the elasto-to-plastic transition, and is partially based upon previous developments of others in the field, especially Hertbert *et al.*[26].

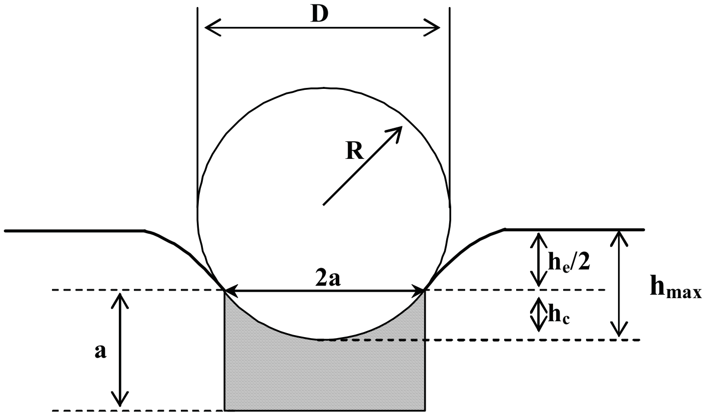

Fig. 1.4. Spherical indentation scheme[27].

Most analytical theory related to spherical nanoindentation is based on the Hertz equation in the elastic region. This theory, developed as early as 1881, is amazingly becoming more and more relevant, rather than the opposite, as technology enable us to make greater use of it. It is given below, as[18,19,28,29]:

$$P = \left(\frac{3}{4} E_{eff} R^{1/2} \right) h_e^{3/2} \qquad \textbf{eq. 1.1}$$

where R is the radius of the indenter, h_e is the elastic penetration depth into the surface, and E_{eff} is the system composite modulus, also known as effective Young's modulus given by the following equation:

$$\frac{1}{E_{eff}} = \frac{1-\nu^2}{E} + \frac{1-\nu_i^2}{E_i} \qquad \textbf{eq. 1.2}$$

where ν is the Poisson's ratio for the test material. The subindex *i* denotes the values of the indenter material. For a diamond tip indenter, the elastic constants $E_i = 1141\ GPa$ and $\nu_i = 0.07$ are often used[3]. While it may seem counterintuitive that one must know the Poisson's ratio of the studied material in order to calculate its E using the *eq. 1.2*, even a rough estimate, say $\nu = 0.25 \pm 0.1$, produces only about 5% uncertainty in the calculated value of E for most materials.

The next relationship, proven by Sneddon[30] for a rigid spherical indenter, exhibits that the elastic displacement of a plane surface above and below the contact circle are equal, and given by:

$$h_e = h_{\max} = \frac{a^2}{R} \qquad \textbf{eq. 1.3}$$

where a is the contact radius during indentation (*see Fig. 1.4*). That is correct, when the indentation is only in the elastic regime, the entire indentation depth is elastic and then total recovery is produced after the indentation process, and determined by the term on the right.

The most well-known typical plot for nanoindentation is that of load (P) versus penetration depth (h). Both the Oliver and Pharr[3] and Field and Swain[19] methods use the slopes of the initial portion of the unloading curves, dP/dh (*also known as Stiffness, S*), to calculate h_e. Differentiating *eq. 1.1* with respect to h yields:

$$\frac{dP}{dh} = 2E_{eff}R^{1/2}h_e^{1/2} \qquad \textbf{eq. 1.4}$$

When this equation is substituted back into *eq. 1.1*, the result gives us:

$$P = \frac{2}{3}\frac{dP}{dh}h_e \quad \textbf{eq. 1.5}$$

And therefore,

$$h_e = \frac{3}{2}\frac{dh}{dP}P \quad \textbf{eq. 1.6}$$

Eq. 1.6, can be re-written as follows:

$$h_e = \frac{3}{2}\frac{P}{S} \quad \textbf{eq. 1.7}$$

This equation gives h_e in terms of P and S, and with that knowledge, the contact point or the radius of the circle of contact, a, between the sample and the indenter from *eq. 1.3*; so a is now known in terms of P, S and R. The contact point can be re-written, as:

$$a = \sqrt[3]{\frac{3}{4}\frac{PR}{E_{eff}}} \quad \textbf{eq. 1.8}$$

In most cases of interest in nanoindentation testing, the indenter is in contact with what is essentially a semi-infinite half space, and so R is the radius of the indenter alone. In a similar manner, the E_{eff} is the combined elastic modulus of the contacting bodies.

Combining *eq. 1.1* and *1.3* yields:

$$\frac{P}{\pi a^2} = \frac{4}{3\pi}E_{eff}\left(\frac{a}{R}\right) \quad \textbf{eq. 1.9}$$

The left hand side of this equation represents the Meyer's hardness, also known as the indentation stress or mean contact pressure, p_m[29]. The expression in parentheses on the right-hand side represents the indentation strain[29]. These are not the same as the stresses and strains measured in uniaxial compression test, nor even the same as those for other nanoindenter tip geometries[13].

The $\frac{4}{3}\frac{E_{eff}}{\pi}$ term in *eq. 1.9* are constants, and so, for a completely elastic contact, the mean contact pressure, or indentation stress, is linearly proportional to the indentation strain as shown by the solid line in *Fig. 1.5*, where the slope is proportional to E_{eff}.

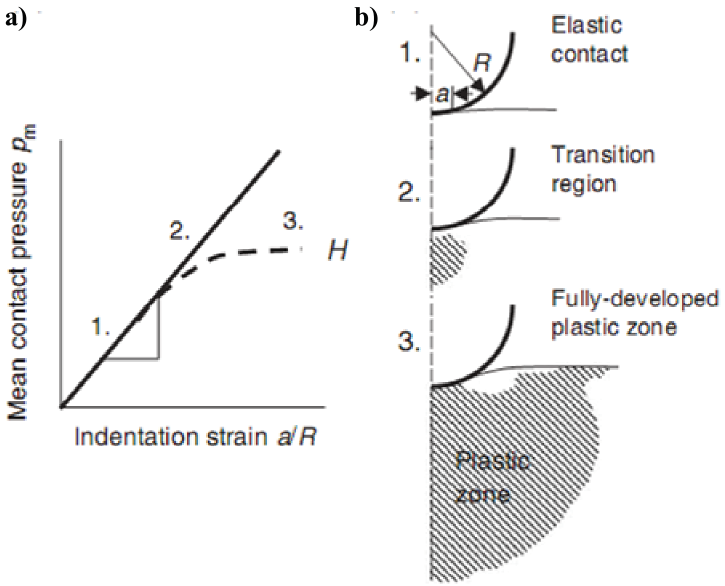

Fig. 1.5. a) Indentation stress vs. indentation strain for spherical indenter and b) schematic of evolution of the plastic zone[31].

Consider the magnitude of the contact stresses, in particular, the shear stress in the specimen material as load is applied to a spherical indenter. For a fully elastic response, the principal shear stress for indentation with a perfect spherical indenter is a maximum at around $\boldsymbol{0.47p_m}$ at a depth of around $\boldsymbol{0.5a}$ beneath the specimen surface directly beneath the indenter[32]. We should employ the Tresca and Von Mises shear stress criteria, where plastic flow takes place at $\tau \sim \boldsymbol{0.5\sigma_{ys}}$, where σ_{ys} is the material yield stress, to show that plastic deformation in the specimen beneath a spherical indenter can be first expected to occur when $\boldsymbol{p_m \sim 1.1\sigma_{ys}}$[29]. As load is further applied, the plastic zone grows in size, and these results in a levelling off of the indentation stress as shown by the dashed line in *Fig. 1.5*. This implies a deviation from the linear elastic response (*eq. 1.9*). There comes a point where any increase in load implies a proportional increase in the contact radius, and so the mean contact pressure remains constant. Under these conditions of a fully developed plastic zone, we call the mean contact pressure the hardness *H* of the specimen.

Another important factor to understand this behaviour is that there is a transition from the elastic to elastic-to-plastic contact, even for a Berkovich indenter. The relative contribution of the elastic regime to the shape of the overall *P-h* curve depends on the indenter tip radius. For an initial elastic contact, the mean contact pressure increases with increasing load. In fact, this property is very difficult to define since it depends on how it is measured. When the penetration depth becomes larger than the tip radius, the pyramidal shape of the indenter becomes the dominant geometrical feature of the indentation. The contact then usually involves a fully plastic deformation within the specimen. As we shall see, the data taken on the unloading is that used to determine the area of contact at the maximum load. This is done by using equations of contact for a conical indenter, which can mathematically transform the actual pyramid geometry into an equivalent cone. This can be easily calculated from geometry, so for a Berkovich indenter of face angle θ, we have:

$$A = 3\sqrt{3}h_c^2 \tan^2 \theta \qquad \textbf{eq. 1.10}$$

and for a conical indenter of half-apical angle α we have:

$$A = \pi h_c^2 \tan^2 \alpha \qquad \textbf{eq. 1.11}$$

where h_c is the distance as measured vertically from the indenter tip, as can be seen in *Fig. 1.6*.

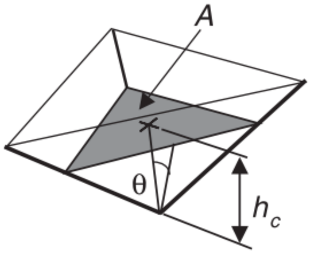

Fig. 1.6. Schematic of indenter geometry. *A* is the projected contact area, θ is the face angle, and h_c is the depth of the circle of contact measured from the apex of the indenter[29].

1.1.2.2. Elastic-to-Plastic regime

Indentation tests of many materials result in both elastic and plastic deformation of the specimen material. In brittle materials, plastic deformations most commonly occur with pointed indenters such as the Vickers diamond pyramid. In ductile materials, plasticity may be readily induced with a *blunt* indenter, such as a sphere or cylindrical punch. Indentation test are widely often used in the measurement of hardness of different materials, but some indenters such as Vickers, Berkovich, and Knoop diamond indenters may be used to investigate other mechanical properties of solids, such as strength, fracture toughness, and internal residual stresses.

Again, taking Oliver and Pharr[4] and Field and Swain[18] equations, the contact depth, h_c, can be defined as the distance from the circle of contact to the maximum penetration depth, h_{max} (see *Fig. 1.4*) as follows:

$$h_c \approx h_{\max} - \frac{h_e}{2} \qquad \textbf{eq. 1.12}$$

Combining *eq. 1.7* and *1.12* yields:

$$h_c = h_{\max} - \frac{3}{4}\frac{P}{S} \qquad \textbf{eq. 1.13}$$

Once h_c can be obtained with *eq. 1.13*. *a* can be calculated as follow:

$$a = \sqrt{2Rh_c - h_c^2} \qquad \textbf{eq. 1.14}$$

Note that the right-hand of *eq. 1.13* is only valid if $h_c << a$, and when the indenter tip is perfectly spherical. In the purely elastic regime, $h_c = h_t/2 = h_e/2$, and *eq. 1.3* and *1.14* become identical. Also, note that for the most part in the plastic regime, $h_{max} >> h_e/2$ and thus h_c is similar to h_{max} (*eq. 1.8*).

During the indentation test, as the indenter is loaded into the specimen, the indenter eventually dominates any tip-rounding effect and the deformation has the property of geometrical similarity[31]. The analysis of force-displacement or load-unload curves (*P-h*) obtained by instrumented indentation systems, is often based on the works by Doener and Nix[33] and Oliver and Pharr[3]. The two mechanical properties measured most frequently by Nanoindentation technique are hardness (*H*) and Young's modulus (*E*) with a sharp indenter like the Berkovich. For materials that do not experience pile-up, which includes most ceramics, hard materials and soft metals that work hardened these mechanical properties can be determined generally within ± 10%, sometimes better. The method was developed to measure the *H* and *E* of materials from indentation load-displacement data (*P-h*), obtained during one cycle of loading and unloading, although it was originally thought for applications with sharp indenter, like Berkovich. A schematic representation of a typical data set obtained with a Berkovich indenter can be observed in *Fig. 1.7*, where *P* designates the load, and *h* the displacement relative to the initial undeformed surface.

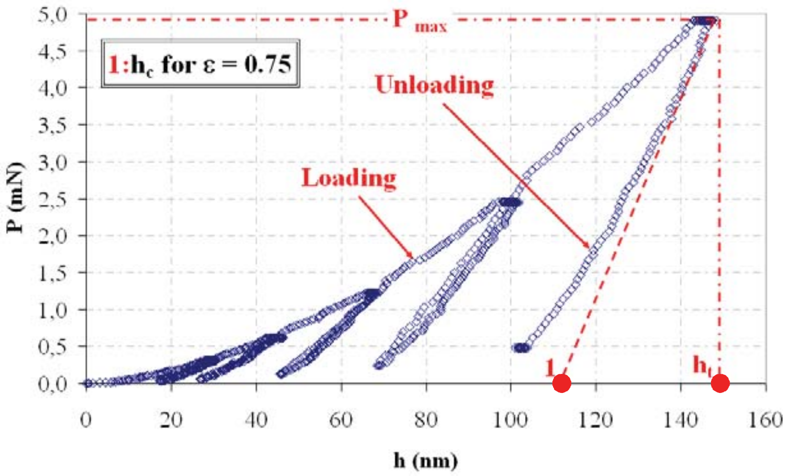

Fig. 1.7. Schematic illustration of indentation *P-h* data showing important measured parameters.

The *P-h* curve exhibits the elastic/plastic behaviour of each sample. From the difference between total indentation depth at maximum indented load (h_{max} or h_t), and depth of residual impression upon loading (h_f), the elastic recovery can be calculated[5]. In *Fig. 1.7,* there are four important magnitudes that must be measured: *i)* the maximum applied load (P_{max}), *ii)* the maximum penetration depth (h_{max} or h_t), *iii)* the final penetration depth (h_f), and *iv)* the elastic unloading stiffness ($S=dP/dh$), defined as the slope of the upper portion of the unloading curve during the initial stages of unloading. The parameter *S* has the dimensions of load per unit distance, and is known as the elastic contact stiffness, or more simply, the contact stiffness. Such experimental results are summarized as follows[2]:

- The initial *P-h* response is elastic and can be described by continuum level contact mechanics.

- The first deviation from this elastic response occurs when the local maximum shear stress level sustained by the indented material is on the order of the theoretical shear strength of material.
- Following this initial plastic event, a series of similar discontinuities in the *P-h* response occurs. Nevertheless, the fundamental mechanisms responsible of the experimentally observed discrete deformation processes under this nanoscale contact are still debated in the literature.

The loading response of the material will show, therefore, if the indentation probe is blunt or sharp, producing an elastic initial response or an elasto-plastic response. Once the loading is sufficiently high, both indenters will produce similar elasto-plastic response in the material. It has to be taken into account that all real sharp indenters have a tip curvature which translated into a blunt indentation at the initial contact depths. The analysis of the *P-h* curves is different if it is a loading curve (*which can be elastic or elasto-plastic*) or an unloading curve, where the material is usually deformed.

The accuracy of the mechanical properties in plastic deformation range depends on how well these three parameters can be experimentally measured. One of these parameters is the residual depth after the indenter is fully unload; in other words, with this value, the plastic work (W_p) necessary to deform the material of the study can be obtained. The suitable procedure used to measure *H* and *E* is based on the unloading process shown schematically in *Fig. 1.8*, in which it is assumed that the behaviour of the Berkovich indenter can be modelled as a conical indenter.

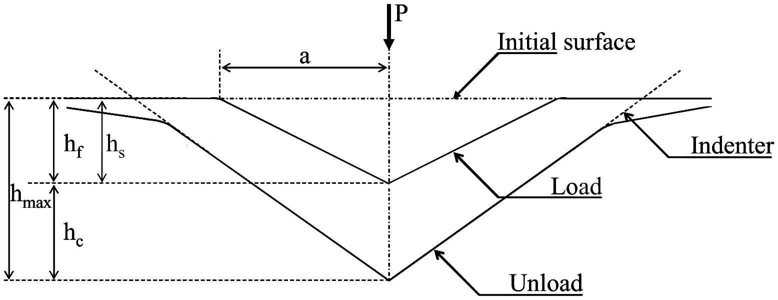

Fig. 1.8. Schematic illustration of the unloading process showing the parameters used to characterize the contact geometry.

The *H* and *E* are calculated as a function of penetration depth using the method of Oliver and Pharr[13]. In this method, the contact depth (h_c) is expressed as:

$$h_c = h_{\max} - \varepsilon \frac{P}{S} \qquad \textbf{eq. 1.15}$$

where ε is a parameter approximately equal to 0.75 for a Berkovich indenter, and S is the contact stiffness. Based on the contact depth, the contact area $A(h_c)$ is calculated using the form factor of the indenter. Once the correct area function is known, the H is calculated by dividing the P_{max} by the projected contact area, as follows:

$$H = \frac{P_{\max}}{A(h_c)} = \frac{P_{\max}}{24.56 h_c^2} \qquad \textbf{eq. 1.16}$$

This H, defined as instrumented indentation hardness, differs from that of a Vickers indentation. *Eq. 1.16* employs the projected area of contact and is calculated at P_{max}. In contrast, Vickers hardness (H_v) is measured upon unloading. Measuring H_v using the residual imprint leads to error because of the elastic relaxation that occurs during or after unloading. This phenomenon is particularly important in ceramic materials, and may explain the difference observed in the literature between instrumented indentation hardness and H_v[8]. E_{eff}, is calculated as follows:

$$E_{eff} = \frac{1}{\beta} \frac{\sqrt{\pi}}{2} \frac{S}{\sqrt{A(h_c)}} \qquad \textbf{eq. 1.17}$$

where β is the geometry shape factor and equal to 1.034 for a Berkovich indentation[4,30,34]. *Eq. 1.17* is found in elastic contact theory[30], and holds for any indenter that can be described as a body of revolution of a smooth function[3]. As this equation was derived for an axysimetric indenter, it is formally applied only to circular contacts, for which the indenter geometry parameter is $\beta = 1$. However, it has been shown that the equation works also well when the geometry is not axysimetric, provided that different values of β are employed[8]. For indenters with square cross sections, like the Vickers pyramid, β is equal to 1.012; for triangular cross sections, like the Berkovich and the cube-corner indenters, β is equal to 1.034[34]. This factor plays a very important role when accurate property measurements are desired. This constant affects not only the elastic modulus calculated from the contact stiffness by means of *eq. 1.17*, but also the H, because it is used for determining the indenter area function which is also based on *eq. 1.17*, and area functions can be erroneous if the wrong value of β is employed. An effective modulus, E_{eff}, is used in *eq. 1.17* to account for the fact that elastic displacements occur in both the indenter and the sample.

The most important matter is to determine the contact stiffness and the contact area as accurate as possible. From *eq. 1.16* and *1.17*, it is clear that, in order to calculate the H and E of the studied material from indentation P-h displacement curves, accurate measurements of the S and the $A(h_c)$ must be performed. One of the main distinctions between nanoindentation and conventional hardness testing equipments, is the way to obtain the $A(h_c)$. Rather than by imaging, the $A(h_c)$ is established from an analysis of the indentation P-h data *(see Fig. 1.7)*.

The analysis used to determine the H and E, is essentially an extension of the method proposed by Doener and Nix[14], which accounts for the fact that unloading curves are distinctly curved, in a manner that cannot be accounted for by that flat punch approximation. Doener and Nix[14] consider that the $A(h_c)$ remains constant as the indenter is withdrawn, and the resulting unloading curve is linear. The Oliver and Pahrr[13] method begins by fitting the unloading portion of the P-h curve to the power-law relation. This can be re-written as follows:

$$P = BA\left(h - h_f\right)^m \qquad \textbf{eq. 1.18}$$

where B and m are power-law fitting constants[3], and h_f is the final displacement after complete unloading process, also determined from the curve fit. The S is established by analytically differentiating *eq. 1.18*, and evaluating the results at the maximum depth of penetration, $h = h_{max}$, that is:

$$S = \left.\frac{dP}{dh}\right|_{h=h_{\max}} \qquad \textbf{eq. 1.19}$$

Differentiating *eq. 1.18*, the S can be obtained with the following equation:

$$S = Bm\left(h_{\max} - h_f\right)^{m-1} \qquad \textbf{eq. 1.20}$$

It is wise prudent, when S has been calculated with *eq. 1.20*, to fit only the upper portion of the unloading curve; moreover, the value of S determined from this fit should be checked by comparing the curve fit to the data. Fitting the upper 25 to 50% of the data is usually sufficient. Now, the contact depth, h_c, has been calculated, which for elastic contact is less than the total depth of penetration, h_{max}, as illustrated in the *Fig. 1.8*. The basic assumption is that the contact periphery sinks in a manner that can be described by models of indentation of a flat elastic half-space by rigid punches of simple geometry[30]. This assumption limits the applicability of the method, because it does not account for the pile-up of material at the contact periphery, which occurs on some elastic-plastic materials.

Assuming, however, that pile-up is negligible, the elastic models show the amount of sink-in, h_s, which is given by the follow equation:

$$h_s = \varepsilon \frac{P_{\max}}{S} \qquad \textbf{eq. 1.21}$$

where ε is a constant that depends on the geometry of the indenter. Typical values are: 0.72 for a conical punch indenter, 0.75 for a parabolic of revolution, and 1 for flat punch[13]. From the geometry in *Fig. 1.8*, the depth along contact between the indenter and the specimen, h_c, can be calculated by:

$$h_c = h_{\max} - h_s \qquad \textbf{eq. 1.22}$$

Using *eq. 1.21* and *1.22*, the contact between the indenter and the specimen can be re-written as *eq. 1.15*. The projected contact area is calculated by evaluating an empirically determined indenter area, as a function of $A = f(h)$[13] at the h_c; that can be re-written as:

$$A = f\left(h_c\right) \qquad \textbf{eq. 1.23}$$

The area function, also known as the shape function or tip function, must be carefully calibrated with standard fused Silica, which presents a constant E value of 72 GPa[13] by independent measurements; so that deviation from non-ideal indenter geometry is taken into account. This deviation can be quite deep near the tip of the Berkovich indenter, where some rounding inevitably occurs during the grinding process. The equation employed to perform the correct contact area calibration can be re-written as follows:

$$A(h) = \sum_{n=0}^{8} C_n (h_c)^{2-n} =$$

eq. 1.24

$$= C_o h^2 + C_1 h + C_2 h^{1/2} + C_3 h^{1/4} + \ldots + C_8 h^{1/128}$$

where C_o to C_8 are constants determined by curve-fitting procedures. A perfect pyramid or cone is represented by the first term alone. The second term describes a paraboloid of revolution, which approximates to a sphere at small penetration depths, and a perfect sphere of radius R is described by the first two terms with $C_o = -\pi$ and $C_1 = 2\pi R$[13].

1.1.3. Considerations to be accounted for during the indentation process

1.1.3.1. Effective Indenter Shape

The effective indenter shape is outlined in *Fig. 1.9*. The basic principles are derived from observation gleaned from finite element simulations of indentation of elastic-plastic materials, by rigid conical indenter with a half included angle of 70.3°[13]. During the initial loading of the indenter, *Fig. 1.9a*, both elastic and plastic deformation processes occur, and the indenter conforms perfectly to the shape of the hardness impression. However, during the unloading process, *Fig. 1.9b*, elastic recovery forces the hardness impression to change its shape. A key observation is that the unload shape is not perfectly conical, but exhibits a subtle convex curvature that has been exaggerated in the *Fig. 1.9*; the $A(h_c)$ increases gradually and continuously until full load is again achieved, a process which must be the reverse of what happens during unloading process because both processes are elastic. It is this continuous change in $A(h_c)$ that produces the nonlinear unloading curves. Furthermore, the relevant elastic contact problem is not that of conical indenter on a flat surface, but a conical indenter pressed into a surface that has been distorted by the formation of the residual impression.

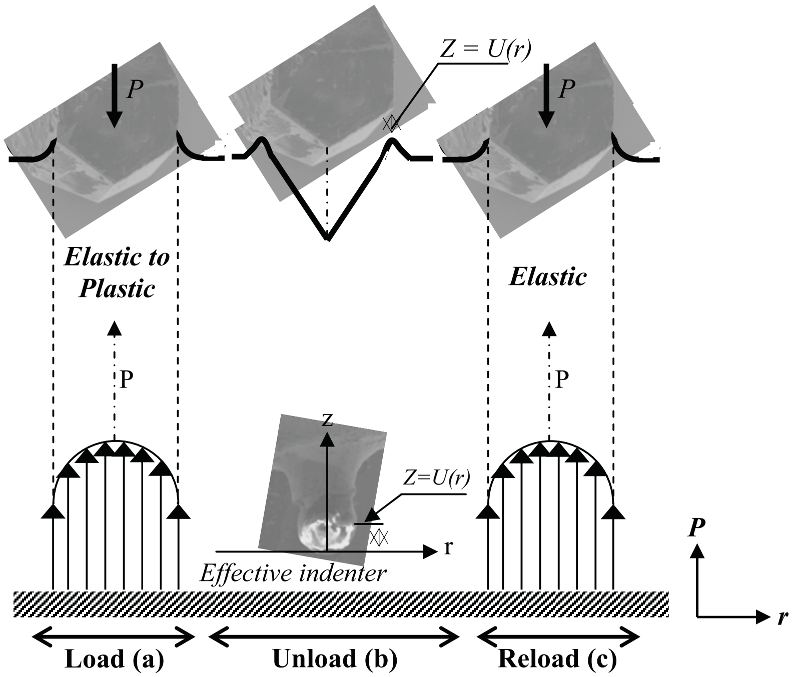

Fig. 1.9. Concepts used to understand and define the effective indenter shape, a) load process, b) unload process, and c) reload process.

1.1.3.2. Errors due to pile-up and sink-in

In an indentation performed on any type of material, the surface of the different specimens is typically drawn inwards and downwards underneath the indenter, and sink-in effect takes place. When the contact involves plastic deformation, the material may present either sink-in, or pile-up effects around the residual indentation imprint. In the fully plastic regime, the behaviour is seen to be dependent on the ratio E/σ_{ys} , where σ_{ys} is the yield strength of the material, and the quotient between E and σ_{ys} is the strain-hardening of the material. The mechanical behaviour of a typical specimen can be described by a conventional stress-strain relationship, which includes a strain-hardening exponent:

$$\sigma = E\varepsilon \qquad when \qquad \varepsilon \le \frac{\sigma_{ys}}{E} \qquad \textbf{eq. 1.25}$$

$$\sigma = k\varepsilon^{n} \qquad when \qquad \varepsilon \ge \frac{\sigma_{ys}}{E} \qquad \textbf{eq. 1.26}$$

where k is equal to:

$$k = \sigma_{ys}\left[\frac{E}{\sigma_{ys}}\right]^{n} \qquad \textbf{eq. 1.27}$$

Such a complication arises from the pile-up or sink-in of the material around the indenter, which is mainly affected by the plastic properties of the material[35]. In a low strain-hardening alloy, plastically displaced material tends to flow up to (*and pile-up against*) the faces of the indenter, due to the incompressibility of plastic deformation. The result is a barrel-shaped impression due to pile-up around the sharp-indenter. In high strain-hardening materials, the region deformed by plasticity is pushed out from the indenter with the imprint sinking below the initial surface level. The results are a pin-cushion like impression around the sharp indenter, as shown in *Fig. 1.10*.

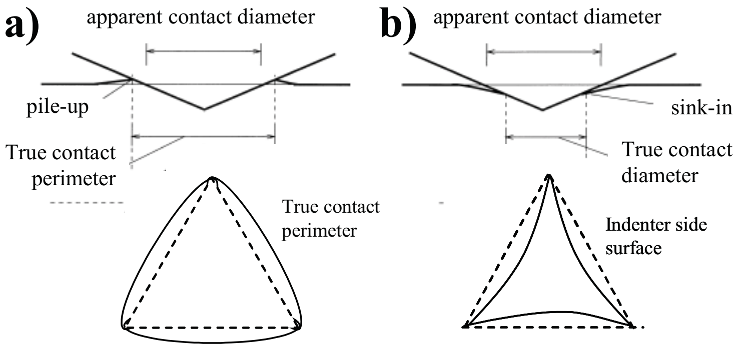

Fig. 1.10. Schematic illustration of a) pile-up and b) sink-in around a sharp indenter.

As a consequence of pile-up or sink-in effects, large differences may arise between the true contact area and the apparent contact area, which is usually observed after the indentation process. One significant problem related to the determination of the contact area with the Oliver and Pharr equations[13], is that this method does not account for pile-up of material around the contact impression. When pile-up takes place, the $A(h_c)$ is greater than that predicted by this method, and the H and E are overestimated, sometimes by as much as 50%[14].

Pile-up is large only when the relation between h_f/h_{max} is close to 1, and the degree of work hardening is small. It should also be noted that when this relation is lower than 0.7, very little pile-up can be observed, no matter what the work-hardening behaviour of the material. In this case, the $A(h_c)$ given by this method matches very well the obtained true contact area. On the other hand, when this relation is higher than 0.7, the accuracy of the method depends on the amount of work-hardening on the material.

For sharp punch indenter (*i.e. Berkovich*), indentation with a large amount of pile-up can be identified by the distinct bowing out at the edges of the contact impression**[13]**. If pile-up is large, accurate measurements of H and E cannot be obtained using the $A(h_c)$ derived from the P-h curve. In this case, the most useful method to correct these problems is known as Cheng and Cheng method**[36, 37]**. These equations are functions of the total work of indentation (W_{tot}), and the work recovered during unloading (W_u).

The method that they proposed to account for pile-up, is based on the work of indentation**[37]**, which is measured from the areas under indentation loading and unloading curves. The relation proposed by Cheng and Cheng can be expressed as follows:

$$\frac{W_{tot}-W_u}{W_{tot}} \cong 1-5\frac{H}{E_{eff}} \qquad \textbf{eq. 1.28}$$

Combining *eq. 1.16* and *1.17* and considering β as 1. Another equation involving H and E_{eff} can be obtained:

$$\frac{4}{\pi}\frac{P_{\max}}{S^2} = \frac{H}{E_{eff}^2} \qquad \textbf{eq. 1.29}$$

where W_{tot}, W_u, P_{max}, and S are all measurable from P-h curves. The *eq. 1.29* or known as Joslin and Oliver's**[38]** widely employed during the calibration procedures, is based on an observation that the ratio of the load to the stiffness square, P/S^2, is a directly measurable experimental parameter that is independent of the penetration depth or contact area, provided that the hardness and elastic modulus do not vary with the penetration depth**[13]**. The utility of the parameter stems from its independence of the contact area. Joslin and Oliver**[38]** exploited this relation to comparatively evaluate the mechanical properties when surface roughness led to uncertainties in the contact area.

Spherical indentation differs from conical or pyramidal indentation in that there is no elastic singularity at the tip of the indenter to produce large stresses. Stress-strain curves can be approximated from indentation data using the classical approach of Tabor[29]. Field and Swain[18,19] have applied Tabor's approach to instrumented indentation, and have developed a method that uses the indentation load-displacement data to approximate the stress-strain curve and the work-hardening exponent. The approach requires the deformation to be fully plastic. Pile-up geometry can change considerably during the course of spherical indentation, and it is therefore not possible to predict the pile-up based on the mechanical properties of the material alone, even when fully plastic deformation is achieved.

1.1.4. Thin solid films characterization

In recent years, the modification of surface properties by applying films and multilayers with a submicron thickness has become widely used. Thin films have been traditionally used in planar microelectronics, sensors, systems of magnetic and optical recording and storage of information, micro-/nanoelectromechanical systems, optics, triboengineering, protection against corrosion and high temperatures, and other multidisciplinary fields. It is clear that the appearance of additional inner boundaries and materials can lead to a substantial change in the mechanical properties, the different behaviours in the course of local loading, and the shape of the P-h curves upon nanoindentation. In this case, it is possible to identify several problems associated with the testing: the correct determination of the thickness or the H and the E of the thin film, without the influence of the underlying materials on the results of measurements, as well as the evaluation of internal stresses in individual layers and their adhesion to each other (or the parameter K_{IC} in the case of fracture along the layer boundaries).

1.1.4.1. Testing of thin films

When an instrumented indentation is performed on a ceramic layer coating a bulk material, at a given penetration depth the response will be given by the first indentation layer, but the substrate may also influence the indentation response. Therefore, the response in the nanoindentation test may be due to the elastic and plastic deformation of the film material and/or to other fracture mechanisms activated during the indentation process [39] . When the mechanical properties of thin films are determined by nanoindentation technique, the influence of the substrate must be considered. In nanoindentation experiments, the P, and the h_{max} or h_t, are measured as a function of time during the loading and unloading processes. Depending on the specific testing system, loads as small as 1 nN can be applied, and displacements of 0.1 nm can be measured. Mechanical properties, such as H, E, K_{IC}, σ_{ys}, and τ, can be obtained from the P-h curves. The response of a coating system will be a combination of the response of the different materials: the coating and the substrate. The H depends on the depth of penetration, as film is constrained by the substrates[31,40]. The nanoindentation imprint induces two different deformation ranges: elastic and plastic. The elastic deformation disappears when the indenter unloads the sample, which leaves just the permanent or plastic deformation. This is an important parameter in the study of a thin film's mechanical properties. The measured H and E is a complex value that depends on the relative indentation depth, and the mechanical properties of both the film and the substrate (H_f, H_s, E_f, and E_s where the subindex f and s denote to the film and substrate properties, respectively). Above a certain critical penetration depth, the composite mechanical properties (E_c or H_c), which includes a component of E_s or H_s, will be measured. Both quantitative and qualitative informations can be obtained from nanoindentation experiments on thin film systems. The presence of some discontinuities in the P-h response reveals information about the cracking, delamination, and plasticity in the film and substrate. The main difficulty found in nanoindentation of thin films is to avoid unintentional probing of the properties of the substrate. To achieve this, it is common to restrict the maximum depth of penetration in a test to no more than 10% of the film thickness (t), although research suggests that this rule has no physical principles[41] for indentation with a conical or pyramidal indenter. As a result of the thin film study, H and E_{eff} of the film are widely affected by its interaction, in the plastic range, with the substrate. *Fig. 1.11a*, shows a plastic deformation zone in which the applied load is very low, and the penetration depth is in the nanometer scale. In this case, the mechanical properties of the thin film have been obtained without substrate contribution. Higher applied loads or penetration depths (see *Fig. 1.11b*) cause deeper plastic deformation. Therefore, the mechanical properties of the interface between the coating and substrate can be studied.

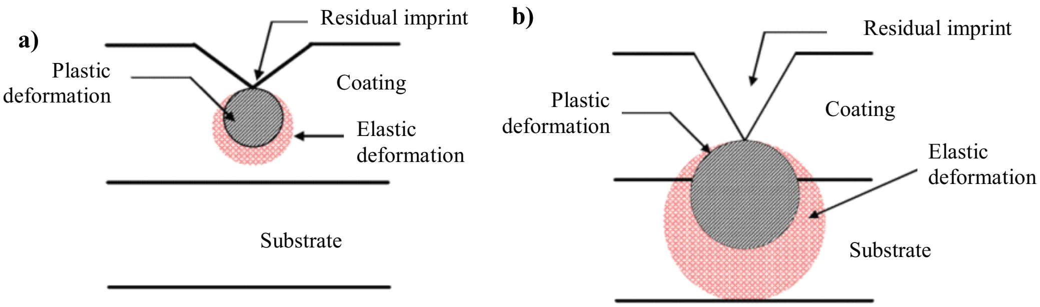

Fig. 1.11. Scheme of the nanoindentation imprint and the plastic deformation zone in a bilayer material when the applied loads were a) small, and b) high.

1.1.4.2. Film thickness

The coating thickness can be determined using the analysis of the *P-h* curves and from the morphology of scratches upon lateral displacement of the indenter under the action of a linearly increasing normal load[1].

1.1.4.3. Film hardness, H_f

When the ranges of measured H_f values are plotted against displacement for a particular film/substrate system, three different regimes become evident. A scheme is exhibited in *Fig. 1.12* for a hard film on a soft substrate. The normalised depth is the h_c divided by the film thickness, *t*. For shallow penetration depths (*I region*), the response is only attributed to the film properties, as *H* presents a constant value. As the depth increases (*II* region), the *H* gradually decreases, and it is associated to the mixed response of the coating and the substrate. At a higher indentation depth (*III region*), the response is mainly dominated by the substrate.

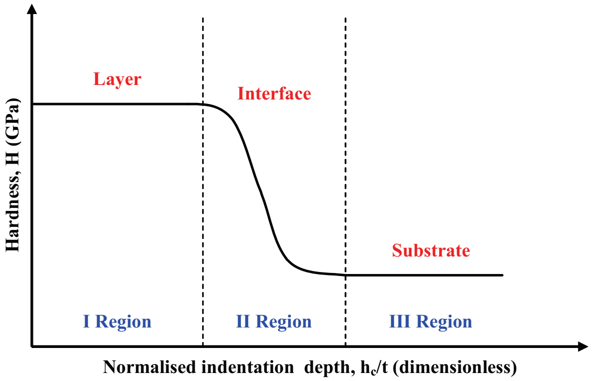

Fig. 1.12. Scheme of the variation in simple hardness with normalised depth for a hard film on a soft substrate.

The standard requirements for the procedure of measuring the H involve the following recommendation: h should not be larger than one -tenth of the thickness, t, of the layer of the material for which the property is to be measured (this reliably excludes the influence of substrate on the results of measurements). For relative hard systems, it is generally accepted that an instrumented indentation with h_{max} of less than 10% of $t_{coating}$ will yield to the H of the coating without any substrate influence[31]. However, it is somewhat not easy to indent to a penetration depth less that this value, because the coating is too thin or because of experimental limitations of nanoindentation technique. In this case, there are several models for fitting the composite hardness (H_c) response of the film-substrate as a function of the h[31]. These models allow us to extract the hardness of the coating (H_f) when the hardness of the substrate (H_s) and the H_c at different penetration depths are known and extrapoling to zero depth. Research in this area is usually focused on establishing a value for the critical indentation depth, expressed as a percentage, below which the influence of the substrate is less than some desired amount. Bückle[42] proposed that the H_c of a thin film system could be expressed as follows:

$$H_c = H_s + \alpha\left(H_f - H_s\right) \qquad \textbf{eq. 1.30}$$

where the subindex s and f denote the mechanical properties of the substrate and the film, respectively, and α is an empirical derived parameter. Jonsson and Hogmark[43] proposed a law of mixtures, proportional to the contact area between the tip and the respective layers. This equation can be written as:

$$H_C = \left(\frac{A_f}{A}\right)H_f + \left(\frac{A_S}{A}\right)H_S \qquad \textbf{eq. 1.31}$$

where A_f and A_s are the relative contact areas carried by the film and the substrate, respectively, and A is the total contact area. A similar treatment, but based on a volume of deformation law of mixtures, was proposed by Burnett and Rickerby[44]. Tsui, Ross and Pharr[45] have proposed an empirical equation to correct pile-up effects for the case of soft materials on hard substrates, which permits A in *eq. 1.31* to be accurately determined without imaging. Bhattacharya and Nix[46] proposed that the H_c can be calculated by the next equation:

$$H_C = H_S + \left(H_f - H_S\right) e^{\left(-\frac{Y_f}{Y_S}\frac{E_S}{E_f}\left(\frac{h}{t}\right)^2\right)} \qquad \textbf{eq. 1.32}$$

where Y_f and Y_s are the material yield stresses for the film and substrate, respectively. However, for hard film on soft substrate, the expression becomes:

$$H_C = H_S + \left(H_f - H_S\right) e^{\left(-\frac{H_f}{H_S}\frac{Y_f}{Y_S}\sqrt{\frac{E_S}{E_f}}\frac{h}{t}\right)} \qquad \textbf{eq. 1.33}$$

Despite of these analytical and, sometimes, empirical treatments, there is still no proposed relationship that can cover a wide range of materials behaviour. In the absence of any rigorous relationship, the conventional 10% of the thickness rule appears to be that most generally used.

1.1.4.4. Elastic modulus of films, E_f

Compared to the H, the contact stiffness is more strongly affected by the substrate, which manifest itself even at $h < 0.1t$[47]. The measurement of the E in coatings and films present the same problems as the measurement of H. In this case, the substrate influences the response at lower penetration depths, as the elastic field has a larger volume than that produced by plastic deformation. Therefore, to accurately characterize the response of the coating, smaller penetrations depths are required. A careful calibration of the indenter tip has to be made with a standard fused silica material, in order to improve the geometric and contact area values employed in the Oliver and Pharr equations[3]. The plot of the E_{eff} values vs. the h_c results in a similar scheme, as shown in *Fig. 1.13*. However, in this case, the first region -corresponding to the thin film's mechanical properties- is smaller than the second one. In this case, the first region is highly dependent on the penetration depth, and the deformation produces a decrease in the E_{eff} of the thin film value (E_{eff} is directly proportional to the correlation between the material under study and the tip indenter material, as given by *eq. 1.17*). There are several models in the literature for extraction of E after the correct analysis of the evolution of E_{eff} for different penetrations depths[31].

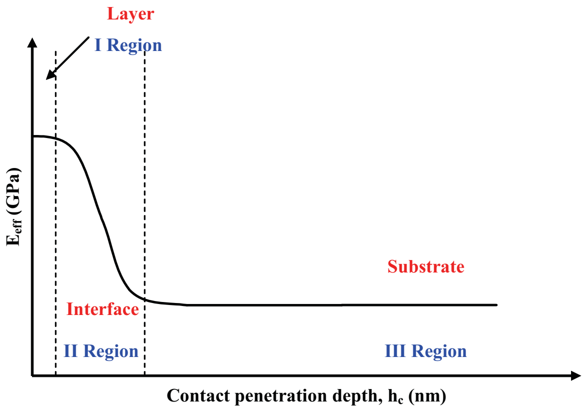

Fig. 1.13. Scheme of the variation in sample E_{eff} with h_c for a hard layer and soft substrate.

Since there is always some elastic displacement of the substrate during an indentation test, the traditional 10% rule does not strictly apply for modulus measurements of thin films. King *et al.*[34] evaluated the empirical treatment of Doener and Nix[33] using the finite element method (FEM), to get an expression for the combined modulus of the film/substrate and indenter denoted E_{eff}:

$$\frac{1}{E_{eff}}=\frac{\left(1-v_f^2\right)}{E_f}\left(1-e^{-\alpha t/\sqrt{A}}\right)+\frac{\left(1-v_S^2\right)}{E_S}\left(1-e^{-\alpha t/\sqrt{A}}\right)+\frac{\left(1-v_i^2\right)}{E_i} \qquad \textbf{eq. 1.34}$$

where the subscripts *f*, *s*, and *i* refer to the film, substrate, and indenter respectively, α is an empirical constant, and A is the contact area. Gao, Chiu, and Lee[48] used a moduli - perturbation method, in which a closed- form solution results in an expression for the E_{eff} of the film/substrate combinations. This relationship can be re-written as follows:

$$E_{eff}=E_S+\left(E_f-E_S\right)I_O \qquad \textbf{eq. 1.35}$$

where I_o is a function of *t/a* (being *t* the film thickness, and *a* the contact radius) given by the follows equation:

$$I_O=\frac{2}{\pi}\tan^{-1}\frac{t}{a}+\left[\left(1-2v\right)\frac{t}{a}\ln\left(1+\frac{\left(t/a\right)^2}{\left(t/a\right)^2}\right)-\frac{t/a}{1+\left(t/a\right)^2}\right]\left(\frac{1}{2\pi\left(1-v\right)}\right) \qquad \textbf{eq. 1.36}$$

The most widely employed model is the Bec *et al.* model[49], which allows to obtain the E_f in an easy way. The Bec *et al.* model can be re-written as:

$$\frac{1}{2\cdot E_{eff}\cdot a}=\frac{1}{1+\frac{2\cdot t}{\pi\cdot a}}\cdot\left(\frac{t}{\pi\cdot a^2\cdot E_f}+\frac{1}{2\cdot a\cdot E_s}\right) \qquad \textbf{eq. 1.37}$$

where a is the projected area, E_f and E_s are the Young's modulus of the film and the substrate, respectively.

1.2. Superconductor materials

The phenomenon of superconductivity has not lost its fascination, since its discovery in 1911. Electric current flows without resistance, in the superconducting (*SC*) state, that is the electrical resistance of the material falls to extremely low values, very close to zero. The ratio of resistance between the normal-conducting and the *SC* state has been tested to exceed 10^{14}, i. e.: it is at least as large as between a usual insulator and copper, the best conducting material known[50].

Nevertheless, superconductivity is more than just the disappearance of resistance. The *Meissner effect*, the expulsion of magnetic fields from a superconductor, discovered in 1933, shows that superconductivity is a true thermodynamical state of matter since, in contrast to the situation for a merely perfect conductor, the expulsion is independent of the experimental history[50]. As the progress of cooling technique gave access to lower and lower temperatures, superconductivity establishes as common low-temperature instability of most, possibly all, metallic systems.

The explanation of superconductivity by the Bardeen, Cooper, and Schrieffer theory (*BCS*) in 1975[51], was a desperately awaited breakthrough of theoretical solid state physics. The starting point was the consideration that phonons introduce an attractive interaction between electrons close to the Fermi surface (*overscreening*). The key idea is that an attractive interaction leads here to bound electron pair states (*Cooper pairs*). These pair states are no longer obliged to obey the Fermi-Dirac statistic, which enforced the electrons to occupy high kinetic energy single particles states due to the Pauli principle. The energy gain of the SC states with respect to the normal state does not result from the small binding energy of the pairs but it is the condensation energy of the pairs merging into the macroscopic quantum state. It can be measured as an energy gap for electron excitation into single particles states.

Since about 1962 it has become universally recognized that there exist a whole new class of superconductors, type II in opposition to metals (Type I), which are characterized by the fact that they exhibit a new type of reversible magnetic behaviour. This discovery has made it possible to better understand many of the previously unexplained superconducting properties of a high number of elements and alloys. Furthermore, it has led to the recognition of the existence of a new thermodynamic state, the mixed state, which is only shown by type II superconductors. In addition to their intrinsic scientific interest, they have a technological importance; niobium-zirconium alloys and the compound Nb_3Sn have been used in the construction of superconducting solenoids capable of producing steady fields of *50* or *100 kOe*[51].

In 1986, Bednorz and Muller[52,53] discovered a new type of superconducting ceramic materials, now known as high temperature superconductors (HTSCs), which drastically improved the superconducting transition temperature, T_c. Further, $YBa_2Cu_3O_{7-\delta}$ (YBCO or Y-123) was discovered by a group of researchers at the University of Houston in 1987[54]. The T_c of YBCO material exceeded the boiling point of liquid nitrogen (92K vs. 77K). As a consequence, the superconducting products were expected to be operable using liquid nitrogen, which is cheaper and easier to handle than Helium; this is one of the most important advantages of HTSCs[53]. Moreover, the next year new superconducting materials were discovered in the Bi (Pb)-Sr-Ca-Cu-O system[55], with a T_c of 110K, and in the Tl-Ba-Ca-Cu-O system[56] with a T_c of 125K. In 1993, $HgBa_2Ca_2Cu_3O_9$, with a T_c of 134 K was discovered[57], and at present, T_c has reached 164 K, under high pressure[58].

The period of 1994 to 1996 was very fruitful for the synthesis of new superconducting materials. A significant success of the last three years was the synthesis of a large group of mercury-containing HTSCs, which have the highest critical temperature of the superconducting transition[57,59,60]. The general formula of these types of compounds is $HgBa_2Ca_{n-1}Cu_nO_{2n+2+\delta}$. The third member of the family ($n=3$) has a sharp superconducting transition at 133K[61]. It was found that, as in the system of $Bi_2Sr_2Ca_{n-1}Cu_nO_x$, doping with Pb helps material growth whilst retaining T_c close to that optimally doped $HgBa_2Ca_2Cu_3O_{8+\delta}$[62]. The second member of this family, $HgBa_2CaCu_2O_{6+\delta}$, has a critical temperature of 127K[63]. Application of pressure can increase the critical temperature of the second member to 154K and that of the third to 160K[64].

The search of organic superconductors had been boosted in the 1960s by the idea that conductive polymer chains with polarizable molecular groups may provide a highly effective Cooper pair coupling for electrons running along the polymer chains, by means of an energy exchange via localized excitons[65]. Since the first discovery of an organic superconductor in 1980[66] remarkable critical temperatures $T_c > 10K$ have been achieved[67]. However, the origin of superconductivity has turned out to be certainly far from the suggested excitonic mechanism. The electric conduction appears here from π-electrons in stacked aromatic rings, which form one- or two-dimensional delocalized electron system. Similar to HTSC, the restriction of the effective dimensionality and strong Coulomb repulsion effects push the systems towards metal-insulator, magnetic and SC transitions.

The huge surprise came in 2001, with the discovery of superconductivity up to T_c = 40K in MgB_2, a compound which was well-known since the 1950s, and which was in 2001 already commercially available in quantities up to metrical tons[68]. As for the fullerides, in spite of the high T_c, a phononic mechanism is highly plausible: Strong Coulomb correlation effects are not expected since the conduction electron system does neither involve inner atomic shells nor a reduction of the effective dimensionality. Nevertheless, new theoretical ingredients are required for a satisfactory explanation of the experiments[50].

This recent example proves that scientific surprises can be encountered, even in seemingly well-investigated research areas, and that superconductivity will certainly remain for a long time to come at the forefront of physics and materials research.

1.2.1. Applications

Besides the scientific interest, the search for applications has always been a driving force for superconductor material science[69]. Right from the discovery, it had been envisioned that *SC* coils with high persistent current might be used to generate strong magnetic fields. However, for the first generation of *SC* materials (*Type-I*), superconductivity was easily suppressed by magnetic fields (critical magnetic field, H_c).

A first step towards this goal was the discovery of *Type-II* superconductors, where the magnetic penetration depth (λ) exceeds the SC coherence length (ξ^{i}). This enables a coexistence of superconductivity and magnetic field, which are allowed to penetrate into the *SC* bulk in the quantized form of vortices. The last ingredient required for technically applicable *"hard"* superconductors was the discovery and engineering of pinning centres, which fix penetrate magnetic flux, and prevent its Lorentz force driven flow through the superconductor that otherwise generates power dissipation.

Nowadays, NbTi and Nb_3Sn conductors are the basis of a billion euro *SC* wire industry, which delivers magnets that cannot be realized by means of conventional metal wire conductors, such as for Magnetic Resonance Imaging (*MRI*) systems, and High-Energy Physics (*HEP*) particle accelerators[50,69,70]. The enormously high critical fields (H_{c2} ~ 100T) of HTSC [71] indicate their potential for extremely high-field applications. However, HTSC vortex physics has turned out to be much more complex than what had been known from classical superconductors[72]. This implies strong restrictions for high-field, high-temperature HTSC magnets hope. Nevertheless, in spite of earlier concerns about the ceramic nature of HTSC, flexible HTSC-based conductors are steadily progressing towards applications, where a substantial size decrease justifies the cryogenic efforts. HTSC current leads are just being introduced worldwide in *HEP* accelerators to transport kA-sized currents at a substantially reduced heat leakage[73].

Nb-based SC radio frequency-cavities represent another recent technological progress of *HEP* accelerators. An extremely high quality factor provides here a much better transfer of acceleration energy to the particle bunches than in conventional cavities. Miniaturized microwave filter, e.g., for mobile phone base stations, are at present the most advanced HTSC electronics application[74].

Josephson junctions[50], well-defined weak links of SC regions, can be coupled to *Superconducting Quantum Interferometric Devices, SQUID* [75, 76], magnetic flux detectors with quantum accuracy that are the most sensitive magnetic field detectors presently available. SQUIDs based on Nb/AlO_x/Nb Josephson junctions achieve today at liquid helium (L_{He}) temperature a magnetic noise floor around 1 $fT/Hz^{1/2}$, which enables diagnostically relevant magnetic detection of human brain signals

---

[i] ***Coherence length*** is the propagation distance from a coherent source to a point where an electromagnetic wave maintains a specific degree of coherence.

(*magnetoencephalography, MEG*[77]). HTSC SQUIDs at liquid nitrogen operation have approached this magnetic sensitivity within one order of magnitude[78], and are already in commercial use for the non-destructive evaluation (*NDE*) of defects in complex computer chips[79] and aircrafts[80].

In the 1970s and 1980s, IBM as well as a Japanese consortium including Fujitsu and Hitachi, have tested in large projects the fast switching of Josephson junctions from the *SC* to the normal stage with respect to a post-semiconductor computer generation[81]. Unfortunately, the switching from the normal to *SC* stage turned out to limit the practical performance to several GHz instead to the theoretical ~ 1THz[12]. Meanwhile, new device concepts, based on the transport of single magnetic flux quanta, re-established the feasibility of THz operation[50]. The hottest topic of present Josephson circuit investigations is the realization of quantum computing[82] with *"Qubits"* encoded by the *SC* wave function around μm-sized loops containing single[83] or even half[84] flux quanta. At present, among all demonstrated Qubit realizations, a *SC* electronics implementation appears to have the largest potential of upscalability to the size of several kQubit, which is required for first real applications: Lithographic requirements, of around 1 μm minimum feature size, are already common practise in present semiconductor circuits.

For all of these applications of different superconducting devices, the need of cryogenics is at least a psychological burden. Nevertheless, with the present progress of small cryocoolers[85], *SC* devices may evolve within foreseeable future to push-button black-box machines, which may be one day as common practice as nowadays vacuum tube devices in ordinary living rooms.

1.2.2. $YBa_2Cu_3O_{7-\delta}$ materials

Cuprate High-Temperature Superconductors (*HTSC*) play an outstanding role in the scientific development and for the present understanding of superconductivity. Except for semiconductors, no other class of materials has been investigated so thoroughly by thousands and thousands of researchers worldwide during the last years:

- A huge number of samples have been produced, in quantities of the order of metrical tons.

- Details of materials science have been diligently elaborated.
- High reproducibility has thus been achieved taking the material complexity into account.
- The whole tool-set of experimental solid-state physics has been applied. For some techniques such as photoelectron spectroscopy[86,87], inelastic neutron scattering[88] or scanning tunnelling microscopy[89,90], HTSC have become a *"drosophila"* -like favourite object of investigation, which still challenges further methodological development.
- HTSC still represent a great challenge to theoretical solid-state physics, since not only the superconducting but even more the normal conducting state of HTSC is awaiting a satisfactory explanation.

1.2.2.1. Crystallographic structure

HTSC material usually has complex crystal structures. Almost all of the compounds consist of at least three different chemical elements, and the materials with the highest T_c have seven elements in the crystal lattice. One of the most actively studied HTSC material is $YBa_2Cu_3O_{7-\delta}$ (YBCO or Y-123). This material presents several advantages compared to other ceramic superconductors:

- the only known stable four-element compound with a T_c above 77K,
- includes neither toxic elements nor volatile compounds,
- easy to make single-crystals of YBCO, and
- less anisotropic than other HTSC materials, carries higher current densities at higher magnetic fields.

The YBCO materials forms in an orthorhombic *Pmmm* structure, whit a single formula per primitive unit cell. The YBCO structure (*Fig. 1.14*) is about as simple as conceivable for a quaternary compound with ratios 1:2:3:7. YBCO samples can be viewed as an oxygen deficient perovskite lattice $(Y\text{-}Ba)_3Cu_3O_{9-x}$, based on three Cu-centered perovskite cubes with both O vacancy ordering and Y-Ba ordering along *c*-axis. Each O vacancy occurs in every Cu-O layer, along *a*-axis at site (1/2, 0, 0), resulting in the orthorhombic symmetry. The Y and two Ba ions order along *c*-axis, and the other O vacancy occur in the Y plane. The unit cell parameters are $a = 3.8185$ Å, $b = 3.8856$ Å, and $c = 11.6804$ Å[91].

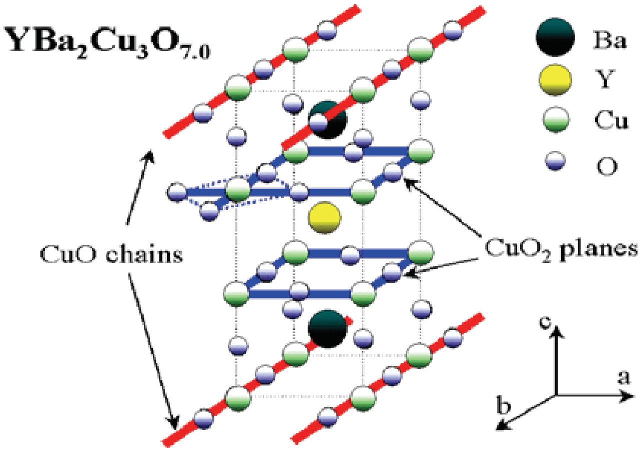

Fig. 1.14. YBCO orthorhombic unit cell[92].

All HTSCs contain the CuO_2 plane in their crystal structure. The layers between the CuO_2 planes are called the charge reservoir layers. Features of the crystal structure of HTSCs include the following:

- The crystal structure is layered and the CuO_2 layer and charge reservoir layer are laminated periodically.
- The parent material is the antiferromagnetic insulator. By doping electrons or holes to the CuO_2 plane from the charge reservoir layer, the CuO_2 plane becomes metallic and the superconductivity appears.
- At least one CuO_2 plane flows must be included in the corresponding unit cell.
- The carrier concentration, when superconductivity appears, is in the CuO_2 plane between 0.15 to 0.20 times the number of copper ions, and then the effect of the antiferromagnetism is strongly exhibited.

In addition, it is possible to consider the crystal structures as being constructed by the stacking of layers consisting of metal ions and oxygen ions in the direction of the *c*-axis.

1.2.2.2. Structural blocks

The YBCO unit cell can be conceptualized from two different structural blocks with distinct electronic properties, as shown in *Fig. 1.15*. The first block consists of one CuO_2 plane. Each Cu atom in the CuO_2 layer is surrounded by four O atoms in a squared-planar configuration (see *Fig. 1.14*). For HTSC structures with more than one CuO_2 planes per unit cell, like TlBCCO, BSCCO, and HgBCCO, the individual layers are separated by a layer of divalent alkaline earth or trivalent rare earth atoms[93]. The CuO_2 planes define the *ab*-planes in all HTSC crystal structures with the *c*-axis of the crystal structure perpendicular to the planes. The second block in this type of unit cell is often referred to as a charge reservoir (*metallic chains in YBCO samples*), and is used to define specific homologous HTSC families of compounds. Within each HTSC compound, this block appears to be largely responsible for providing charge carriers to the CuO_2 planes. It also determines the degree of anisotropy in the individual superconducting compounds.

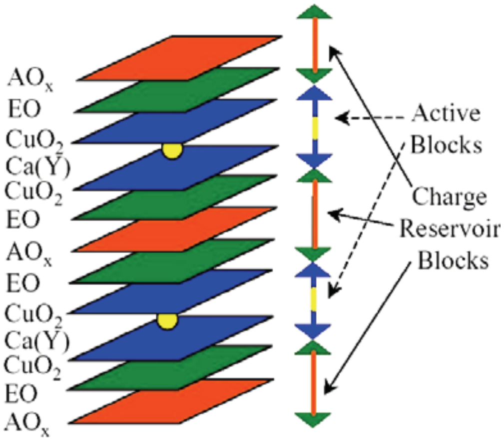

Fig. 1.15. General structure of a cuprate HTSC $A\text{-}m_2(n\text{-}1)_n(A_mE_2Ca_{n-1}Cu_nO_{2n+m+2+y})$ for m = 1. For m = 0 or m = 2 the missing (additional) AOx layer per unit cell leads to a (a/2, b/2, 0) "side step" of the unit cells adjoining in *c*-axis direction[92].

1.2.3. *Growth of $YBa_2Cu_3O_{7-\delta}$ single crystals*

The grain boundary between adjacents grains decreases the SC properties. So, it is very interesting with the lowest grain boundary. The main goal is to obtain a single crystal. Different methods have been developed to achieve this purpose. Efforts to achieve high-quality and large YBCO single crystals have been made extensively by many groups[94,95]. The superconducting properties of bulk melt-textured materials, especially the critical current density, depend on the growth method and on the growth conditions. In order to achieve high critical current densities two different aspects are required during the manufacturing processing;

- A matrix, Y-123, with well connected and orientated grains with a lower values of misorientations, and

- also, well dispersed particles which act as pinning centers at superconducting conditions, in order to pin the magnetic vortices and thus increase the critical current density of this material. But these pinning centers must be heterogeneously distributed in order to obtain the maximum effect of these defects. Y_2BaCuO_5 (Y-211) particles act as pinning centers. It has been proven that their presence in Y-123 matrix increases the critical current density of this superconductor material[96], and they have more advantages, such as preventing the liquid flow so as to decrease the amounts of hole.

Recent studies of YBCO materials pointed to two major issues: creating pinning centers and eliminating weak-lines between grain boundaries. It has been reported that some defects may act as pinning centers. Pinning strength and critical current density were increased by the introduction of fine Y-211 inclusions[97]. Flux pinning may be effective by two ways: first, the defects around the Y-211/Y-123 boundary, such as dislocations or stacking faults, and second, the magnetic pinning caused by the different induction generated in Y-123 superconducting matrix and Y-211 non-superconducting phase[98]. However, the weak-link can be caused by impurity phases, micro-cracks, or high-angle misalignement of the crystals[99].

Only the Y-123 phase can be formed at room pressure since the formation of other phases, $YBa_2Cu_4O_x$ and $Y_2Ba_4Cu_7O_x$, require high pressure. The Y-123 phase is formed by a peritectic reaction from Y_2BaCuO_5 (Y-211) solid and Ba-Cu-O liquid, and it is impossible to grow Y-123 crystals from a congruent melt directly, so flux methods have been used to grow Y-123 single crystals. No suitable flux materials for crystal growth have been found, apart from self-flux, BaO-CuO flux.

In 1993, Yamada and Shiohira[94] overcame the difficulties of flux methods and succeeded in growing Y-123 single crystals by the solute rich liquid-crystal pulling (SRLCP) method. In this method, the flux was settled in a temperature gradient so that the Y-211 solid could exist at the bottom of the crucible. As a solute, the melt equilibrated to Y-211 at higher temperature near the bottom of the crucible and was transported to the melt surface by forced and natural convection in the melt, so that the surface of the melt was supersaturated by Y. In the SRLCP method for growing Y-123 single crystals, melt convection is more essential than crystal pulling of those materials[100]. Typical crystal growth conditions were as follows: the temperature at the center of the melt surface was 997-1000ºC; the temperature difference between the surface and the bottom of the melt was 12 up to 15K; the pulling rate was 0.05-0.1 $mm\cdot h^{-1}$; the crystal rotation rate was 80-120 rpm; and it was grown under an air atmosphere[101]. By the SRLCP method, large and high quality Pr-123 and Sm-123 crystals were also grown by Tagami *et al.*[102], and Nakamura *et al.*[103]. Nd-123 and Sm-123 samples prepared by oxygen-controlled melt growth were reported to have increased, rather than reduced, T_c (96 K) values. The critical current density at 77 K of these samples was higher than those of melt-processed Y-123 with finely distributed Y-211 inclusions under high magnetic fields. Y-123 single crystals were also grown under 1 atm oxygen pressure by Yao *et al.*[104]. It was found that the substitution of Y by Ba is not sensitive to the oxygen partial pressure of the growth atmosphere. Besides, it was reported that a high oxygen partial pressure has a deep effect on the growth rate, which is about 1.5-2.5 times larger under 1 atm oxygen pressure than under air.

1.2.3.1. Phase diagram

The phseudoternary phase diagram of $YO_{1.5}$-BaO-CuO system at 900ºC and oxygen partial pressure of 0.21 atm. can be observed in *Fig. 1.16*[105]. There are four types of quaternary compounds [$YBa_2Cu_3O_7$ (Y-123), Y_2BaCuO_5 (Y-211), $Y_2Ba_8Cu_6O_{18}$ (Y-143), $YBa_6Cu_3O_{11}$ (Y-163)] and five types of ternary compounds [Y_2BaO_4 (Y-210), $Y_3Ba_3O_9$ (Y-340), Ba_2CuO_3 (Y-021), $BaCuO_2$ (Y-011), and $Y_2Cu_2O_5$ (Y-101)].

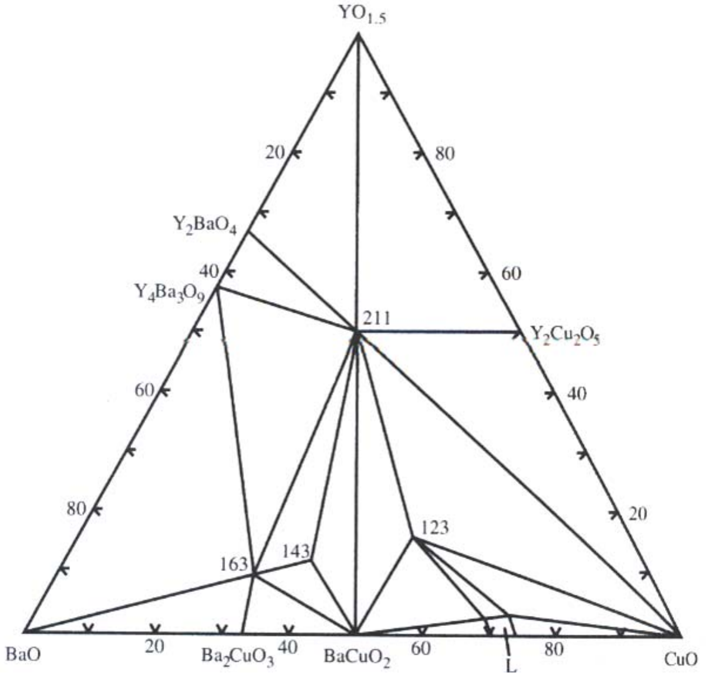

Fig. 1.16. Phseudoternary phase diagram of $YO_{1.5}$-BaO-CuO system at 900ºC and oxygen partial pressure of 0.21 atm[105].

Fig. 1.16, exhibits the isothermal phase diagram including Y-123 and Y-211 compounds[105]. The Y-123 phase is produced by the following peritectic reaction at 1010ºC;

$$L + Y\text{-}211 \rightarrow Y\text{-}123 \qquad \textbf{reac. 1. 1}$$

The peritectic transformation of *L + Y-211 → Y-123* proceeds with the solute diffusion through liquid between Y-211 particles and Y-123 interface, and the undercooling acts as a driving force of the diffusion[106, 107]. All texturing techniques make use of the peritectic reaction where Y-123 phase grows from the Ba- and Cu-rich liquid ($BaCuO_2$ + CuO) and the solid Y-211 phase[108]. From the viewpoint of solute diffusion, the large amount of Y-211 phase can supply more yttrium solute to the growing interface. During heating the YBCO bulk to a high temperature, CuO reacts with Y-123 to form Y-211 and liquid.

$$CuO + Y\text{-}123 \rightarrow Y\text{-}211 + L \qquad \textbf{reac. 1. 2}$$

The solidification temperature of the liquid is lower than that of the peritectic liquid. Thus, no Y-123 grain nucleates at the sample surface. In order to improve the performances, several groups have modified this process: the maximum temperature of the process was decreased to the point just above the peritectic temperature of YBCO material (*T_p ~ 1010ºC*[109]). This method is called melt textured growth (*MTG*) and consists of a partial melting of the material followed by a slow cooling step.

For a better understanding of the growth process and to establish the growth parameters, a binary phase diagram of the YBCO material is needed[105]. In *Fig. 1.17*, it is schematically represented by a pseudobinary phase diagram.

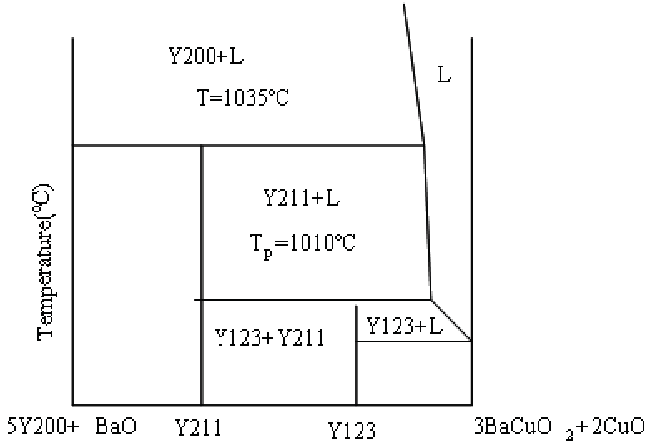

Fig. 1.17. Pseudo-binary phase diagram for YBCO material[151].

The YBCO system has a peritectic reaction at 1010ºC, as it can be seen in *Fig. 1.17*. This peritectic reaction corresponds to the descomposition of Y-123 phase as follows:

$$Y\text{-}123 \rightarrow Y\text{-}211 + L\ (3BaCuO_2 + 2CuO) \qquad \textbf{reac. 1.3}$$

Thus, when the material is heated to a temperature above its peritectic temperature, T_p, the Y-123 phase decomposes into a liquid phase and a solid one, *Y-211*. By cooling down the semi-solid (*L+S*) to a temperature below the melting point of YBCO, the nucleation of Y-123 starts. The solidification of YBCO starts at a temperature below the T_p, where the Y-211 phase and the liquid react producing the superconducting phase Y-123 through the peritectic reaction;

$$S\ (Y\text{-}211) + L\ (3BaCuO_2 + 2CuO) \rightarrow 2YBa_2Cu_3O_{6.5} \qquad \textbf{reac. 1.4}$$

Melt textured materials present a large number of defects which are induced during the solidification process. The most common defects encountered in these materials are *micro- and macrocracks, twin boundaries, non-superconducting phases, and grain boundaries.*

By using this method, YBCO samples with a low connectivity between grains and with grain boundaries with misorientation angles less than 5º have been achieved. However, the critical current density values are typically between *2000* and $4000\ A/cm^2$ at *77K* and *1T*, which are too low for practical applications.

1.2.3.2. Solidification process

The crystallization process consists of disposing the different atoms or molecules into an arranged solid state. This process takes place into two different steps: first of all the nucleation, and after the growth process.

Nucleation: During the nucleation process the different atoms form clusters. When they have a certain size, named critical radius, r_c or r^*, they become stables. There are two different types of nucleation;

- *Homogeneous* → this type is a spontaneous process and the different atoms from the liquid phase form the nucleus or cluster at the solid state.
- *Heterogeneous* → this is stimulated by the presence of grain boundaries, impurity particle, defects existent in the crystal or interface, seeded, and others.

A crystal that grows with faceted interfaces, such as Y-123 crystal, needs some driving force of interface kinetics for growth; e.g. it needs the saturation of Y in the L/S interphase. The saturation or the undercooling kinetics, σ, can be written as:

$$\sigma = \frac{\left(C_i - C_{L,Y-123}\right)}{C_{L,Y-123}} \qquad \textbf{eq. 1.38}$$

where C_i and $C_{L,Y\text{-}123}$ are the Y-123 concentration in the growth interface and in the liquid, respectively. From another point of view, the kinetics undercooling is the difference between the chemical potential of a crystal and its surroundings. This concept is schematically illustrated in *Fig. 1.18*[110].

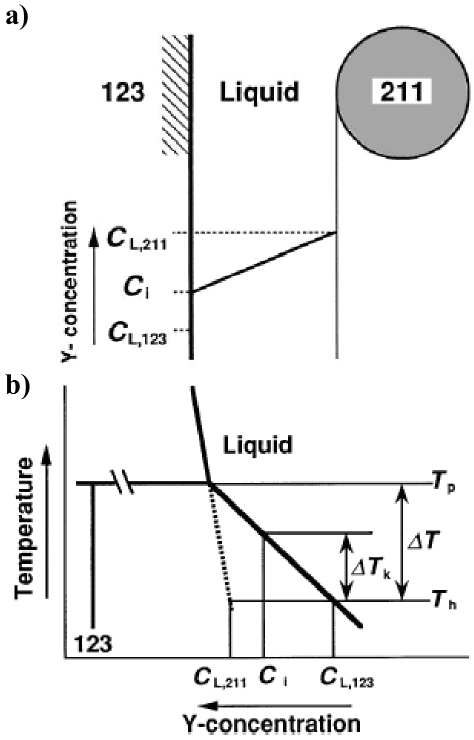

Fig. 1.18. Schematic illustration of a) the yttrium concentration profile between the Y-211 particle and the Y-123 interface, and b) the phase diagram showing the relation between the concentration and the undercooling[110].

The growth of atomically flat space takes place by a step flow mechanism, the so-called lateral growth. Some probable mechanisms are schematically shown in *Fig. 1.19*. The Y-211 particle is the yttrium source for Y-123 growth, and the yttrium concentration near the particle is higher than that the Y-123, which causes the concentration on the growing interface to be higher by approaching close to the interface and promotes the two-dimensional nucleation (*Fig. 1.19a*). The boundary between the Y-123 crystal and the Y-211 particles on the growing interface can act as the heterogeneous two-dimensional nucleation sites (*Fig. 1.19b*), and the entrapment of the Y-211 particles may field the misfit dislocation behind it (*Fig. 1.19c*). These nucleation and/or dislocations act as the step sources. These sites may become dominant when more Y-211 particles are entrapped. Therefore, the undercooling dependence of growth rate of the sample with Y-211 phase excess becomes linear, see *Fig. 1.18b*[110].

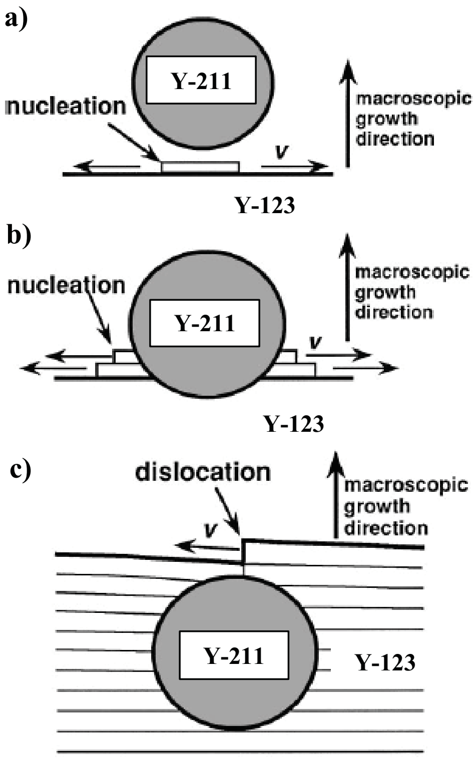

Fig. 1.19. Schematic illustration showing some possible step sources on the Y-123 interface. a) A two-dimensional nucleation resulting from higher concentration with approaching Y-211 close to the interface, b) heterogeneous nucleation at the Y-211/Y-123 interface and c) a misfit dislocation caused by the entrapment of Y-211 particle[110].

Crystal growth: After the nucleation process, the crystal growth takes place. In this step, the liquid phase is totally eliminated. In homogenous nucleation, it is assumed that the system is free from impurities. In this nucleation type, the creation of different types of particles as a new phase is associated with a change in the free energy of the system. This energy change takes place by two different factors: generation of volume of the new phase, ΔG_v, and creation of an interface due to the increasing size of nucleus, ΔG_s.

Then, the crystal growth energy can be calculated by the following expression:

$$\Delta G = \Delta G_V + \Delta G_S$$ **eq. 1.39**

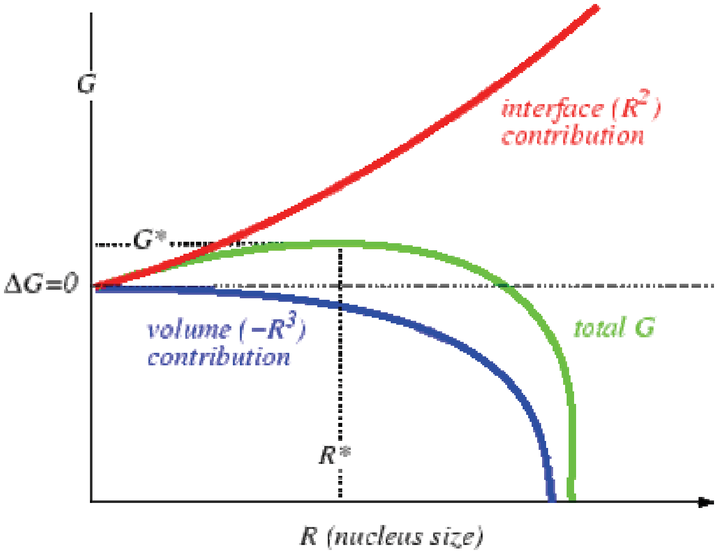

Fig. 1.20. Total (*spherical*) nucleation energy as a function of nucleus size[111].

Fig. 1.20 shows the different changes in free energy and its components during the nucleation process. The change of free energy associated to the increasing volume of a nucleus, ΔG_v can be observed. The interfacial contribution opposes nucleation, while the volumetric driving force propels nucleation. For small sizes, the interfacial term dominates, and nucleation is prevented. At largest sizes, the volumetric term dominates and the crystal grows[111].

1.2.3.3. Manufacturing process

Fabrication of single crystals usually involves the building of a structure, adding atoms layer by layer. Techniques to produce large monodomains include slowly dragging a rotating seed out of a molten bath of feeder materials, such as in the *Crochralski process* and *Bridgman technique*. Previously to the thermal treatment, we must have a perform with shape and dimensions close to the final ones. These green bodies are obtained after pressing and sintering stages. The application of pressure varies within methods: it could be uniaxial form or with an isostatic pressure field, etc. By the other hand, the sintering step could be performed previously to texturing process, such in the Bridgman, self-flux technique or included in it, such in the TSMG method. Melt processing has been shown to be a suitable technique for the fabrication of bulk YBCO high-temperature superconductors with good flux pinning properties and high critical current densities[112]. Several variations of melt texturing technique under a variety of names have been developed based on this principle, with a view to improving either features of the melt process or the quality of the product bulk.

The different superconductor materials can be manufactured in the form of thin film structures. YBCO thin film material presents several advantages respect the bulk material:

- Bulk technique allows to obtain YBCO samples of several centimetres, while thin film technique yields to samples around several *km*. Different devices can be manufactured with YBCO wires with certain versatility, such us rotors, current wires, etc.
- Thin film materials are cheaper than bulk materials due to their manufacturing process. Moreover, bulk material present different micro-/macrocracks produced during its texture and oxigentation processes, which produce a reduction of its superconducting properties. On the other hand, YBCO wires present a lower density of micro/macrocracks, thus giving better superconducting properties.

YBCO-Bulk materials: Two techniques are the most widely employed in the texture process of YBCO bulk samples: TSMG and Bridgman.

<u>TSMG technique:</u> is known as the most effective process to fabricate block-type samples used, for example, in energy storage applications, such as superconducting flywheel systems, and others. In this technique, a long isothermal step and therefore, so great processing times, is regarded as one of the most significant weak points. In the case of melt texturing with a temperature gradient, processing time is shorter, but the sample shape and size are restricted. The TSMG technique has been widely used to grow $YBa_2Cu_3O_X$ crystals of 4 cm[107], but these crystals were intended for applications such as magnetic levitation. The size of single-domain is generally limited to 10 cm for high quality YBCO bulk up to now, because of the grains mis-orientation during the melt growth process[113]. The resulting cubic YBCO crystals are further annealed to obtain the oxygen-ordered orthorombic phase (x = 6.5). Uniquely, the TSMG process yield large, single grains of approximately the dimensions of the green body[114,115,116]. The TSMG technique has become the preferred method for the fabrication of rare earth bulk superconductors, (RE)BCO, and is used routinely in the processing of single-grain cylindrical/square shape samples of up to 50 mm in diameter[117]. TSMG processing is

classified into two types depending on the seeding method: cold seeding and hot seeding. Cold and hot seeding are named for the moment when the seed crystal is placed onto the powder compact. In handling the sample, the cold seeding method is easier than hot seeding, because the seeding is performed at room temperature[118]. In this Thesis, the seeding method used has been cold seeding. In order to obtain large-domain-sized YBCO and to control the growth orientation, seeding effects should be taken into consideration[119]. The seed should not only have a similar structure and lattice constant to those of as-grown YBCO bulks, but also control the orientation and ensure single-domain growth[120]. The seed crystal initiates the nucleation and growth of the Y-123 phase in the incongruent melt, which subsequently solidifies into a single grain during controlled cooling. A variety of seeds have so far been applied for the melt-textured (MT) growth of YBCO bulks[119], which can be classified into three major categories:

- Non-superconductors, such as MgO.
- Bulk superconductors, such as RE123 MT bulks or single crystal, such as Nd-123, Sm-123, and others.
- RE-123 thin films[121].

In principle, the seed materials should not melt during the texture process, because the maximum process temperature is below their melting points. But the seed crystals were observed to dissolve frequently when they were in contact with the Ba-Cu-O liquid that was formed as a result of the incongruent melting of Y-123 compact during a high temperature holding period[118]. The growth mode of YBCO grains is significantly dependent on seed dimensions[122]. During the oxygenation process, cracks in the *ab*-planes appeared as a major drawback for the *c*-axis elements. The occurrence and propagation of cracks was found to be directly related to the oxygenation of the material. The oxygen uptake results in a decrease of the cell unit in the *c*-direction producing tension stresses, which are responsible of cracks generation. The cracks are then an easy diffusion path and the shrinkage of the unit cell along the *c*-axis at the crack tip provides the driving force for the cracks propagation. The low oxygen diffusion rate yields large oxygen gradient during a classical annealing treatment. Ceramic superconductors exhibit an extensive zone defects ranging from point-like defects of various natures, such as chain oxygen vacancies in some RE substituted Y-123 compounds, to a variety of extended defects. In addition, Y-123 compounds typically display ferroelectric transition, which takes place well above room temperature and results in extensive twin formation. Dislocations, as well as their dissociated configurations are confined onto a prominent glide plane (001), although dislocation lines out of this plane may be frequently found building grain boundaries or as non-assembled segments that have climbed out the glide plane. This high anisotropy of dislocation configurations is consistent with the anisotropy of the crystal structure: cell contraction occurs preferently to the *c*-axis. So, microcracks appear in the basal plane. The melt processed ceramic composites contain a dense population of fine peritectic (non-reacted) particles, which drastically affect the microstructure, acting as nucleation sites for dislocations and stacking faults as well as microcrack stoppers, thus enhancing the mechanical toughness of the composite[123].

Bridgman technique: The Bridgman technique is a method to grow single crystal ingots or boules. It is a popular method of producing semiconductor crystals, such as gallium arsenide, II-V Crystals (ZnSe, CdS, CdTe), where the Crochralski process is more difficult. The method involves heating polycrystalline material in a container above its melting point, and slowly cooling it from one end. Single crystal material is progressively formed along the length of the container. The process can be carried out in an horizontal or vertical geometry. The two main problems found when obtaining YBCO samples with this technique are:

- The optimal viscosity have to be found between minimize the sample flowing and maximize atomic diffusion.
- It is well known that the liquid phase generally migrates to the cold zone. In this case, the bar looses the correct stochiometry, and a rich Y-211 zone accumulates at the end of the bar. So, limited lengths can be obtained.

After the texture process, the YBCO bars are introduced in an oxygenation furnace at 450ºC for 240h[124]. *Fig. 1.21* shows a schematic drawing and Optical Microscopy (OM) image of YBCO bars textured by Bridgman technique. By means of polarized light microscopy, an initial region can be observed where polynucleation and growth competition phenomena take place. This competition region has a length which is inversely proportional to the processing rate, thus indicating that the nucleation is promoted by an enhanced undercooling[125]. In the single domain region, the *c*-axis of Y-123 has a tilt angle of 45º respect to the long axis of the bars.

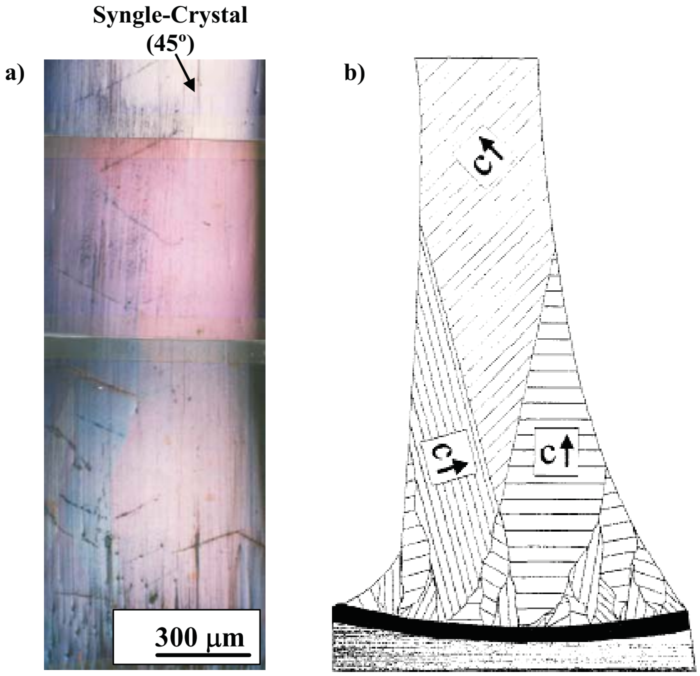

Fig. 1.21. a) OM and b) schematic drawing[126] showing from bottom to top, a multinucleation region, a growth competitive region and a single domain region of a Bridgman melt-grown samples.

YBCO-coated conductors, YBCO-cc: Coated conductors are seen nowadays to prompt the market of fault current limiters, transformers, power cables, motors, superconducting magnetic energy storage (SMES), nuclear magnetic resonance (NMR) and magnetic resonance imaging (MRI). At the date, researches are focusing on the investigation and industrial production of YBCO coated conductors (*YBCO-cc*) highly biaxially textured.

<u>*Substrate:*</u> One of the most important materials issues in *cc* growth concers the choice of the right substrate and the possible buffer layers. To obtain YBCO films with a highly quality, the substrate must have the desirable properties[127] such as: chemical compability, similar thermal expansion coefficients, good lattice matching with the YBCO phase, low roughness, and must be flexible, hard, cheap and available in long lengths. However, YBCO-cc need a metallic textured substrate, see *Fig.1.22*.

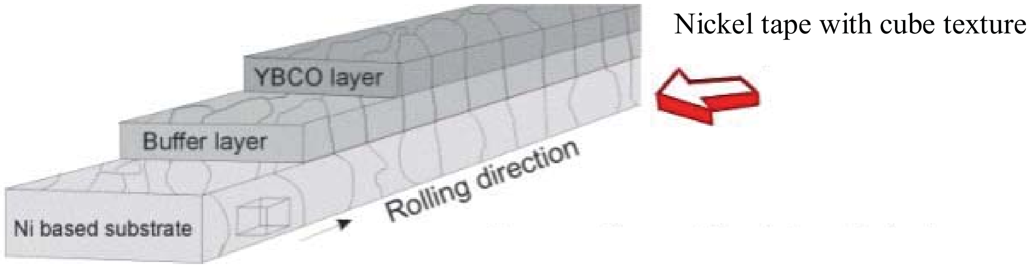

Fig.1.22. Scheme of the metallic substrate tapes for coated conductors[128].

Moreover, if YBCO reacts with it, several ceramic buffer layers must be introduced in the wire, which must grow epitaxially prior to the YBCO phase (*Fig.1.23*).

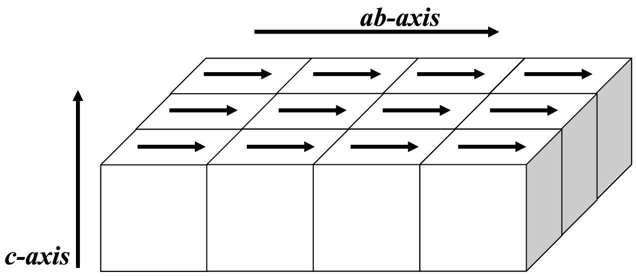

Fig. 1.23. Schematic diagram of biaxially aligned structure.

Despite the synthesis of YBCO superconducting films is not easy, several techniques to grow them are widely employed, each one with a characteristic morphology, and therefore with determined physical properties. The growth of YBCO films can be achieved by physical and chemical methods. The different samples employed in this Thesis have been obtained by physical route, concretely by Pulsed Electron Deposition (PED)[129].

1.2.3.4. Oxygenation process

An important step in the production bulk superconductors fabricated by Bridgman and TSMG techniques, is the oxygenation process. YBCO exhibits a tetragonal (T) to orthorhombic (O) phase transformation as oxygen content exceeds 6.4[130]. In large domain YBCO prepared by seeded melt growth method[131] it has been found that *ab*-plane cracks are formed due to volume changes that occur during the *T*-to-*O* phase transition. These microcracks are highly undesirable in both fundamental studies and engineering applications. The importance of such progress lines in the industrial aspects of the research: a large domain structure allows engineering designers to consider many potential applications including magnetic levitation, long conductors, and microwave components while in polycrystalline materials, however, the glassy grain boundaries "*smear*" the sharpness of superconductivity leading to the weakly coupled nature of ceramic material.

1.2.3.5. Microstructural defects generated during the texture process

YBCO-Bulk materials: The texture and oxygenation processes, introduce several kinds of defects inside the single crystal, such as cracks, which are not desirable because they decrease the mechanical properties. Other kind of defects could act as pinning centres achieving better SC properties[97,132]:

a) *Y_2BaCuO_5, Y-211 precipitates:* In order to prepare a bulk piece, a fine and well-dispersed Y-211 precipitate distribution in the Y-123 superconducting matrix has to be achieved. These defects, increase the irreversibility line by acting as pinning centres. It is possible to modify the size of the Y-211 particles by varying the concentration of the Y-211 in the composite (see *Fig.1.24*). It has been reported that, when the concentration of the Y-211 phase is around 30 vol %, the average size of precipitates is drastically reduced down to 0.1-3 µm[132]. This size reduction effect can be accounted for considering that any Y-211 excess in the semisolid melt increases the number of nucleation sites for Y-211 released during the *Y-211 + liquid → Y-123* peritectic reaction.

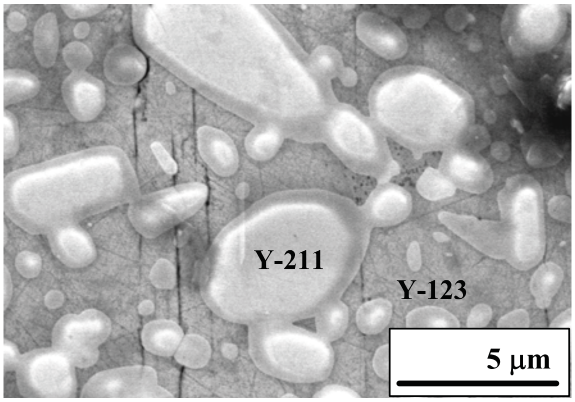

Fig. 1.24. FE-SEM micrograph of Bridgman sample of a region containing several Y-211 inclusions with different sizes.

b) *Twin boundaries:* The similarity between the unit cell parameters *a* and *b* in the crystalline structure of Y-123, and the transition existing during the oxygenation process (*from tetragonal to orthorhombic phase*) at high temperatures, promotes the existence of interfaces between zones having the cell parameters interchanged. These interfaces consist of two families of orthogonal planes (45º from the in-plane crystallographic axis) and containing the *c*-direction (see *Fig.1.25*). Twin boundaries may be also able to act as linear pinning centres[133].

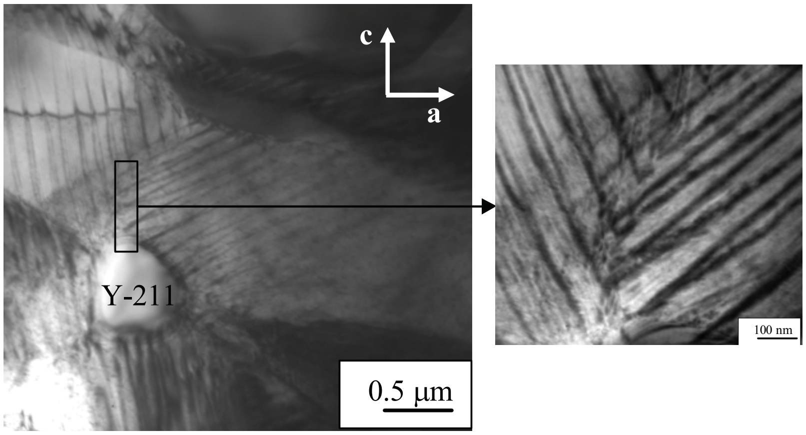

Fig. 1.25. TEM micrograph of the different twins in the *c*-axis present in the Y-123 for different Bridgman samples.

c) <u>*Dislocations:*</u> Dislocations are capable to strongly influence vortex pinning in the solid vortex state, either acting as pint-like or linear-like pinning centers, depending on the direction of the applied magnetic field. The bulk samples textured by Bridgman and TSMG technique exhibit a high amount of dislocations, which can be observed by TEM in the Y-123 phase (see *Fig. 1.26*). Dislocation field of Y-123 is highly anisotropic, being confined to *ab*-plane. Lubenets *et al.*[134] reported that strong covalent and ionic bonds create high Peierls barriers, which constrain the dislocation mobility in YBCO single crystals.

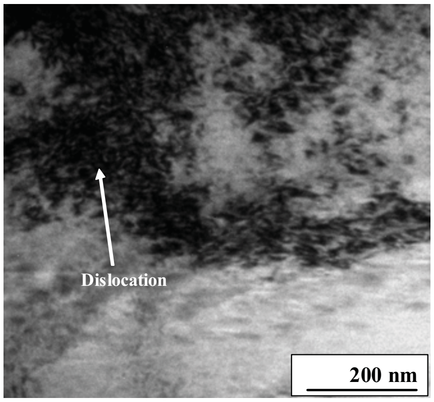

Fig. 1.26. TEM micrograph of a Bridgman sample observed of a region containing high quantity of dislocations in the maximum anisotropy plane (*ab*-plane).

The micrograph presented in *Fig. 1.27* also shows dislocations placed preferently in the grain boundary between Y-123 and Y-211. Moreover, the trajectories of the dislocations appear to be either unaffected or changed across the twin boundaries. On the other hand, this micrograph exhibits a higher amount of twins inside the precipitates. These defects could be due to three different factors:

- the compressive strain during the undercooling treatment in the texture process,
- the different thermal expansion coefficients between the matrix and the different Y-211 inclusions (*from 20ºC to 900ºC are* $1.24\cdot10^{-3}$ K^{-1} *and* $1.70\cdot10^{-3}$ K^{-1} *for Y-211 and Y-123, respectively*[123]). The first takes into account the thermal expansion and elastic modulus mismatch between the two phases[123], and
- the stress is though to result from the incorporation of Y-211 decomposition products into the matrix. Below the peritectic temperature, there is a thermodynamically driving force for solid-state dissolution of Y-211 inclusions.

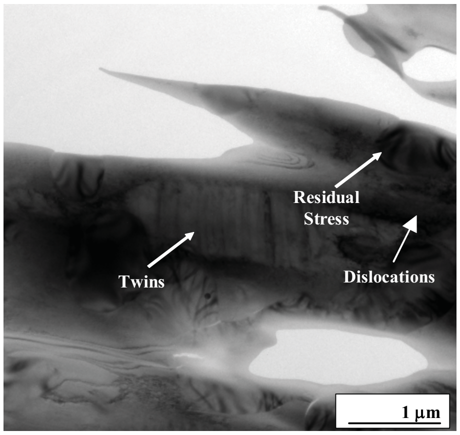

Fig. 1.27. TEM micrograph of Bridgman sample of a region containing several precipitates with different sizes. Note that several twins and residual stress produced during the textured process are present into the precipitates.

Under uniaxially pressing conditions, plastic deformation is only possible if there is some kind of anisotropy in the material. In melt textured Y-123 composites, two kinds of anisotropy exist: elastic in the matrix[123], and plastic between the peritectic inclusions and the matrix.

Inside the Y-211 particles dislocations can be generated. Microcracks and residual stresses at the edges of the particle, produced during the texture process, can be observed in *Fig. 1.28*.

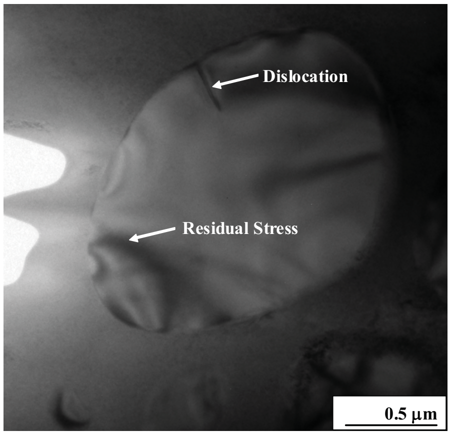

Fig. 1.28. TEM micrograph of a simple textured by Bridgman technique, which shows a precipitate with residual stress and dislocation. Both defects are due to the compressive strain produced during the texture process of material.

d) Stacking faults: Y-123 + CuO, under certain conditions is unstable against the formation $YBa_2Cu_4O_8$, with a structure similar to Y-123 but with an extra CuO plane incorporated into the crystalline structure. Although superconducting, its critical temperature (82K) is lower than that of Y-123, and therefore, the existence of a local transformation from Y-123 to $YBa_2Cu_4O_8$, being an extended planar defect, could have detrimental effects on vortex pinning. The local formation of a unit cell of $YBa_2Cu_4O_8$ is, from a crystallographic point, a stacking fault.

e) *Cracks:* An important phenomenon in bulk superconductors fabricated by TSMG and Bridgman technique is the formation of cracks, due to the inherent brittleness of the Y-123 phase matrix. These form during the fabrication of the superconducting monolith, and play an important role in the limitation of current flow. As-grown Y-123/Y-211 bulk superconductors prepared by these different techniques must be oxygenated in order to transform from tetragonal to orthorhombic phases. Oxygenation temperatures around 400-450 ºC are lower than diffusion could explain, and it is therefore clear that bulk oxygen diffusion alone cannot assist this process. Two different types of macrocraks are generated: parallel to the *a/b*-plane and *a/c*-plane. While the first extend over almost the whole sample, the *c*-macrocrak length is limited by the *a/b*-macrocraks spacing[135]. *c*-crak network represents a mesoscopic defect in bulk superconductors fabricated by TSMG and Bridgman techniques, which limits the local supercurrent density in the studied sample. Also, Reddy and Rajasekharan[136] studied the interior structure of partially oxygenated Y-123 bulk melt-textured material. During the oxygenation process microcraks parallel to the *a/b*-plane (*a/b*-microcracks) appear in the melt processed YBCO (dark lines in *Figure 1.29*). Y-211 phase particles (dark), and twins can also be seen in the same figure.

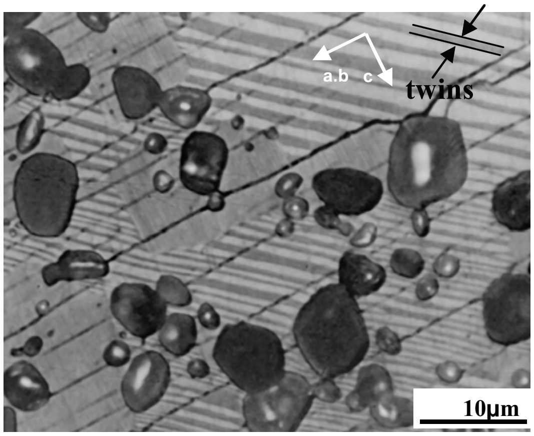

Figure 1.29. Microcracks parallel to the *a/b*-planes (*a/b*-microscracks) in the melt processed YBCO (dark lines). Y-211 phase particles (dark) and twins can also be seen[137].

f) <u>*Grain boundaries:*</u> Two main classes of grain boundary may exist in these type of materials: the low angle grain boundary with a misorientations lower than 3º, that do not have strongly detrimental effects on superconducting properties, and the high angle misorientations higher than 4º, that act as weak link and reduce its superconducting properties.

YBCO-coated conductors: All the defects presented before also exist in coated conductors (cc). New kinds of defects are related to the existence of an interphase. The main problem that YBCO-cc samples can present after their texture process is a bad interfacial adhesion, due to a high difference between the YBCO and buffer layer expansion coefficients. Samples with good adhesion and some residual stresses between the layers are achieved recently[138].

1.2.3.6. Microstructural defects generated during the oxygenation process

YBCO-Bulk materials: Although in standard melt-growth YBCO microcracks also appear in the vicinity of Y-211 particles due to the thermal expansion difference of Y-211 and Y-123[112], these defects do not propagate across the Y-211 precipitates, and their length is limited. The Y-211 particles are under compression when the material is cooled, and can therefore break the Y-123 matrix along *ab*-plane[139]. These are the intrinsic microcracks, which are generated during the tetragonal to orthorhombic phase transition. Large secondary phase inclusions (*unreacted liquid and Y-211*) can also create macrocracks due to thermal expansion mismatch. Oxygen annealing, necessary to make Y-123 samples superconducting, is reported to be responsible for further macro and microcracking [140]. That is why oxygen concentration gradients lead to large mechanical stress in the material. The oxygenation diffusion coefficient in the *ab*-plane is about 10^4-10^6 times larger than in *c*-axis[140]. Mechanical stress and propagation of cracks during the oxygenation process are different for samples textured with TSMG and/or Bridgman technique[140]:

a) *Mechanical stresses:* Macrocracks in textured pellets appear during the final cooling stage to room temperature. Three major causes for large mechanical stresses, schematically illustrated in *Fig. 1.30*, are considered at this stage: *i)* increasing Y-211 concentration is observed with the distance from the seed in the *c*-growth sector while it remains relatively homogeneous in the *ab*-growth sector. Thermal expansion coefficients (in *ab*- and *c*-direction) of a Y-123/Y-211 composite are a function of the Y-211 content. The *c*-axis stress due to Y-211 inhomogenities described above can reach 50-100 MPa in the center of the pellet, and will tend to open *ab*-plane macrocracks (*Fig. 1.30a*); *ii) d*uring cooling, a thermal gradient builds up with a colder surface and a hotter bulk, due to relatively low thermal conductivity of Y-123 (*Fig. 1.30b*), and *iii)* during cooling to room temperature it takes up oxygen mostly in *ab*-direction and in the vicinity on the surface (*Fig. 1.30c*).

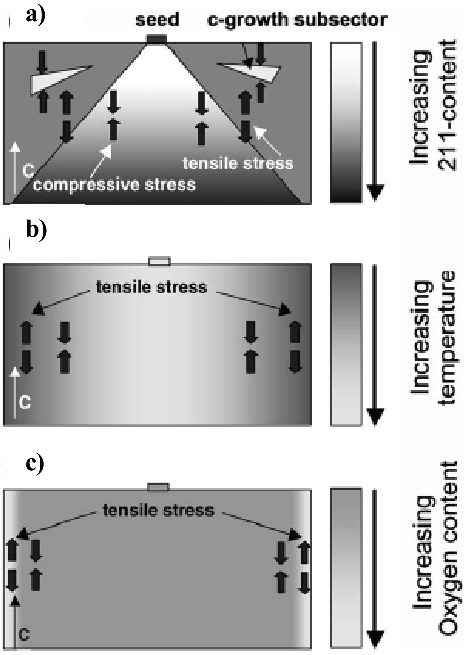

Fig. 1.30. Schematic of mechanical (*compressive or tensile*) stresses associated with a) the Y-211 distribution into a pyramid pattern, b) thermal gradient during cooling, and c) oxygen[140].

b) *Propagation of cracks during the oxygenation process:* Cracking due to the oxygen uptake of the surface does not seem to severely damage the sample. The mechanism can be described as follows. In first stage, stress is building up at the exterior surface which creates the regular cracking pattern. Oxygen will then penetrate in the cracks and oxygenate their walls. The concentration in *c*-axis due to the oxygen uptake will then create a stress field around the crack tip, that tends to make the crack progress inside the material, see *Fig. 1.31*.

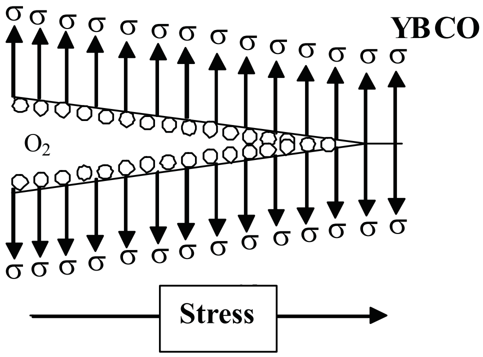

Fig. 1.31. Schematic of mechanism of propagation of cracks during the oxygenation process[141].

YBCO-coated conductors: The oxygenation process for YBCO-cc samples takes place during a short time due to the small thickness that oxygen must diffuse.

1.3. Mechanical properties of YBCO samples

The mechanical properties of YBCO samples have been studied during the last years. The most important properties studied have been the hardness, H (*at micro-/ nanometric scale*), the Young's modulus, E, and the toughness fracture, K_{IC}. Some authors studied the mechanical properties at room or at cryogenic temperatures, also known as work temperature (T_w). Lots of different techniques could be used to determine the value of these parameters. The reported values of E, H and K_{IC} of YBCO composite are summarized in *table 1.1, 1.2 and 1.3,* respectively.

Table 1.1. Literature values of E for YBCO obtained by different techniques.

Author	Material	E (GPa)	Method	Year
Joo. et al.[142]	Y-123	110	Pulsed echo technique	1999
	Y-123 + 5% vol. Ag	103		
	Y-123 + 10% vol. Ag	103		
	Y-123 + 15% vol. Ag	97		
Lucas et al.[143]	Y-123	154.30 ± 16.34	Indentation	1996
Soifer et al.[144]	Film	210	Nanoindentation	2005
Güçlü et al.[145]	Polycrystalline, 50K	47.20	Vickers indentation	2005
	Polycrystalline, 160K	29.63		
	Polycrystalline, 180K	28.47		
	Polycrystalline, 293K	9.39		
Ledbetter et al.[146]	Polycrystalline	90.8-101.8	Ultrasonic	1987
Sheahen et al.[147]	Syntherized with Ag	75-120	-	1990
Goyal et al.[148]	Syngle crystal	220 ± 20	Ultrasonic	1992
Soifer et al.[149]	Thin film	210	FS[ii]-AFM	2004
Goyal et al.[150]	Y-211	213	Nanoindentation	1991
Goyal et al.[150]	Texturized	182	Nanoindentation	1991
Reddy et al.[151]	Texturized	95.89	Ultrasonic	1996

[ii] ***FS:*** Force Spectroscopy

Table 1.2. Literature values of *H* for YBCO obtained by different techniques.

Author	Material	H (GPa)	Method	Year
Lucas et al.[143]	Y-123	10.28 ± 1.67	Indentation	1996
Li et al.[152]	MTG-1100ºC, 5min	5.4	Vickers indentation	1997
	MTG-1100ºC, 10min	11.0		
	MTG-1100ºC, 15min	10.3		
	Solid State reaction	10.3		
Soifer et al.[144]	Film	8.5	Nanoindentation	2005
Yoshimo et al.[153]	YBCO 40K	18 ± 2.5	Vickers Indentation	2001
	YBCO 293K	5.2 ± 0.5		
Güçlü et al.[145]	Polycrystalline, 50K	3.58		2005
	Polycrystalline, 160K	1.03		
	Polycrystalline, 180K	0.95		
	Polycrystalline, 293K	0.53		
Lim et al.[154]	Single crystal	7.81 ± 0.23	Nanoindentation	2001
Cook et al.[155]	YBCO	8.7	Vickers Indentation	1987
Goyal et al.[148]	Textures	6.7		1992
		10.8	Nanoindentation	
Soifer et al.[149]	Thin film	8.5	FS	2004
Goyal et al.[148]	Y-211	14.0	Nanoindentation	1992

Table 1.3. Literature values of toughness fracture, K_{IC}, for YBCO obtained by different techniques.

Author	Material	K_{IC} (MPa·m$^{1/2}$)	Method	Year
Joo et al.[142]	YBCO	1.60	Single-edge-notch beam	1999
	Y-123 + 5% vol. Ag	2.10		
	Y-123 + 10% vol. Ag	2.50		
	Y-123 + 15% vol. Ag	2.80		
Lenblond-Harnois et al.[156]	YBCO	1.53	Vickers Indentation	2000
	Y-123 + 5% wt Ag	1.88		
Li et al.[152]	MTG-1100ºC, 5min	1.9		1997
	MTG-1100ºC, 10min	1.7		
	MTG-1100ºC, 15min	1.7		
	Solid State Reaction	1.3		
Yoshino et al.[153]	YBCO 40K	0.4		2001
	YBCO 293K	1.3		
Joo et al.[157]	YBCO	1.6	Single-edge-notch beam	1998
	Y-123 + 5 vol% Ag	2.2		
	Y-123 + 10 vol% Ag	2.6		
Lenders et al.[158]	Y-123 + 30 mol% Y-211	1.01	Vickers Indentation	1999
	Y-123 + 60 mol % Y-211	1.44		
Cook et al.[157]	YBCO	1.10		1998
Sheahen et al.[147]	YBCO	0.8-1.0	Bending	1990
	Textured	1.6		
Fujimoto et al.[112]	Textured	0.99-1.20	Vickers Indentation	1992
	Y-123 with Ag	1.60-2.10		
Sheahen et al.[147]	Y-123 with 5, 15 and 25% Ag	1.6	Bending	1990
	Y-123 with 20% Ag	3.8		

1.4. Plastic deformation mechanism of YBCO samples

Altough YBCO is a brittle material, certain plasticity can be achieved. Some of the plastic deformation mechanisms involve dislocations movement and twining processes. These effects have been studied in the past.

Rabier *et al.* [159, 160] studied the microscopic mechanisms concerned in plastic deformation of YBCO ceramics, as well as the effects of lattice defects on the physical properties of these materials. After the plastic deformation, several dislocations have been observed by TEM. Moreover, a dislocation with 1/2<110> Burgers vector is nucleated in the orthorhombic structure[161].

Also, another plastic deformation mechanism exists, called twining[161, 162]. Recently, some authors induced twining in single crystals of YBCO using Vickers tip indenter[163] and observed by AFM. Tall *et al.*[163] showed that, besides residual imprint, plasticity takes place at room temperature through the nucleation of mechanical twins located on both {100} and {110} twin planes.

1.5. References

[1] Y. I. Golovin; *Physics of the Solid State* 50 **(2008)** 2205.
[2] Y. Choi, K. J. Van Vliet, J. Li, S. Suresh; *J. Appl. Phys.* 94 **(2003)** 6050.
[3] W. C. Oliver, G. M. Pharr; *J. Mater. Res.* 7 **(1992)** 1564.
[4] G. M. Pharr, W. C. Oliver, F. R. Brotzen; *J. Mater. Res.* 7 **(1992)** 613.
[5] J. J. Roa, X. G. Capdevila, M. Martinez, F. Espiell, M. Segarra; *Nanotechnology* 18 **(2007)** 385701.
[6] Y. Gaillard, C. Tromas, J. Woirgard; *Acta Mater.* 54 **(2006)** 1409.
[7] Y. Choi, S. Suresh; *Scri. Mater.* 48 **(2003)** 249.
[8] Y. Gaillard, E. Jiménez-Piqué, F. Soldera, F. Mücklich, M. Anglada; *Acta Mater.* 56 **(2008)** 4206.
[9] D. Beegan, M. T. Laugier; *Surf. Coat. Technol.* 199 **(2005)** 32.
[10] G. M. Pharr; *Mater. Sci. Eng. A* 253 **(1998)** 151.
[11] T. D. Shen, C. C. Koch, T. Y. Tsui, G. M. Pharr; *J. Mater. Res.* 10 **(1995)** 2892.

[12] D. Stone, W. R. LaFontaine, P. Alexopoulos, T. W. Wu, C.-Y. Li; *J. Mater. Res.* 3 **(1988)** 141.

[13] W. C. Oliver, G. M. Pharr; *J. Mater. Res.* 19 **(2004)** 3.

[14] M. F. Doerner, D. S. Gardner, W. D. Nix; *J. Mater. Res.* 1 **(1986)** 845.

[15] B. N. Lucas, C. T. Rosenmayer, W. C. Oliver; *Mat. Res. Society* 505 **(1998)** 97.

[16] M. J. Mayo, W. D. Nix; *Acta Metall.* 36 **(1988)** 2183.

[17] B. N. Lucas, W. C. Oliver; *Metall. Mater. Trans. A* 30 **(1999)** 601.

[18] J. S. Field, M. V. Swain; *J. Mater. Res.* 8 **(1993)** 297.

[19] J. S. Field, M. V. Swain; *J. Mater. Res.* 10 **(1995)** 101.

[20] D. S. Harding, W. C. Oliver, G. M. Pharr; *Mater. Res. Soc.* 356 **(1995)** 663.

[21] T. Y. Tsui, W. C. Oliver, G. M. Pharr; *Mater. Res. Soc.* 436 **(1997)** 147.

[22] J. C. Hay, A. Bolshakov, G. M. Pharr; *J. Mater. Res.* 14 **(1999)** 2296.

[23] J. B. Pethica, W. C. Oliver; *Mater. Res. Soc.* 130 **(1989)** 13.

[24] B. N. Lucas, W. C. Oliver, J. E. Swindeman; *Mater. Res. Soc.* 552 **(1998)** 3.

[25] H. Hertz, J. Reine Angew. Math. 92 **(1881)** 156 (Translated and reprinted in English in Hertz's Miscellaneous Papers, Macmillan and Co., London (1986) Ch. 5).

[26] E. G. Herbert, G. M. Pharr, W. C. Oliver, B. N. Lucas, J. L. Hay; *Thin Solid Films* 398-399 **(2001)** 331.

[27] J. J. Roa, E. Jiménez-Piqué, X. G. Capdevila, M. Segarra; *J. Eur. Ceram. Soc.* **(2009)** Accepted.

[28] S. Basu, A. Moseson, M. W. Barsoum; *J. Mater. Res.* 21 **(2006)** 2628.

[29] D. Tabor; *Hardness of Metals* (Clarendon, Oxford, U. K., **1951**).

[30] I. N. Sneddon; *Int. J. Engineering Science* 3 **(1965)** 47.

[31] A. C. Fischer-Cripps; *Surface & Coatings Technologies* 200 **(2006)** 4153.

[38] M. T. Huber; *Ann. Phys.* 14(1) **(2004)** 3.

[33] M. F. Doerner, W. D. Nix; *J. Mater. Res.* 1 **(1986)** 601.

[34] R. B. King; *Int. J. Solids struct.* 23 **(1987)** 1657.

[35] A. E. Giannakopoulus, S. Suresh; *Scrip. Mater.* 40 **(1999)** 1191.

[36] Y. T: Cheng, C. -M. Cheng; *J. Appl. Phys.* 84 **(1998)** 1284.

[37] Y. T: Cheng, C. -M. Cheng; *J. Appl. Phys. Lett.* 73 **(1998)** 614.

[38] D. L. Joslin, W. C. Oliver; *J. Mater. Res.* 5 **(1990)** 123.

[39] E. Jiménez-Piqué, Y. Gaillard, M. Anglada; *Key Eng. Mater.* 333 **(2007)** 107.

[40] P. J. Burnett, T. F. Page; *J. Mater. Sci.* 19 **(1984)** 3524.

[41] J. L. Hay, M. E. O'Hern, W. C. Oliver; *Mat. Res. Soc. Symp. Proc.* 522 **(1998)** 27.

[42] H. Bückle, J. W. Westbrook, H. Conrad, ed. *The Science of Hardness Testing and its Applications, American Society for Metals*, Metals Park, OH, **1973**, p. 453.

[43] B. Jonsson, S. Hogmark; *The Solid Films,* 114 **(1984)** 257.

[44] P. J. Burnett, D. S. Rickerby; *Thin Solid Films,* 148 **(1987)** 41.

[45] T. Y. Tsui, C. A. Ross, G. M. Pharr; *J. Mater. Res.* 18 **(2003)** 1383.

[46] A. K. Bhattacharua, W. D. Nix; *Int. J. Solids Structures,* 24 **(1988)** 1287.

[47] M. Sakai, J. Zhang, A. Matsuda; *J. Mater. Res.* 20 **(2005)** 2173.

[48] H. Gao, C. – H. Chiu, J. Lee; *Int. J. Solids Structures* 29 **(1992)** 2471.

[49] S. Bec, A. Tonck, J. L. Loubet; *Philos. Mag.* 86 **(2006)** 5347.

[50] T. H. Geballe; *Science* 293 **(2001)** 223.

[51] J. Bardeen, L. N. Cooper, J. R. Schrieffer; *Phys. Rev.* 108 **(1957)** 1175.

[52] K. A. Muller, M. Takashige, J. G. Bednorz; *Phys. Rev. Lett.* 58 **(1987)** 1143.

[53] M. Ulrich, H. Walter, A. Leenders, H. C. Freyhardt; *Physica C* 311 **(1999)** 86.

[54] M. K. Wi, J. R. Ashburn, C. J. Torng, P. H. Hor, R. L. Meng, L. Gao, Z. J. Huang, Y. Q. Wang, C. W. Chu; *Phys. Rev. Lett.* 58 **(1987)** 908.

[55] H. Maeda, Y. Tanaka, M. Fujimoto, T. Asano; *Jpn. J. appl. Phys.* 27 **(1988)** L209.

[56] Z. Z. Sheng, A. M. Hermann; *Nature* 332 **(1988)** 55.

[57] A. Schilling, M. Cantoni, J. D. Guo, H. R. Ott; *Nature* 363 **(1993)** 56.

[58] L. Gao, Y. Y. Xue, F. Chen, Q. Xiong, R. L. Meng, D. Rameriz, C. W. Chu; *Physica C* 235-240 **(1994)** 1493.

[59] S. N. Putilin, E . V. Antipov, O. Chmaissem, M. Marezio; *Nature* 362 **(1993)** 226.

[60] C. W. Chu, L. Gao, F. Chen, Z. J. Huang, R. L. Ment, Y. Y. Xue; *Nature* 365 **(1993)** 323.

[61] H. M. Chao, L. J. Chen, J. C. Chen, X. Y. Hua, P. F. Yuan, X. X. Yao; *Physica C* 232 **(1994)** 5.

[62] C. C. Kim, A. R. Drews, E. F. Skelton, S. B. Qadri, M. S. Osofsky; *Phys. Rev. B* 50 **(1994)** 13778.

[63] Q. -L-Xu, T. B. Tang, Z. -J. Chen; *Supercond. Sci. Technol.* 7 **(1994)** 828.

[64] L. Jansen, R. Block; *Physica A* 212 **(1994)** 143.

[65] W. A. Little; *Phys. Rev. A* 134 **(1964)** 1416.

[66] K. Tanigaki, T. W. Ebbesen, S. Saito, J. Mizuki, J. S. Tsai, Y. Kubo, S. Kuroshima; *Nature* 352 **(1991)** 222.

[67] G. Saito, H. Yamochi, T. Nakamura, T. Komatsu, M. Nakashima, H. Mori, K. Oshima; *Physica B* 169 **(1991)** 372.

[68] J. Nagamatsu, N. Nakagava, T. Muranaka, Y. Zenitani, J. Akimitsu; *Nature* 410 **(2001)** 63.

[69] J. L. Sarrao, L. A. Morales, J. D. Thompson, B. L. Scott, G. R. Stewart, F. Wastin. J. Rebizarnt, P. Boulet, E. Colineau, G. H. Lander; *Nature* 420 **(2002)** 297.

[70] P. Komarek; *Supercond. Sci. Technol.* 13 **(2000)** 456.

[71] Y. Wang, S. Ono, Y. Onose, G. Gu, Y. Ando, Y. Tokura, S. Uchida, N. P. Ong; *Science* 299 **(2003)** 86.

[72] G. Blatter, M. V. Feigel'man, V. B. Geshkenbein, A. I. Larkin, V. M. Vinokur; *Rev. Mod. Phys.* 66 **(1994)** 1125.

[73] P. Renton; *Nature* 428 **(2004)** 141.

[74] H. J. Chaloupka, T. Kässer; *High Temperature Superconductivity 2-Engineering Applications* (Ed. A. V. Narlikar), Springer Verlag, Berlin **(2004)** 411.

[75] K. K. Likharev, *Dynamics of Josephson Junctions and Circuits,* Gordon & Breach Science Publishers **(1986)** 30.

[76] *SQUID Handbook* (Ed. J. Clarke, A. Braginski), WILEY-VCH Verlag, Berlin **(2003)**.

[77] O. V. Lounasmaa, H. Seppä; *J. Low Temp. Phys.* 135 **(2004)** 295.

[78] D. Koelle, R. Kleiner, F. Ludwig, E. Dantsker, J. Clarke; *Rev. Mod. Phys.* 71 **(1999)** 631.

[79] L. A. Knauss, A. B. Cawthorne, N. Lettsome, S. Kelly, S. Chatraphorn, E. F. Fleet, F. C. Wellstood, W. E. Vanderlinde; *Micrelectronics Reliability* 41 **(2001)** 1211.

[80] M. V. Kreutzbruck, *High Temperature Supercondcuting 2-Engineering Applications* (Ed. A. V. Narlikar), SpringerVerlag, Berlin **(2004)** 223.

[81] A. Galindo, M. A. Martín-Delgado; *Rev. Mod. Phys.* 74 **(2002)** 347.

[82] A. Ekert, R. Jozsa; *Rev. Mod. Phys.* 68 **(1996)** 733.

[83] I. Chiorescu, Y. Nakamura, C. J. P. M. Harmans, J. E. Mooij; *Science* 299 **(2003)** 1869.

[84] H. Hilgenkamp, H.-J. Ariando, H. Smilde, D. H. A. Blank, G. Rijnders, H. Rogalla, J. R. Kirtley, C. C. Tsuei; *Nature* 422 **(2003)** 50.

[85] H. J. M. ter. Brake, G. F. M. Wiegerinck; *Cryogenics* 42 **(2002)** 705

[86] A. Damascelli, Z. Hussain, Z.-X. Shen; *Rev. Mod. Phys.* 75 **(2003)** 473.

[87] M. R. Norman, C. Pepin; *Rep. Prog. Phys.* 66 **(2003)** 1457.

[88] *Neutron Scattering in Layered Copper-Oxide Superconductors* (Ed. A. Furrer), Kluwer Academic Publishers **(1998)**, ISBN 0-7923-5226-2.

[89] B. W. Hoogenboom, M. Kugler, B. Revarz, I. Maggio-Aprile, Ch. Renner; *Phys. Rev. B* 62 **(2000)** 9179.

[90] K. McElroy, D. -H. Lee, J. E. Hoffman, K. M. Lang, E. W. Hudson, H. Eisaki, S. Uchida, J. Lee, J. C. Davis; *Nature* 428 **(2004)** 542.

[91] J. D. Jorgensen, M. A. Beno, D. G. Hinks, L. Soderholm, K. J. Volin, R. L. Hitterman, J. D. Grace, I. K. Schuller; *Phys. Rev. B.* 36 **(1987)** 3608.

[92] D. R. Harshman, A. P. Mills; *Phys. Rev. B* 45 **(1992)** 10684.

[93] R. J. Cava; *J. Am. Ceram. Soc.* 83 **(2000)** 5.

[94] Y. Yamada, Y. Shiohara; *Physica C* 217 **(1993)** 182.

[95] C. T. Lin, E. Schoenherr, H. Bender, W. Y. Liang, J. S. Abell; *J. Crystal. Growth* 128 **(1993)** 747.

[96] S. Piñol, V. Gomis, B. Martínez, A. Labarta, J. Fontcuberta, X. Obradors; *J. Alloys Compounds* 11 **(1993)** 195.

[97] M. Murakami, M. Morita, N. Koyama; *Jap. J. Appl. Phys.* 28 **(1989)** L1125.

[98] D. Hugues; *Phil. Mag.* 30 **(1974)** 293.

[99] T. Matsushita; *IEEE Trans. Appl. Supercond.* 3 **(1993)** 1045.

[100] Y. Namikawa, M. Egami, Y. Shiohara; *J. Mater. Res.* 2 **(1996)** 288.

[101] T. E. Os'kina, D. Wehler, H. Piel, R. Roeth, Yu. D. Tretyakov; *Physica C* 242 **(1995)** 85.

[102] M. Tagami, M. Sumida, Ch. Krauns, Y. Yamada, T. Umeda, Y. Shiohara; *Physica C* 250 **(1995)** 240.

[103] M. Nakamura, C. Krauns, Y. Yamada, Y. Shiohara; *J. Crystal Growth* 166 **(1996)** 859.

[104] X. Yao, T. Mizukoshi, M. Egami, Y. Shiohara; *Physica C* 263 **(1996)** 197.

[105] T. Doi, *Chemical Processing of Ceramics* ; 2nd Edition. Edited by Burtrand Lee and Sridhar Komarneni ; Taylor & Francis : Hardcoverm U. S. Vol. 1, **2005**. pages 595-611.

[106] Y. Nakamura, T. Izumi, Y. Shiohara, S. Tanaka; *J. Jpn. Inst. Metal.* 56 **(1992)** 810.

[107] M. J. Cima, M. C. Flemings, A. M. Figueredo, M. Nakade, H. Ishii, H. D. Brody, J. S. Haggerty; *J. Appl. Phys.* 72 **(1992)** 179.

[108] M. P. Delamare, H. Walter, B. Bringmann, A. Leenders, H. C. Freyhardt; *Physica C* 329 **(2000)** 160.

[109] T. Asalage, K Keefer; *J. Mater. Res.* 3 **(1988)** 1279.

[110] Y. Nakamura, A. Endo, Y. Shiohara; *J. Mater. Res.* 11 **(1996)** 1094.

[111] www.lassp.cornell.edu/sethna/Nucleation/, visited 05/05/2009

[112] H. Fujimoto, M. Murakami, N. Koshizuka; *Physica C* 203 **(1996)** 103.

[113] W. M. Yang, L. Zhou, Y. Feng, P. X. Zhang, C. P. Zhan, Z. M. Yu, X. D. Tang, R. Nicolsky, R. Andrade; *Cryogenics* 42 **(2002)** 589.

[114] D. A. Cardwell; *Mater. Sci. Eng. B* 53 **(1998)** 1.

[115] D. Shi, K. Lahiri, S. Sagar, D. Qu, V. Pan, V. F. Solovjov, J. R. Hull; *J. Mater. Res.* 12 **(1997)** 3036.

[116] R. E. Sudhakar, G. J. Schmitz; *Supercond. Sci. Technol.* 15 **(2002)** L21.

[117] P. G. Picard, X. Chaud, E. Beaugnon, A. Erruad, R. Tournier; *Mater. Sci. Eng. B* 53 **(1998)** 66.

[118] Y. A. Jee, C. -J. Kim, T. -H. Sung, G. -W. Hong; *Supercond. Sci. Technol.* 13 **(2000)** 195.

[119] D. A. Cardwell, W. Lo, H. D. E. Thorpe, A. Roberts; *J. Mater. Sci. Lett.* 14 **(1995)** 1444.

[120] A. D. Bradley, W. Lo, M. Mironova, N. H. Babu, D. A. Cadwell, A. M. Campbell, K. Salama; *J. Mater.Res.* 16 **(2001)** 2298.

[121] C. Cai, H. Mori, H. Fujimoto, H. Liu, S. Dou; *Physica C* 357 **(2001)** 734.

[122] C. -J. Kim, G. -W. Hong, Y. A. Jee, Y. -H. Han, S. -C. Han, T. -H. SPNG; *IEEE Transaction on Magnetics* 35 **(1999)** 4070.

[123] F. Sandiumenge, T. Puig, J. Rabier, J. Plain, X. obradors; *Adv. Mater.* 12 **(2000)** 375.

[124] E. Mendoza **2002** Obtenció I caracterització de ceràmiques texturados de YBCO per l'aplicació de limitació de corrent. *Tesis Doctoral*. Departament de física aplicada, Universitat de Barcelona.

[125] X. Granados, R. Yu, B. Martínez, S. Piñol, F. Sandiumenge, N. Vilalta, M. Carrera, V. Gomis, X. Obradors; *IEEE Transaction on Applied Superconductivity* 7 **(1997)** 1743.

[126] M. Ullrich, A. Leenders, J. Krelaus, L. -O Kautschor, H. C. Freyhardt, L. Schmitdt, F. Sandiumenge, X. Obradors; *Mat. Sci. eng. B.* 53 **(1998)** 143.

[127] M. N. Illiev, V. G. Hadjiev, V. G. Ivanov; *J. Raman Spectros* 27 **(1996)** 333.

[128] http://www.ifw-dresden.de/institutes/imw/sections/26/, visited 10/02/2010.

[129] E. Gilioli, M. Baldini, M. Bindi, F. Bissoli, F. Pattini, S. Rampino, S. Ginocchio, A. Gauzzi, M. Rocca, S. Zannella; *Physica C.* 463-465 **(2007)** 609.

[130] D. Shi, X. Chaud, P. Odier, A. Sulpice, D. Isfort, R. Tournier, Y. Guo, P. He, L. Guo, L. Feng Li, R. Singh; *Physica C* 443 **(2006)** 18.

[131] D. Shi, D. Isfort, X. Chaud, P. Odier, D. Mast, R. Tournier; *Physica C* 402 **(2004)** 72.

[132] F. Sandiumenge, S. Piñol, X. Obradors, E. Snoeck, C. Roucou; *Phys. Rev. B* 50 **(1994)** 7032.

[133] S. Sanfilipo, A. Sulpice, O. Laborde, D. Dourgault, Th. Fournier; *Phys. Rev. B* 58 **(1998)** 15189.

[134] S. V. Lubenets, V. D. Natsik, L. S. Fomenko, N. J. Kaufman, V. S. Bobrov, A. N. Izotov; *Low Temp. Phys.* 23 **(1997)** 902.

[135] P. Diko, G. Krabbes; *Physica C* 339 **(2003)** 151.

[136] E. S. Reddy, T. Rajasekharan; *Physica C* 279 **(1997)** 56.

[137] P. Diko, G. Krabbes; *Supercond. Sci. Technol.* 16 **(2003)** 90.

[138] M. Coll, J. Gazquez, A. Pomar, T. Puig, F. Sandiumenge, X. Obradors; *Phys. Rev. B: Condensed Matter and Materials Physics* 73 **(2006)** 075420/1.

[139] D. Isfort, X. Chaud, R. Tournier, G. Kapelski; *Physica C* 390 **(2003)** 341.

[140] J. Leggett; *Phys. Rev. Lett.* 83 **(1999)** 392.

[141] T. Kawashima, Y. Matsui, E. Takayama-Muromachi; *Physica* C 254 **(1995)** 131.

[142] J. Joo, S.-B. Jung, W. Nah, J.-Y. Kim, T. S. Kim; *Cryogenics* 39 **(1999)** 107.

[143] B. N. Lucas, W. C. Oliver, R. K. William, J. Brynestad, M. E. O'Hern; *J. Mater. Res.* 6 **(1996)** 2519.

[144] Y. M. Soifer, A. Verdyan, J. Azoulay, E. Rabkin, M. Kazakevich; *Physica C* 15 **(2005)** 3585.

[145] N. Güçlü, U. Kölemen, O. Uzum, S. Selebi; *Physica C* 433 **(2005)** 115.

[146] H. M. Ledbetter, M. W. Austin, S. A. Kim, M. Lei; *J. Mater. Res.* 2 **(1987)** 786.

[147] R. F. Giese, T. P. Sheahen, A. M. Wolsky; *Proc. American. Power Conf.* 52 **(1990)** 776.

[148] A. Goyal, P. D. Funkenbusch, D. M. Kroeger, S. J. Burns; *Physica C* 71 **(1992)** 2363.

[149] Ya. M. Soifer, A. Verdyan, J. Azoulay, M. Kazakevich, E. Rabkin; *Physica C* 402 **(2004)** 80.

[150] A. Goyal, W. C. Oliver, P. D. Funkenbusch, D. M. Kroeger, S. J. Burns; *Physica C* 183 **(1991)** 221.

[151] R. R. Reddy, M. Murakami, S. Tanaka, P. V. Reddy; *Physica C* 257 **(1996)** 137.

[152] L. F. Li, K. Zhang, D. Jin, Y. Y. Li, S. Meriani; *Physica C* 282-287 **(1997)** 2599.

[153] Y. Yoshino, A. Iwabuchi, K. Noto, N. Sakai, M. Murakami; *Physica C* 357-360 **(2001)** 796.

[154] Y. Y. Lim, M. M. Chaudhri; *J. Phys. D : Appl. Phys.* 34 **(2001)** L70.

[155] R. F: Cook, T. R. Dinger, D. R. Clarke; *Appl. Phys. Lett.* 51 **(1987)** 454456.

[156] C. Leblond-Harnois, R. Caillard, I. Monot-Laffez, G. Desgardin, B. Raveau; *Physica C* 341-348 **(2000)** 2439.

[157] J. Joo, J.-G.M. Kim, W. Nah; *Supercond. Sci. Technol.* 11 **(1998)** 645.

[158] A. Leenders, M. Ullrich, H. C. Freyhardt; *IEEE Trans. Appl. Supercond.* 9 **(1999)** 2074.

[159] W. J. Galler, T. K. Worthington, T. R. Dinger, F. Holtzberg, D. L. Kaiser, R. L. Sandstrom; *Physica B* 148 **(1987)** 221.

[160] J. Rabier, P. D. Tall, M. F. Denanot; *Philosophical Magazine A* 67 **(1993)** 1021.

[161] J. Rabier; *Philosophical Magazine A* 73 **(1996)** 753.

[162] J. Rabier, M. F. Denanot; *Philosophical Magazine A* 65 **(1992)** 427.

[163] P. D. Tall, C. Coupeau, J. Rabier; *Scripta Materialia* 49 **(2003)** 903.

OBJECTIVES

Knowledge is recognition of
something absent; it is a
salutation, not an embrace

George Santayana (1862-1952)
American philosopher and poet

The main purpose of this Thesis is the characterization of the mechanical properties of YBCO bulk and coated conductors. This characterization has been performed at micro/nanometric scale, in order to evaluate and differentiate the mechanical properties in elastic and elasto-plastic deformation ranges.

One issue to study is the hardness and Young's modulus of each phase (matrix, inclusions and intherphase) at room temperature. The correct visualization of the different fracture mechanisms produced under and in the vicinity of the different indentation imprints generated by the stress field during the indentation process supply us a correct knowledge of the different fracture mechanisms.

Another issue in this Thesis is the determination of the stress-strain curves, which can help us to understand elasto-to-plastic deformation in superconductor ceramics with the correct knowledge of the different deformation mechanisms taking place in the elasto-to-plastic transition.

Another issue to be account in this Thesis is the determination of the quality across the YBCO joints and obtains a correlation between the microstructural, mechanical and critical current density performance of melt-textured YBCO welds fabricated by the silver welding technique.

One of the most important purposes of this Thesis correlated with coated conductor materials is the correct characterization of the hardness and Young's modulus of different CeO_2 buffer layers grown on Ni-5%W substrates by pulsed electron deposition. Finally, we would like to obtain an ideal candidate as a reliable and efficient buffer layer to be employed as a coated conductor for superconducting applications.

3

EXPERIMENTAL PROCEDURE

Acquire new knowledge whilst thinking over the old, and you may become a teacher of others

Confucius (BC 551 – BC 479)
Chinese philosopher

3.1. Synthesis, texture and oxygenation process

Some of the samples used in this Thesis have been obtained in our research laboratory by TSMG and Bridgman techniques, while some others have been supplied by other research groups (welded and *cc*).

3.1.1. Synthesis of YBCO powders

From the point of view of powder preparation, solid state concepts involve firing the oxide/carbonate precursor several times until the reaction is complete, along with intermediate grindings and pelletising steps. This method is labour-intensive, time consuming and may introduce contamination from the grinding media.

One possible simplification is the use of a solution of the cationic salts in which an intimate mixing of the components is produced by different techniques: the acetate route, coprecipitation, freeze-drying, etc, which results in a better degree of mixing, although some microsegregation can nonetheless appear[1]. These difficulties can also be overcome by quick solvent evaporation using spray drying or pyrolysis techniques. Although very scalable industrially, these methods need expensive equipment and maintenance.

Sol-gel methods are particularly effective in obtaining an amorphous precursor by means of soluble organic compounds, which reticulate to form a gel, in which the cationic salts become trapped by complex hydrolysis-condensation mechanisms. The calcination at relatively low temperatures render the desired phase. However, sol-gel methods are complex and they involve the use of toxic compounds. Other major concerns are carbon content in the final powder and organic precursor combustion risk. It has been shown by a number of authors[2,3,4] that polyvinyl alcohol (PVA) can be a useful and rather simple way for obtaining intimate mixing of cationic species. For this reason, this method has been employed in this Thesis to obtain the different YBCO powders.

The reagents used were Y_2O_3 (99.9%) and CeO_2 (99.9%) supplied by Merck, Cu (99.99%) manufactured in our laboratory, and $Ba(NO_3)_2$ (99.99%) supplied by Quality Chemical, while Alcohol Polyvinylic, *PVA*, was purchased from FLUKA (PVA 49000). The approximate mean degree of polymerization is around 1100[5].

Stoichiometric quantities of the oxides and carbonates were weighted to give 69% w/w Y-123, 30% w/w Y-211 and 1% w/w CeO_2. This proportion has been demonstrated to maximize critical current density[6]. Firstly, yttrium and copper oxides are dissolved in a 10% excess hot concentrated nitric acid (HNO_3), forming a blue-green solution. In a separate beaker, barium nitrate is dissolved with hot water (H_2O). Cerium oxide is dissolved in the same way that yttrium and copper, but by adding some hydrogen peroxide (H_2O_2). Then, solid PVA is dissolved in hot water to obtain a concentrated PVA solution in a separate glass beaker. PVA mass was calculated according to the results of Gülgun *et al*[7], who report that the ratio of positive charges due to cation species to PVA monomer ($-CH_2\text{-}CHOH-$), should be 4:1 to obtain an optimum synthesis entrapment.

After dissolving the necessary amount of PVA in water, the resulting solution is slowly added to the cation dissolution to prevent an excessive foam formation. The mixed cation solution then quickly turns from blue to green. Moreover, the solution was stirred to assure good homogeneity between the mixed cation solution and PVA. Then, a hot plate is used to evaporate the excess of H_2O and HNO_3 in the form of NO_x gas. The solution progressively increases in viscosity until a point is reached when a gel develops. By applying more heat (*around 500 ºC*), the gel transforms into a black ash, with spongy structure due to the pores formed during the combustion gases evacuation. Then these ashes are easy to ground in an agate mortar. The calcinated powder is deagglomerated by ball milling. The heat treatment of the xerogel consists of a 5ºC/min heating ramp to a soak at 990ºC for 48 h in air. Cooling to room temperature was also carried out at the same speed.

3.1.2. Texture and oxygenation process

3.1.2.1. TSMG samples

TSMG is known as the most effective process to fabricate block-type samples. To obtain the green bodies, the powder fabricated by *PVA* method, with 1% w/w CeO_2, was uniaxially pressed at 500 MPa into pellets, with a diameter of 25 mm and thickness from 10 to 20 mm[5,6]. *Fig. 3.1.*, exhibits the handmade furnace employed to obtain TSMG samples. This furnace has been assembled in a way that isothermal conditions are maintained at least under the seed. So, the thermal gradient is controlled by another furnace surrounding this one.

Fig. 3.1. Image of the furnace employed to obtain TSMG samples.

The $NdBa_2Cu_3O_7$ (*NdBCO or Nd-123*) single crystals were manufactured by Bridgman technique[8] (see *section 3.1.2.2*). The (001) Nd-123 seed was placed on the top of sample. The Y-123 crystal grows from the Nd-123 seed crystal epitaxially with a squared sharp interface. The growth distance is defined as the length from the edge of the seed crystal to the solid-liquid interface. *Fig. 3.2* shows the heat treatment pattern followed in this Thesis to produce YBCO-TSMG samples. The optimization of the temperature profile is crucial for the production of large-single crystals of bulk YBCO. The TSMG samples were manufactured by the following process: the YBCO samples were heated up to 1055ºC at a rate of 300ºC/h, and held for 2 h for homogeneous melting; after that, the sample was cooled down to about 1010ºC at a rate of 30ºC/h, and further cooled to 1008ºC in 100 h; then the samples were cooled to room temperature at a rate of 300ºC/h in air; after growth process, the different samples were annealed at 450ºC for 240 h, to allow the transformation from tetragonal to orthorhombic phase.

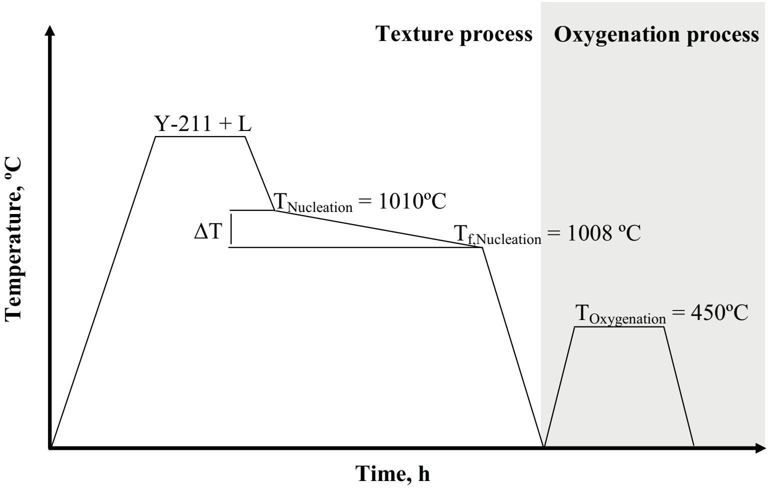

Fig. 3.2. Heat pattern of the experimental procedure in the manufacture of YBCO samples by TSMG technique.

To define the degree of undercooling, the equilibrium peritectic temperature of Y-123 phase is needed. *Fig. 3.3* shows YBCO samples with tetragonal structure, obtained with the thermal treatment previously explained. *Fig. 3.3a*, shows a single YBCO crystal and *b*, exhibits a poly crystal YBCO sample.

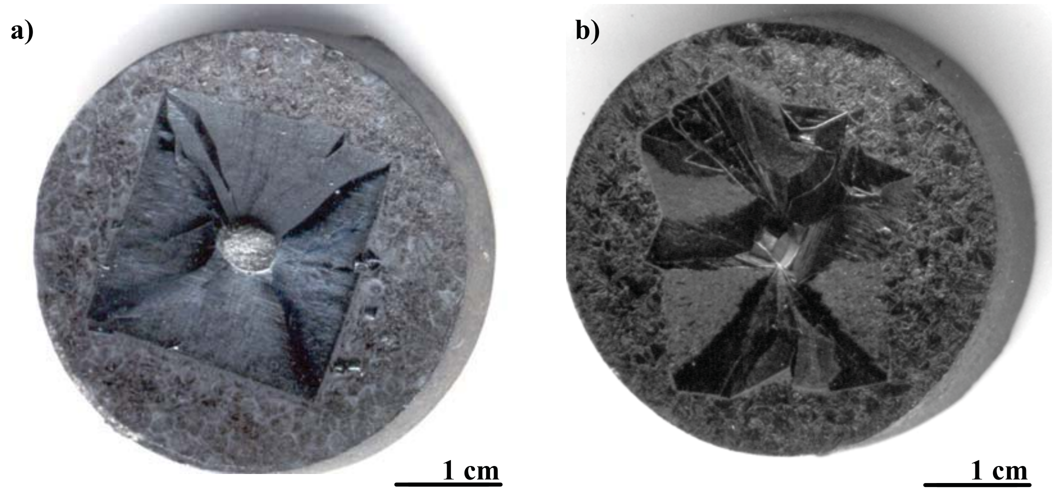

Fig. 3.3. Photograph of the top view of the typical seeded grown sample, a) single crystal, and b) poly-crystal.

Welding technique: YBCO welds with asymmetric (001)-tilt boundaries were prepared by the silver welding technique[9] supplied by the Institute of Materials Science of Barcelona (ICMAB). Samples were fabricated from commercial YBCO bulk single-domains with nominal composition Y-123 + 25% mol. Y_2O_3 + 1% wt. CeO_2[10]. 1 cm^3 cubes were extracted from the as-grown tetragonal samples. Each YBCO cube halved parallel to the *c*-axis, and then cut again with a relative misorientation (Θ) in one of the adjacent grains. The two joining surfaces thus obtained were polished with diamond powder, down to a size of 1μm, and a 10 μm thick Ag foil was introduced between them. The sandwich-like assembling so obtained was fixed between two alumina plates parallel to the joint, and placed in horizontal position in the furnace. The specimen was first heated up to T_{max} of 995ºC and dwelt for 3 hours; then it followed at slow-cooling ramp at 0.6 ºC/h down to 950ºC, and a fast-cooling to room temperature. Finally, the welded samples were annealed in flowing oxygen at 1.1 bar for 120 hours at 450ºC, to achieve the orthorhombic, superconducting phase. Samples were halved parallel to the *ab*-plane for measurements, so final dimensions were 1x1x0.5cm^3.

3.1.2.2. Bridgman samples

In this case, the powder mixture is compressed under isostatic pressure as a bar. The main characteristic of this method is the use of a furnace with a thermal gradient, so that the maximum reached temperature is slightly higher than the peritectic temperature of the mixture (see *Fig. 3.4.*).

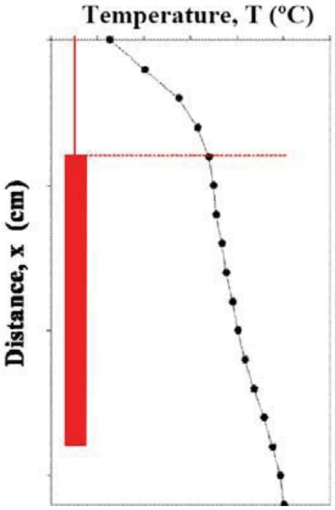

Fig. 3.4. Temperature profile inside of the Bridgman furnace

A region of the bar, the one placed on the hottest region of the furnace, is found to be in the melt state (the largest viscosity of the mixture, even in the liquid state, avoids the bar from falling). As the liquid region of the bar is moved away from the hottest zone, it starts to solidify. Different grains appear at the beginning of this process, but the different growth rate between them promotes the existence of a single grain (see *Fig. 1.21b*).

After heating the presintered YBCO bars well above the peritectic temperature, T_p, the semisolid bars hanged inside the furnace and moved at a constant rate of 1 or 2 mm·h^{-1} through a region having an axial temperature gradient of 20 K·cm^{-1} at the peritectic[8]. *Fig. 3.5.* shows a figure of the handmade furnace employed to obtain the different samples textured by Bridgman technique.

Fig. 3.5. Figure of the Bridgman furnace employed in this Thesis.

The thermal treatment can be observed in *Fig. 3.6*.

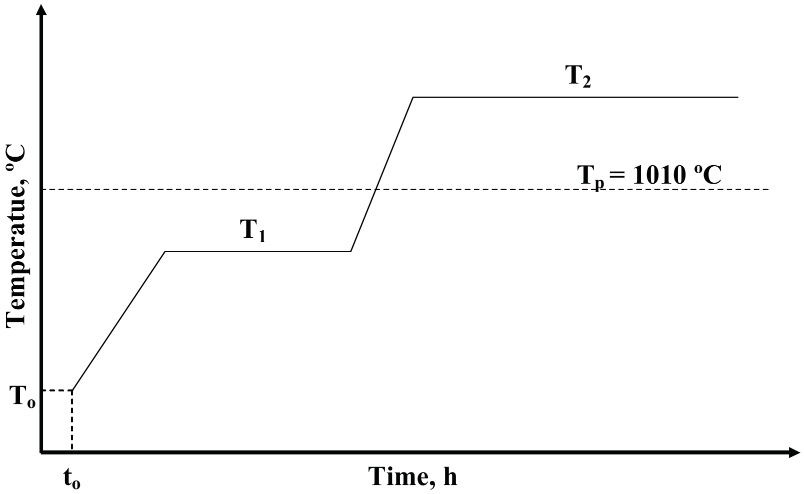

Fig. 3.6. Thermal treatment of bulk superconductor samples textured by Bridgman technique.

After the texture process, the YBCO pieces were oxygenated in a horizontal furnace at 450ºC for 240 h[11]. From the oxygenated pieces with a common *c*-axis tilt of 45º respect to the longitudinal direction of the bar, small pieces of 2 mm height were cut by the *ab*-plane[12].

NdBCO seeds: The NdBCO or Nd-123 single crystals were manufactured in our laboratory using the Bridgman technique as explained before, with a temperature gradient 1-4ºC/m in vertical direction, and using a constant dragging speed of 1 mm/h.

3.1.2.3. YBCO-Coated Conductors, YBCO-cc

YBCO-*cc* samples consisting of Ni-5%W substrate and CeO_2 layer used in this Thesis for mechanical characterization have been supplied by the Instituto Materiali per Elettronica e Magnetismo IMEM-CNR (Parma, Italy) and obtained by Pulsed Electron Deposition technique (PED)[13].

3.2. Specimen preparation

The first step after the sample obtention is to prepare the surface specimen for indentation measurements. Nowadays, different techniques are widely employed to reduce the superficial roughness, which can be classificated in four different groups: *mechanical polish, electropolish, chemical etching, and ionic etching.*

Most of the samples require some degree of mechanical polishing. There are six different steps to complete the mechanical polish: sectioning, coarse grinding, mounting, fine grinding, rough polishing, and final polishing.

Sectioning is the removal of a representative volume from a parent specimen. The final specimen must be small enough to allow for Nanoindentation, SEM, AFM, and FIB mounting and examination. The limiting size will be AFM dependent. Two different types of sectioning can be performed: high-speed abrasive and low speed, low deformation precision sectioning. Then, specimens are sometimes mounted in a solid medium for further grinding and polishing. There are two different types of mounting processes, hot and cold. After this process, the grinding begins to remove the deformation layer introduced during sectioning, and produces a flat surface for examination. Typically, these steps start with 240 grift SiC paper, either in disk or belt form, and continues through about 800 or 1200 grift SiC. For YBCO, water cannot be used as a lubricant, however, for this type of samples ethanol is used for this purpose. It is useful to use an optical microscope (OM) to examine the surface more closely. After that, the polishing process starts. This step is used to remove any deformation introduced earlier during grinding process. This process has many more variables to consider. Many types of abrasives, suspension mediums, and polishing cloths are available. This process consists of five different steps, starting at about a 9 micron abrasive, and ending with a 0.05 micron abrasive. Finally, in order to reduce the superficial roughness, a suspension of colloidal silica in isopropanol is used for a final polishing medium. This commercially available solution consists of negatively charged particles of silicon dioxide (SiO_2) with a pH value between 8 and 11. This solution works well with nearly all materials, with particular effectiveness on ceramic and geological samples that are otherwise difficult to prepare. The suggested mechanical polishing sequence used in the different YBCO samples textured by TSMG and Bridgman technique employed in this Thesis are:

- Sectioning and mounting the sample.
- Grinding until planarity using 240, 400, 600, 800 and 1200 grift SiC paper (the last being repeated 2 or 3 times).
- Polishing with 9 and 3 microns diamond suspension for 5 to 10 minutes.
- Polishing with 1 micron alpha alumina suspension for 5 to 20 minutes.
- Finally, polishing with a suspension colloidal silica in isopropanol for 25 minutes.

3.3. Mechanical characterization

3.3.1. H and E measurements

Nanoindentation tests were performed with a Nanoindenter® XP System (Agilent Technologies, see *Fig. 3.7*) in order to obtain the *H* and *E* for Bridgman and TSMG samples. Forty indentations were made on each sample for each applied load in order to obtain a correct average using a Berkovich tip. In all cases, the different mechanical properties were calculated as a function of penetration depth using the Oliver and Pharr approach[14].

In the case of the thin films studies, the *H* and *E* for each studied sample were calculated as a function of penetration depth using the Oliver and Pharr algorithm[14]. Depth was limited to less than 10% of the film thickness, which will yield *H* of the coating without any influence of the substrate[15]. In the case of thin films, this becomes interestingly difficult. It has also been found in many cases that this rule is too restrictive for soft films, and may be not restrictive enough for hard films[16]. Therefore, *E* values had been obtained using the Bec and Rar *et al.* models. More than eighty indents were performed per load, over a range of loads from 0.5 to 500 mN, on two different surface regions of the same sample, in order to achieve statistical significance.

In order to investigate the variation of mechanical properties across the welds, we performed nanoindentation scans on the *ab*-plane in a range of 2 cm across each boundary. The separation between imprints was 50 μm in order to isolate the plastic behaviour generated under the residual imprint. Six hundred indentations were performed for each studied sample in order to achieve statistical significance. Each of the *E* and *H* values plotted in Chapter 7 is the average of 15 scans performed across the boundary, separated 50 μm from each other.

Fig. 3.7. Image of the nanoindentation equipment employed in this Thesis.

3.3.2. *σ–ε curves*

During the stress(σ)-strain(ε) determination for YBCO samples textured by Bridgman and TSMG techniques and the mechanical characterization of YBCO thin films, the nanoindentation tests were carried out with a Nanoindenter® XP System (Agilent Technologies) with Continuous Stiffness Measurement (CSM), which allows continuous measurements of stiffness (*S*), and applied load (*P*), as a function of penetration depth (*h*). Indentations were carried out at a maximum applied load of 650mN (in order to maximize the residual penetration depth at around 2000 nm), and under a constant strain rate of $0.05s^{-1}$. Sixteen indentations were made on each material in order to obtain a correct average using a spherical tip with 25 μm of radius. The different mechanical properties were calculated using Hertz equations[17].

3.4. Residual imprint characterization

Of special interest in microtechnology are, quite naturally, the methods with high spatial resolution, in particular, those which can identify unknown substances in small volumes and determine their composition with enough accuracy. The particle beam methods have proved to be outstanding for such applications[18,19,20,21,22,23].

Different techniques (i.e. Field Emission Scanning Electron Microscopy, FE-SEM and Atomic Force Microscopy, AFM) are widely emploed in order to observe the different residual imprints and observe different fracture and deformation mechanisms generated during the indentation process. Recently, a new technique has been implemented in order to observe the different response behaviour under the indentation imprint, this technique is widely known as a Focused Ion Beam (FIB).

3.4.1. Field Emission Scanning Electron Microscopy, FE-SEM

SEM can provide information on surface topography, crystalline structure, chemical composition, and electrical behaviour of the top of an specimen[24]. The electron beam interacts with the surface material, causing a variety of signals: secondary electrons, backscattered electrons, X-Ray, Auger electrons, cathadoluminiscence. In this Thesis only secondary electrons have been used in order to characterize the different residual imprints. A scheme diagram of typical FE-SEM can be observed in *Fig. 3.8*.

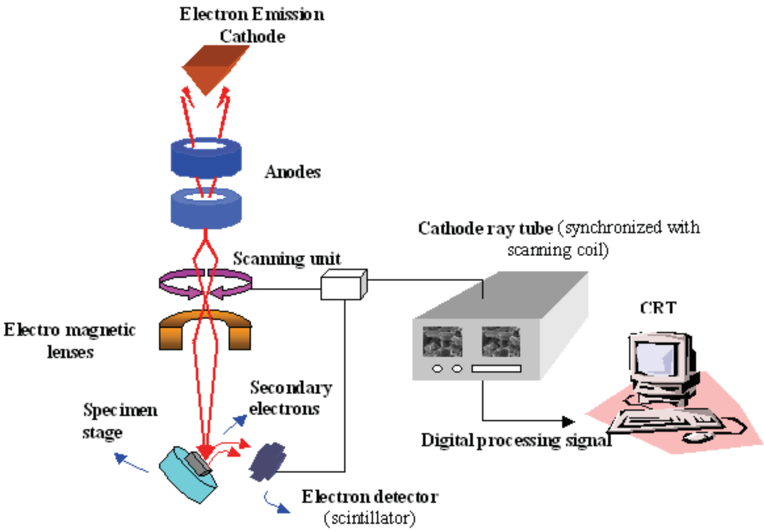

Fig. 3.8. Scheme diagram of typical FE-SEM[25].

A field-emission cathode in the electron gun of a scanning electron microscope provides narrower probing beams at low as well as high electron energy, resulting in both improved spatial resolution and minimized sample charging and damage. FE-SEM is widely employed for applications which demand the highest magnification possible. For this reason, this equipment has been employed to observe the residual nanoindentation imprints and the fracture mechanisms present in the surface of the different studied samples.

Under vacuum, electrons generated by a FE-SEM are accelerated in a field gradient. The beam passes through *electromagnetic lenses*, focusing onto the specimen. As a result of this bombardment, different types of electrons are obtained, and an image of the sample surface is constructed by comparing the intensity of these secondary electrons to the scanning primary electron beam. Finally, the resulting image is displayed on a monitor.

In addition, this equipment presents different advantages compared to often conventional equipments:

- FE-SEM produces cleared, less electrostatically distorted images with spatial resolution down to 1 ½ nm. That is 3 to 6 times better than conventional SEM.
- Smaller-area contamination spots can be examined at electron accelerating voltages compatible with Energy Dispersive X-Ray Spectroscopy.
- Reduced penetration of low kinetic energy electrons probes closer to the immediate material surface.
- High quality, low voltage images are obtained with negligible electrical charging on samples; accelerating voltages range from 0.5 to 30KV.

The SEM images were obtained by a Hitachi H-4100 FE-SEM in the *Serveis Cientificotènics of the University of Barcelona, SCT-UB*, at acceleration voltages of 15 KV. YBCO samples must be prepared as they are not conducting. In this case, the samples with a residual indentation imprint lower than 10 mN of applied load were just placed on the specimen stub of the SEM and small bridges of silver have been painted between the sample and the SEM stub. However, for samples with an applied load higher than 10 mN, it is necessary to coat them with a thin conductive layer such as gold or carbon. This technique is complementary to the information acquired by AFM and FIB.

3.4.2. Atomic Force Microscopy, AFM

The AFM, invented by Binning, Quate, and Gerber**[26]** in 1986, was developed to exploit contact and non-contact forces for imaging surface topology, and to study new physical phenomena at microscopic dimensions.

AFM images were obtained by an AFM Dimension 3100 and Multimode (Veeco, see *Fig. 3.9a* and *b*, respectively) in the SCT–UB.

a) **b)**

Fig. 3.9. Image of the different AFM employed during this Thesis to visualize the different residual nanoindentation imprints, a) AFM-Dimension 3100, and b) Multimode.

3.4.3. Focused Ion Beam, FIB

The damage produced under the residual nanoindentation imprint of YBCO samples (bulk and thin film materials) were characterized by a dual beam FIB/SEM (FIB Strata DB235, see *Fig. 3.10*). The residual indentation imprints were cross-sectioned along the *c*-axis to evaluate the damage after the indentation process. A thin platinium layer was deposited on the sample prior to FIB machining, in order to minimize ion beam damage. A Ga^+ ion source was used for milling the surface at a voltage of 30 KV. The final polishing of the different cross-sections was performed under less aggressive conditions.

Fig. 3.10. Image of the chamber of the FIB equipment, with the different detectors employed to perform the different trenchs[27].

3.5. Microstructural characterization

The transmission electron microscope (TEM) makes use of high-energy electrons to irradiate electrotransparent specimens, around 0.1 μm or less in thickness. The electrons are transmitted and form an image of the specimen magnified in several steps with the aid of electron-optical lenses. The entire image can be observed directly on a fluorescent screen.

3.5.1. *Transmission electron microscopy, TEM, and High Resolution-TEM, HR-TEM*

With TEM, a bulk sample with a thickness lower than 200 nm is bombarded by a highly focused beam of single-energy electrons. The beam has enough energy for the electrons to be transmitted through the sample (see *Fig. 3.11*). The samples are YBCO thin foils textured by Bridgman and TSMG techniques, and prepared by the conventional cutting, gluing and grinding procedures, followed by a final milling step with Ar ions down to perforation[28]. The transmitted electron signal is greatly magnified by a series of electromagnetic lenses up to atomic resolution. The magnified transmitted signal may be observed in two ways: through electron diffraction or direct electron imaging. Electron diffraction patterns were used to determine the different inherent defects, and grain orientation present in YBCO structure. Direct electron images yield information about the microstructure and size.

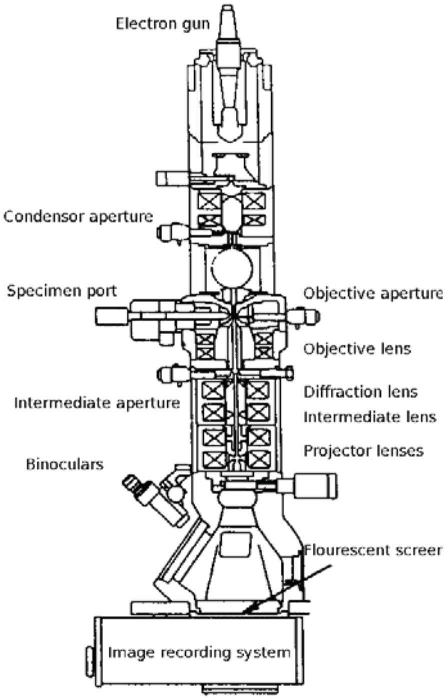

Fig. 3.11. Schematic diagram of typical TEM[29].

The TEM images and electron diffraction patterns were obtained by a Philips CM30 TEM, while HR-TEM images patterns were obtained by a JEOL1010 electron microscope operated at 200 kV (point to point resolution 0.19 nm), equipped with a Gatan Image filter 2000 Energy Electron Loss Spectroscopy (EELS) spectrometer with an energy resolution of 0.8eV in the *SCT-UB*. The EELS spectrometer allowed us to perform quantitative element analysis of the Y-211 inclusions present in the Y-123 matrix.

3.5.2. Tomography with TEM

Tomography is a 3D reconstruction departing from a sequence of closing bidymensional images. The Tomography with TEM allows us to understand and visualize the different residual stresses created inside the Y-211 inclusions during the manufacturing process due to the different expansion coefficients[30] between Y-123 and Y-211. Then, we fully characterize the tensile stress by HR-TEM, high angular annular dark field (HAADF), scanning TEM (STEM), and HAADF electron tomography, by using the new developed GATAN 3D Tomography-Acquisition Software, as well as the 3D Reconstruction and 3D Visualization Pluging[31]. The feedback of the obtained results by electron microscopy is used to better understand the different residual stresses created during the solidification process[32].

3.6. References

[1] P. Odier, B. Dubois, M. Gervais, A. Douy ; *Mater. Res. Bull.* 24 **(1989)** 11.

[2] H. Kweon, G. B. Kim, H. S. Lim, S. S. Nam, D. G. Park; *J. Power Sources* 83 **(1999)** 84.

[3] S. Lee, E. A. Benson, W. M. Kriven; *J. Am. Ceram. Soc.* 82 **(1999)** 2049.

[4] M. A. Gülgün, M. H. Nguyen, W. M. Priven; *J. Am. Ceram. Soc.* 82 **(1999)** 556.

[5] I. G. Serradilla, A. Calleja, X. G. Capdevila, M. Segarra, E. Mendoza, J. Teva, X. Granados, X. Obradors, F. Espiell; *Supercono. Sci. Technol.* 15 **(2002)** 566.

[6] S. Piñol, V. Gomis, B. Martinez, A. Labarta, J. Fontcuberta, X. Obradors; *J. Alloys Compounds* 11 **(1993)** 195.

[7] M. A. Gülgün, W. M. Priven; *J. Am. Ceram. Soc.* 82 **(1999)** 556.

[8] N. Vilalta, F. Sandiumenge, S. Piñol, X. Obradors; *J. Mater. Res.* 12 **(1992)** 38.

[9] S. Iliescu, X. Granados, E. Bartolomé, S. Sena, A. E. Carrillo, T. Puig, X. Obradors, J. E. Evetts; *Supercond. Sci. Technol.* 17 **(2000)** 182.

[10] M. Ullrich, H. Walter, A. Leenders, H. C. Freyhardt; *Physica C* 311 **(1999)** 86.

[11] E. Mendoza, *Obtenció i caracterització de ceràmiques texturades de YBCO per l'aplicació de limitació de corrent.* Tesis Doctoral Departament de física Aplicada, Universitat de Barcelona **(2002)**.

[12] M. Ullrich, A. Leenders, J. Krelaus, L. –O. Kautschor, H. C. Freyhardt, L. Schmidt, F. Sandiumenge, X. Obradors; *Mater. Sci. Eng. B*. 53 **(1998)** 143.

[13] E. Gilioli, M. Baldini, M. Hindi, F. Bissoli, F. Pattini, S. Rampino, S. Ginocchio, A. Gauzzi, M. Rocca, S. Zannella; *Physica C* 463 **(2007)** 609.

[14] W. C. Oliver, G. M. Pharr; *J. Mater. Res.* 7 **(1992)** 6.

[15] P. J.. Burnett, T. F. Page; *J. Mater. Sci.* 19 **(1984)** 3424.

[16] A. C. Fisher-Cripps; *Vacuum* 58 **(2000)** 569.

[17] S. Basu, A. Moseson, M. W. Barsoum; *J. Mater. Res.* 21 **(2006)** 2628.

[18] E. Fuchs; *Microelectronic Enging.* 1 **(1983)** 143.

[19] *Powder diffraction File*, JCPDS, International center for Diffraction data, Swarthmore, PA, USA **1985** (supplemented yearly).

[20] *Structure Reports*, International Union of Crystallography,D. Reidel Publishing Company, Dordrecht (Holland), Boston (USA) **1984**.

[21] *Powder diffraction*, An international journal of materials characterization, JCPDS-International Centre for Diffraction Data, Swarthmore, PA, USA.

[22] T. Ambridge, B. Wakefield; *Brit. Telecom. Technol. J.* 3 **(1985)** 47.

[23] H. W. Werner; *Mat. Sci. Eng.* 42 **(1980)** 1.

[24] K. D. Vernon-Parry; *Análisis* 14 **(2000)** 40.

[25] http://www.photometrics.net/fesem.html, visited 10/05/2009.

[26] G. Binning, H. Rohrer; *J. Res. Dev.* 30 **(1986)** 355.

[27] http://petroleum.berkeley.edu/UCOil/ECR/projects/fib.htm, visited 07/07/2009

[28] D. B. Williams, C. B. Carter. "*Transmission Electron Microscopy: a textbook for material science*", Chapter 10 page 155. Ed. Plenium. **1996**.

[29] http://upload.wikimedia.org/wikipedia/commons/5/58/Scheme_TEM_en.png, visited 07/07/2009

[30] F. Sandiumenge, S. Piñol, X. Obradors, E. Snoeck, C. Roucau; *Phys. Ver. B.* 50 **(1994)** 7032.

[31] http://www.gatan.com/products/software/tomography.php, visited 07/07/2009.

[32] M. Heigoldt, J. Arbiol, D. Spirkoska, J. M. Rebled, S. C. Boj, G. Abstreiter, F. Peiró, J. R. Morante, A. Fontuberta; *J. Mater. Chem.* 19 **(2009)** 840.

4

MEASUREMENT OF NANOHARDNESS AND YOUNG's MODULUS

> ***Knowledge is that which, next to***
> ***virtue, truly raises one person***
> ***above another***
>
> *Joseph Addison (1672-1719)*
> *English essayist, poet, and dramatist*

In the following section the different H and E for YBCO samples textured by Bridgman and TSMG techniques have been studied with a sharp Berkovich indenter and using the Oliver and Pharr approach[1].

The results achieved by the study of Bridgman samples have been already published in an international review presented here. The TSMG samples were studied in the same way, in order to extend our knowledge of the material, and compare both growing techniques. These results are still under revision and are going to be published soon.

4.1. YBCO samples textured by Bridgman technique

YBCO materials show high critical current density and high trapped magnetic field at cryogenic temperatures (*liquid nitrogen, 77K*). However, practical applications of these type of materials are often limited by their poor mechanical performance, especially at cryogenic temperatures. Hence, mechanical properties such as hardness, microhardness, elastic modulus, etc., are crucial for industrial applications of these kind of materials.

The following paper, published in *Nanotechnology* in August 2007, describes the mechanical properties (*H and E*) of the matrix (Y-123), the inclusions (Y-211) and the interphase between matrix and inclusions (Y-123/Y-211) for samples textured by Bridgman technique using a sharp diamond indenter (*Berkovich*) at different applied loads. The residual nanoindentation imprints have been characterized by FE-SEM and AFM.

More recently, a review work entitled ***Mechanical characterization at nanometric scale of ceramic superconductor composites***, has been published by *NovaScience Publisher*, as a chapter of the book entitled "Nanotechnology: Nanofabrication, Patterning, and Self-Assembly" (To be published in 2010).

Following the article, additional results concerning this topic are included.

IOP Publishing NANOTECHNOLOGY

Nanotechnology **18** (2007) 385701 (6pp) doi:10.1088/0957-4484/18/38/385701

Nanohardness and Young's modulus of YBCO samples textured by the Bridgman technique

J J Roa, X G Capdevila, M Martínez, F Espiell and M Segarra

Centro DIOPMA, Departamento de Ciencia de los Materiales e Ingeniería Metalúrgica;
Instituto de Nanociencia y Nanotecnología de la Universidad de Barcelona (IN^{2}UB), Facultat
de Química, Universidad de Barcelona, Martí i Franqués 1, Barcelona E-08028, Spain

E-mail: joanjosep_roa@ub.edu

Received 26 April 2007, in final form 27 July 2007
Published 31 August 2007
Online at stacks.iop.org/Nano/18/385701

Abstract

Mechanical properties of the orthorhombic phase of $YBa_2Cu_3O_{7-\delta}$ (Y123) at room temperature have been investigated at different applied loads: 5, 10, 30 and 100 mN using a nanoindentation technique. This study was carried out for different monodomains on the (001) plane for textured Bridgman samples with dispersed particles of Y211 as pinning centres. Hardness and Young's modulus values were calculated using the Oliver–Pharr approach.

Nanohardness and Young's modulus for the Y123, Y_2BaCuO_5 (Y211) and Y123/Y211$_{\text{composite}}$ (YBCO) were determined using an applied load of 5 and 10 mN. For higher loads, it is not possible to differentiate the matrix (Y123) from the precipitates (Y211). In this case, only hardness and Young's modulus of the YBCO composite can be determined.

Finally, the ultra-low load imprints obtained by nanoindentation have been correlated with parameters obtained by atomic force microscopy (AFM) and field emission scanning electron microscopy (FE-SEM).

(Some figures in this article are in colour only in the electronic version)

1. Introduction

It is well known that high-T_c bulk superconductors show high critical current density and high trapped magnetic field at cryogenic temperatures (liquid nitrogen). However, practical applications of these superconducting materials are often limited by their poor mechanical performance, especially at cryogenic temperatures. Hence, mechanical properties such as nanohardness, microhardness, elastic modulus, creep behaviour, etc., are crucial for industrial applications of these materials.

In order to prepare bulk pieces, a fine and well-dispersed Y211 precipitate distribution in the Y123 superconducting matrix has to be achieved. The effects of Y211 are an increase of the irreversibility line by acting as pinning centres, an improved crystal growth, reduction of macrocracks and thus enhancement of mechanical toughness.

It is possible to modify the size of the Y211 particles by varying the concentration of the Y211 in the composite. It has been reported that, when the concentration of the Y211 phase is ∼30 vol% Y211, the average size of precipitates is drastically reduced down to ∼0.1–3 μm [1]. This size reduction effect can be accounted for by considering that any Y211 excess in the semisolid melt increases the number of nucleation sites for Y211 released during the Y211 + liquid → Y123 peritectic reaction.

However, references about the mechanical properties such as nanohardness and Young's modulus of Y211 precipitates distributed in the Y123 matrix could not be found.

Nanoindentation is a versatile technique for measuring mechanical properties at very small scales, namely in the micron and sub-micron range [2]. Nanoindentation is a versatile, non-destructive and selective technique. It can work from 50 nN to 500 mN. Nowadays, nanoindentation is routinely used for mechanical characterization of thin films, surface layers and bulk materials. Ultra-low load indentation uses high resolution sensors and actuators to continuously control and monitor the loads and displacements

0957-4484/07/385701+06$30.00

Table 1. Test inputs of nanoindentation.

Name	Value	Units
Allowable drift rate	0.05	nm s^{-1}
Load rate multiple for unload rate	1	—
Maximum load	5, 10, 30 and 100	mN
Number of times to load	5	—
Peak hold time	30	S
Per cent to unload	90	%
Time to load	15	s

on an indenter as it is driven into and withdrawn from a material [3–5]. In some systems, forces as small as a nano-newton and displacements of about an ångström can be accurately measured.

One of the greatest advantages of the technique is that most of the mechanical properties of materials can be directly extracted from analyses of the indentation load–displacement data, thus avoiding the need to display the hardness impression and facilitating property measurement at the sub-micron scale. Besides, the measurements are non-destructive.

The purpose of this experimental study is to determine mechanical properties of each phase (Y123 and Y211) at room temperature. So different loads (5, 10, 30 and 100 mN) have been applied on the *ab* plane (001) of textured Bridgman samples.

Nanohardness and Young's modulus of the different phases have been calculated through the Oliver and Pharr approach [6].

2. Experimental procedure

2.1. Preparation of bulk YBCO pieces and monodomain growth

The YBCO powders were prepared by the PVA method [7]. The ratio used here (69% w/w Y123, 30% w/w Y211 and 1% w/w $CeO_2 \cdot nH_2O$) has been demonstrated to maximize critical current density [8]. The calcined powder is deagglomerated by ball milling in an agate mortar.

Green bulk pieces were obtained by uniaxially isostatic cold pressure and further textured using the Bridgman method [9, 10]. After this, bulk textured pieces were oxygenated in a vertical furnace at 450 °C for 240 h [11]. From the oxygenated pieces with a common *c*-axis tilt of 45°, small pieces of 2 mm height were cut by the (001) planes [12].

2.2. Measurement of hardness and Young's modulus

The nanoindentation technique was performed by a Nano Indenter® XP system (Systems Corporation) equipped with Test Works 4 Professional level software. Nanoindentation imprints were observed with an AFM NanosCope III-A atomic force microscope and with a field emission Hitachi H-4100 scanning electron microscope (SCT Barcelona). The experiments were performed on the (001) plane at room temperature. Applied loads were 5, 10, 30 and 100 mN. The loading/unloading time was selected to be constant for all indentations, 15 s. Table 1 shows fixed test parameters to perform measurements of nanoindentation.

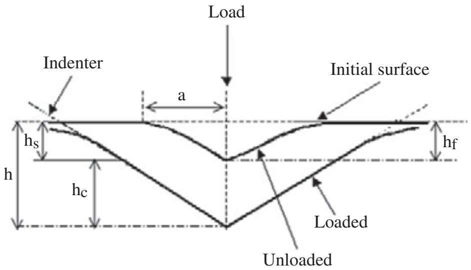

Figure 1. Typical indentation load–displacement data defining key experimental data.

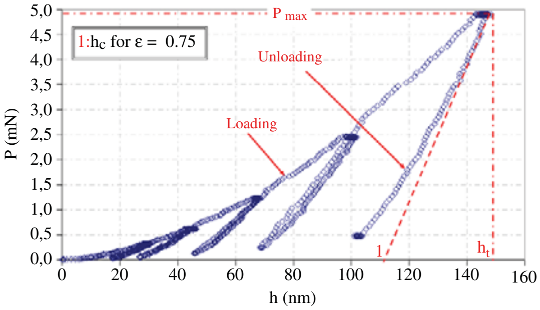

Figure 2. Characteristic curves obtained after loading/unloading when the applied load was 5 mN.

The small nanoindentations were made by a three-sided pyramid Berkovich diamond indenter. The displacement (*penetration depth*) was continuously monitored and load–time history of indentation recorded.

Typical indentation load–displacement and characteristic curves obtained after loading/unloading are shown in figures 1 and 2, respectively. The load/unload curve shows the elastic/plastic behaviour of each sample. From the difference between total indentation depth at maximum indented load (h_t) and depth of residual impression upon unloading (h_f), the elastic recovery can be calculated.

Each hardness and Young's modulus value listed in table 2, are an average of 40 measurements performed on two different samples in order to achieve statistical significance.

The indentation load–displacement data were analysed to determine Young's modulus (E) and nanohardness (H). According to Oliver and Pharr [6], these quantities can be derived using the following relations:

$$h_c = h_t - \varepsilon \frac{P_{max}}{S} \tag{1}$$

$$A = A(h_c) = 24.56 \cdot h_c^2 \tag{2}$$

$$H = \frac{P}{A} \tag{3}$$

$$E_{eff} = \frac{\sqrt{\pi}}{2} \frac{S}{\sqrt{A}} \tag{4}$$

$$\frac{1}{E_{eff}} = \frac{1-\nu_i^2}{E_i} + \frac{1-\nu^2}{E} \tag{5}$$

Table 2. Nanohardness and Young's modulus of orthorhombic phase of YBCO for applied loads of 5, 10, 30 and 100 mN.

Monodomain	Applied load (mN)	Phase	Hardness; H (GPa)	Young's modulus; E (GPa)
Sample 1	5	Y123	11.0 ± 0.5	193 ± 7.60
		Y211	20.0 ± 1.0	199 ± 10.20
		Y123/Y211$_{\text{composite}}$	15.2 ± 0.3	204 ± 7.12
Sample 2		Y123	9.8 ± 0.4	200 ± 6.53
		Y211	18.1 ± 0.5	189 ± 8.56
		Y123/Y211$_{\text{composite}}$	14.4 ± 0.7	198 ± 7.02
Sample 1	10	Y123	11.4 ± 0.4	185 ± 3.16
		Y211	17.1 ± 0.5	209 ± 4.29
		Y123/Y211$_{\text{composite}}$	15.3 ± 0.3	201 ± 6.92
Sample 2		Y123	11.0 ± 0.3	192 ± 4.21
		Y211	16.7 ± 0.6	203 ± 3.56
		Y123/Y211$_{\text{composite}}$	14.9 ± 0.2	206 ± 5.49
Sample 1	30	Y123/Y211$_{\text{composite}}$	11.2 ± 0.3	179 ± 5.49
Sample 2			11.0 ± 0.3	181 ± 4.35
Sample 1	100	Y123/Y211$_{\text{composite}}$	8.8 ± 0.2	171 ± 2.51
Sample 2			9.1 ± 0.1	175 ± 3.87

where ε is the strain (0.75 for Berkovich indenter) and $P_{\max}$ is the maximum indenter load calculated from the load/unload curve (figure 2) for each experiment; A is the projected area at that load; E_{eff} is the effective elastic modulus, S the elastic constant stiffness calculated from the load/unload curve (figure 2) for each experiment, E the elastic modulus and ν the Poisson's ratio of the test material. E_i and ν_i are the elastic modulus and Poisson's ratio for the diamond indenter, which are 1141 GPa and 0.07, respectively [2].

Also, we compared the measurements with a known standard material (commercial stainless steel (Low-Carbon Steel '1020')) in order to give a statistical approach of this technique regarding the uncertainty in the measurement.

The values obtained by the Oliver and Pharr equation (equation (2)) have been corroborated by FE-SEM and AFM measurements.

3. Results and discussion

Table 2 shows the calculated nanohardness and Young's modulus values of the orthorhombic Y123 and Y211 phases for the different monodomain samples studied when the applied loads were 5, 10, 30 and 100 mN.

Nanohardness and Young's modulus of each phase (*Y123 matrix and Y211 inclusions*) can be determined when the applied load was ultra-low, at which nanohardness values are independent of the applied load. Values for Y211 phase were higher than for Y123, for all studied samples. Nanohardness of Y211 was about twice as high as for Y123. This fact could be due to different reasons: (i) ionic bond of Y211 is stronger than Y123 (related to the different melting point of the two phases: $T_{\text{Y123}} \sim 1010\,^{\circ}\text{C}$ and $T_{\text{Y211}} \sim 1200\,^{\circ}\text{C}$ [13]), (ii) high anisotropy of dislocations confined onto a (001) plane [14], and/or (iii) the melt-processed ceramic composites contain a dense population of fine peritectic particles, which drastically affects the microstructure acting as nucleation sites for dislocations [14]. Moreover, nanohardness can be strongly affected by the presence of defects and impurities that can cause almost no change in dislocation movement, which would affect the hardness.

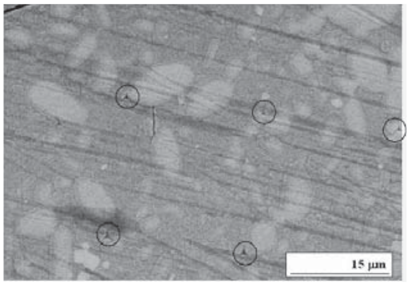

Figure 3. SEM micrographs of nanohardness impressions developed on the surface of a sample of YBCO orthorhombic phase (*ab* plane) at room temperature when the applied load was 10 mN.

In table 2, we observed that Young's modulus decreases when the applied load is increased. It is due to surface defects. We have found that Young's modulus is independent of applied load when it is higher than 10 mN, and it only depends on the Poisson ratio of the studied material.

Figure 3 shows indentation imprints performed when applying 10 mN (imprints performed at 5 mN cannot be observed by FE-SEM, only by AFM). When the applied load was ultra-low (less than 10 mN) each phase can be indented separately. In this figure can be observed the nanoindentation imprints in Y123, Y211 and YBCO composite at ultra-low loads.

Figure 4 shows indentation imprints performed by applying 30 and 100 mN on the *ab* plane of the monodomain, the Y123 matrix and Y211 inclusions. Also in this figure, Y211 particles can be observed homogeneously distributed in the textured sample, so that they can be easily identified but not indented separately. It is important to highlight that the size of Y211 inclusions (1–5 μm, approximately) is smaller than the nanoindentation imprint performed at these loads, so that we can only measure the mechanical properties of the composite (Y123 + Y211) when the applied load is higher than 10 mN.

When the applied loads are 30 and 100 mN, only mechanical properties of composite (Y123 + Y211) can be determined (see table 2 and figure 4) and we cannot separate

Table 3. Literature values of Young's modulus for YBCO with different techniques.

Author	Young's modulus (GPa)	Method
Ledbetter *et al* [18]	90.8–101.8	Ultrasonic techniques
Block *et al* [19]	235 ± 20	X-ray diffraction
Blendell *et al* [20]	107 measured, 139–143 porosity corrected	Ultrasonic techniques
Chang *et al* [21]	226	Indentation (spherical)
Alford *et al* [22]	141–165	Bending
Martínez *et al* [23]	221 ± 20	Indentation (pyramidal)
Johansen *et al* [17]	40–200	Nanoindentation
Sakai *et al* [24]	370	Nanoindentation
This work	171–206 (orthorhombic phase)	Nanoindentation

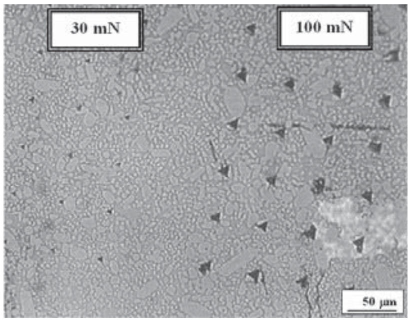

Figure 4. Optical microscope (OM) micrographs of nanohardness impressions developed on the surface of a sample of YBCO orthorhombic phase (*ab* plane) at room temperature when the applied load was 30 and 100 mN.

the contribution of each phase. When the applied load is 100 mN, overall nanohardness is very similar for both samples (~8.9 GPa) but is lower than the nanohardness of the Y123 phase. These results are in agreement with a previous work reported by Lim and Chaundhri [15]. When the applied load is higher than 10 mN we are working within the microindentation range and we can observe microcracks at the corners of imprints (figure 4), thus causing the reduction of nanohardness value ($H_{100\ \text{mN}} < H_{30\ \text{mN}}$).

Verdyan *et al* [16] reported a nanohardness of ~8.5 GPa for orthorhombic YBCO thin films when the applied load varies between 0.1 and 9 mN, which are similar values to those found in the present study for the orthorhombic phase. Values of the Young's modulus are also comparable to our results for the orthorhombic composite, studied at loads of 30 and 100 mN.

Reported values of Young's modulus of Y123/Y211$_{\text{composite}}$ obtained using different experimental techniques are depicted in table 3.

We realized a calibration of the nanoindentation technique with a commercial stainless steel indenter. These results are reported in table 4. In this table, we can observe the uncertainty of this technique.

If we compare our data for Young's modulus with data reported for YBCO (see table 3) we conclude that the broad distribution of Young's modulus observed in table 3 can be attributed both to the different measuring techniques and to the different quality of the investigated YBCO samples (grain structure, texture, etc.).

Table 4. Young's modulus of a commercial stainless steel indenter.

Applied load (mN)	Young's modulus (GPa)	Method
5	230.56 ± 9.67	Nanoindentation
10	209.50 ± 4.60	
30	208.04 ± 3.31	
100	206.86 ± 1.58	

Several measurements of Young's modulus for Y123 have resulted in values scattered within the range $E = 40–200$ GPa. Most probably, this scatter is caused by residual porosity and bad contacts between the grains [17]. Sakai *et al* [18] reported a value of $E = 370$ GPa for 5 mm^3 cubic specimens cut from a single-crystalline Y123 prepared by TSMG using a single-domain Sm123 bulk crystal as a seed. The authors attribute the difference of E to the 40% excess of Y211 phase present in the material. Obtained results of Young's modulus are in agreement with Johansen *et al* [17] and Alford *et al* [22] when the applied loads were 30 and 100 mN.

Figure 5 shows a Y123, Y211 and YBCO composite imprints. Figure 5(b) shows a propagation of the cracks in the sample following the corners of the indentation, for Y211 precipitate. Nanohardness of Y211 is twice as high as the Y123 matrix (see table 2): for this reason this phase presents a brittle toughness. The analysis of SEM images can be used to determine the profile of the impression with nanometer resolution and to provide information about the shape change on unloading. As can be seen in this figure, the indentation exhibits triangular geometry.

Figures 6(a) and (c) show AFM nanoindentation images. The different phases of each component and the different nanoindentation imprints are observed in these figures. The depth and diagonal length were measured directly from the line traces of the AFM images along the diagonal section of the indentation (between the arrows a and b). The markers are displayed in figures 6(b) and (d). The indentation size effect is generally attributed to strain gradient plasticity that generates geometrically necessary dislocations; for ceramic compounds where the plasticity is limited at low loads, the elastic recovery can be significant. When the indentation size is smaller, the density of geometrically necessary dislocations decreases and, as a result, hardness becomes higher at small loads [25]. In fact, from the present calculations of the indentation height before and after removal of the load, it is found that 10% of total work done during the indentation at loads of 5, 10, 30 and 100 mN is due to elastic deformation.

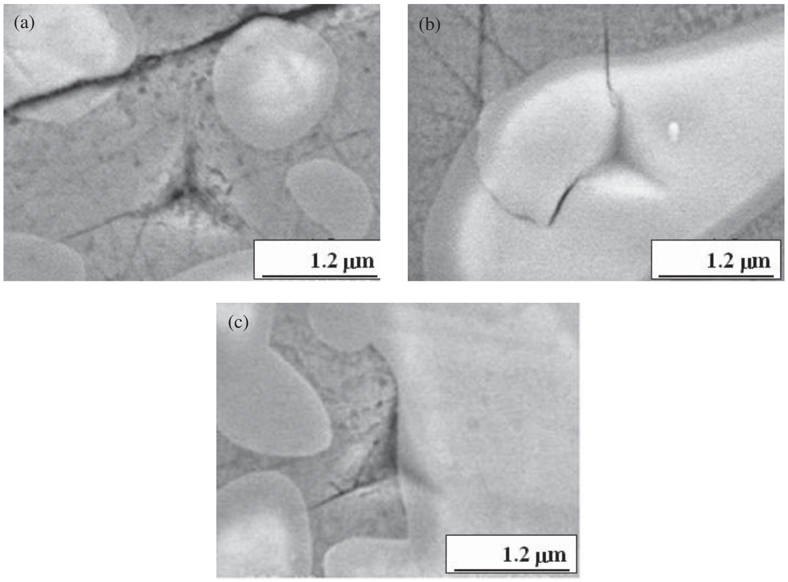

Figure 5. Nanoindentation imprints obtained by FE-SEM when the applied load was 10 mN. (a) Matrix imprint, Y123; (b) precipitated imprint, Y211 and (c) YBCO composite imprint.

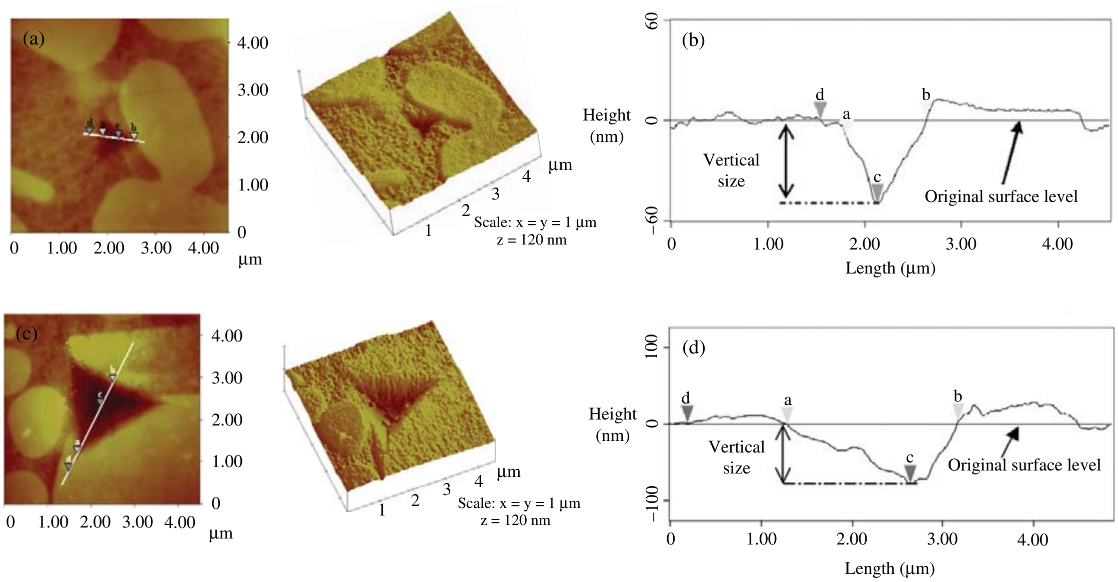

Figure 6. 'Illustrated-top-view' mode image of a residual nanoindentation in a single crystal (sample 1) of orthorhombic phase of the high-temperature superconductor YBCO made using a Berkovich diamond indenter under a load of 5 mN (*image* (a) and (b)) and 10 mN (image (c) and (d)). The surface profile of the indentation is along the direction marked by arrows a, b, c and d. (a) Two-and three-dimensional AFM images of the surface; (b) corresponding analysis of the nanoindentation shape; (c) two-and three-dimensional AFM images of the surface; (d) corresponding analysis of the nanoindentation shape.

4. Conclusions

The nanoindentation technique is an essential tool in the optimization of the mechanical properties of thin coated systems, bulk materials and advanced materials, for applications where hardness and stiffness are important.

Nanohardness and Young's modulus for each phase present in the YBCO compound (Y123 and Y21), pile-up effect and elastic/plastic behaviour of each sample can be studied using nanoindentation tests at different applied loads.

Nanoindentation at low applied load (5 and 10 mN) allows us to determine the nanohardness and Young's modulus of each phase separately. The Y211 nanohardness is nearly twice that for the Y123 ($H_{Y211} \approx 2 \cdot H_{Y123}$).

The measurements at high applied load (30 and 100 mN) do not permit differences each phase. Thus, mechanical properties of the YBCO composite can be measured because the size of Y211 inclusions is lower than the resulted imprints.

Acknowledgments

We would like to thank CeRMAE (*Centre de Referència en Materials Avançats per a l'Energia, Generalitat de Catalunya*) for financial support and Serveis Cientificotècnics (Universidad de Barcelona) for AFM and SEM data. We also acknowledge Silvia Illescas (Centre de Projecció Tèrmica, Department of Materials Science and Metallurgical Engineering, Chemistry Faculty, UB) and Emilio Jiménez (Centre d'Integritat Estructural i Fiabilitat dels Materials, UPC) for experimental data.

References

[1] Sandiumenge F, Piñol S, Obradors X, Snoeck E and Roucau C 1994 *Phys. Rev.* B **10** 7032
[2] Pharr G M 1998 *Mater. Sci. Eng.* A **253** 151
[3] Loubet J L, Georges J M, Marchesini O and Meille G 1984 *J. Tribol.* **43** 106
[4] Pethica J B, Hutchings R and Oliver W C 1983 *Phil. Mag.* A **48** 593
[5] Newey D, Wilkens M A and Pollock H M 1982 *J. Phys. E: Sci. Instrum.* **19** 119
[6] Oliver W and Pharr G 1992 *J. Mater. Res.* **7** 1564
[7] Serradilla I G, Calleja A, Capdevila X G, Segarra M, Mendoza E, Teva J, Granados X, Obradors X and Espiell F 2002 *Supercond. Sci. Technol.* **15** 566
[8] Piñol S, Gomis V, Martinez B, Labarta A, Fontcurberta J and Obradors X 1993 *J. Alloys Compounds* **11** 195
[9] Granados X, Piñol S, Martín B, Galante F, Sandiumenge F, Fontcuberta J and Obradors X 1994 *Cryogenics* **34** 833
[10] Piñol S, Obradors X, Martín B, Fontcuberta J and Sandiumenge F *Spanish Patent Specification* 2111435
[11] Mendoza E 2002 Obtenció i caracterització de ceràmiques texturades de YBCO per l'aplicació de limitació de corrent *Tesis Doctoral* Departamento de física aplicada, Universidad de Barcelona
[12] Ullrich M, Leenders A, Krelaus J, Kautschor L-O, Freyhardt H C, Schmidt L, Sandiumenge F and Obradors X 1998 *Mater. Sci. Eng.* B **53** 143–8
[13] Aselage T and Keefer K 1988 *J. Mater. Res.* **3** 1279
[14] Sandiumenge F, Puig T, Rabier J, Plain J and Obradors X 2000 *Adv. Mater.* **12** 375
[15] Lim Y Y and Chaudhri M M 2001 *J. Phys. D: Appl. Phys.* **34** L70
[16] Verdyan A, Soifer Y M, Azoulay J, Rabkin E and Kazakevich M 2005 *IEEE Trans. Appl. Supercond.* **15** (2)
[17] Johansen T H 2001 *Supercond. Sci. Technol.* **13** R121
[18] Ledbetter H M, Austin M W, Kim S A and Lei M 1987 *J. Mater. Res.* **2** 786
[19] Block S, Piermarini G J, Munro R G and Wong-Ng W 1987 *Adv. Ceram. Mater.* **2** 601
[20] Blendell J E *et al* 1987 *Adv. Ceram. Mater.* **2** 512–29
[21] Chang G C S, Burns S J, Goyal A and Funkenbusch P D 1988 *Ceram. Supercond.* **2** 580–9
[22] Alford N M, Birchall J D, Clegg W J, Harmer M A, Kendall K and Jones D H 1988 *J. Mater. Sci.* **23** 761–768
[23] Martinez L, Albarran J L, Valdes S and Fuentes J 1988 *Physica* C **152** 518–22
[24] Sakai N, Munakata F, Diko P, Takebayashi S, Yoo S I and Murakami M 1997 *Adv. Supercond.* X 645
[25] Mukhopadhyay N K, Weatherly G C and Embury J D 2001 *Mater. Sci. Eng.* A **A315** 202

Plastic behaviour under the residual imprint

Working beyond the objectives of the previous article, the residual nanoindentation imprints performed at 10 mN of applied load have been visualized by FIB, in order to understand the fracture mechanism that takes place under the residual nanoindentation.

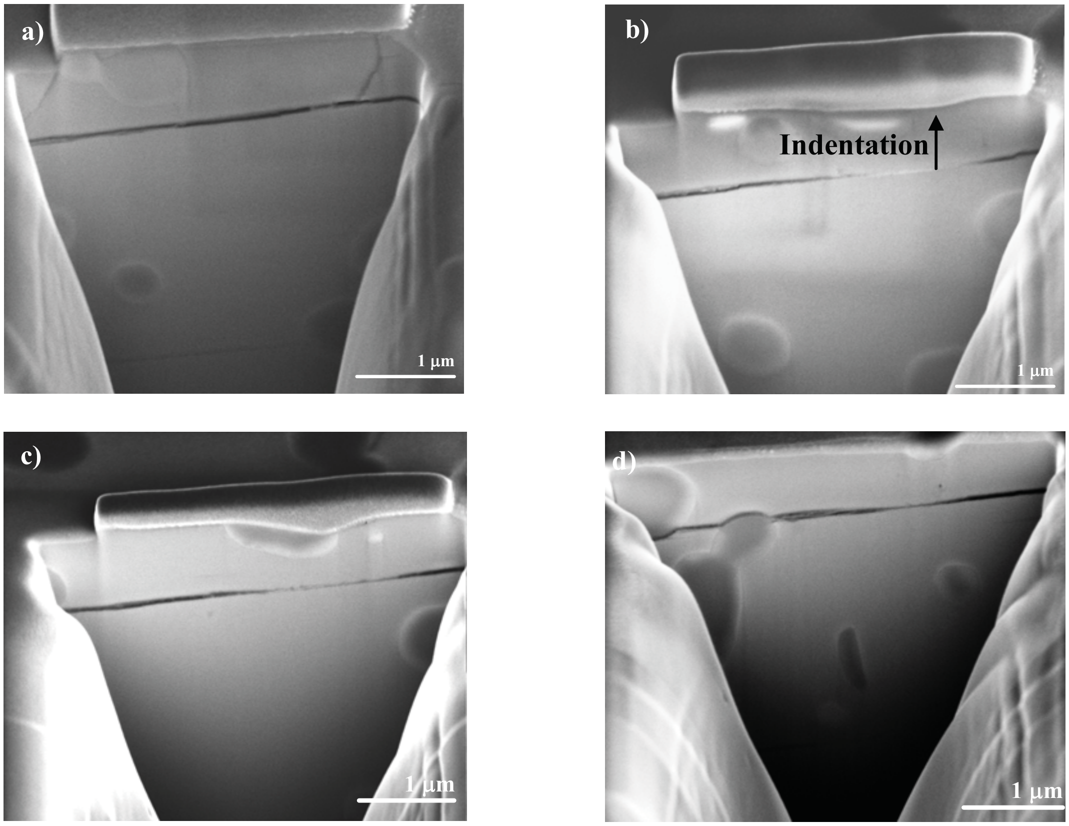

Fig. 4.1. Cross-sectioning and imaging of damage under an indentation using the FIB-SEM: a) trench milled at high ion beam current in front of the residual indentation imprint, b) cross-sectioning of the border of the indentation, c) cross-sectioning in the middle of the imprint, and d) cross-sectioning at the end of the residual nanoindentation imprint.

The effect produced during the indentation test with a Berkovich tip indenter was examined by cross-sectioning the samples by FIB technique, and are presented in *Fig. 4.1*, in order to see the deformation mechanism, that take place during the indentation process. These images exhibit different cracks below the indentation imprint originated during the texture process. Each image shows a heterogeneous distribution of Y-211 particles around the matrix, with different sizes from 1 to 5 µm. Finally, it is seen that no cracks or failure events can be appreciated under the nanoindentation imprint, thus implying that the deformation can be attributed to the oxygenation microcracks closing.

Study of the residual stresses present in Y-211 by TEM-tomography

The different inclusions present in the Y-123 matrix, exhibit several stresses inside there, created during the texture process due to a high different coefficient expansion between Y-211 and Y-123[2]. These residual stresses are the responsible to originate several macrocracks around the Y-211 particles. In this study, several images of TEM have been performed from -50º to 50º with 10º of step and using goniometric equipment in order to observe the evolution of the different residual stresses.

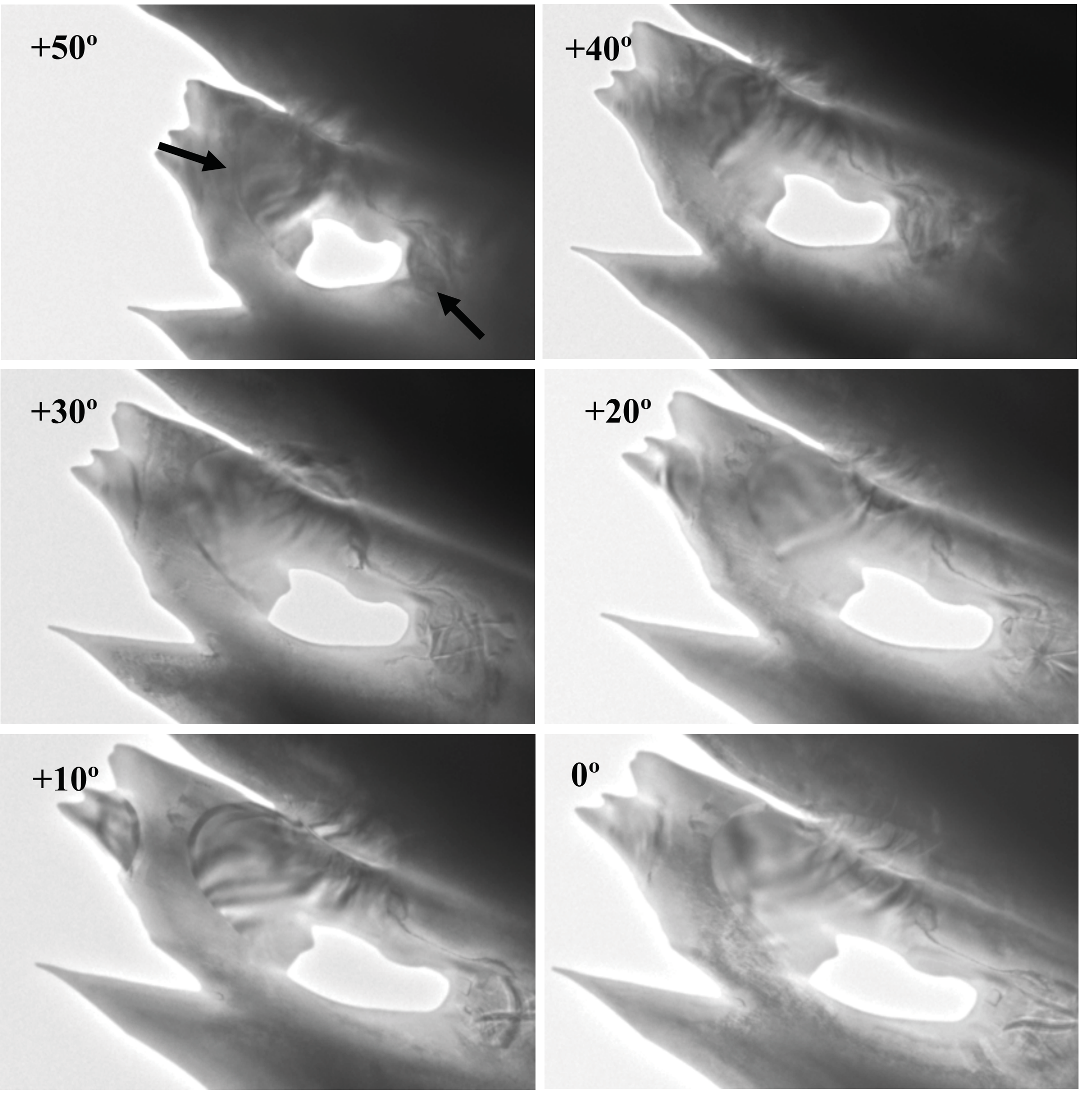

Fig. 4.2. TEM images of Y-211 inclusions with different sample orientations.

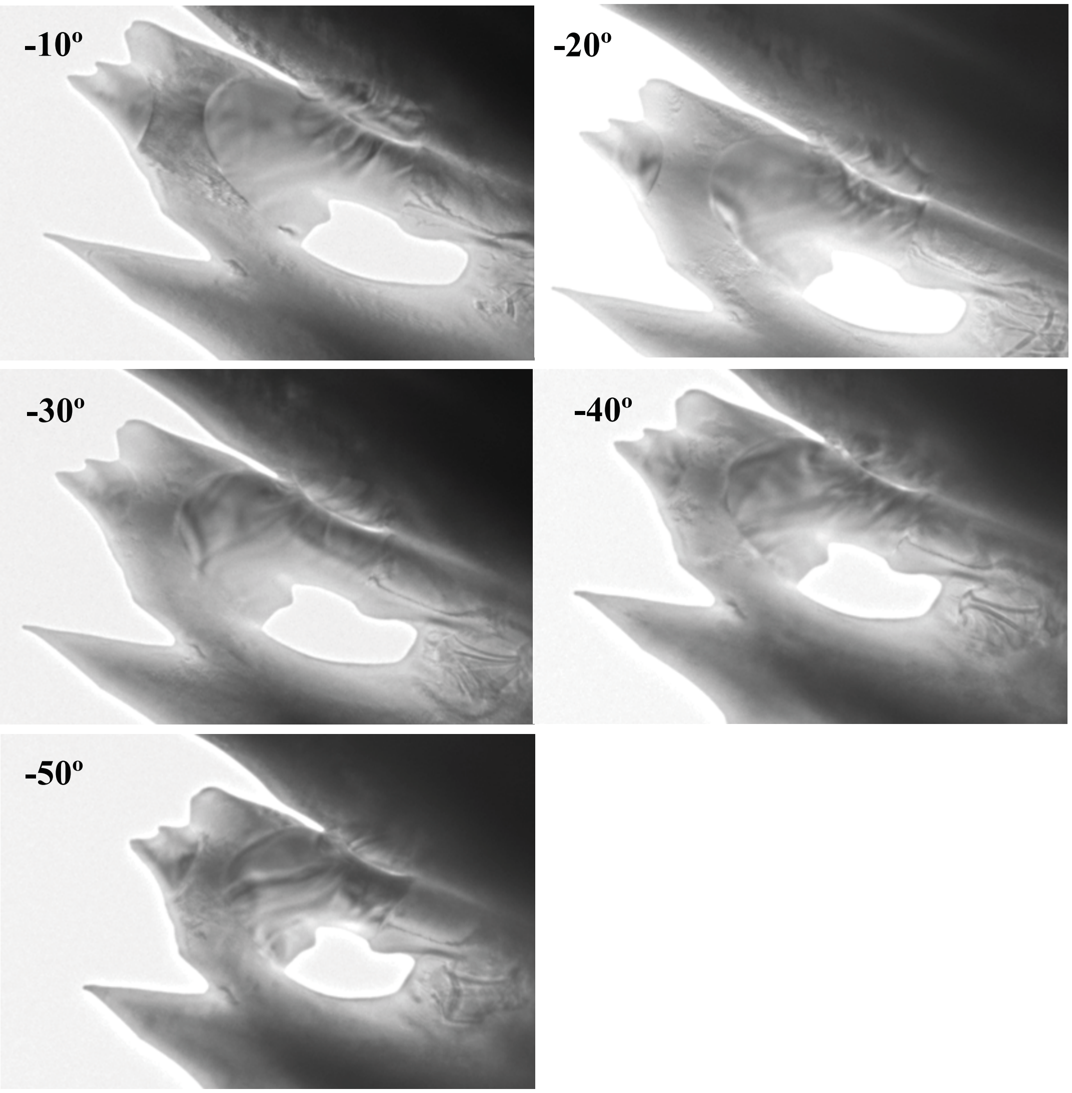

Fig. 4.2. TEM images of Y-211 inclusions with different sample orientations (continuation).

These images exhibit the evolution of the residual stresses inside of a Y-211 particle by TEM. Theses stresses produce several macro- and microcracks around the Y-211 inclusions.

4.2. YBCO samples textured by TSMG technique

A similar study for YBCO samples textured by TSMG technique was presented as an Oral communication in the National ***XXV Encuentro del Grupo Español de Fractura (Sociedad Española de integridad Estructural)***, Sigüenza, 2008, and the manuscript has been published at the *“Anales de la Mecánica de la Fractura XXV,* Vol. 1 (2008) pp. 55-60" in March 2008. The main results are presented below. Recently, a review work entitled ***Mechanical characterization at nanometric scale of ceramic superconductor composites***, has been published by NovaScience Publisher as a chapter of book, in May 2009.

The different mechanical properties (such as *H* and *E*) for each phase were obtained with a Berkovich indenter. These properties were studied at different applied loads: 5, 10, 30 and 100 mN. The loading/unloading time was selected to be constant for all indentations, 15s. Each *H* and *E* values listed in this section are an average of forty measurements performed on two different samples, in order to achieve statistical significance. The values obtained by the Oliver and Pharr equation**[1]** have been corroborated by FE-SEM.

Loading/Unloading curves

The load/unload curves can give us a qualitatively information of the *H* of each phase of the study, when the applied load is lower than 10 mN. *Fig. 4.3*, exhibits the load/unload curves for each different phase in YBCO samples textured by TSMG technique (Y-123, Y-211 and Y-123/Y-211$_{\text{interphase}}$) when the applied load was 5 mN.

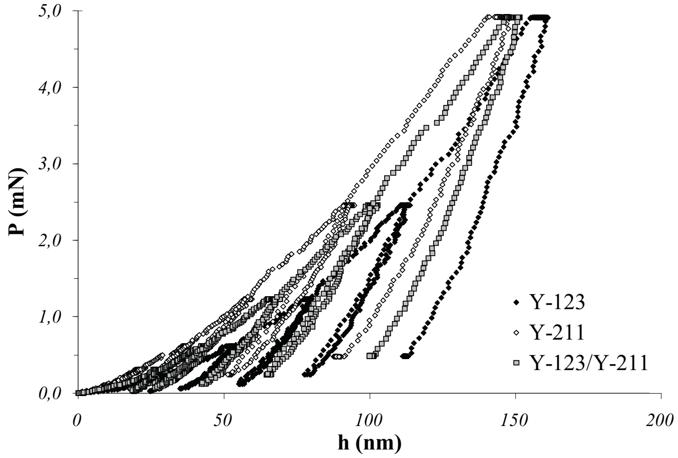

Fig. 4.3. Load/Unload curves for each phase that form YBCO samples textured by TSMG technique when the applied load was 5mN.

The YBCO samples textured by TSMG technique present the following distribution of *H* for each phase: $H_{Y\text{-}123} < H_{Y\text{-}123/Y\text{-}211\ interphase} < H_{Y\text{-}211}$. The nanoindentation technique presents a small difference in the *H* value at ultra low load such as 5 mN, because after the oxygenation process, the orthorhombic phase presents a high pore density in the *ab*-plane. Moreover, the different superficial roughness produces an over- or underestimation of the $A(h_c)$, giving a wrong H value.

Characterization imprints

All residual nanoindentation imprints have been observed with FE-SEM, in order to know the correct value of the $A(h_c)$, and thus correct the H, and E of YBCO using the Oliver and Pharr equations**[1]**.

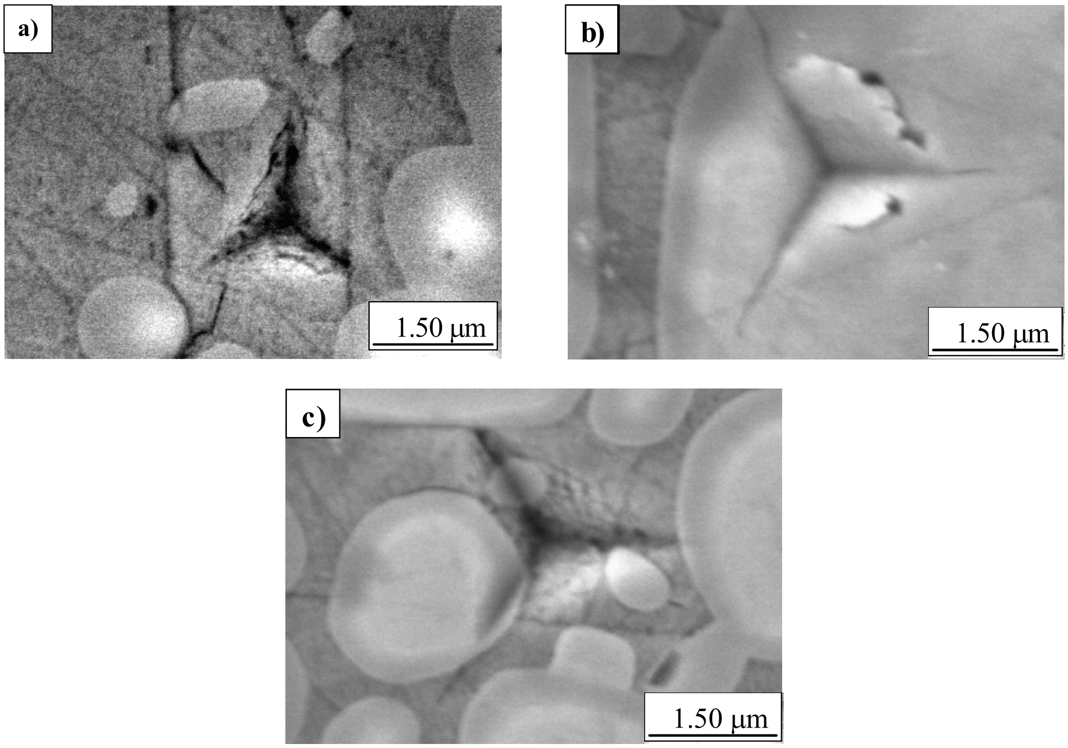

Fig. 4.4. Micrograph of nanoindentation imprints obtained by FE-SEM when the applied load was 10 mN, a) Y-123 matrix, b) Y-211 precipitated, and c) Y-123/Y-211$_{\text{interphase}}$.

In *Fig. 4.4b*, we can observe the residual imprints for different tests at 10 mN. Showing several radial cracks at the corners of the imprint, and another fracture mechanism known as chipping. The mechanical properties of each phase cannot be isolated because the size of the residual imprint is higher than the size of Y-211.

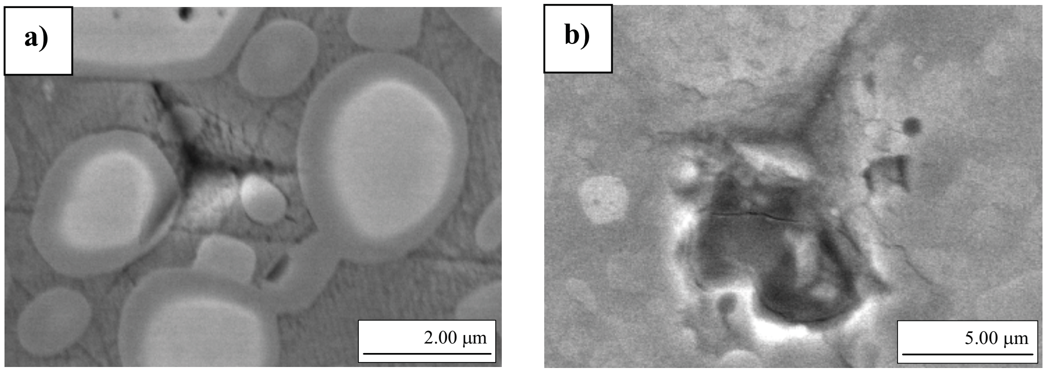

Fig. 4.5. Nanoindentation imprints obtained by FE-SEM of samples textured by TSMG technique, a) 30mN of applied load and b) 100mN of applied load.

In *Fig. 4.5a*, radial cracks at the corners of the imprints cannot be observed, but only microcracks inside of the imprint. Note that when the applied load was 100mN (*Fig. 4.5b*), the residual indentation imprint exhibits a chipping effect and high pore density in the vicinity of the imprint.

Hardness and Young's modulus

Table 4.1 shows the mechanical properties for different YBCO samples textured by TSMG technique, which have been calculated for the orthorhombic phase of Y-123, Y-211 and Y-123/Y-211 composite.

Table 4.1. *H* and *E* of orthorhombic phases of YBCO samples textured by TSMG technique for applied loads of 5, 10, 30 and 100 mN.

Monodomain	Applied load (mN)	Phase	H (GPa)	E (GPa)
1	5	Y-123	11.4 ± 0.5	176 ± 15
		Y-211	15.0 ± 1.1	224 ± 20
		Y-123/Y-211$_{interphase}$	14.9 ± 1.1	207 ± 22
2		Y-123	10.6 ± 0.5	176 ± 15
		Y-211	15.4 ± 0.6	223 ± 16
		Y-123/Y-211$_{interphase}$	14.9 ± 0.9	208 ± 19
1	10	Y-123	11.1 ± 0.9	173 ± 18
		Y-211	17.1 ± 0.3	207 ± 11
		Y-123/Y-211$_{interphase}$	14.6 ± 0.8	190 ± 17
2		Y-123	9.59 ± 0.8	175 ± 15
		Y-211	16.9 ± 0.9	207 ± 10
		Y-123/Y-211$_{interphase}$	14.9 ± 0.9	190 ± 15
1	30	Y-123/Y-211$_{interphase}$	8.71 ± 0.95	140 ± 14
2			8.26 ± 0.79	139 ± 13
1	100	Y-123/Y-211$_{interphase}$	7.96 ± 0.72	128 ± 6
2			7.88 ± 0.89	130 ± 5

H and *E* of each phase can be determined when the applied load was ultra-low (less than 10 mN). For higher loads, the mechanical properties of the interaction of both phases can be obtained by the YBCO composite or Y-123/Y-211$_{\text{interphase}}$. The different H and E values obtained are in correct agreement with previous values related in the literature (see *Table 1.1* and *1.2*). The H values are in agreement with a previous work of Goyal *et al*.[3] performed using Vickers indentation. Lucas *et al*[4], obtained the E value for Y-123 of 154 GPa, which is around the E value obtained for the composite at 100 mN of applied load. The E value for Y-211 phase is in agreement with Soifer *et al*[5], who obtained a value of 210 GPa for thin films of YBCO.

4.3. Conclusions

Nanoindentation technique allows us to isolate the mechanical properties of each phase in YBCO bulk materials, independently of the growing technique used (Y-123, Y-211, and Y-123/Y-211$_{\text{interphase}}$). The mechanical properties for Bridgman samples are higher than for TSMG samples. This phenomenon can be attributed to the texture process, as TSMG process creates a high density of macro- and microcracks during the texture and oxygenation steps, respectively.

4.4. References

[1] W. C. Oliver, G. M. Pharr; *J. Mater. Res.* 7 **(1992)** 1564.

[2] F. Sandiumenge, S. Piñol, X. Obradors, E. Snoeck, C. Roucau; *Phys. Ver. B,* 50 **(1994)** 7032.

[3] A. Goyal, W. C. Oliver, P. D. Funkenbusch, D. M. Kroeger, S. J. Burns; *Physica C* 183 **(1991)** 221.

[4] B. N. Lucas, W. C. Oliver, R. K. William, J. Brynestad, M. E. O'Hern; *J. Mater. Res.* 6 **(1996)** 2519.

[5] Y. M. Soifer, A. Verdyan, J. Azoulay, E. Rabkin, M. Kazakevich; *Physica C* 15 **(2005)** 3585.

5

MEASUREMENT OF THE STRESS-STRAIN CURVES

The next best thing to knowing something is knowing where to find it

Samuel Johnson (1709 - 1784)
British author

In the following section, the stress (σ)-strain (ε) curves for YBCO samples, textured by Bridgman and TSMG techniques, have been studied with a sharp spherical indenter and using the Hertzian equations[1].

5.1. YBCO textured by Bridgman technique

The following paper, published in *Journal of the European Ceramic Society* in January 2010, describes the mechanical properties (*yield strength, shear stress, mean contact pressure, and the stress-strain curves*) for YBCO samples textured by Bridgman technique. The main purpose of this work was to use a spherical tip indenter to explore the elasto-plastic transition, and to obtain the yield strength of orthorhombic phase of YBCO samples at room temperature. This parameter could be found in a macroscopic scale using a mechanical test machine coupled with a very precise extensometer, which is not usual. The same measurement could be done in a more routinely way by using instrumented indentation representing great benefits, especially in materials where it is difficult to obtain a probe for the tensile test, which is our case. Also, inspection of the *P-h* curves for penetration depth lower than 200 nm allows the observation of the elasto-to-plastic transition. The residual spherical imprints have been characterized by AFM and FIB. FIB trenches have been performed in order to observe the different fracture mechanisms produced under the residual imprint during the indentation process.

More recently, a review work entitled ***Mechanical characterization at nanometric scale of ceramic superconductor composites***, has been published by *NovaScience Publisher* as a chapter of the book "Nanotechnology: Nanofabrication, Patterning, and Self-Assembly" (To be published in 2010).

Following the article, additional results for TSMG samples concerning this topic are included.

Available online at www.sciencedirect.com

ScienceDirect

Journal of the European Ceramic Society 30 (2010) 1477–1482

www.elsevier.com/locate/jeurceramsoc

Nanoindentation with spherical tips of single crystals of YBCO textured by the Bridgman technique: Determination of indentation stress–strain curves

J.J. Roa [a,*], E. Jiménez-Piqué [b], X.G. Capdevila [a], M. Segarra [a]

[a] *Centro DIOPMA, Departamento de Ciencia de los Materiales e Ingeniería Metalúrgica, Instituto de Nanociencia y Nanotecnología de la Universidad de Barcelona (IN^{2}UB), Facultat de Química, Universidad de Barcelona, Martí i Franquès 1, Barcelona E-08028, Spain*

[b] *Departamento de Ciencia de los Materiales e Ingeniería Metalúrgica, Universidad Politécnica de Cataluña, Diagonal 647 (ETSEIB), Barcelona E-08028, Spain*

Received 16 June 2009; received in revised form 15 October 2009; accepted 28 October 2009
Available online 16 December 2009

Abstract

The mechanical properties of superconductor ceramics are of interest in the manufacture of superconducting devices. The current trend is to produce smaller devices (using, e.g., thin films), and the correct characterization of small volumes of material is critical. Nanoindentation is used to assess mechanical parameters, and several studies determine hardness and Young's modulus by sharp indentation. However, studies on the elasto-plastic transition with spherical indentation are scare. Here we used, spherical diamond tip indenter experiments to explore the elasto-plastic transition and to measure the yield strength of the orthorhombic phase of $YBa_2Cu_3O_{7-\delta}$ (YBCO or Y-123) at room temperature. The study was carried out for a range of monodomains on the (1 0 1)-plane for Bridgman samples. Inspection of the load–unload curves for penetration depths lower than 200 nm allows for observation of the elasto-plastic transitions. Focused ion beam (FIB) trenches showed no cracking due to the indentation, although oxygenation cracks were apparent. The mean pressure for the onset of elasto-plastic deformation is 3.5 GPa, and the elastic modulus, E, calculated using the Hertzian equations is 123.5 ± 3.4 GPa.

Keywords: Superconducting; Nanoindentation; Stress–strain relationship

1. Introduction

The mechanical properties of YBCO superconducting ceramics are critical to the design of superconducting devices such as cables and motors. Precise knowledge of the elastic and deformation behaviour is a prerequisite for successful manufacturing and operation of such devices. However, very little information on the elastic-to-plastic transition is available in the literature.

The superconducting matrix of YBCO materials, $YBa_2Cu_3O_{7-\delta}$, (Y-123), contains a fine, well-dispersed distribution of Y_2BaCuO_5 (Y-211) precipitates. The Y-211 particles increase the irreversibility line by acting as pinning centres, improve crystal growth, and reduce macro-cracks.[1] The peritectic reaction is slow, so a fraction of non-reacted peritectic Y-211 can be retained in the final product in the form of inclusions with a size lower than few micrometers.[2] The crystal of YBCO is highly anisotropic, as dislocations are confined to the (0 0 1) plane. Ledbetter et al.[3] reported that strong covalent and ionic bonds create high Peierls' barriers which constrain the dislocation mobility in YBCO single crystals. The incorporation of Y-211 particles into the bulk Y-123 would favour particular orientations in which the direction is parallel to *ab*-plane.

YBCO has suitable properties for ceramic materials, such as hardness and stiffness, together with tendency to fracture. However, references about the mechanical properties of this material, particularly yield strength and stress–strain curve, are scarce. The mechanical properties (hardness, Young's modulus and fracture toughness) of YBCO samples have been examined with techniques such as ultrasound,[3] X-ray diffraction[4] and nanoindentation.[5] Reported values of Young's modulus for Y-123 are within the range $E = 40–200$ GPa. This large scatter may be due to the residual porosity and poor contact between the grains.[5] Other authors,[1] also using nanoindentation, reported a value of $E = 171–181$ GPa for YBCO samples textured by the Bridgman technique, which is in agreement with Johansen,[5]

---

* Corresponding author.
E-mail address: joanjosep_roa@ub.edu (J.J. Roa).

0955-2219/$ – see front matter © 2009 Elsevier Ltd. All rights reserved.
doi:10.1016/j.jeurceramsoc.2009.10.021

who applied between 30 and 100 mN. Nanohardness values in the range of 7.8–8.0 GPa at maximum loads of 30 mN were recently reported by Lim and Chaudhri[6] for bulk, single-crystal YBCO. Roa et al.[1] found a hardness value of 8.9 ± 0.1 GPa by nanoindentation on YBCO samples textured by the Bridgman technique.

All these measurements were performed by sharp tips (mainly Berkovich), so an elasto-plastic regime was achieved from the beginning of the test, which yielded no information about the elasto-plastic transition. This transition can be observed if a blunt indenter is used to perform the test.

Spherical nanoindentation stress–strain curves can help us to understand elasto-to-plastic deformation in superconducting ceramics. This is relevant for the fabrication of superconducting devices at room temperature. Here we determine the elastic, plastic and elasto-plastic ranges at room temperature for YBCO samples textured by the Bridgman technique using nanoindentation with a spherical tip, and we measure the yield stress of YBCO materials by nanoindentation.

2. Experimental procedure

2.1. Preparation of bulk YBCO samples and monodomain growth

The YBCO powders were prepared by the PVA method.[7] The ratio used 69% (w/w) Y-123, 30% (w/w) Y-211 and 1% (w/w) $CeO_2 \cdot H_2O$ was chosen to maximize critical current density.[8] The standard composition of the starting material was Y-123 with an excess of 30% (w/w) Y-211. $CeO_2 \cdot H_2O$ was added to improve the distribution of Y-211 particles. The calcinate powder was deagglomerated by ball milling in an agate mortar.

Green bulk pieces were obtained by cold isostatic pressure (*CIP*) and further textured using the Bridgman method.[9,10] After this, bulk textured pieces were oxygenated in a horizontal furnace at 450 °C for 240 h.[11] From the oxygenated pieces all of which had a common *c*-axis tilt of 45°, small pieces of 2 mm height were cut along the *ab*-plane[12] and further polished.

2.2. Measurement of elastic properties with a spherical tipped nanoindenter

Nanoindentation tests were performed with a Nano Indenter® XP System (Agilent Technologies) with continuous stiffness measurement, CSM (harmonic displacement 2 nm and frequency of 45 Hz). The strain rate was held constant at $0.05\,s^{-1}$. The experiments were performed on the (1 0 1) plane at room temperature using a spherical diamond tip of 25 μm in radius, and performed at a maximum load of 650 mN.

In nanoindentation it is critical to correctly determine the initial contact point, especially for spherical indenters. Various methods have been used,[13] but all options require some subjectivity. For instruments with CSM capabilities, Oliver and Pharr[14] proposed, using the point at which *S* increases steadily, a method that works satisfactorily when using sharp indentations. Alternatively, they suggested using abrupt changes in CSM harmonic displacement or phase angle if they are clearer, but all options require some subjectivity.

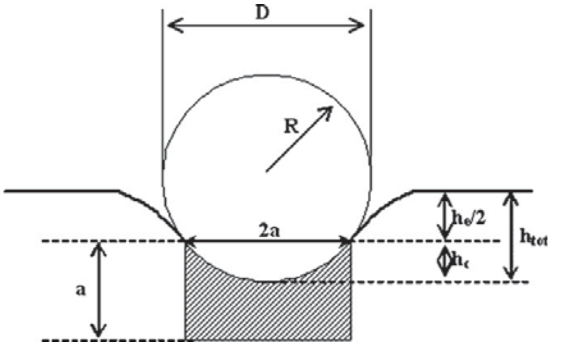

Fig. 1. Schematic representation of spherical indentation.

When using spherical tips, the contact point is more difficult to determine, due to the moderate increase in stiffness during initial contact, and the interaction between tip and sample before contacting.

Recently Barsoum et al.,[15] proposed fitting the stiffness vs. penetration depth data, and extrapolating to zero, as predicated by a relation between effective modulus and contact point, as follows[15]:

$$S = 2E_{\text{eff}}a \qquad (1)$$

The stresses and deflections arising from the contact between two elastic solids are of particular interest to those undertaking indentation testing. The contact between a rigid sphere and a flat surface is shown in Fig. 1.

The mean contact pressure, p_o, is the load applied divided by the contact area. For small penetration depths, it can be obtained from the Hertzian equation[16]:

$$p_o = \frac{P}{A} = \frac{P}{\pi a^2} = \left(\frac{4E_{\text{eff}}}{3\pi}\right)\frac{a}{R}, \qquad (2)$$

where *P* is the applied load, *A* is the contact area, *a* is the radius of the contact point, *R* is the radius of the tip and E_{eff} is the effective Young's modulus. Eq. (2), allows us to plot the σ–ε curves when we use the spherical nanoindentation test. The left side of this equation represents the indentation stress or mean contact pressure, also referred to as the Meyer hardness.[17] The expression in parentheses or *a*/*R* on the right side represents the indentation strain.[17]

The E_{eff} can be obtained from:

$$\frac{1}{E_{\text{eff}}} = \frac{1-\nu^2}{E} + \frac{1-\nu_i^2}{E_i}, \qquad (3)$$

where ν is the Poisson's ratio, and *E* is the Young's modulus. The subindex *i* denotes the values of the indenter. For a diamond indenter, the elastic constants are $E_i = 1141$ GPa and $\nu_i = 0.07$.[18]

The radius of the circle of contact *a* is related to the indenter load *P*, the indenter radius *R*, and the elastic properties of the contacting material by:

$$a = \sqrt[3]{\frac{3}{4}\frac{PR}{E_{\mathrm{eff}}}} \tag{4}$$

The indentation load–displacement data were analysed based on the Hertz equation in the elastic region[14,19,20] as follows:

$$P = \frac{3}{4}E_{\mathrm{eff}}R^{1/2}h_e^{3/2} \tag{5}$$

The σ–ε in a typical traction test can be written in the elastic region as:

$$\sigma = E\varepsilon, \tag{6}$$

where σ is the stress applied, E is the Young's modulus and ε is the strain. In a spherical nanoindentation, the σ–ε curves follow the same tendency; for more information see Eq. (2).

2.3. Focused ion beam sectioning

The damage produced under the residual spherical nanoindentation imprint of YBCO samples textured by the Bridgman technique was characterized using a dual beam FIB/SEM (FIB Strata DB235). The residual indentation imprints were cross-sectioned along the *c*-axis to evaluate the damage after indentation. A thin platinum layer was deposited on the sample prior to FIB machining in order to minimize ion-beam damage. A Ga^+ ion source was used to mill the surface at a voltage of 30 kV. The final polishing of the cross-sections was performed at 10 pA.

3. Results and discussion

Typical indentation load–displacement curves are presented in Fig. 2 for the (1 0 1)-plane orientation obtained with the 25 μm indenter. In Fig. 2a (maximum penetration depth of 100 nm), the response was elastic (the slight disagreement between the curves may be attributable to the holding time at maximum load). In Fig. 2b (maximum penetration depth of 200 nm), the response was plastic as the unload curve does not match the load curve. So, the elasto-plastic transition took place at a penetration depth of between 100 and 200 nm; the response was elastic until 150 nm

$$P = Ch_e^{3/2}, \tag{7}$$

after this point, the load curve can be adjusted with an elasto-plastic curve:

$$P = Ch_p^{2}. \tag{8}$$

In both equations (7 and 8, respectively) P is the applied load, C is the slope of the load curve, and h is the penetration depth. The intersection of these two curves is the yield stress of the material, which can present a pop-in event.[13]

Fig. 3 shows residual indentation imprints observed by optical microscopy. The Y-211 inclusions are heterogeneously distributed in the textured sample and this phase is not uniform below the indentation region.

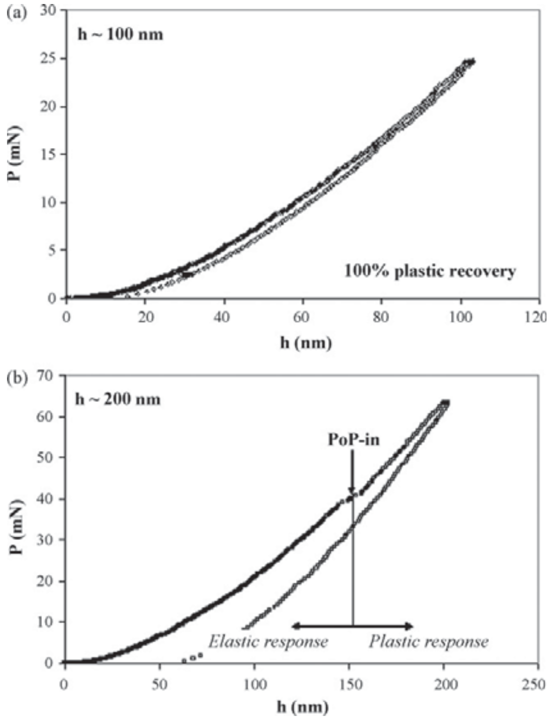

Fig. 2. Characteristic curves obtained after loading/unloading for a spherical tip indenter of 25 μm of radii at different penetration depths: (a) 100 nm, elastic response and (b) 200 nm, elastic recovery and a little plastic deformation.

An imprint is visible only by atomic force microscopy (AFM) when the test is performed at penetration depths greater than 150 nm, which correlates with the change in the slope of the loading curve due to the elasto-plastic transition (Fig. 2b). For greater penetration depths ($h > 150$ nm), different residual imprints can be observed by AFM (see Fig. 4). In Fig. 4a–c, it is seen that the Y-211 inclusions are not deformed, because this phase is harder.[1]

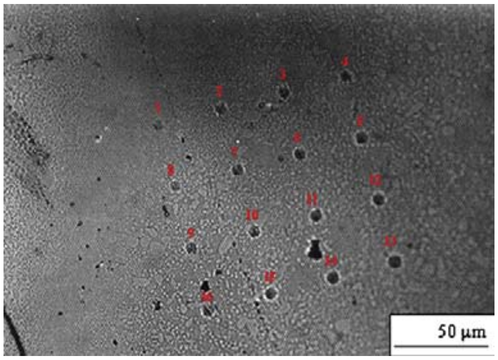

Fig. 3. Micrograph of nanoindentation imprint obtained by O.M. at an applied load of 650 mN.

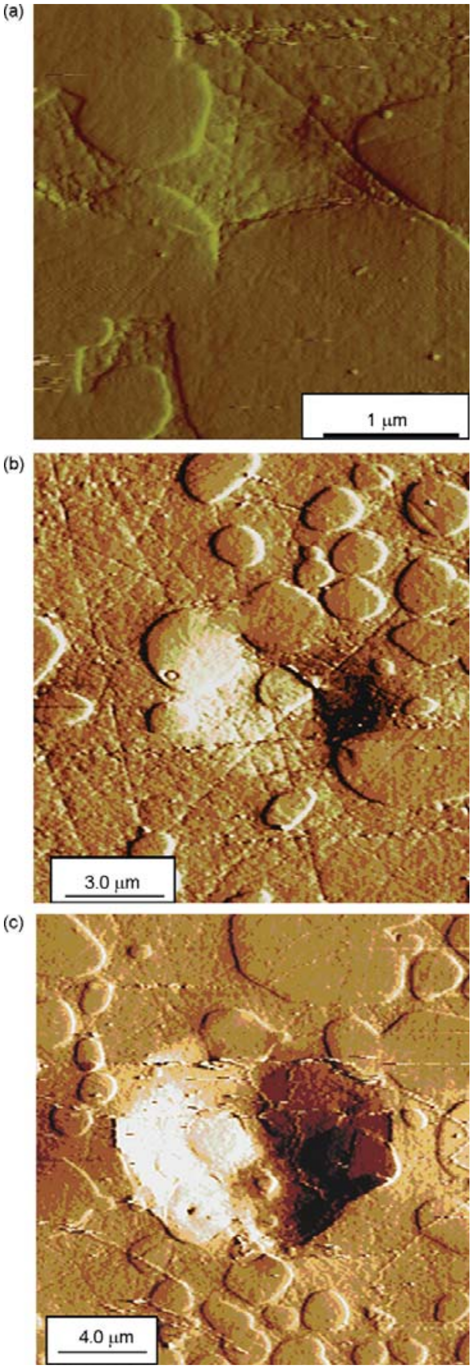

Fig. 4. AFM image at different penetration depths: (a) 300 nm, (b) 400 nm and (c) 800 nm.

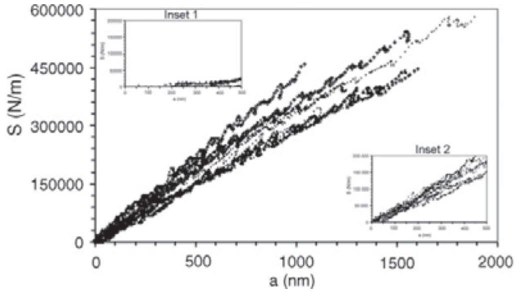

Fig. 5. Contact point (S vs. a) for samples textured by the Bridgman technique with (inset 1) elasto-plastic regimen and (inset 2) elastic regimen.

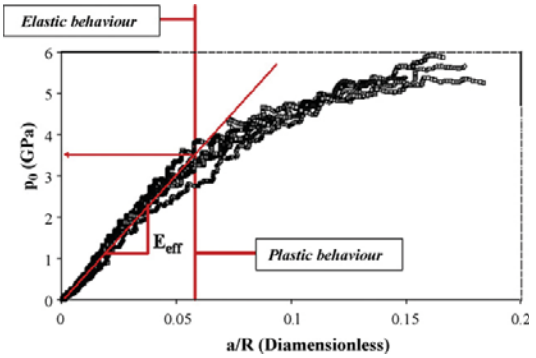

Fig. 6. Stress–strain curve textured by Bridgman technique. The solid line is the expected slope calculated from $4E_{\text{eff}}/3\pi$ (Hertzian behaviour).

For a properly zeroed sample, according to Eq. (1), a plot of S versus a should be a straight line that goes through the origin, with a slope of $2E_{\text{eff}}$. Linear regression is used to assess whether the S-versus-a curve is linear and goes through the origin. Fig. 5 shows the results of tests performed in the (1 0 1)-plane of YBCO samples textured by the Bridgman technique with the 25 μm radius indenter. The differences between the slopes presented in the S–a figure are due to the second Y-211 phase, which is not uniform under the indented region. Moreover, this phase presents a higher Young's modulus value than Y-123. However, since the tip is spherical, the single response of each phase cannot be isolated and the response of the composite is obtained (Y-123/Y-211). Inset 1 and Inset 2 in Fig. 5 shows the different tests with a bad and good contact points between the surface of the sample and the indenter. Fig. 5b plots the linear regression with a high correlation coefficient, which ensures that the contact point of the YBCO samples can be obtained correctly. After this, the Young's modulus of the material can be obtained by Hertzian equations (see Eq. (3)–(5)), giving a constant value of 123 GPa for the complete penetration range. This value is in agreement with that reported by Ledbetter et al.,[3] who obtained the E value by Ultrasonic technique and Roa et al.,[1] who used a sharp indenters. By plotting the mean contact pressure against a/R (indentation strain) it is possible to determine the point at which the elasto-plastic transition was produced. As shown in Fig. 6; the contact pressure for the elasto-plastic

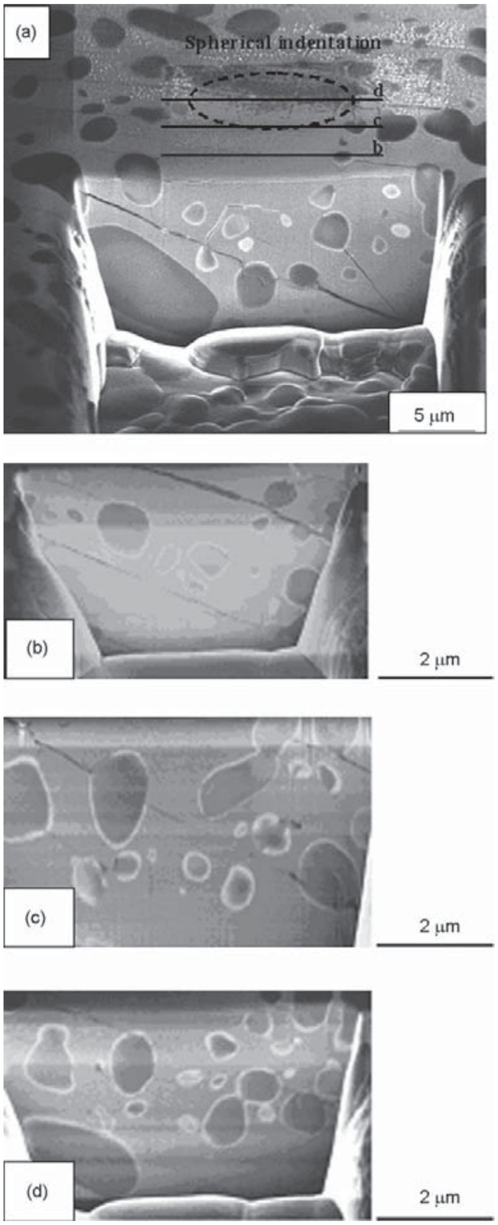

Fig. 7. Cross-sectioning and imaging of damage under indentation using the FIB-SEM: (a) indentation and platinum layer deposited on the indentation to minimize beam damage, and trench milled at high ion-beam current in front of the residual indentation imprint, (b) cross-sectioning before the imprint, (c) cross-sectioning of the border of the indentation and (d) cross-sectioning in the middle of imprint 3.

transition is 3.5 GPa (close to the hardness) beneath the indenter. There are three different regimes, which can be observed in this figure[21] depending on the contact pressure applied: (i) initially, when $p_o < 1.1\sigma_{ys}$, there is a full elastic response, and no residual impression can be observed after the removal of the applied load; (ii) $1.1\sigma_{ys} < p_o < C\sigma_{ys}$, plastic deformation occurs beneath the surface but is constrained by the surrounding elastic material, where C is a constant whose value depends on the material and the indenter geometry; (iii) finally, when $p_o = C\sigma_{ys}$ the plastic region extends to the surface of the specimen and continues to grow. One of the purposes of this work is to calculate the yield strength of YBCO samples textured by the Bridgman technique. In Fig. 6, the elasto-plastic transition can be calculated to a value of around 3.5 GPa. The value of yield stress obtained for Bridgman samples can be estimated to be 3.2 GPa.

The effect of the spherical tip indenter was examined by cross-sectioning the samples by Focused ion beams (FIB) technique. Fig. 7 illustrates the possible deformation mechanisms and the presence of cracking or porosity below the indentation imprint. First, the image shows a heterogeneous distribution of Y-211 particles around the samples, with sizes ranging from 1 to 5 μm. Also, intrinsic microcracks appear at 45° of *ab*-plane, which are generated during the tetragonal–orthorombic phase transformation. Large secondary phase inclusions (unreacted liquid and Y-211) can also create macrocraks due to thermal expansion mismatch.[22] Oxygen annealing, necessary to make Y-123 samples superconducting, is reported to be responsible for further macro and microcracking.[23] Finally, it is seen that no cracks or failure events can be appreciated under the nanoindentation imprint, indicating that the deformation can be attributed to dislocation movement or twinning of the sample, without effect of porosity or microcracking.[22] Previous studies have reported that the *ab*-plane presents a high density of dislocations. But, on the other hand, the *c*-axis presents a high quantity of twins.[2,24] Also, we believe that the plastic work produced during the indentation process contributed to closing the oxygenation crack. For this reason, we believe that the elasto-plastic transition is produced by an activation of different dislocations and twins present in the *ab*-plane and *c*-axis.

4. Conclusions

In this study we performed spherical nanoindentation tests in YBCO samples in order to examine the elastic properties and the stress–strain curves. The contact point was determined by the methodology of Barsoum et al. The following results were obtained:

(i) The Young's modulus for YBCO material was calculated with the Hertzian equations, obtaining a value of 123.5 ± 3.4 GPa. This value is in agreement with the published results obtained using sharp indentations.
(ii) The elastic-to-plastic transition occured at mean contact pressure of 3.5 GPa (at 150 nm of penetration depth) which implies that the indentation yield strength is around 3.2 GPa.
(iii) With a cross-section employing FIB technique, we showed that the samples present a heterogeneous distribution of Y-211 particles imbedded in a Y-123 matrix. No porosity or microcracking were observed, so the deformation mechanisms can be attributed to dislocations and twin generation in the *ab*-planes and *c*-axis, respectively.

Acknowledgments

We thank Dr. Y. Gaillard for assistance in AFM and Michel Barsoum and Alexander J. Moseson for helpful discussions on the determination of the contact point.

J. J. Roa acknowledges financial support from the "Comissionat per la Universitat i la Investigació del Departament d'innovació Universitari i d'Empresa de la Generalitat de Catalunya i el Fons Social Europeu".

We would also like to thank the Language Service at the University of Barcelona for linguistic and stylistic advice.

References

1. Roa JJ, Capdevila XG, Martinez M, Espiell F, Segarra M. Nanohardness and Young's modulus of YBCO samples textured by the Bridgman technique. *Nanotechnology* 2007;**18**, 385701/1.
2. Sandiumenge F, Puig T, Rabier J, Plain J, Obradors X. Optimization of flux pinning in bulk melt textured 1–2–3 superconductors. Bringing dislocations under control. *Adv Mater* 2000;**12**:375.
3. Ledbetter HM, Austin MW, Kim SA, Lei M. Elastic constants and Debye temperature of polycrystalline yttrium barium copper oxide ($YBa_2Cu_3O_{7-x}$). *J Mater Res* 1987;**2**:786.
4. Block S, Piermarini GJ, Munro RG, Wong-Ng W. The bulk modulus and Young's modulus of the superconductor $Ba_2Cu_3YO_7$. *Adv Ceram Mater* 1987;**2**:601.
5. Johansen TH. Flux-pinning-induced stress and magnetostriction in bulk superconductors. *Supercond Sci Technol* 2000;**13**:R121.
6. Lim YY, Chaudhri MM. Nanohardness mapping of the curved surface of spherical macroindentations in fully annealed polycrystalline oxygen-free copper. *Phys Status Solidi A: Appl Res* 2002;**194**(1):19–29.
7. Serradilla IG, Calleja A, Capdevila XG, Segarra M, Mendoza E, Teva J, et al. Synthesizing the Y-123/Y-211 composite by the PVA method. *Supercond Sci Technol* 2002;**15**:566.
8. Piñol S, Gomis V, Martinez B, Labarta A, Fontcurberta J, Obradors X. Bridgman growth and enhanced critical currents in textured yttrium barium copper oxide. *J Alloys Compd* 1993;**195**:11.
9. Granados X, Piñol S, Martín B, Galante F, Sandiumenge F, Fontcuberta J, et al. Direccional solidification of YBCO rods for current lead applications. *Cryogenics* 1994;**34**:833.
10. Piñol S, Obradors X, Martín B, Fontcuberta J, Sandiumenge F. Patent ES-2111435.
11. Tournier RF, Bourgault D, Buzon D, Chaud X, Folch E, Isfort D, et al. $YBa_2Cu_3O_{7-x}$ single domain growth and shaping for fault current limiting applications. *Adv Sci Technol* 2003;**38**:3.
12. Ullrich M, Leenders A, Krelaus J, Kautschor L-O, Freyhardt HC, Schmidt L, et al. High temperature deformation of Bridgman melt-textured YBCO. *Mater Sci Eng* 1998;**B53**:143.
13. Basu S, Barsoum MW. Deformation micromechanisms of ZnO single crystals as determined from spherical nanoindentation stress–strain curves. *J Mater Res* 2007;**22**:2470.
14. Oliver WC, Pharr GM. Measurement of hardness and elastic modulus by instrumented indentation: advances in understanding and refinements to methodology. *J Mater Res* 2004;**19**:3.
15. Moseson AJ, Basu S, Barsoum MW. Determination of the effective zero point of contact for spherical nanoindentation. *J Mater Res* 2008;**23**: 204.
16. Jiménez-Piqué E, Gaillard Y, Anglada M. Instrumented indentation of layered ceramic materials. *Key Eng Mater* 2007;**333**:107.
17. Basu S, Moseson A, Barsoum MW. On the determination of spherical nanoindentation stress–strain curves. *J Mater Res* 2006;**21**:2628.
18. Oliver WC, Pharr GM. An improved technique for determining hardness and elastic modulus using load and displacement sensing indentation experiments. *J Mater Res* 1992;**7**:1564.
19. Field JS, Swain MV. A simple predictive model for spherical indentation. *J Mater Res* 1993;**8**:297.
20. Field JS, Swain MV. Determining the mechanical properties of small volumes of material from submicrometer spherical indentations. *J Mater Res* 1995;**10**:101.
21. Fisher-Cripps AC. *Nanoindentation*. 2nd ed. New York, United States of America: Springer-Verlag Press; 2004. pp. 3, 9–10.
22. Gaillard Y, Jiménez-Piqué E, Soldera F, Mücklich F, Anglada M. Quantification of hidrotermal degradation in zirconio by nanoindentation. *Acta Mater* 2008;**56**:4206.
23. Isfort D, Chaud X, Tournier R, Kapelski G. Cracking and oxygenation of YBaCuO bulk superconductors: application to *c*-axis elements for current limitation. *Physica C* 2003;**390**:341.
24. Diko P, Gawalek W, Habisreuther T, Klupsch T, Gornert P. Macro- and microcracking, subgrains, twins and thermal stresses in $YBa_2Cu_3O_{7-x}$ (123)-Y_2BaCuO_5 (Y211) melt-textured superconductors studied by means of polarized light microscopy. *J Microsc* 1996;**184**:46.

5.2. YBCO textured by TSMG technique

Following the scheme presented at the previous section, spherical indentations were carried out on TSMG samples and performed by nanoindenter XP (Agilent Technologies) equipped with a CSM attachment. The harmonic displacement for CSM was 2 nm with a frequency of 45 Hz. The different tests were carried out in two different samples performed when the maximum load was 650 mN on the *ab*-plane of the monodomain, with a spherical tip nanoindenter.

As a result of this work and its diffusion, an oral communication talking about the σ–ε curve for YBCO samples textured by TSMG has been presented in the National ***XXVI Encuentro del Grupo Español de Fractura (Sociedad Española de integridad Estructural)***, Santander, 2009, and the manuscript has been published at the *"Anales de la Mecánica de la Fractura XXVI, Vol. 2 (2009) pp. 495-500"* in March 2009. More recently, a review work entitled ***Mechanical characterization at nanometric scale of ceramic superconductor composites***, has been published by *NovaScience Publisher* as a chapter of the book "Nanotechnology: Nanofabrication, Patterning, and Self-Assembly" (To be published in 2010).

Stiffness versus contact point

Before plotting the indentation stress (σ)-strain (ε) curves, it is crucial to determine the effective elastic modulus of the YBCO material examined, in order to apply the Hertz equations, and obtain the slope in the elastic range of the σ–ε curves. Plot of *S vs. a* into surface shows if the interaction between the indenter and the sample is good or not. The *Fig. 5.1*, shows the contact point of YBCO sample in the *ab*-plane. σ–ε curve will be accepted if no high scattered values are present.

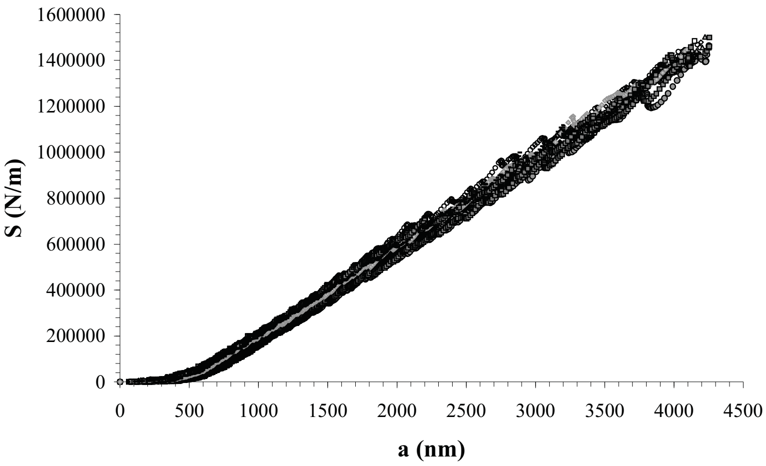

Fig. 5.1. Plot of contact harmonic stiffness versus contact radius as determined from spherical nanoindentation for YBCO materials textured by TSMG technique.

In this case, *Fig. 5.1* shows a bad contact point because the slope does not pass through zero. Also, in this figure, it can be observed the linearity over the entire penetration depth, which implies that *S* is not affected by pop-ins or plastic deformation. In other words, effective Young's modulus is not a function of indenter radius, as one would expect. The *S vs. a* curve is widely used when a spherical study was carried out. Non linear *S-a* curve can be observed at the beginning of the first 500 nm of contact point in *Fig. 5.1*, due to superficial defects, such as: roughness, etc. A bad contact point can give us an overestimated strain value; in this case a false yield strength value can be obtained.

After an appropriate correction of the *S-a* curves as presented in *Fig. 5.2*, the contact point between the indenter and the sample shows a linear trend.

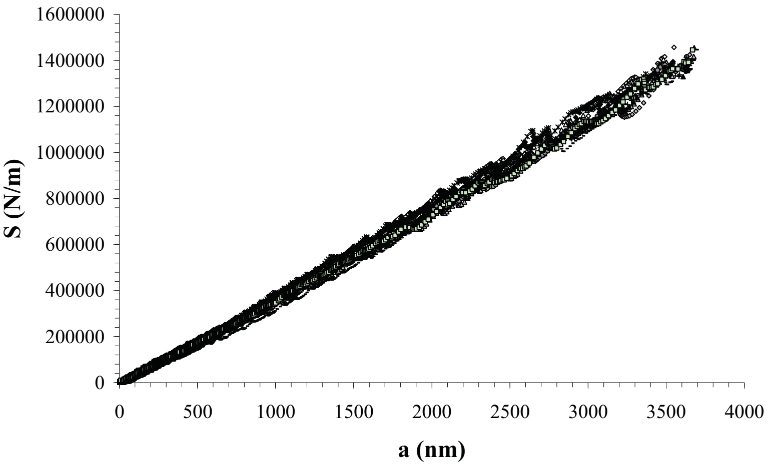

Fig. 5.2. Corrected contact point for samples textured by TSMG technique.

After that, the E_{eff} has been calculated with linear experimental fitting points and employing the Sneddon equation[2];

$$S = 2E_{eff}\,a \qquad \textbf{eq. 5.1}$$

Using the *eq. 5.1*, the E value is equal to 120 ± 4 GPa, which is in correct agreement with the previous value obtained in *section 5.1*.

Determination of the elasto-plastic transition: In most materials, and according to the Tresca criterion[3], when the value of τ_{max} reaches a certain limit ($\tau_{max} = \sigma_{ys}/2$, where σ_{ys} is the yield strength of the material), the material will start to flow and develops a permanent deformation. This criterion has been also used to explain the nucleation of dislocations during pop-in effects[4], yielding the material to make the transition from an elastic to an elasto-to-plastic response[3]. In this case, mean contact pressure (p_m) will converge on the H of the material.

σ–ε curves: In the case of spherical indentation, by plotting p_m against *a/R* (*contact radium/indenter radium*), it is possible to determine the point at which there is the transition from elastic to elasto-to-plastic regime, shown in *Fig. 5.3* as a change in the slope for TSMG samples.

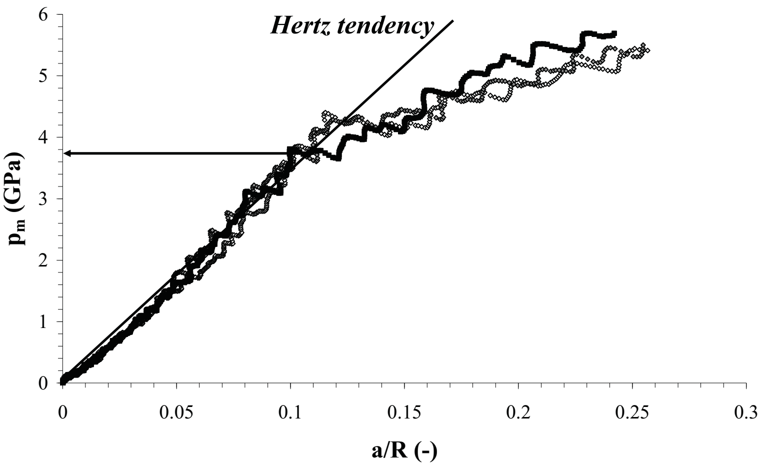

Fig. 5.3. Indentation σ–ε curves for YBCO textured by TSMG technique.

The p_m for TSMG samples is around 3.9 GPa. To obtain the yield strength, σ_{ys}, maximum yield strength, σ_{max}, and the maximum shear stress, τ_{max}, next equations have been used:

$$p_m = 1.1\sigma_{ys} \qquad \textbf{eq. 5.2}$$

$$\sigma_{\max} = \frac{1}{2}(1-2v)p_m \qquad \textbf{eq. 5.3}$$

$$\tau_{\max} = 0.46 p_m \qquad \textbf{eq. 5.4}$$

where, v is the Poisson ratio of the material. Values obtained for TSMG samples are $p_m = 3.55 \pm 0.10$ GPa, $\sigma_{max} = 0.78 \pm 0.02$ GPa, and $\tau_{max} = 1.79 \pm 0.05$ GPa.

5.3. Conclusions

The mechanical properties obtained using spherical tip indenters are similar for both texturing methods, as these properties are intrinsic of the material, and only depend on its composition and not on the processing method. These values cannot be compared to previous works, as scare information in the literature is available.

5.4. References

[1] H. Hertz, J. Reine Angew. Math. 92 **(1881)** 156 (Translated and reprinted in English in Hertz's Miscellaneous Papers, MacMillan and Co., London (1986) Ch. 5).

[2] I. N. Sneddon; *Int. J. Engineering Science* 3 **(1965)** 47.

[3] Y. Gaillard, C. Tromas, J. Woigard; *Phil. Mag. Let.* 83 **(2003)** 553.

[4] D. Lorenz, A. Zeckzer, U. Hilpert, P. Grau, H. Johansen, H. S. Leipner; *Phys. Rev. B,* 67 **(2003)** 172101/1.

6

STUDY OF THE DIFFERENT PLASTIC MECHANISMS

Knowledge is a treasure, but practice is the key to it

Thomas Fuller (1608-1661)
British clergyman and author

In the two previous chapters, we tried to find some values for the mechanical properties of YBCO. Once we have them, we want to make one step forward and understand what happens when plastic deformation takes place. If we know it, maybe we could control these mechanisms and thus improve the materials performances.

An arbitrary deformation of a material can always be described as the sum of a change in volume or a change in shape at constant volume (shear). Considering constant structure, the change in volume can be recovered when the applied load is removed, since the atoms can simply relax back to their equilibrium position. The change in shape may or may not be recovered, since the atoms can relax into new positions that are configurationally identical to the original. In other words, the part of the shear that is recovered is elastic, and the part that remains is plastic.

Dislocations in ceramics share many aspects with metals and alloys in explaining plastic deformation properties. However, most ceramic materials have low symmetry crystals structures with large unit cells, giving a number of consequences regarding dislocations. The plastic deformation mechanisms take place when dislocations multiply and glide with a surface; the characteristics determining the easiest glide plane follow well-established rules, such as electrostatic interactions in cubic zirconia[1] or low elastic energy, especially in extremely anisotropic crystals such as TeO_2[2].

Usually, ceramic materials are brittle due to several factors: the number of slip systems is insufficient for the deformation of polycrystals, such as MgO, NiO, etc, or the covalent character of the chemical bonds in ceramic materials, this is associated with large Peierls stresses, or lattice friction, which impedes dislocation glide at low temperature.

The subject of plastic deformation mechanism nucleated during the indentation process is essential for understanding many of the physical and mechanical properties of advanced ceramic materials like YBCO. The nanoindentation test allows introducing locally plastic deformation in brittle materials. AFM only allows surface observation compared to TEM, but samples preparation (thin foil) is easier, which is a great deal for the treatment of large number of measurements. This technique supplies different thypes of images (the most common ones are the topographic and the error images). The main requeriment to perform this type of experiments is the surface preparation: we need very low roughness. Moreover, no work hardnening induced during the polishing process is required; this is a key element in this kind of study and the actual limit. Surface preparation is particularly difficult with YBCO samples, due to the presence of two different phases with different hardness, and this material presents a superficial degradation when the polishing process is performed with water (more details of the polishing process is presented in *section 3.2 page 76*).

In this section, the micro-structures of defects induced by indentation techniques such as twins, slip lines or cross-slip have been characterized by AFM. Moreover, this AFM image mode (*tapping mode*) is particularly suited to the investigation of constant slope surface features, such as those resulting from slip-lines and twining mechanisms. The effect of indenter orientation in the formation of slip-lines and twins near imprints is described.

The results presented in this chapter were mainly obtained during my stage at University of Poitiers, and we have reached the conclusion that more experiments must be performed before having these results published.

6.1. Bridgman poly-crystaline samples

In this section, some of the different plastic deformation mechanisms (i.e. slip lines, twins, chipping, etc) induced during the indentation process, has been observed by AFM. In order to activate these mechanisms, several indenter shapes have been employed. The different experiments will be performed on a polycrystal sample at 45º of the basal plane (*ab*-plane or [001]).

6.1.1. Deformation induced by a Berkovich indenter

The use of a Berkovich indenter to study the different plastic deformation mechanisms can be useful as it allows to concentrate all the field stresses in only one point. Moreover, this tip allows to apply low loads and know the minimum load employed, in order to activate this phenomenon. *Fig.* 6.1, exhibits an AFM micrograph of several YBCO grains with different crystallographic orientations, and the indentations matrix performed at 10 mN of maximum applied load.

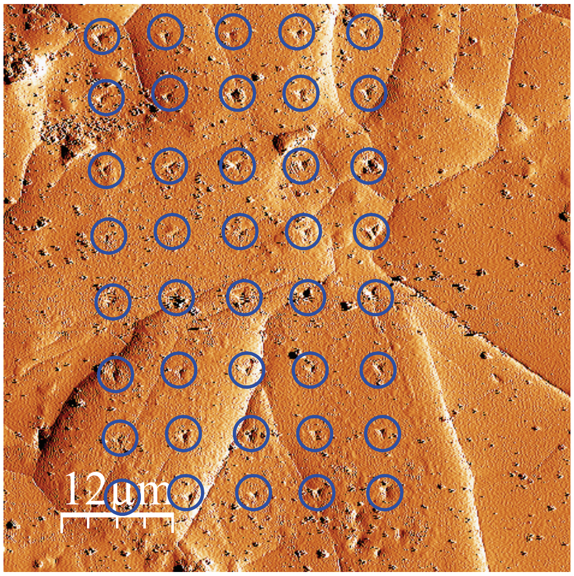

Fig. 6.1. AFM micrographs (error signal mode) of nanohardness impressions developed on 45º of the basal plane [001] at room temperature, when the applied load was 10 mN.

In addition, *Fig. 6.1.* shows a high grain size distribution from 1 to 50 µm. Moreover, each grain presented in this image has different roughness, due to the different crystallographic orientation. Then, each grain presents different hardness values.

The different error signal mode images of AFM, where the typical plastic deformation mechanisms induced during the nanoindentation process can be observed, are shown in *Fig. 6.2*.

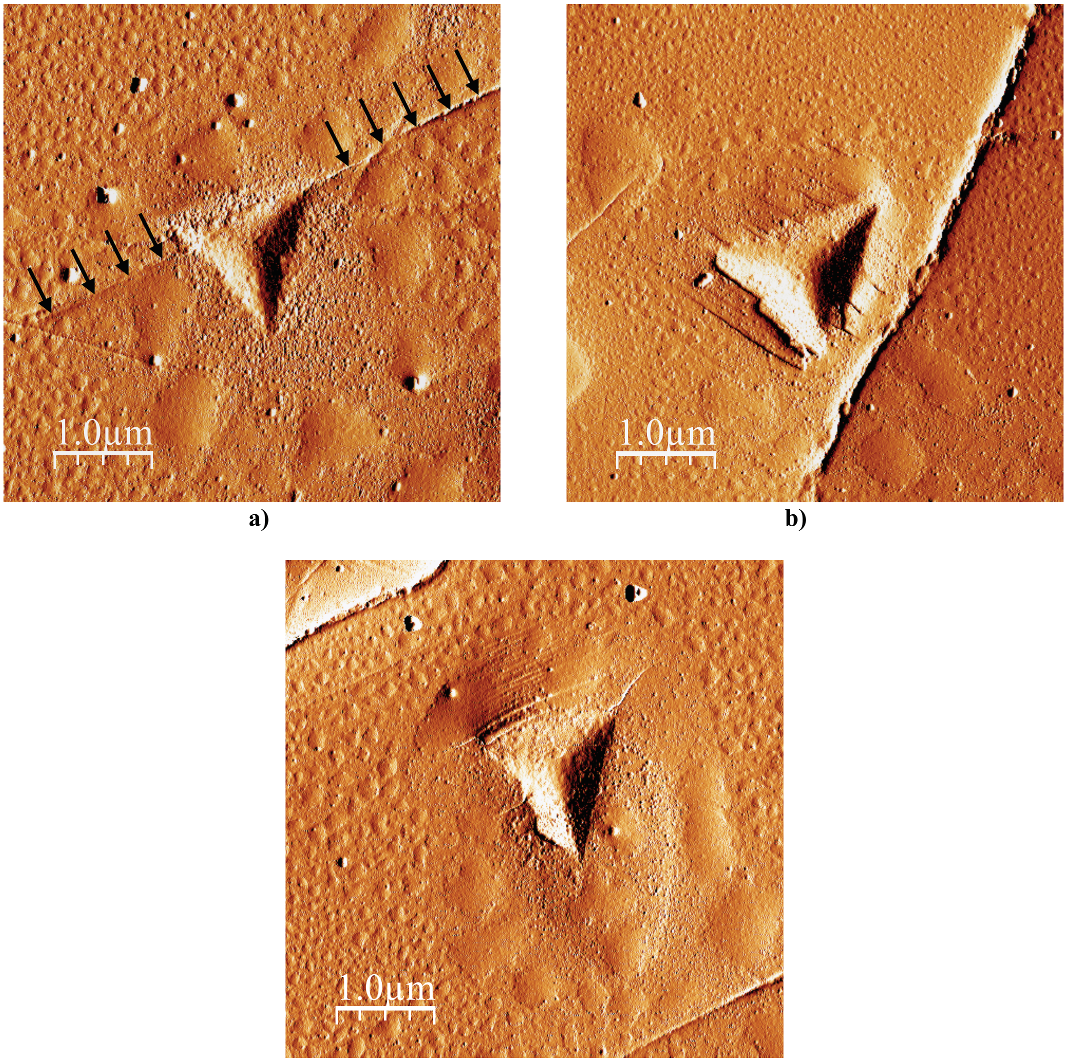

a)

b)

c)

Fig. 6.2. AFM images (error signal mode) of the several features observed around the residual imprints, with the most frequently plastic mechanisms nucleated during the indentation process. a) Residual imprint with no other deformation around (Plastic means irreversible deformation, so, this indent is plastic). b) and c) Steps (Slip lines) surrounding the imprint

Fig. 6.2a, shows a residual imprint performed on a grain boundary (black arrows). In this case, no deformation is observed outside the indent. The authors believe that the grain boundary absorbs some of the plastic energy induced by the tip thus closing it. However, *Fig.* 6.2*b*, exhibits an imprint performed in the center of one grain. Linear and parallel steps can be observed around the indent. They can be slip lines due to the emergence and propagation of dislocations around the indent. The same kind of feature is observed in other direction, see *Fig. 6.2c*. This phenomenon is attributed to the different crystallographic orientation between the different grains studied.

In some cases, when the residual nanoindentation imprint is performed near the grain boundary, residual radial cracks are activated, as can be seen in *Fig. 6.3*. In both AFM images a radial crack is observed, which is nucleated due to the tensile stress originated during the indentation process can be seen. Normally, the crack propagation is induced by the tensile stress accumulated at the corner of the residual imprint, and it is produced during the relaxation process. In these images, an abnormal behaviour takes place due to the radial crack, which in both cases, is not propagated from the corner of the imprint. We believe that this behaviour is due to the influence of the grain boundary, which modifies the plastic deformation range nucleated during the indentation process. Moreover, the residual face of the imprint near the grain boundary presents abnormal geometry due to the grain boundary vicinity. This phenomenon is not attributed to the thermal drift effect but to the grain boundary, which acts as a crack, and during the indentation process, the tensile stress produces a movement of the material in the grain boundary direction.

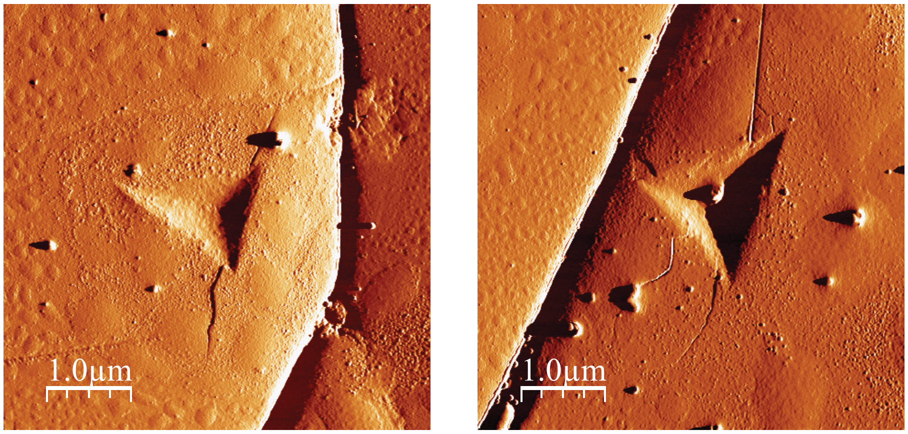

Fig. 6.3. AFM images of the different residual imprints performed near the grain boundary with different fracture mechanisms nucleated during the indentation process.

6.1.2. Deformation induced by a Spherical indenter

Spherical indenter produces a higher stress field under the residual imprint. Then, a different plastic deformation mechanism is going to be activated. In this case, a spherical indenter (10 µm radius of curvature, controlled by direct AFM observation and indentation on a material with known Young's modulus) will be employed. Using this type of indenter, the stress distribution below the indenter is completely different from that of a Berkovich indenter. Then, another plastic deformation mechanism could be induced. The density of dislocations is function of the angle between surface and the *ab*-plane of the indented grain. The higher misorientation, the hughest density showing several linear steps (slip lines) inside of the contact radius of the indenter, see *Fig. 6.4.*

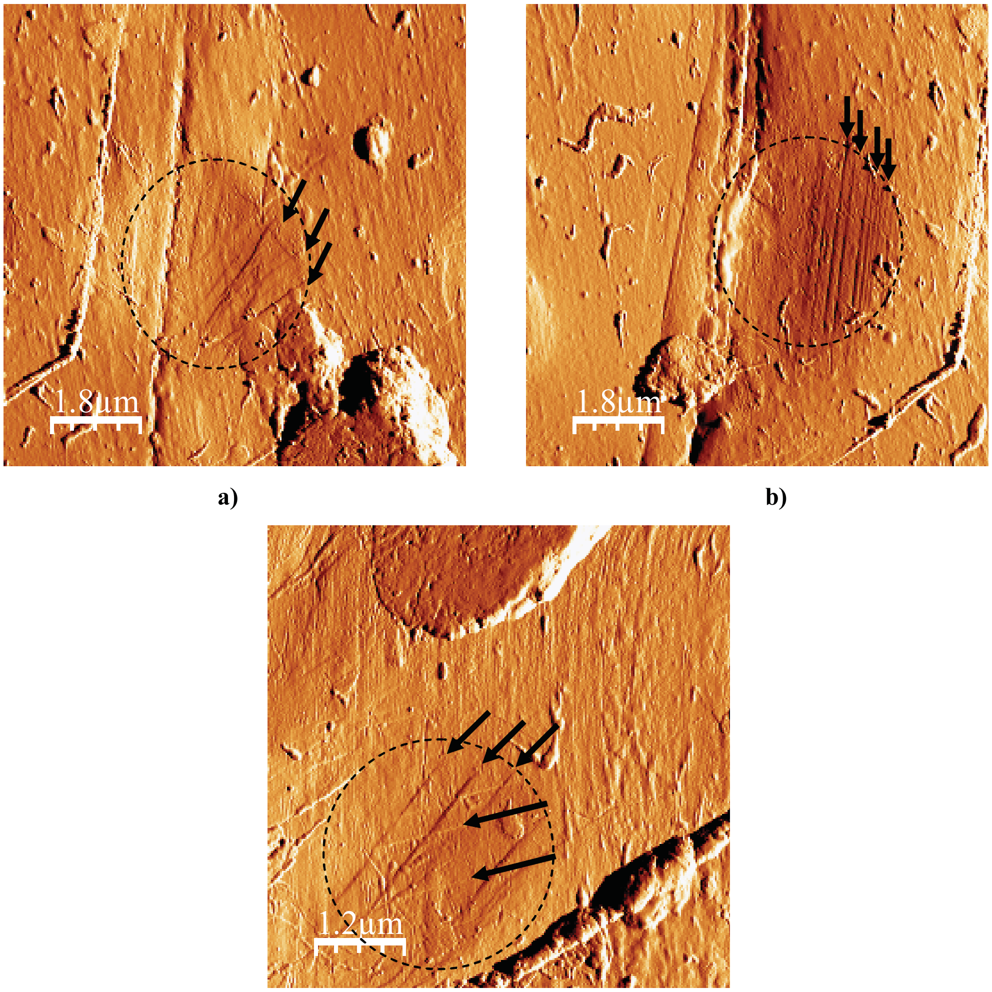

a) b)

c)

Fig. 6.4. AFM micrograph (error image) of residual spherical imprints. a) 100 mN, 1 cycle. b) 50 mN, 1 cycle. c) 50 mN, 5 cycles. The arrows denote the different slip lines inside of the residual imprint.

Fig. 6.4a, shows a residual imprint performed at 100 mN of maximum applied load. This imprint exhibits a spherical shape, which reproduces the indenter shape. Moreover, inside of the contact circle generated by the spherical indenter, several lines can be observed and no external displacement has been promoted. A similar effect exhibits the residual imprint performed at 50 mN (1 cycle), see *Fig. 6.4b*. In this case, several slip lines are observed inside of the residual imprint. *Fig. 6.4c*, shows a different plastic deformation mechanism two slip line orientations[3]. One line with a certain orientation always ends on one line with the other orientation with that can be due to cross slip (a dislocation from one kind of slip plane to another) or to dislocation interactions between to types of dislocations. It is also important to emphasize that two slip line directions means that dislocations are gliding in non collinear slip planes: they cannot be all in the basal plane. This can be an evidence for the activation of other slip systems than basal one.

A 3D image of *Fig. 6.4c* shows in more detail the cross-slip effect, see *Fig. 6.5*.

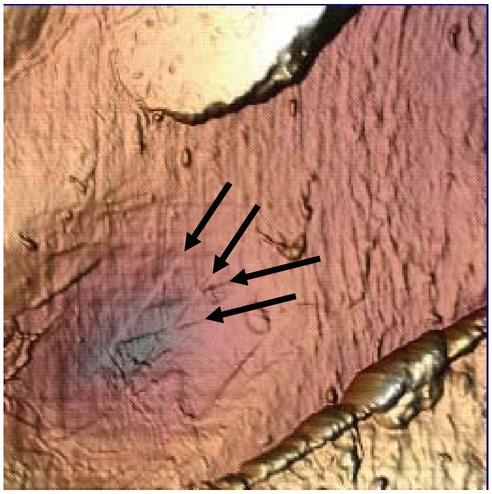

Fig. 6.5. 3D-AFM image of the cross-slip effect.

6.2. TSMG single crystal samples

6.2.1. Deformation induced by a Berkovich indenter

In this section, the different plastic deformation mechanisms have been studied at 10 mN of applied load. *Fig. 6.6*, exhibits an AFM micrograph of single crystal of YBCO oriented in the basal plane. Concretely, the study is carried out in a zone without inclusions of Y-211. Then, interactions of the different plastic deformation mechanisms will not be affected by the presence of Y-211.

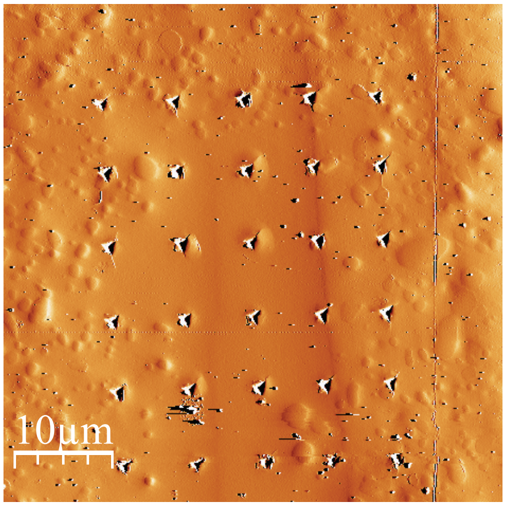

Fig. 6.6. AFM micrographs of nanohardness impressions developed on the basal plane [001] at room temperature, when the applied load was 10 mN.

All the residual imprints presented in the *Fig. 6.6* show some fracture mechanisms called chipping, and also radial cracks due to the stress field induced by the tip. *Fig. 6.7*, show in more detail, the fracture effects and also some plastic deformation mechanisms induced during the indentation process.

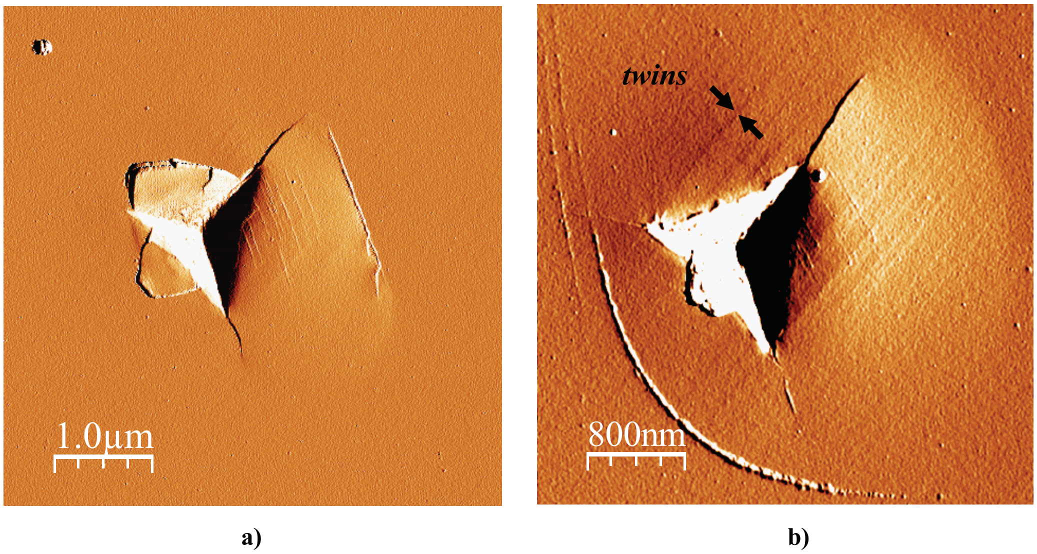

a)

b)

Fig.6.7. AFM images of two different nanoindentation imprints and their fracture and plastic deformation mechanisms activated during the indentation process induced by a Berkovich indenter.

First of all, *Fig.6.7a* shows some fracture mechanisms called chipping and radial cracks nucleated at the corners of the imprints. The radial cracks are a typical effect produced to dissipate the tensile stress originated at the corners of the imprints. This residual imprints have been performed on the basal plane. As in this image the slip lines can be observed on the surface, they necessarily correspond to the activation of other slip systems than basal one. This is new for this material, and unexpected. The nanoindentation technique allows to produce specific deformation conditions. This effect has nothing to compare with conventional uniaxial test, particularly in this kind of materials. The YBCO sample presents a nanolaminar structure (for more details see *section 1.2.2, page 33*). Also, it is interesting to note that the radial cracks, far away from the indent, is oriented in the same direction as the slip lines. In order to know the correct slip system activated here, an EBSD image is required, which will be performed in the future.

In addition, inside of the chipping effect, there are high amounts of lines parallel to one side of the imprint, and activated as a consequence of the plastic deformation mechanism. *Fig.6.7b* shows the typical fracture mechanism of ceramic materials -i.e. radial cracks at the corners. These bands can be attributed to another plastic deformation mechanism called twining. However, this mechanism cannot be observed in an easy way. The misorientation angle between the different bands and twins is around 75º.

6.2.2. Deformation induced by a Spherical indenter

In this section, we study the plastic behaviour of a typical *P-h* curve (monocycle) and also with a polycyclic process (5 cycles of indentation). *Fig. 6.8*, shows the typical *P-h* curves for this type of material performed at 25 mN (monocycle) and 50 mN (polycyclic).

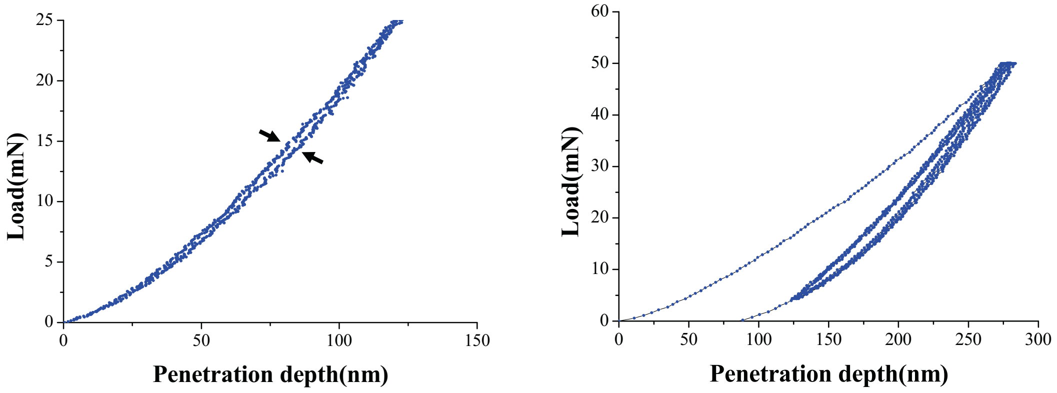

a) **b)**

Fig. 6.8. Typical P-h curves performed at 25 and 50 mN. a) monocycle, and b) polycyclic (5 cycles).

Fig. 6.8a shows a reversible indentation cycle with no residual deformation. This is an open cycle that is, some energy is dissipated during the unloading process; for this reason loading and unloading curves do not overlap. A similar effect takes place in *Fig. 6.8b*. In this case, five cycles have been applied, being all of them opened. The amount of energy dissipated (that is the opening of the cycle) depends mainly on the maximum applied load and the number of cycles. This effect is well known in geology, but it had not been reported for YBCO in the literature up to now.

6.3. Conclusions

AFM technique allows to study the different plastic deformation mechanisms activated during the nanoindentation process on brittle materials. Several slip lines have been visualized in the vicinity of the residual imprint performed by Berkovich and spherical indenters. TSMG samples, also present an activation of the different twins. The direction of the slip lines presents a high correlation with the crystallographic orientation for Bridgman samples. The field stress generated by spherical tip produces a nucleation of slip lines and cross-slip movement inside the contact radius.

6.4. References

[1] A. Domínguez Rodríguez, A. H. Heder, J. Castaing; *Rad. Effects Defic. Sol.* 119-121 **(1991)** 759.

[2] A. Meter, E. Fries, J. Janszky, J. Castaing; *Rev. Phys. Appl.* 21 **(1986)** 289.

[3] D. Hull, D. J. Bacon; *Introduction to Dislocations*. Fourth edition **2001**. ISBN 0-7506-4681-0.

7

CORRELATION BETWEEN MECHANICAL VERSUS ELECTRICAL PROPERTIES

> ***The greater our knowledge increases, the greater our ignorance unfolds***
>
> *John F. Kennedy (1917-1963)*
> *35th President of USA*

The generation of some bulk superconducting applications, such as large magnets or bearings, could be drastically enhanced by using larger YBCO blocks. Unfortunately, YBCO pellets of only a few centimetres can be achieved by melt-texturing growth. This fact has motivated the development of alternative procedures to obtain larger tiles. In this experimental study, the silver assisted welding appears to be the most attractive method in order to build up or repair complex-shaped pieces. Superconducting joining represents a key enabling technology for the fabrication of large YBCO blocks, allowing an enhancement in the performance of several large-scale applications. Efficient joints must probe not only high electrical connectivity but also mechanical stability. We have evaluated the mechanical and critical current density properties of melt-textured YBCO welds fabricated by silver welding.

The following paper, published in *Superconductor Science and Technology* in March of 2010, describes the correlation between the microstructural, mechanical and critical current density performances of melt-textured [001]-tilt YBCO welds, fabricated by the silver welding technique. These samples were supplied by E. Bartolomé from ICMAB, as well as superconducting measurements. The hardness reduction across the weld, measured by nanoindentation, correlates linearly with the decrease of intergranular critical current density, measured at 77K and self-field by magnetic Hall mapping.

Results presented in this chapter are further discussed in chapter 9.

IOP PUBLISHING SUPERCONDUCTOR SCIENCE AND TECHNOLOGY

Supercond. Sci. Technol. **23** (2010) 045013 (6pp) doi:10.1088/0953-2048/23/4/045013

Effective silver-assisted welding of YBCO blocks: mechanical versus electrical properties

E Bartolomé[1], J J Roa[2], B Bozzo[3], M Segarra[2] and X Granados[3]

[1] Escola Universitaria Salesiana de Sarrià (associated with the University Autònoma of Barcelona), Passeig Sant Joan Bosco 74, E-08017 Barcelona, Spain
[2] Centro DIOPMA, Departamento Ciencia de los Materiales e Ingeniería Metalúrgica; Instituto de Nanociencia y Nanotecnología de la Universidad de Barcelona (IN2UB), Facultad de Química, Universidad de Barcelona, Martí i Franqués 1, E-08028 Barcelona, Spain
[3] Institut de Ciència de Materials de Barcelona—CSIC, Campus UAB, E-08193 Bellaterra, Spain

Received 2 November 2009, in final form 23 December 2009
Published 10 March 2010
Online at stacks.iop.org/SUST/23/045013

Abstract

Superconducting welding of bulk YBCO is a key technology allowing the fabrication of large, complex-shaped pieces for applications such as levitation, bearings or large magnets. Ideally, the electrical and mechanical properties of welds should be comparable to that of the joint grains. In this paper, we have investigated the correlation between the microstructural, mechanical and critical current density performances of melt-textured [001]-tilt YBCO welds fabricated by the silver welding technique. The hardness reduction across the weld, measured by nanoindentation, correlates linearly with the decrease of intergranular critical current density, measured at 77 K and self-field by magnetic Hall mapping. Remarkably, we show that high quality zero-angle welds could be fabricated with unaltered current and hardness performances across the joint, paving the way for the implementation of silver welds in large-scale systems.

(Some figures in this article are in colour only in the electronic version)

1. Introduction

The performance of some bulk superconducting applications, such as levitation, large magnets or bearings, could be drastically enhanced by using larger $YBa_2Cu_3O_{7-x}$ (YBCO) blocks. Unfortunately, YBCO pellets of only a few centimetres can be achieved by melt-texturing growth. This fact has motivated the development of alternative procedures to obtain larger tiles, like multi-seeding [1, 2] and welding [3] techniques. Silver-assisted welding appears to be the most attractive method in order to build up or repair complex-shaped pieces by assembling primary domains previously fabricated by the standard melting technique; meanwhile, multi-seeding allows us to obtain large pieces during the same growth process. In any case, ideal efficiency is achieved only if the joint pieces are electrically and mechanically comparable to single-domain blocks.

In the scope of this research, we developed a robust superconducting welding technique based on the use of a metallic Ag foil as the welding agent [4]. The process is based on the controlled melting of the foil and diffusion of the Ag into the YBCO matrix at an annealing temperature $T_{max} = 985\,^{\circ}C$ above the peritectic temperature of the YBCO/Ag composites ($T_p \approx 980\,^{\circ}C$), but below that of YBCO ($T_p \approx 1010\,^{\circ}C$). The use of a silver foil as welding agent presents several advantages: (i) the large temperature window existing among the peritectic temperatures of pure YBCO and YBCO/Ag composite facilitates the seeding process of the molten interface from the lateral tiles to be welded; (ii) no dissimilar interfaces are created [5] and (iii) the process is easily scalable.

The silver welding technique enables us to produce both symmetric and asymmetric, [001]-tilt [6] or [110]-tilt [7] superconducting welds in a large range of misorientation angles, as required for flexible fabrication of different complex-shaped parts. Details of the microstructure were reported elsewhere [7]. The magnetic properties of melt-textured [001]-tilt YBCO welds have been thoroughly studied

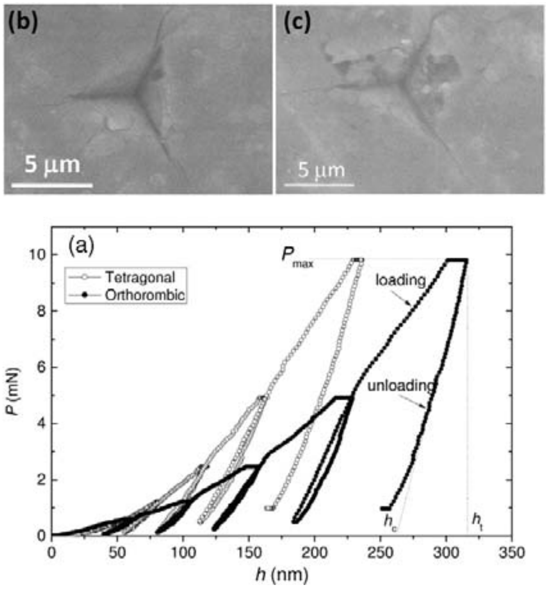

Figure 1. (a) Load versus indenter displacement curves after five loading/unloading processes with a maximum applied force of $P_{max} = 10$ mN for reference bulk sample in the tetragonal and orthorhombic phases. On top: the projected area A_c is obtained from an FE-SEM image of the nanoindentation imprint: (b) tetragonal phase and (c) orthorhombic phase.

in the past, using Hall magnetic mapping [8]. The critical current density across the weld, J_c^{GB}, and at the adjacent grains, J_c^G, were simultaneously determined as a function of the applied magnetic field at 77 K. Inductive results demonstrated that high quality zero-angle welds could be fabricated, with inter-to-intragrain critical current density ratios $J_c^{GB}/J_c^G \approx 1$. For misoriented welds, the dependence of the intergrain critical current density on the applied magnetic field and the angle, $J_c^{GB}(\theta, H)$, was established. Guidelines for the choice of the most adequate θ weld for each application were provided, as a function of operational field requirements.

It is worth remarking that, for superconducting welds to become functional in applications, mechanical stability in addition to high electrical performance must be guaranteed. Despite that, the mechanical properties of superconducting joints have never been studied.

In this paper, we report results on the mechanical properties of melt-textured YBCO silver welds in correlation with their microstructure and critical current density performance. We determined the nanohardness and Young's modulus across welds of different [001]-tilt angles using a nanoindentation technique at room temperature [9]. In the last decade nanoindentation has become one of the most versatile methods for the characterization of the mechanical properties at the micro–nanoscale of a broad spectrum of materials [10, 11], among which are YBCO bulk ceramics [12–14] and thin films [15]. Contact phenomena activated during the indentation process at different areas of the weld have been studied by observation of the indentation imprints with field emission scanning electron microscopy (FE-SEM). The critical current densities across the joints have been determined from quantitative Hall mapping in the remanence at 77 K. We will show that the silver welding technique can provide high quality zero-angle YBCO joints with unaltered current and mechanical properties across the boundary.

Table 1. Experimental parameters for nanoindentations.

Name	Value
Allowable drift rat	0.05 nm s^{-1}
Maximum load	10 mN
Number of loads	5
Peak hold time	30 s
Unload percentage	90%
Time to load	15 s

2. Experimental procedures

YBCO welds with asymmetric [001]-tilt boundaries were prepared by the silver welding technique [3, 4]. Samples were fabricated from commercial YBCO bulk single domains with nominal composition Y123 + 25 mol% Y_2O_3 + 1 wt% CeO_2 [16]. 1 cm^3 cubes were extracted from the as-grown tetragonal samples. We halved each YBCO cube parallel to the c axis and then made a second cut with a relative misorientation θ in one of the adjacent grains. The two joining surfaces so obtained were polished with diamond powder down to a size of 1 μm, and a 10 μm thick Ag foil was introduced between them. The sandwich-like assembling so obtained was fixed between two alumina plates parallel to the joint and placed in a horizontal position in the furnace. The specimen was first heated up to $T_{max} = 995\,°C$ and kept there for 3 h; then it followed a slow-cooling ramp at 0.6° h^{-1} down to 950 °C and a fast cooling to room temperature. Finally the welded samples were annealed in flowing oxygen at 1.1 bar for 120 h at 450 °C to achieve the orthorhombic, superconducting phase. (Details on the optimization of the thermal process can be found in [5].) Samples were halved parallel to the *ab* plane for measurements, so the final dimensions were $1 \times 1 \times 0.5\ cm^3$. For this study we considered two $\theta = 0°$ welds (a standard 0° weld and a non-optimized, low quality one, chosen to test the sensitivity of the technique to variations of H across the weld); two different $\theta = 14°$ welds (A and B), and a bulk reference sample (without weld) for comparison.

Nanoindentation measurements at room temperature were performed with a Nanoindenter XP® system (Agilent Technologies) equipped with Test Works 4 Professional level software and a Berkovich tip. In a typical indentation process, the diamond indenter was repeatedly pushed and withdrawn from the material at a given position, and the load (P) versus tip penetration (h) was recorded (figure 1). The maximum applied load was chosen as 10 mN, small enough to produce net imprints which allowed the accurate measurement of the imprint area A_c. At this load, obtained values of H and E correspond to the YBCO compound and not to each of the separate Y123 and Y211 phases [13]. Table 1 summarizes other measurement parameters chosen for nanoindentations. The loading/unloading P–h curve characterizes the elastic/plastic response of a sample. The elastic recovery is calculated from the difference between the total indentation depth (h_t) at maximum indented load (P_{max}) and depth of residual impression upon unloading (h_t).

From the analysis of the P–h curves, the nanohardness (H) and Young's modulus (E) at each point was obtained using the Oliver and Pharr [17] relations:

$$h_c = h_t - \varepsilon \frac{P_{max}}{S}, \tag{1}$$

$$A_c = A(h_c) = 24.56 \cdot h_c^2, \tag{2}$$

$$H = \frac{P}{A_c}, \tag{3}$$

$$E_{eff} = \frac{\sqrt{\pi}}{2} \frac{S}{\sqrt{A_c}}, \tag{4}$$

$$\frac{1}{E_{eff}} = \frac{1-\nu_i^2}{E_i} + \frac{1-\nu^2}{E}, \tag{5}$$

where ε is the strain (0.75 for the Berkovich indenter), A_c is the projected area under the load, E_{eff} is the effective Young's modulus, S is the elastic constant stiffness (obtained from the load/unload curve $\mathrm{d}P/\mathrm{d}h$), E is the Young's elastic modulus, ν is Poisson's ratio of the tested YBCO material ($\nu = 0.3$ [18]), $E_i = 1141$ GPa and $\nu_i = 0.07$ are the elastic modulus and Poisson's ratio of this nanoindenter [9]. The tip was calibrated against a fused silica standard before measurements.

In order to investigate the variation of mechanical properties across the welds, we performed nanoindentation scans on the *ab* plane in a range of 2 cm across each boundary. The separation between imprints was 50 μm in order to isolate the plastic behaviour generated under the residual imprint (as a general rule, the imprint separation should be 20–30 times the maximum penetration depth). Six hundred indentations were performed for each studied sample in order to achieve statistical significance. Each of the E and H values plotted in subsequent figures is the average of 15 scans performed across the boundary, separated 50 μm from each other (figure 1(a)).

Nanoindentation imprints were observed with a field emission Hitachi H-4100 scanning electron microscope (FE-SEM). These images served a threefold purpose: (i) to discard nanoindentation measurements performed on sample pores; (ii) to measure the contact area A_c required for the E, H determination, thus avoiding over- or underestimations due to *sink-in* or *pile-up* events [19] and (iii) to investigate the different fracture mechanisms activated during the indentation process.

A magnetic Hall probe scanning system with 160 μm spatial resolution was used to determine $B_z(x, y)$ maps of the *ab* plane of welds in the remanence at 77 K. Details of the system can be found elsewhere [20–22]. The grain and intergrain critical current densities, J_c^G and J_c^{GB}, were simultaneously determined from inversion of the measured B_z map, following the methodology described in [23, 24].

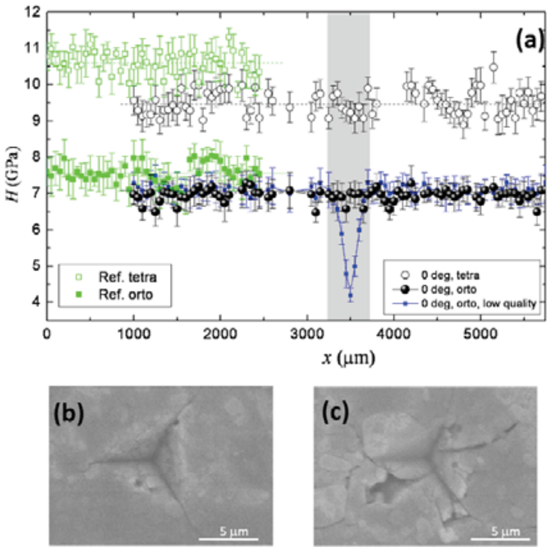

Figure 2. Top: (a) nanohardness scans, $H(x)$, across a high quality $\theta = 0°$ weld in the tetragonal (○) and orthorhombic (●) phases; $H(x)$ across a low quality $\theta = 0°$ weld in the orthorhombic phase (■). The shadowed region indicates the approximate weld position. For comparison, the nanohardness of the bulk reference sample in tetragonal (□) and orthorhombic (■) phases are shown; below: FE-SEM images of indentation imprints in the weld region for the high quality 0° weld (b), and the low quality 0° weld (c).

3. Results and discussion

First, the mechanical properties of a melt-textured sample were measured to have a reference of the material characteristics prior to the welding procedure. Figure 1 displays typical loading/unloading P–h curves measured for the reference sample in the tetragonal and orthorhombic phases. As a result of the oxygenation process, the penetration depth in the orthorhombic phase is larger than in the tetragonal phase, and thus, according to equation (3), the hardness is smaller in the former phase. The FE-SEM image of the nanoimprint in the orthorhombic phase (figure 1, inset) shows superficial defects such as cracks at the corners of the imprint and a chipping effect, which were activated during the indentation process.

The nanohardness values for the bulk reference sample in the tetragonal phase, $H = 10.6 \pm 0.4$ GPa, and orthorhombic phase, $H = 7.6 \pm 0.4$ GPa are shown in figure 2. As expected, the hardness is smaller in the less compact crystalline phase. However, the Young's modulus remains constant in both phases, within the error ($E = 120 \pm 5$ GPa). This value is in good agreement with different values reported in the literature for melt-textured YBCO [25, 26] and smaller than those reported for Bridgman-grown YBCO at similar applied loads [13]. The Young's modulus depends basically on the composition of the material, thus E does not change significantly with the crystalline phase, but it is influenced by the texturing process affecting the microstructure.

Figure 2 depicts as well the H measured across a $\theta = 0°$ weld. We observe a decrease of around 10% in the grain

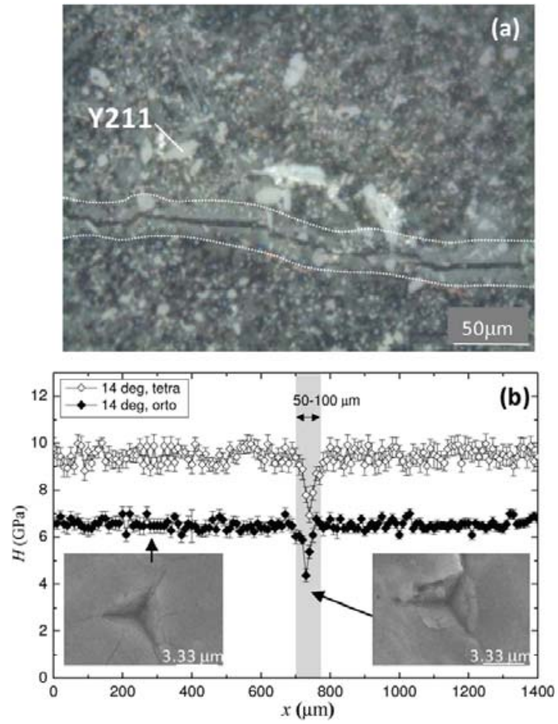

Figure 3. YBCO silver weld with a $\theta = 14°$ angle. (a) Optical micrograph showing the decrease in the density of Y211 particles in a 'welding path' of around 50 μm, after oxygenation process; (b) nanohardness scan $H(x)$ across the weld in the tetragonal (◇) and orthorhombic phase (◆), and FE-SEM images far from the weld and at the weld region.

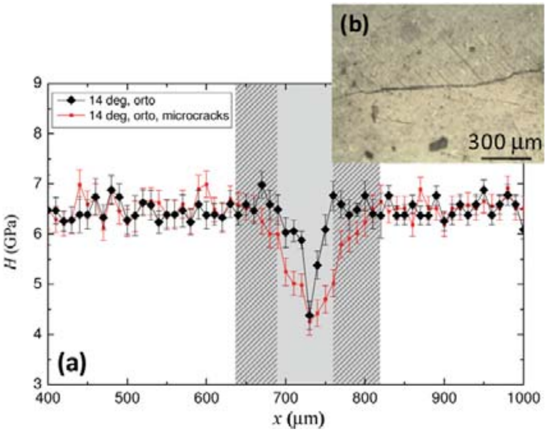

Figure 4. (a) Nanohardness scan $H(x)$ across a $\theta = 14°$ weld in the orthorhombic phase, in a region (b) affected by microcracks (■). For comparison, $H(x)$ across a region free of microcracks (◆).

nanohardness with respect to the reference sample in the two phases. This fact may be explained by the presence of silver in the YBCO matrix, migrated from the weld region during the thermal treatment. The maximum silver content could be estimated taking into account the welding path width and the amount of silver used for welding, although it was not directly detected in the weld. This percentage has been established in 0.5 wt% in the 5 mm scanned region, considering densities of Ag and YBCO to be $\rho_{\mathrm{Ag}} = 10.4$ g cm^{-3} and $\rho_{\mathrm{YBCO}} = 4.7$ g cm^{-3}. It could be possible that the addition of a small percentage of silver decreases the nanohardness for the small contact depths used in our indentations. It has been earlier reported that a 5 wt% $\mathrm{Ag_2O}$ in YBCO decreases H for contact depths $h < 300$ nm, whereas for larger contact depths H was observed to increase [27]. This means that if silver is in the origin of the grain softening, it occurs only in the sample surface.

Remarkably, the nanohardness was not degraded at all across the 0°-weld boundary. In order to verify that our technique was sensitive to variations of H across the weld, we also measured a low quality 0° weld, obtained after a non-optimized thermal treatment. The degradation of the nanohardness at the weld region can be clearly appreciated in this case. For the high quality 0° weld, the FE-SEM image of the nanoimprint in the weld region (figure 2(b)) looks similar to that in the adjacent grains. In contrast, the imprint in the weld region of the low quality 0° weld (figure 2(c)) showed incipient chipping effects.

Figure 3 shows the nanohardness measured across a $\theta = 14°$ weld in the tetragonal and orthorhombic phases. The H values at the grains were similar for all measured welds, in the order of $H = 9.42 \pm 0.39$ GPa (in tetragonal phase), with a decrease of 25–30% in the orthorhombic phase. A decrease of 40% in the hardness in a 50–100 μm region around the weld is observed. A microstructure analysis (figure 3(a)) reveals that the density of Y211 particles vanishes in a *welding path* of approximately the same width. The existence of this welding path in silver welds has been explained by the higher Y content in the melt produced by diffusion and dissolving of solid bulk phases in melted Ag during heating, and by leaking of this melt out of the weld [7]. The nanohardness of the Y211 phase is almost a factor of two larger than that of the Y123 phase ($H_{\mathrm{Y211}} \approx 2.H_{\mathrm{Y123}}$), as concluded from nanoindentation measurements at very low loads [13]. Thus, the absence of Y211 particles in the welding path produces a reduction of the YBCO compound hardness measured at the weld region.

Occasionally, the oxygenation process induced microcracks in certain weld areas arising from the boundary and extending over widths of the order of 200–1000 μm (figure 4(b)). In that case, the nanohardness was reduced in a region of that size, broader than the *welding path* (figure 4(a)). Moreover, in some cases large macrocracks developed at both sides of the weld as a result of the oxygenation, as observed in figure 5(a). The nanohardness across the weld decreased then in a broad area of approx. 3 mm (figure 5(b)). Notice that the $H(x)$ reduction is asymmetric, the steeper reduction corresponding to the grain affected by the major crack. The FE-SEM imprint image in a region affected by macrocracking presents unusual fracture effects (figure 5): there seems to be a stress field dragging material inside the imprint region, but due to the small force applied, there is not enough energy

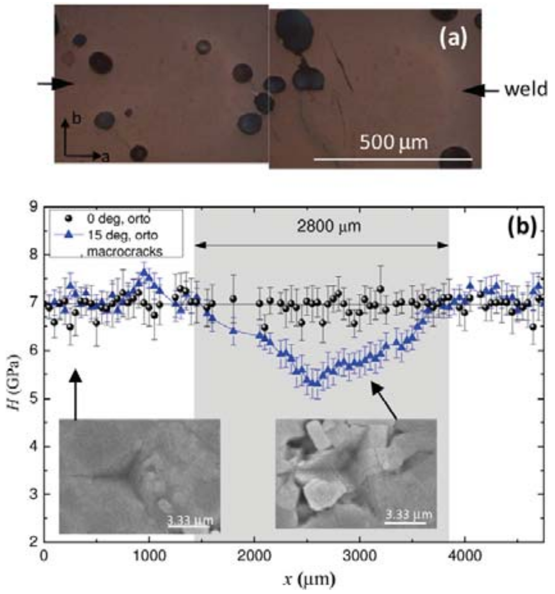

Figure 5. $\theta = 14^\circ$ (B) weld. (a) Optical micrograph of the *ab* plane of the oxygenated weld (indicated by arrows), in a region affected by macrocracks; (b) nanohardness scan $H(x)$ across the weld region affected by the microcracks (▲). FE-SEM images of the indenter imprints at the grains, and at the grain region.

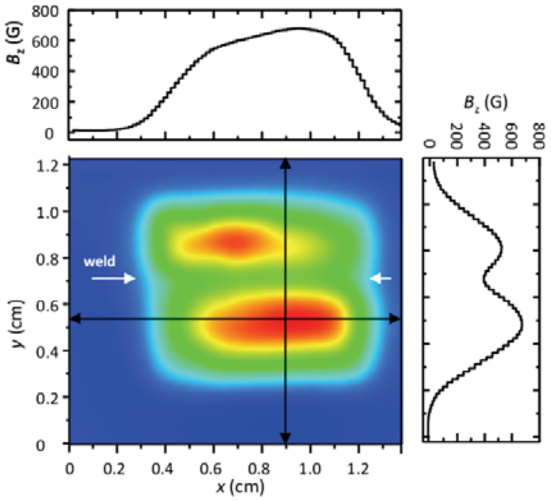

Figure 6. Magnetic field distribution $B_z(x, y)$ of a $\theta = 14^\circ$ (B) weld measured in the remanence at 77 K with a Hall scanning microscope.

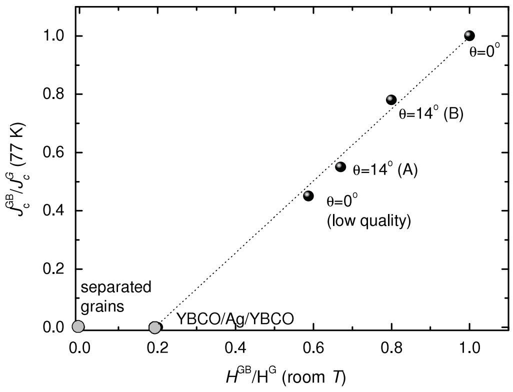

Figure 7. Correlation between the inter-to-intragranular mechanical nanohardness at room temperature (H^{GB}/H^{G}) obtained from nanoindentation scans, and critical current density (J_c^{GB}/J_c^{G}) at 77 K determined by quantitative magnetic Hall microscopy. The linear fit extrapolates to the nanohardness ratio of a YBCO–Ag–YBCO sandwich sample, $H^{GB}(\mathrm{Ag})/H^{G}(\mathrm{YBCO}) \approx 0.2$.

to produce chipping. This effect is only observed in welds affected by macrocracks and not in neat regions (figure 3).

Concerning the Young modulus, values of $E = 120 \pm 5$ GPa (in tetragonal and orthorhombic phases) were measured for all samples, without noticeable variation across the weld. It should be noted that E is basically determined by the interatomic bonds, i.e. the chemical composition of the material, and secondarily, on its inhomogeneous microstructure. The gradient of Y211 particles or presence of micro/macrocracks at the weld region did not significantly modify E, within our determination error.

Finally, we studied the relation between the electrical and mechanical performance of YBCO silver welds, the later described in terms of the ratio H^{GB}/H^{G} between the minimum nanohardness value at the weld region and that of the grains. The intergrain-to-intragranular critical current density of each weld, J_c^{GB}/J_c^{G}, was determined from the magnetic field distribution $B_z(x, y)$ at 77 K, in the remanence (see, e.g., figure 6), following the procedure already described in [23].

We have found that the nanohardness ratio at the weld H^{GB}/H^{G} linearly correlates with the inter-to-intragrain critical current density ratio J_c^{GB}/J_c^{G} at 77 K, in self-field (figure 7). The extrapolation of the linear fit tends to the expected nanohardness ratio for a YBCO/Ag/YBCO sandwich sample (with no passage of current across the weld, $J_c^{GB}/J_c^{G} = 0$), of $H^{GB}(\mathrm{Ag})/H^{G}(\mathrm{YBCO}) \approx 1.4/7.5 = 0.2$. This result has a potential practical implication: by measuring a mechanical property at room temperature, one can obtain the current performance in the superconducting state, thus avoiding the use of cryogenics tests which are expensive and cumbersome to perform in industry.

For the non-disoriented weld, the critical current density and the mechanical properties across the weld remain unchanged ($H^{GB}/H^{G} = 1$, $J_c^{GB}/J_c^{G} = 1$). This result shows that mechanically robust, high quality 0° welds for system applications can be readily achieved by the silver welding methodology.

In this work we presented nanoindentations at room temperature. This represents an initial, non-destructive way of evaluating the mechanical properties of welds, which already provides useful information about the superconducting current performance across the weld through the correlation function shown in figure 7. In the future, more work should be done to gain knowledge of the mechanical properties of welds at superconducting temperatures. Nanoindentation at cryogenic temperatures still presents many technological problems. However, tensile [28] and three-point bending [29] tests could be used to deduce the Young's modulus, fracture strength and toughness at superconducting temperatures.

4. Conclusions

Superconducting joining represents a key enabling technology for the fabrication of large YBCO blocks, allowing an enhancement in the performance of several large-scale applications. Efficient joints must prove not only high electrical connectivity but also mechanical stability. We have evaluated the mechanical and critical current density properties of melt-textured YBCO welds fabricated by silver welding.

The nanoindentation technique has been demonstrated to be a powerful technique to characterize the mechanical properties of superconducting joints at room temperature. We determined the variation of the nanohardness and Young's modulus across the ab plane of YBCO silver welds of different [001] misorientation angles. A reduction of 30% in the value of the grain nanohardness is measured as the sample is oxygenated and passes from tetragonal to the orthorhombic phase. For misoriented welds the nanohardness is reduced in a 50 μm width welding path along the boundary due to the absence of the harder Y211 phase. The oxygenation process induces in some cases micro- and macrocracks arising from the weld, which decrease the nanohardness in a broader area ranging between 100 μm and 3 mm, respectively. The decrease in nanohardness across the weld correlates with the intergranular reduction of critical current density, determined from Hall magnetic microscopy at 77 K. Interestingly, high quality zero-angle welds could be fabricated without degradation of either their mechanical or magnetic properties across the joint. This represents an important step forward towards the implementation of welds in bulk, large-scale systems.

Acknowledgments

We acknowledge the financial support from MICINN (MAT2008-01022, NAN2004-09133-CO3-01, Consolider NANOSELECT), Generalitat de Catalunya (Catalan Pla de Recerca 2009-SGR-770 and XaRMAE) and EU (HIPERCHEM and NESPA). We would like to thank W Boch from NEXANS Superconductors for providing the bulk material.

References

[1] Jee Y A, Kim C J, Sung T H and Hong G W 2000 *Supercond. Sci. Technol.* **13** 195
[2] Kim C J *et al* 2000 *Physica* C **338** 205
[3] Iliescu S *et al* 2004 *Supercond. Sci. Technol.* **17** 182
[4] Iliescu S, Granados X, Puig T and Obradors X 2006 *J. Mater. Res.* **21** 2534
[5] Iliescu S *et al* 2005 *Supercond. Sci. Technol.* **18** S168
[6] Bozzo B *et al* 2006 *J. Phys. Conf. Proc.* **43** 401
[7] Sefcikova M *et al* 2008 *Mater. Sci. Eng.* B **151** 107
[8] Bartolome E *et al* 2008 *Supercond. Sci. Technol.* **21** 12502
[9] Pharr G M 1998 *Mater. Sci. Eng.* A **253** 151
[10] Loubet J L *et al* 1984 *Trans. ASME, J. Tribol.* **106** 43
[11] Doener M F and Nix W D 1986 *J. Mater. Res.* **1** 601
[12] Goyal A *et al* 1991 *Physica* C **183** 221
[13] Roa J J *et al* 2007 *Nanotechnology* **18** 385701
[14] Lim Y Y *et al* 2001 *J. Phys. D: Appl. Phys.* **34** L70
[15] Soifer Ya M *et al* 2004 *Physica* C **402** 80
[16] Ullrich M *et al* 1999 *Physica* C **311** 86
[17] Oliver W and Pharr G 1992 *J. Mater. Res.* **7** 1564
[18] Xiong J *et al* 2007 *J. Cryst. Growth* **300** 364
[19] Giannakopoulos A E and Suresh S 1990 *Scr. Mater.* **40** 1191
[20] Granados X *et al* 2003 *IEEE Trans. Appl. Supercond.* **13** 3667
[21] Bartolomé E *et al* 2004 *Phys. Rev.* B **70** 144514
[22] Bartolomé E *et al* 2005 *Phys. Rev.* B **72** 024523
[23] Bozzo B *et al* 2005 *Supercond. Sci. Technol.* **18** 1227
[24] Granados X *et al* 2005 *IEEE Trans. Appl. Supercond.* **15** 3632
[25] Lucas B N *et al* 1996 *J. Mater. Res.* **6** 2519
[26] Giese R F *et al* 1990 *Proc. Am. Power Conf. (Chicago, Apr. 1990)* **52** 776–92
[27] Foerster C E *et al* 2008 *Braz. J. Phys.* **38** 341
[28] Okudera T *et al* 2003 *Physica* C **392** 628
[29] Sato T *et al* 2006 *Physica* C **445** 422
Katagiri K *et al* 2006 *Supercond. Sci. Technol.* **19** S545

8

NANOINDENTATION OF MULTILAYERS EMPLOYED AS COATED CONDUCTORS

I am not young enough to know everything

Oscar Wilde (1854-1900)
Irish poet and dramatist

The electrical loss properties in the grain boundary between different YBCO bulk pieces, the actual tend is to perform large length of YBCO materials as wires, called coated conductors (cc). In order to produce this, several buffer layers has been investigated during the last decade. The YBCO-cc consist to growth YBCO in the correct direction using a metallic substrate, normally Ni or hastelloy. Due to the size grain present in these layers, a buffer layer will be deposited with a physical method, such us Pulsed Electron Deposition (PED). Due to its interesting mechanical and structural properties, particularly its dielectric strength, hardness and good mismatch with YBCO, ceria is widely used as a suitable buffer layer for high-temperature-superconductor coated conductors (HTSC-cc).

This study has been published in *Thin Solid Films* in July 2009, which describes the mechanical properties (H and E) of CeO_2 layers that are undoped or doped with other elements (e.g. Zr and Ta) are a topic of specially interest in the manufacturing of superconductor buffer layers by PED. The CeO_2 with Zr is a suitable solution for industrial application. These samples and their superconducting measurements were supplied by E. Gilioli from Instituto Materiali per Elettronica e Magnetismo (IMEM-CNR). Moreover, the different results presented in this chapter are further discussed in chapter 9.

Thin Solid Films 518 (2009) 227–232

Contents lists available at ScienceDirect

Thin Solid Films

journal homepage: www.elsevier.com/locate/tsf

Study of the mechanical properties of CeO_2 layers with the nanoindentation technique

J.J. Roa [a],*, E. Gilioli [b], F. Bissoli [b], F. Pattini [b], S. Rampino [b], X.G. Capdevila [a], M. Segarra [a]

[a] Centro DIOPMA, Departamento de Ciencia de los Materiales e Ingeniería Metalúrgica, Facultad de Química, Universidad de Barcelona, C/Martí i Franquès, 1, 08028, Barcelona, Spain
[b] IMEM-CNR, Area delle Scienze 37/A, 43010 Fontanini-Parma, Italy

ARTICLE INFO

Article history:
Received 3 October 2008
Received in revised form 6 July 2009
Accepted 15 July 2009
Available online 23 July 2009

Keywords:
Thin films
CeO_2 buffer layers
Nanoindentation technique
Mechanical properties
Hardness
Young's modulus

ABSTRACT

The mechanical properties of CeO_2 layers that are undoped or doped with other elements (e.g. Zr and Ta) are a topic of special interest specially in the manufacturing of superconductor buffer layers by pulsed electron deposition. Nowadays, the trend is to produce small devices (i.e. coated conductors), and the correct mechanical characterization is critical. In this sense, nanoindentation is a powerful technique widely employed to determine the mechanical properties of small volumes. In this study, the nanoindentation technique allow us determine the hardness (H) and Young's modulus (E) by sharp indentation of different buffer layers to explore the deposition process of CeO_2 that is undoped or doped with Zr and Ta, and deposited on Ni–5%W at room temperature. This study was carried out on various samples at different ranges of applied loads (from 0.5 to 500 mN). Scanning electron microscopy images show no cracking for CeO_2 doped with Zr, as the doping agent increases the toughness fracture of the CeO_2 layer. This system, presents better mechanical stability than the other studied systems. Thus, the H for Zr–CeO_2 is around $2.75 \cdot 10^6$ Pa, and the elastic modulus calculated using the Bec et al. and Rar et al. models equals $249 \cdot 10^6$ Pa and $235 \cdot 10^6$ Pa respectively.

1. Introduction

In recent years, ceria (CeO_2) has gained increasing relevance in the thin film deposition. Ceria or ceria-based materials are widely used in many applications, such as ceramics, glass polishing, photosensitive glass, catalysts, solid oxide fuel cells, etc. (see [1] and references therein for a comprehensive review). Due to its interesting mechanical and structural properties, particularly its dielectric strength, hardness (H) and good mismatch with $YBa_2Cu_3O_{7-\delta}$ (YBCO), ceria is widely used as a suitable buffer layer for high-temperature-superconductor coated conductors (HTS-CC) deposited on hastelloy or Ni–5%W metallic tapes. When CeO_2 is doped with smaller cations, such as zirconium (Zr^{4+}) or tantalum (Ta^{5+}), a better mismatch is formed with the Ni–5%W substrate, due to the reduction in the lattice parameters (responsible for crack formation). The mismatch value with YBCO remains constant. Recently, thick and crack-free layers (up to 700 nm) based on (Zr or Ta) doped-CeO_2 have been reported [2,3]. Thus, this material is a suitable candidate for single buffer layer long length HTS-CC architecture.

The purpose of this study was to examine the mechanical properties of CeO_2 films grown on Ni–5%W metallic tapes, and to evaluate the influence of chemical doping on them.

The CeO_2 layer presents typical ceramic mechanical properties, such as high H and Young's modulus (E), and low fracture toughness (K_{IC}). However, references about the mechanical properties of this material doped with Zr and Ta are scare.

When an instrumented indentation is performed on a ceramic coating rather than on bulk materials, at a given penetration depth the response will be given by the first indentation layer, but the substrate may also influence the indentation response. Therefore, the response in the instrumented indentation test may be due to the elastic and plastic deformation of the material and to other fracture mechanisms activated during the nanoindentation test [5].

Therefore, when we determine the mechanical properties of thin film by the indentation or nanoindentation techniques, the influence of the substrate must be considered. In nanoindentation experiments, the load (P) and the total penetration or maximum displacement depth (h_t or h_{max}) are measured as a function of time during the loading and unloading processes. Depending on the specific testing system, loads as small as 1 nN can be applied, and displacements of 0.1 nm can be measured. Mechanical properties, such as H, E, K_{IC}, yield strength (σ_{ys}) and shear stress (τ), can be obtained with the load–displacement curve (P–h curves). A schematic representation of a typical data set obtained with a Berkovich indenter can be observed in Fig. 1. Five important quantities must be measured: i) the maximum applied load, P_{max}, ii) h_{max} or h_t, iii) the elastic unloading stiffness, $S = dP/dh$, defined as the slope of the upper portion of the unloading curve during the initial stages of unloading, iv) the final depth, h_f,

---

* Corresponding author.
E-mail address: joanjosep_roa@ub.edu (J.J. Roa).

0040-6090/$ – see front matter © 2009 Elsevier B.V. All rights reserved.
doi:10.1016/j.tsf.2009.07.132

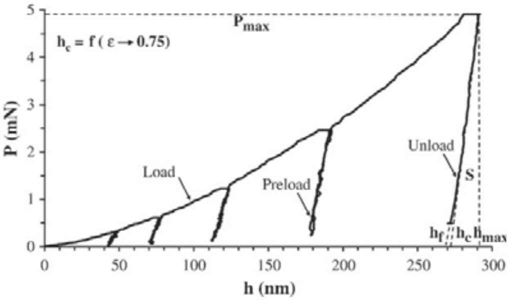

Fig. 1. Schematic illustration of indentation *P*–*h* for the CeO_2 layer showing important measured parameters when *P* was 5 mN.

and v) the contact depth, h_c. The *P*–*h* curve shows the elastic/plastic behaviour of each sample. The elastic recovery can be obtained from the difference between h_t, and h_f, [4].

The different nanoindentation imprints were made by a three-sided pyramid Berkovich diamond indenter. The displacement (also known as the penetration depth) was continuously monitored and the load–time history of indentation was recorded. Fig. 1 shows low elastic recovery and high plastic deformation. It also shows an elastic response at the beginning of the *P*–*h* curve that can be described by continuum level contact mechanics, and can be modelled by $P = C \cdot h^{3/2}$ at low penetration depths. From this point, deviation from the elastic response can be explained by the Tresca criterion (the local maximum shear stress (τ_{max}) level sustained by the indented material is of the order of the theoretical τ of material) [5].

The response of a coating system will give us a combination of the response of the different materials: the coating and the substrate. The hardness depends on the depth of penetration, as films are constrained by their substrates. A commonly used rule of thumb is to limit the indentation depth to less than 10% of the thin film thickness, which will yield the *H* of the coating without the influence of the substrate [7,9]. This is difficult in the case of thin films. It has also been found in many cases that this rule is too restrictive for soft films, but may not be restrictive enough for hard films [8]. Sometimes, it is difficult to isolate the contribution of the substrate. In this case, several models have been developed to fit the composite hardness (H_c) of the coating–substrate, as a function of a quotient between the contact depth and the thickness of thin films, h_c/t. This is widely known as the relative penetration depth or normalised penetration depth [8,9], and avoids the sample thickness effect. The procedure used to measure *H* is based on the unloading process, which is shown schematically in Fig. 2. In this procedure, it is assumed that the behaviour of the Berkovich indenter can be modelled by a conical indenter. The mechanism behind the experimentally observed discrete deformation processes under nanoscale contact is still debated in the literature [4]. The nanoindentation imprint induces two different deformation ranges: elastic and plastic. The elastic deformation disappears when the indenter unloads the sample, which leaves just the permanent or plastic deformation. This is an important parameter in the study of a thin film's mechanical properties. The measured *H* and *E* is a complex value that depends on the relative indentation depth and the mechanical properties of both the film and the substrate (H_f, H_s, E_f and E_s respectively). Above a certain critical penetration depth, the composite hardness (H_c), which includes a component of H_s, will be measured.

When the ranges of measured film hardness values are plotted against displacement for a particular film/substrate system, three different regimes become evident. A scheme is shown in Fig. 3 for a hard film on a soft substrate. The normalised depth is the h_c divided by the film thickness (t). For shallow penetration depths (I region), the response is only attributed to the film properties, as *H* presents a constant value. As the depth increases (II region), the *H* decreases gradually, and is associated with the mixed response of the coating and the substrate. At a high indentation depth (III region), the response is mainly dominated by the substrate. The nanoindentation imprint induces two different deformation ranges: elastic and plastic. The elastic deformation disappears when the indenter unloads the sample, which leaves just a permanent or plastic deformation. This is an important parameter in the study of the thin film mechanical properties.

The measurement of the Young's modulus in coatings and laminates presents the same problems as the measurement of hardness. In this case, the substrate influences the response at lower penetration depths, as the elastic field has a larger volume than that produced by plastic deformation. Therefore, to correctly characterize the response of the coating, smaller penetrations depths are required. A careful calibration of the indenter tip has to be made with a fused silica material, in order to improve the geometric and contact area values employed in the Oliver and Pharr equations [10]. The plot of the effective Young's modulus (E_{eff}) values vs. the h_c results in a similar scheme, as shown in Fig. 4. However, in this case the first region (corresponding to the thin film's mechanical properties) is smaller than the second region. This is due to the high plastic and elastic deformation ranges produced at very low penetration depths. In this case, the second region is highly dependent on the penetration depth and the plastic deformation range produces a decrease in the E_{eff} of the thin film (E_{eff} is directly proportional to a correlation between the material under study and the tip indenter material, as given by the Oliver and Pharr equation [4]).

Currently, spherical tip indenters with different radii are used instead of sharp indenters to obtain *E* at much lower penetration depths. Therefore, the use of this geometry is a powerful tool which permits the determination of other mechanical properties (e.g. shear stress, τ; mean contact pressure, p_o, and yield strength, σ_{ys}).

The *H* and E_{eff} of the film are affected by its interaction, in the plastic range, with the substrate. Fig. 5a shows a plastic deformation

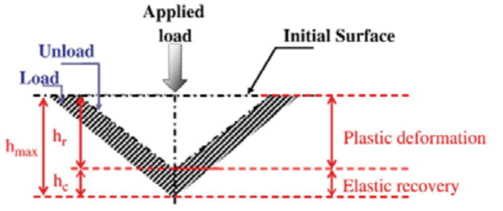

Fig. 2. Schematic illustration of the unloading process showing parameters characterizing the contact geometry.

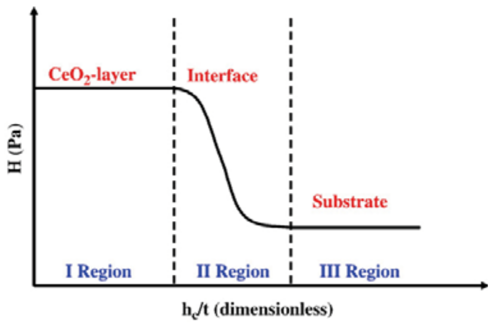

Fig. 3. Scheme of the variation in sample hardness with normalised depth for a hard film on a soft substrate.

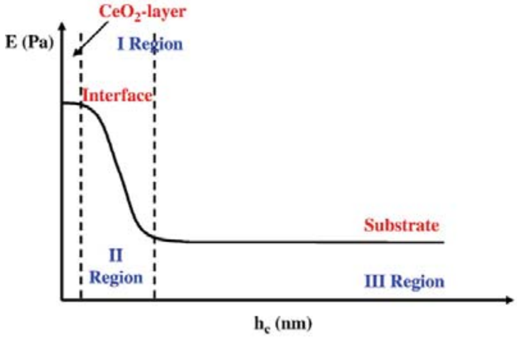

Fig. 4. Scheme of the variation in sample E_{eff} with h_c for a hard film and soft substrate.

zone in which the applied load is very low and the penetration depth is in the nanometer scale. In this case, the mechanical properties of the thin film have been obtained without substrate contribution. Higher applied loads or h_c (Fig. 5b) cause deeper plastic deformation. Therefore, we can study the mechanical properties of the interface between the thin film and substrate. The main scope of this experimental study was to determine the *H* and *E* of different CeO_2 layers (with or without a doping agent) at room temperature. The layers were grown on Ni–5%W substrates by pulsed electron deposition (*PED*).

2. Experimental details

2.1. Preparation of the samples

CeO_2 and doped-CeO_2 films were grown by *PED* [2]. The targets were prepared by mixing the oxides (CeO_2, ZrO_2, Ta_2O_5) in stoichiometric ratios. The powders, which were finely ground in a ball mill, were pressed into pellets with 200 bars (5 min at room temperature) and sintered at 1300 °C for 8 h in air. Biaxially textured Ni–5 at.%W alloy (RABiTS, from Evico GmbH) were used as substrates. They were cut into 2 cm long pieces and annealed in 10 mbar of forming gas (Ar–5%H_2) at 750 °C for 60 min. Subsequently, doped and undoped layers were deposited using a commercial *PED* source (Organic Spintronics). Depending on the different targets, the experiments were performed with a source voltage of 14–18 kV and a pulse frequency of 4–6 Hz. *PED* operates with O_2 internal pressure as the discharge ignition gas. Deposition conditions were: O_2 pressure from 10^{-4} to 10^{-3} mbar at a temperature from 650 to 750 °C. The post-growth treatment was carried out for 10 min under the same thermodynamic conditions (closed shutter). In Table 1, the main characteristics of the studied samples are summarized and compared to undoped CeO_2.

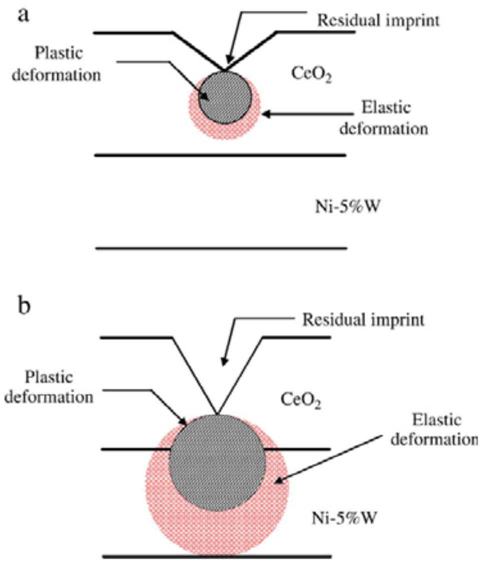

Fig. 5. Scheme of the nanoindentation imprint and the plastic deformation zone in a by-layer material when the applied loads were a) small and b) high.

2.2. Mechanical properties of thin films

The mechanical properties of the films were characterized using a nanoindentation technique, with which properties such as *H*, K_{IC} and interfacial adhesion (σ) can be obtained [4–8]. Nanoindentation tests were performed with a Nano Indenter® XP System (Agilent Technologies), equipped with Test Works 4 Professional level software. A three-sided pyramid Berkovich diamond indenter and the Oliver and Pharr approach [4] were used to obtain the *H* and *E*. More than eighty indents were performed per load over a range of loads from 0.5 to 500 mN on two different parts on the same sample in order to achieve statistical significance. Table 2 shows the test parameters for nanoindentation measurements. The indenter tip was calibrated with a fused silica standard, and the frame stiffness and thermal drift were automatically corrected. The displacement or penetration depth was continuously monitored vs. the load-time history indentation.

The indentation *P*–*h* data were analyzed to determine *E* and *H*, according to Oliver and Pharr relations [4,9,10]. Finally, the residual nanoindentation imprints were observed by FE-SEM.

3. Results and discussion

Ceramics are generally brittle and prone to generate cracks when indented. In the nanoindentation technique, a Berkovich indenter is applied on a material with a load that is high enough to nucleate cracks at the corners of the imprints. Indentation imprints performed on undoped-CeO_2, 15%Zr–CeO_2 and 10%Ta–CeO_2 with loads of 10, 20, 30 and 40 mN are shown in Fig. 6 (imprints performed at loads lower than 10 mN cannot be observed by FE-SEM). As shown in Fig. 6, the size of the residual imprint rose as the applied load increased. For the same load, the contact area varied in the different layers under study. Thus, these images provide a qualitative value for the resistance of the material when it is penetrated by a Berkovich indenter. The thin layer doped with Zr had a smaller contact area. Therefore, this material was harder than the other layers that were tested. We observed the following for the undoped sample: a network of radial cracks inside the indented region; crack propagation at the corners of the imprints; and a fracture mechanism known as the "sink-in" effect [10]. These samples were around 100 nm thick (*t*). The fracture mechanisms could have been produced by bad interface contact between the layer and the substrate, or by residual tensile stress generated during the deposition process. A brittle thin film was produced when CeO_2 was doped with Ta. The residual nanoindentation imprints presented radial cracks inside, which were vertical half penny type cracks that only occurred on the surface of

Table 1
Main characteristics of the studied samples.

Sample	Critical thickness, t_c (nm)	Out-of-plane (200) orientation degree, $C_{(200)}$ (%)	Out-of-plane (200) $\Delta\varpi$, FWHM (°)	Dielectric strength (MV/cm)	Mismatch with Ni–W substrate (%)
15%Zr–CeO_2	>500	99.7	6.1	>5.9	8.0
10%Ta–CeO_2	>550	99.6	6.6	4.1	8.1
Undoped-CeO_2	~100	~100	6.0	0.3	8.9

Table 2
Test inputs of nanoindentation.

Name	Value	Units
Allowable drift rate	0.05	nm·s^{-1}
Load rate multiple for unload rate	1	–
Applied loads	From 5 to 500	mN
Number of times to load	5	–
Peak hold time	30	s
Per cent to unload	90	%
Time to load	15	s

the specimen outside the plastic zone. These cracks produced a considerable reduction in the mechanical properties of the thin film. They were formed by hoop stress and extended downwards into the specimen, but were usually quite shallow. The residual nanoindentation imprints of the samples doped with Zr did not present radial cracks inside or at the corners. This indicates that the mechanical properties were better than those of the other samples.

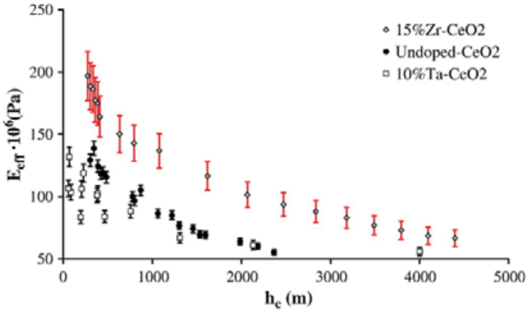

Fig. 7. Representation of E_{eff} *vs.* h_c for all films studied.

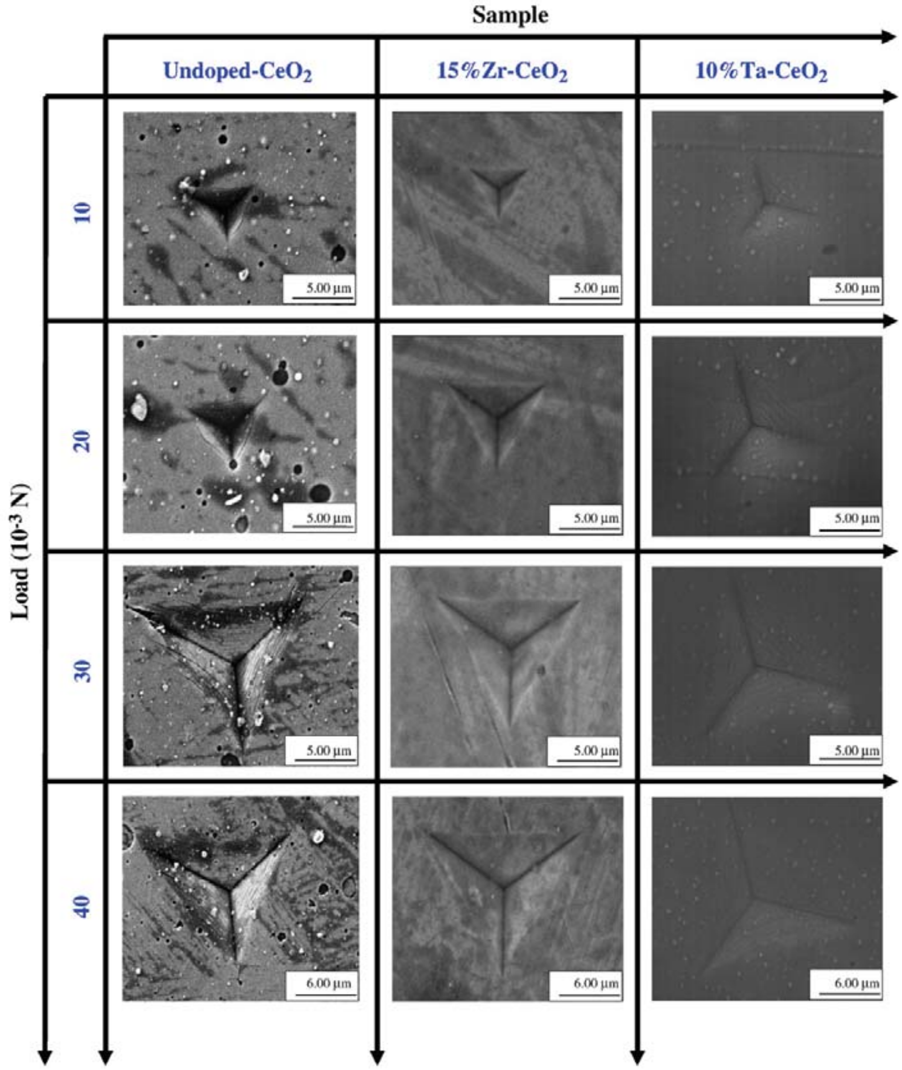

Fig. 6. Residual nanoindentation imprints at different applied loads observed by FE-SEM.

Table 3
E of the different thin film layers studied by nanoindentation (applying the Bec et al. and Rar et al. model).

Sample	$E \cdot 10^6$ (Pa)	
	Bec et al. model	Rar et al. model
Undoped-CeO_2	150	145
10%Ta–CeO_2	152	136
15%Zr–CeO_2	249	235

Fig. 7 shows the evolution of the E_{eff} values at different penetration depths. In this case, when the P was lower than 0.9 mN (corresponding to an h_c below 250 nm), a non-constant value of E_{eff} could be observed. For this reason, we applied two different models to obtain the true E_{eff} value without the interference of the Ni–5%W substrate:

i. Bec et al. model [11]:

$$\frac{1}{2 \cdot E_{eff} \cdot a} = \frac{1}{1 + \frac{2 \cdot t}{\pi \cdot a}} \cdot \left(\frac{t}{\pi \cdot a^2 \cdot E_f} + \frac{1}{2 \cdot a \cdot E_s} \right) \tag{1}$$

where a is the projected area, E_f and E_s are the Young's modulus of the film and the substrate respectively ($E_s = E_{Ni-5\%W} = 181 \cdot 10^6$ Pa [12]).

ii. Rar et al. model [13]:

$$\frac{2 \cdot (1 - \nu^2)}{E_{eff}} = \frac{(1 - \nu_s) \cdot (1 - \nu_f)}{[1 - (1 - I_1) \cdot \nu_f - I_1 \cdot \nu_s]} \cdot \left[(1 - I_0) \cdot \frac{2 \cdot (1 + \nu_s)}{E_s} + I_0 \cdot \frac{2 \cdot (1 + \nu_f)}{E_f} \right] \tag{2}$$

where I_0 and I_1 can be rewritten as follows:

$$I_0 = \frac{2}{\pi} \cdot \arctan\left(\frac{t}{a}\right) + \frac{1}{2 \cdot \pi \cdot (1 - \nu)} \cdot \left[(1 - 2 \cdot \nu) \cdot \frac{t}{a} \cdot \ln \frac{1 + \left(\frac{t}{a}\right)^2}{\left(\frac{t}{a}\right)^2} - \frac{\frac{t}{a}}{1 + \left(\frac{t}{a}\right)^2} \right] \tag{3}$$

$$I_1 = \frac{2}{\pi} \cdot \arctan\left(\frac{t}{a}\right) + \frac{t}{a \cdot \pi} \cdot \ln \frac{1 + \left(\frac{t}{a}\right)^2}{\left(\frac{t}{a}\right)^2} \tag{4}$$

where υ is the Poisson's ratio of the sample (*thin film + substrate*), and the subindex s and f denote the substrate and the film coefficients, respectively. We considered the values of 0.3 [12] for Ni–5%W and 0.33 [14] for CeO_2 and doped-CeO_2.

Table 3 shows the E calculated with the Bec et al. and Rar et al. models. From an analysis of these data, we concluded that the Bec et al. model resulted in higher values of the Young's modulus for the different layers. The film of CeO_2 doped with Zr presented a higher E for both models, whereas the film doped with Ta and the undoped film presented similar values. Sikimachi et al. [15] reported an E value of $140 \cdot 10^6$ Pa for samples of CeO_2 deposited by pulsed laser deposition (*PLD*). This value is very similar to those found in this work for films of undoped-CeO_2 and CeO_2 doped with Ta.

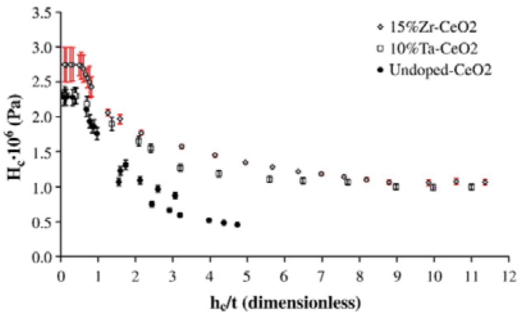

Fig. 8. Representation of H *vs.* h_c/t for all films studied.

Table 4
H of the different thin film layers studied by nanoindentation (applying the 10% rule).

Sample	$H \cdot 10^6$ (Pa)
Undoped-CeO_2	2.28 ± 0.20
10%Ta–CeO_2	2.32 ± 0.14
15%Zr–CeO_2	2.75 ± 0.25

The measured H values for the different samples have been plotted in Fig. 8. This figure exhibits a constant value for applied loads below 0.9 mN. Some authors [16] consider that for a constant H, if the 10% rule is met at different h_c/t values, the coating H can be isolated without any substrate contribution. In this figure, the three distinct stages discussed above are clearly visible: at low normalised depth, we see what appears to be the "film-only" H; as the h_c/t increases, H decreases; and the substrate H is reached at higher h_c/t. For undoped-CeO_2 100 nm thick film the transition between regimes I to III is more abrupt. For this sample, the H decreases very quickly due to different fracture mechanisms such as radial cracks, propagation of cracks at the corners of the imprints and sink-in effects. These fracture mechanisms produce an overestimated contact area value. Therefore, in order to obtain the correct H value, the contact area was directly obtained from the FE-SEM images. We can estimate the film H directly from this figure with the 10% rule, as previously defined. Although this rule is rather approximate, it can be applied in this study as the CeO_2 films, both doped and undoped, present constant values of hardness at low loads. As can be seen, H can be strongly affected by the presence of the different dopants. The H of the thin film rises when the amount of dopant increases. In order to corroborate that the coating H value presented in Table 4 was not influenced by the Ni–5%W substrate, the plastic zone radius (see Fig. 5a) at 0.9 mN of applied load was calculated with Lawn's equation [17]. This assumes that the size of the hemispherical plastic zone is related to the size of the indentation, as follows:

$$b_i = h_c \cdot \left(\frac{E_i}{H_i} \right)^{1/2} \cdot \cot^{1/3} \xi \tag{5}$$

where b_i is the plastic zone radius, E_i and H_i are the Young's modulus and hardness values for each coating, respectively; and ξ is the indenter semi-angle (for a Berkovich tip indenter this value is equal to 65.27° [9]). Table 5 shows the plastic zone radius for each sample, as obtained by Eq. (5). The calculated values are lower than the thickness of the different layers. The values presented in this table correspond to an applied load of 0.9 mN. Thus, it can be verified that the plastic zone radius is less than, but of the same order as, the thickness of the thin film. Consequently, if we use lower loads, the plastic zone radius will decrease and we can ensure that the value obtained with the 10% rule is not affected by the substrate. Thus we conclude that the H values for the coatings presented in Table 4 are not influenced by the Ni–5% substrate.

Table 5
Plastic zone radius for each studied sample.

Sample	t (nm)	b_i (nm)
Undoped-CeO_2	~100	92
10%Ta–CeO_2	>550	512
15%Zr–CeO_2	>500	490

4. Conclusions

Instrumented indentation is a powerful technique for extracting mechanical properties at nanometric scale, once correctly calibrated with fused silica. In tests of ceramic materials, special care has to be taken in data acquisition and analysis, due to the high hardness and stiffness of these kinds of materials. When ceramic coating is indented, the influence of the underling material (substrate) has to be taken into account.

In this study, we performed sharp nanoindenter tests on doped and undoped CeO_2 layers, in order to obtain their *H* and *E* values without the influence of the substrate. Two different models were applied to determine the *E* of the different thin films. From an analysis of these data, we can conclude that the Bec et al. model overestimates the *E* of the tested layers, while the Rar et al. model is more conservative.

For relatively hard coating–substrate systems, it is generally accepted that nanoindentation with a maximum depth of less than 10% of the coating thickness will yield the *H* of the coating without any influence of the substrate. In this work, the *H* of each sample was obtained using the nanoindentation test at *P* lower than 0.9 mN and the 10% rule was applied. Moreover, the plastic deformation zone was calculated by the Lawn equation and all samples exhibited a plastic deformation radius that was lower than the thickness of the different coatings. This indicates the absence of substrate contribution to the coating hardness values. Coating hardness was highly influenced by the doping agent. Thus, the CeO_2 layer doped with Zr presented a higher hardness than the others.

Zr-doped CeO_2 showed better mechanical properties among the studied samples, with *E* that were higher than the undoped or Ta-doped samples. Furthermore, this layer did not present any cracks or fractures within the indented region. Thus, this material is an ideal candidate as a reliable and efficient buffer layer in HTSC-CC or, in general, in thin film applications where good mechanical properties like H, K_{IC} and E are required. The results obtained on different CeO_2-based film grown by *PED* are similar to the ones reported for CeO_2 layers deposited by *PLD* [15].

Acknowledgments

J. J. Roa acknowledges financial support from the “Comissionat per la Universitat i la Investigació del Departament d'innovació Universitari i d'Empresa de la Generalitat de Catalunya i el Fons Social Europeu”.

The authors would like to thank the Serveis Cientificotècnics for SEM data, and Emilio Jiménez (Centre d'Integritat Estructural i Fiabilitat dels Materials, UPC) for experimental data. We would also like to thank the Language Service at the *Universitat de Barcelona* for linguistic and stylistic advice.

References

[1] V.V. Kharton, F.M. Figueiredo, L. Navarro, E.N. Naumovich, A.V. Kovalevsky, A.A. Yaremchenko, A.P. Viskup, A. Carneiro, F.M.B. Marques, J.R. Frade, J. Mater. Sci. 36 (2001) 1105.
[2] E. Gilioli, M. Baldini, M. Bindi, F. Bissoli, F. Pattini, S. Rampino, S. Ginocchio, A. Gauzzi, M. Rocca, S. Zannella, Physica C 463–465 (2007) 609.
[3] A. Gauzzi, M. Baldini, M. Bindi, F. Bissoli, E. Gilioli, S. Ginocchio, F. Pattini, S. Rampino, S. Zannella, IEEE Trans. Appl. Supercond. 17 (2007) 3413.
[4] J.J. Roa, X.G. Capdevila, M. Martínez, F. Espiell, M. Segarra, Nanotechnol. 18 (2007) 385701/1.
[5] E. Jiménez-Piqué, Y. Gaillard, M. Anglada, Key Eng. Mater. 333 (2007) 107.
[6] A.M. Korsunsky, M.R. McGurk, S.J. Bull, T.F. Page, Surf. Coat. Technol. 99 (1998) 171.
[7] P.J. Burnett, T.F. Page, J. Mater. Sci. 19 (1984) 3524.
[8] A.C. Fischer-Cripps, Vacuum 58 (2000) 569.
[9] A.C. Fischer-Cripps, Surf. Coat. Technol. 200 (2006) 4153.
[10] W.C. Oliver, G.M. Pharr, J. Mater. Res. 7 (1992) 1564.
[11] S. Bec, A. Tonck, J.L. Loubet, Philos. Mag. 86 (2006) 5347.
[12] I.S. Choi, A.J. Detor, R. Schwaiger, M. Dao, C.A. Schich, S. Suresh, J. Mech. Phys. Solids. 56 (2008) 172.
[13] R. Andrei, H. Song, G.M. Pharr, Mater. Res. Soc. Symp. Proc. 695 (2002) 431.
[14] A. Selçuk, A. Atkinson, J. Eur. Ceram. Soc. 17 (1997) 1523.
[15] K. Shikimachi, N. Kashima, S. Nagaya, T. Muroga, S. Miyata, T. Watanabe, Y. Yamada, T. Izumi, Y. Shiohara, IEEE Trans. Appl. Supercod. 15 (2005) 3548.
[16] D. Beegan, M.T. Laugier, Surf. Coat. Technol. 1999 (2005) 32.
[17] B.R. Lawn, A.G. Evans, D.B. Marshall, J. Am. Ceram. Soc. 63 (1980) 574.

9

DISCUSSION

Who knows most believes less

Proverb

In the following section, the mechanical properties at nanometric scale (*i.e.,* H, E, p_m, σ_{ys}, $\sigma-\varepsilon$, *and* τ_{max}) are going to be discussed for the different YBCO conformations. First, we study several samples obtained by Bridgman and TSMG techniques to determine their main mechanical parameters. On the other hand, hardness values across the weld in bulks fabricated by the silver welding technique, are also measured, trying to find a the correlation between the mechanical and the superconducting properties. Moreover, the H and E for different buffer layers employed in YBCO-cc are also discussed, to find the best mechanical stability. At the end of this section, the plastic behaviour will be discussed to better understand the different fracture mechanisms activated during the indentation process.

Table 9.1 and *9.2* exhibit the different mechanical properties obtained in this Thesis using the Nanoindentation technique for YBCO samples textured by Bridgman and TSMG, and YBCO tapes with different buffer layers.

Table 9.1. Summary of the different mechanical properties obtained in this Thesis at nanometric scale for YBCO samples textured by Bridgman and TSMG technique.

Mechanical properties	Phase	Tip employed	Bridgman	TSMG
H (GPa)	*Y-123@ 5mN*	Berkovich	10.4 ± 0.5	11.0 ± 0.5
	Y-211@ 5mN		19.1 ± 0.8	15.2 ± 0.9
	YBCO@ 5mN		14.8 ± 0.5	15.0 ± 1.0
	YBCO@100mN		8.9 ± 0.2	7.9 ± 0.8
E (GPa)	*Y-123@ 5mN*		197 ± 7	176 ± 15
	Y-211@ 5mN		194 ± 9	224 ± 18
	YBCO@ 5mN		201 ± 7	208 ± 21
	YBCO@100mN		173 ± 3	129 ± 6
p_m **(GPa)**	*YBCO*	Spherical	3.5 ± 0.2	3.9 ± 0.2
σ_{ys} **(GPa)**			3.2 ± 0.2	3.6 ± 0.1
σ_{max} **(GPa)**			0.7 ± 0.1	0.8 ± 0.1
τ_{max} **(GPa)**			1.6 ± 0.1	1.8 ± 0.1

Table 9.2. Summary of the mechanical properties at nanometric scale for YBCO coated conductors with different buffer layers.

Sample	Tip employed	$H_{10\%rule}$ (GPa)	E_{Bec} (GPa)	E_{Rar} (GPa)
Undoped-CeO$_2$	Berkovich	2.28 ± 0.2	150	145
10%Ta-CeO$_2$		2.32 ± 0.1	152	136
15%Zr-CeO$_2$		2.75 ± 0.3	249	235

9.1. Elastic contact

The elasto-plastic transition for Bridgman and TSMG samples using a spherical tip indenter, takes place over 40 mN of applied load (around 150 nm of penetration depth). The load curve follows an elastic behaviour: $P = Ch_e^{3/2}$. After this point, the loading curve can be adjusted with an elasto-plastic curve: $P = Ch_p^2$. The intersection between these two trends is the yield stress of the material, which can present a pop-in[i] event in the *P-h* curve[1], which is often associated to the first stage of plastic deformation.

In order to obtain the *σ–ε* curves for Bridgman and TSMG samples, a correct analysis of the contact point should be performed. The stiffness vs. contact point (*S-a*) figures (*see Inset 1 Fig.5* page 110 and *Fig. 5.1 page 114* for Bridgman and TSMG samples, respectively), exhibit a bad contact point between the spherical indenter and the sample surface, thus giving an erroneous yield stress value. This phenomenon is attributed to

---

[i] ***Pop-in*** is an abrupt increase in penetration depth on a nanoindentation curve (force controlled mode)

the superficial roughness present in the several samples; in order to reduce this effect, an accurate polishing process should be carried out to decrease the roughness.

The superficial roughness and the different density of defects modify the stress (*a/R*) generated by the spherical tip on the samples. As can be seen in *Table 9.1*, the intrinsic properties obtained using the σ–ε plots and *equations 5.2*, *5.3* and *5.4*, present similar values for both samples. The TSMG samples, present a higher density of macro/microcracks and pore density along the *c*-axis than Bridgman samples. Then, during the first contact between the indenter and the sample, the energy applied by the tip onto the surface is employed to close the different cracks produced during the oxygenation process. For this reason, TSMG samples present a higher contact radius value than Bridgman samples. Using the Sneddon[2] equations (*eq. 5.1*) we observed that these samples present a higher *S* value.

By TEM, several defects (such as dislocations movement or twining) present inside of the sample have been observed, whose are the responsible of the elasto-to-plastic transition, see *Fig. 9.1*.

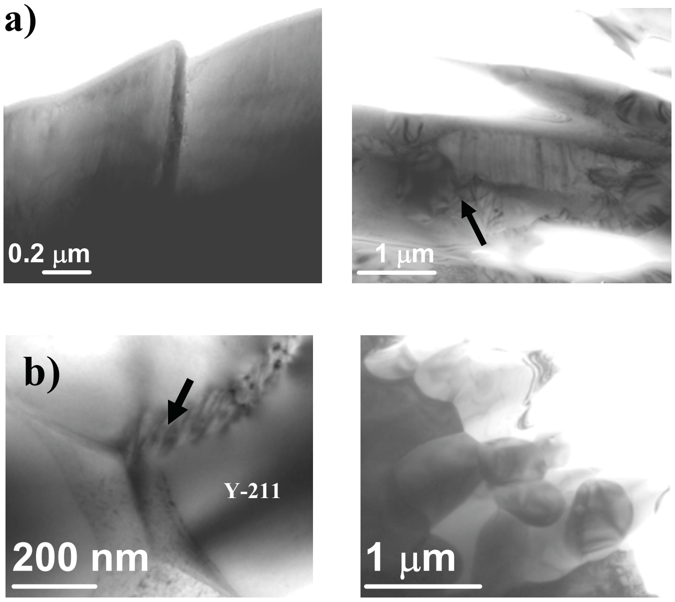

Fig. 9.1. TEM images showing the different defects presents in the sample after the texture and oxygenation processes. a) Bridgman, and b) TSMG samples.

As can be seen in *Fig. 9.1*, the typical defects present in both texture processes are the dislocations (see arrows present in this figure), surrounding the Y-211 particles. For Bridgman samples several twins and dislocations have been observed in the basal plane. However, for samples textured by TSMG only different dislocations can be observed surrounding the Y-211 particles. The different dislocations for both samples are activated due to the different stresses present inside of the Y-211 particles, as can be obtained in *Fig. 9.2*.

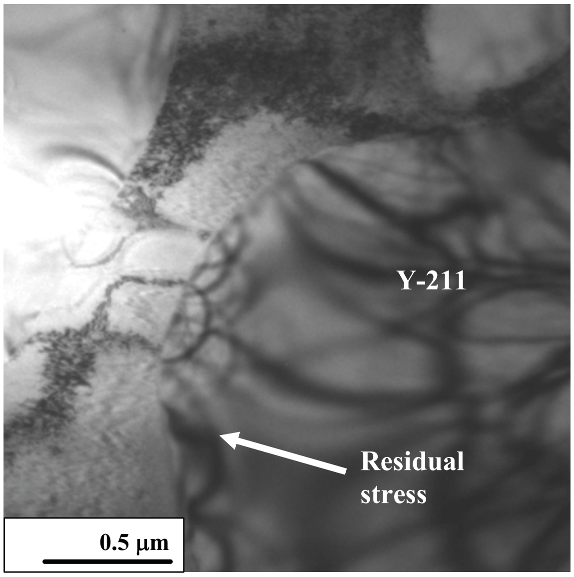

Fig. 9.2. Residual stress inside of the Y-211 particles for YBCO samples textured by Bridgman technique and observed by TEM.

These results are in correct agreement with previous values reported by Rabier *et al.*[3,4], who studied the microscopic mechanisms concerned in plastic deformation of YBCO ceramic, as well as the effects of lattice defects on the physical properties of these materials. Also, Tall *et al.*[5] reported the twins generation under uniaxial pressure originated during the indentation process using a Vickers tip indenter. We have performed several nanoindentations employing Berkovich and spherical tip indenters to induce different stress fields on the materials surface and nucleate different defects. The main goal to obtain a surface with a roughness around several Å is to find an adecuate polishing process. This effect, has been solved using an acurate mechanical polishing, and employing a coloidal silica suspension in isopropanol during the final step.

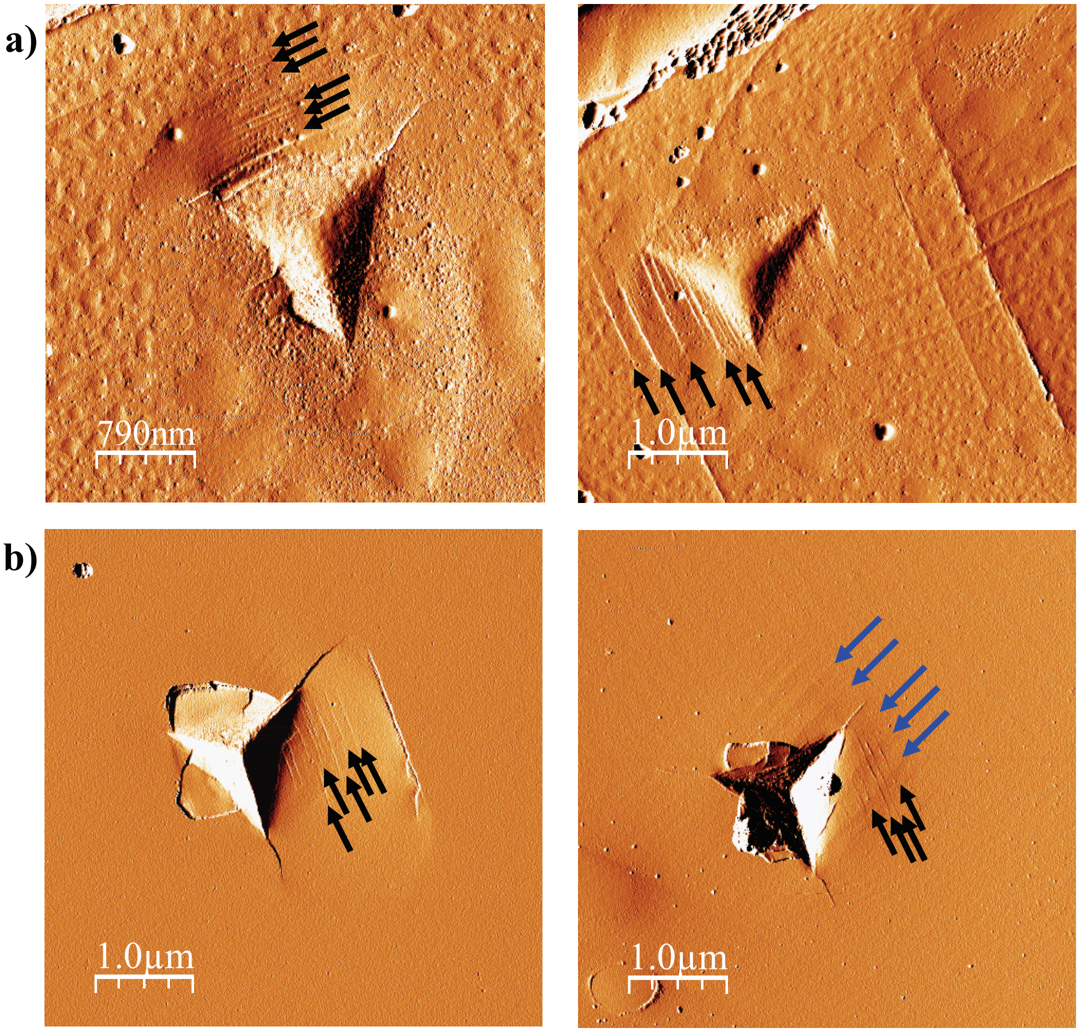

Fig. 9.3. AFM error images of the different plastic deformation mechanisms activated by Berkovich indentation process. a) Bridgman and, b) TSMG samples (black arrows show the different steps corresponding to slip lines and the blue arrows exhibit the different twins).

In *Fig. 9.3*, different plastic deformation mechanism can be observed. In the case of the polycrystalline Bridgman samples (*Fig. 9.3a*), the different steps present in the vicinity of the imprint can be attributed to different slip lines. Moreover, the different plastic mechanisms are strongly affected by the crystallographic orientation; for this reason, we observe different directions of slips. However, *Fig. 9.3b* exhibits that the plastic deformation mechanisms for single crystals of YBCO, which are the different slip lines and also the chipping fracture mechanisms follow the same direction. This phenomenon could be attributed to the fact that tests were performed on the same crystallographic plane. Also, this type of materials shows another plastic mechanism called twining process. The movement of the slip lines takes place parallel to the basal plane (*ab*-

plane). So, the polishing process must be performed at another angle, to observe the slip lines on the surface. In *Fig. 9.3b*, the angle between slip lines and twins are related to this polishing deviation, in this case 15º.

After this study, we believe that the elastic to plastic transition is produced by an activation of different dislocations and twins present in the *ab*-plane and *c*-axis. But more tests should be performed in order to better understanding this transition and supply more conclusive information.

9.2. Elasto-Plastic contact

When the field stress applied is higher than the yield stress, we are working in a plastic range, where a plastic deformation remains after the unloading process although an elastic recovery also takes place. The most important properties in this range of work are the hardness and also the Young's modulus value, using the Oliver and Pharr method[6]. In this case, we will discuss the several properties obtained by Berkovich indenter.

9.2.1. Hardness value

*Table 9.*1, exhibits the *H* values at different applied loads. In general terms, *H* does not remain constant at different applied loads due to a physical phenomenon known as Indentation Size Effect (ISE). Normally, *H* presents a maximum value for low loads. However, when the applied load increases this property is widely modified by the superficial defects, such as roughness, macrocracks, etc. When this phenomenon takes place, the contact area could be over- or underestimated giving us a false *H* value. The different *H* values presented in *Table 9.1,* have been corrected and the true contact area has been obtained directly through the FE-SEM image.

Our material of study presents a heterogeneous microstructure with Y-123 matrix and a minor phase (Y-211 or inclusions). One of the purposes of this experimental work is to obtain the *H* value for each phase. In order to do that, several applied loads have been tested. The minimum force applied to isolate the different phase's contribution was 10 mN for each sample. With this applied load, the residual contact area is lower than the size of the inclusions. Then, the mechanical property can be obtained. We can observe that the H value for Y-211 is around twice times that for Y-123. If the different residual imprints have been performed near the grain boundary, the plastic deformation mechanism under the imprint could be affected by the Y-123 matrix, and the H value would be modified, thus giving us an average of the studied property.

Samples obtained using the welding technique with a Θ=0º misorientation present the same H that the value for TSMG reported in *Table 9.1* at 100 mN. No degradation of the H value across the welding zone is observed in these samples. However, for samples with a higher difference between grains (i.e. Θ=14º), the hardness value decreases considerably in the welding zone. In all cases, the reduction of this mechanical property has been attributed to different microstructural defects, such as microcracks generated during the oxygenation process. Moreover, an unexpected correlation between the superconducting properties obtained at 77 K and the mechanical properties measured at room temperature has been obtained. This relation can be written as:

$$\frac{J_c^{GB}}{J_C^{G}} = 0.2 + m \cdot \frac{H^{GB}}{H^{G}} \qquad \textbf{eq. 9.1}$$

where m is the slope of the experimental points presented in *Figure 7* of *chapter 7* (*page 135*). This expression allows to obtain a qualitative value of the superconducting properties without the need to perform the magnetic measurements.

When the applied load is 100 mN, overall nanohardness is very similar for both samples and both techniques (*for Bridgman technique 8.9 GPa, and TSMG technique 7.9 GPa*), but is lower than the nanohardness of the Y-123 phase. These results are in agreement with a previous work reported by Lim and Chaudhri[7], which studied the H of YBCO single crystals by Nanoindentation technique, and the H value obtained was 7.81 GPa. This value is in agreement with the result obtained for samples textured by TSMG technique. On the other hand, the H value obtained for samples textured by Bridgman technique is in agreement with a previous work reported by Soifer *et al.*[8] and Cook *et al.*[9]. When the applied load is higher than 10 mN we are working within the microindentation range, and we can observe radial cracks at the corners of imprints, thus causing the reduction of the hardness value ($H_{100mN} < H_{30mN}$). Verdyan *et al.*[10] reported nanohardness for orthorhombic YBCO thin films being around 8.5 GPa, when the applied load varies between 0.1 and 0.9 mN, which are similar values to those found in this Thesis for the orthorhombic phases. If we compare our data for H with data reported of YBCO (*see table 1.2, page 58*), we can conclude that the broad distribution of hardness observed can be attributed both to the different measuring techniques and to the different quality of the studied YBCO samples (*i.e. grain structure, porosity, texturing process, etc*).

9.2.2. Young's modulus value

The Young's modulus values presented in *Table 9.1* for both techniques present a dependency with the applied load. This phenomenon is far from what expected, as E value is an intrinsic property of the studied material and only depends on its composition. This effect has been observed until the first 300 nm of penetration depth which corresponds to an applied load around 30 mN. In this case, E measurements are strongly affected by the superficial defects. Values reported in *Table 9.1* at 100 mN are in correct agreement with values reported in the literature as these superficial defects do not strongly modify this parameter. As stated in the Introduction (*Chapter 1, equation 1.17*), the effective Young's modulus is a function of the stiffness, contact area and the geometry factor of the indenter. Then, the overestimation of the E value at applied loads equals or less than 100 mN is produced by a bad estimation of one of these factors. In *section 9.2.1*, we discussed the effect of the $A(h_c)$ value, which is strongly affected by the presence of macro/microcracks, porosity, roughness and a wide variety of defects. As we have seen in *eq. 1.17*, the Effective Young's modulus is function of the square root of the $A(h_c)$. The E value is obtained using the unloading slope of the P-h curve, also called S. If the contact point between the sample and the indenter is not well estimated, the S value will be underestimated, yielding to a lower E_{eff}. Finally, the β factor could not modify this value because it remains equals to 1.034 for each test performed in this type of materials[6]. After considering all the different parameters that can modify the E_{eff} value, we believe that the main contribution to change this parameter is the contact area, and then the scattered values presented in the *chapter 4* are attributed to this effect. The Bridgman samples present higher Young's modulus value than TSMG, as this last presents a higher density of macro- and microcracks, which can produce a relaxation of the elastic deformation range. Finally, the different values are influenciated by the other factors but with a less contribution.

Fig. 9.4, exhibits the *E* evolution using CSM equipment at 2000 nm of penetration depth. In this case, in *Fig. 9.4a* the *E* reaches a constant value of 120 GPa at penetration depths around 500 nm. However, the *E* value for TSMG samples increases softer and do not remain constant, see *Fig. 9.4b*. For the TSMG samples, the value are widely modified by the presence of macro/microcracks activated during the oxygenation process (see *Fig. 9.5*).

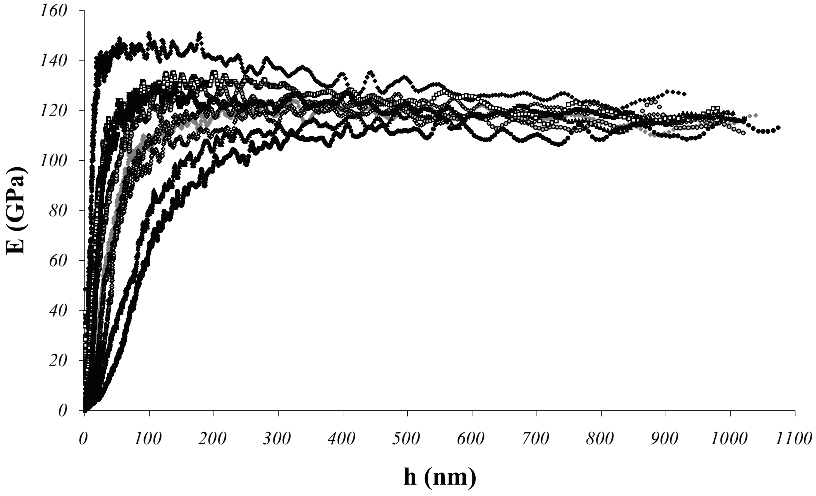

a)

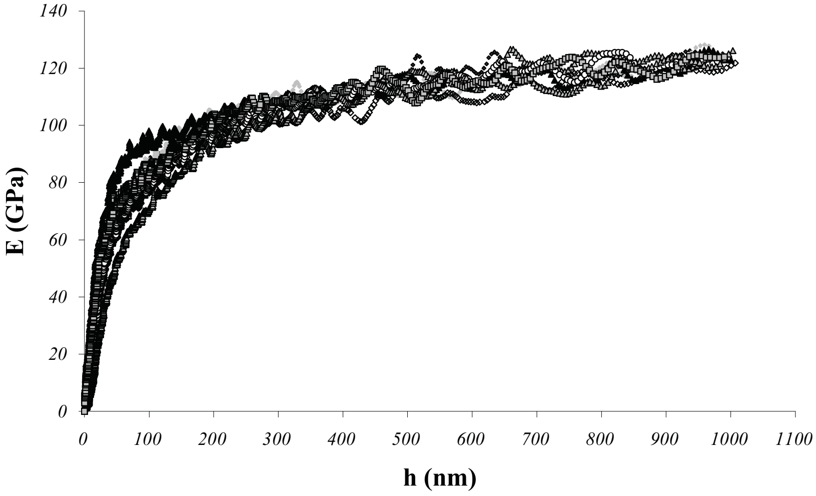

b)

Fig. 9.4. E-h tendency for orthorhombic YBCO samples conformed by different texture techniques, a) Bridgman, and b)TSMG.

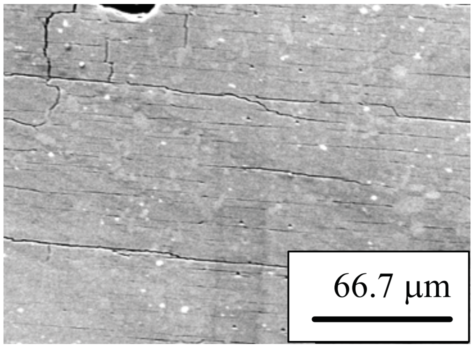

Fig. 9.5. FE-SEM image of the *ab*-plane of TSMG samples, which present a high microcracks density performed during the oxygenation process due to the tetragonal to orthorhombic transition.

Several measurements of Young's modulus for Y-123 have resulted in values scattered within the range *E = 40-200 GPa*, caused by residual porosity and bad contact between the grains[11]. Sakai *et al.*[12] reported a value of 370 GPa for 5 mm^3 cubic specimens cut from a single-crystal Y-123 prepared by TSMG using a single domain of Sm-123 as a seed. The authors attribute the difference of *E* to the 40% excess of Y-211 phase present in the material. Obtained results of *E* are in agreement with Johansen *et al.*[11] and Alford *et al.*[13] when the applied loads were 30 and 100mN. Also, the different values present in *Table 9.1* are in agreement with the values reported by Joo *et al.*[14], who used pulsed echo technique for the YBCO samples with a different silver addition (0, 5, 10, and 15% vol. respectively). If we compare our data for *E* values with those reported in the literature (*see table 1.1, page 58*), we can conclude that the broad distribution of *E* observed can be attributed both to the different measuring techniques and to the different quality of the studied YBCO samples (grain structure, texture, and others).

9.3. Fracture mechanisms

Advanced ceramic materials (such as YBCO) have interesting design properties. They have excellent mechanical properties under compression, but are terrible when tensile loads are applied to them, and are typically very brittle. The difference between the tensile and compressive performance of a ceramic is caused by the presence of preexiting cracks in the material. When the YBCO was placed under tension, these cracks act as stress amplifiers, which in turn lead to create a single dominant crack starting at the tip of a flaw. The dominant crack will quickly cut through the material, ending its life prematurely. If we use YBCO in compression, the cracks will not behave like stress amplifiers. As a consequence, the ceramic can handle compressive stresses very well.

In this section, we have analysed the different brittle effects appearing in as grown Bridgman, TSMG and melt-textured welded samples (at the weld region and at the adjacent grains).

All imprints present the sink-in effect, typically found in brittle materials[6]. Sink-in is a displacement of the surface at the contact perimeter. This effect can lead to an overestimation of the contact area, and therefore an underestimation of the hardness value is obtained by nanoindentation.

As can be seen in the residual imprints performed at 10 mN for Bridgman and TSMG samples, showed in *chapter 4*, Y-123 does not present any fracture mechanism. However, Y-211 inclusions, present a typical fracture of ceramic materials called chipping. This phenomenon occurs as a result of Palmqvist cracks nucleating at the lateral sides of the imprint, beneath the surface. Chipping phenomenon takes place due to the tensile field created around the imprint during the indentation process, and shows up as an elevation, at the sides of the imprint. Therefore, in the interphase crack propagation only appears in one corner of the imprint, and also an abnormal geometry is present, as can be seen in the paper published in Nanotechnology; the deformation is not homogenous, due to the different hardness of the implied phases. First of all, the indenter goes into the Y-211 particle and after that, the Y-123 can be indented. The FIB images presented in the same chapter, exhibit that the Y-211 particles contribute to the plastic deformation of the matrix. The stress field supplied by the indenter contributes to produce the fracture of the YBCO material, and also to close the oxygenation cracks, as can be seen in *Fig. 4.1* (*page 95*).

When the applied load is higher than 10 mN, several fracture mechanisms take place, due to the field stresses induced during the indentation process. As can be seen in *chapter 4*, YBCO samples obtained by Bridgman and TSMG present similar fracture mechanisms. We can observe radial cracks at the corners and microcracks inside of the imprints, sink-in and also chipping. This kind of damage is found in brittle materials containing inclusions harder than the matrix, in this case Y-211 particles. Upon indentation, microcracks tend to be generated at inclusions, and are recognised as microflaws within the imprint when observed from the surface. Another common feature in all imprints was the presence of radial cracks starting from the corners. This fracture mechanism, typical of ceramic materials, is nucleated as a consequence of the tensile strength originated during the indentation process. In all of these cases, a dissipation of energy takes place, which is supplied by the indenter to produce the deformation, thus creating an overestimation of the contact area. Then, the *H* value for heterogeneous materials could be underestimated. For this reason, all the imprints performed in this Thesis have been recalculated using FE-SEM micrographs to obtain the true hardness value.

All the residual imprints performed on the welded samples show the presence of microcracks inside the imprints, generated by the different pre-loading during the indentation process. For the welded TSMG sample, imprints showed only the three above described phenomena (*Fig. 9.6a*). Notably, for the high quality θ=0º weld, residual imprints showed the same aspect as those in the TSMG sample, both at the grain (*Fig. 9.6b*) and at the boundary regions (*Fig. 9.6c*). For comparison, we analysed as well the behaviour of a θ=14º weld (*Fig. 9.6d*) at the boundary region. In this case, in addition to the phenomena previously described, two other effects were observed. First, a high density of micrometric pores around the residual imprint can be noted. The size of these pores was much larger than the diameter of pores (100-200 μm) originally present in the as-grown melt-textured tiles. Presumably, this micrometric porosity is created during the recrystalization process of the interface region between tiles. The nanoindentation process would lead the pores exposed to the surface, an effect that has been previously described[15]. Second, *chipping*, i.e. partial removal of surface material around the imprint, is observed.

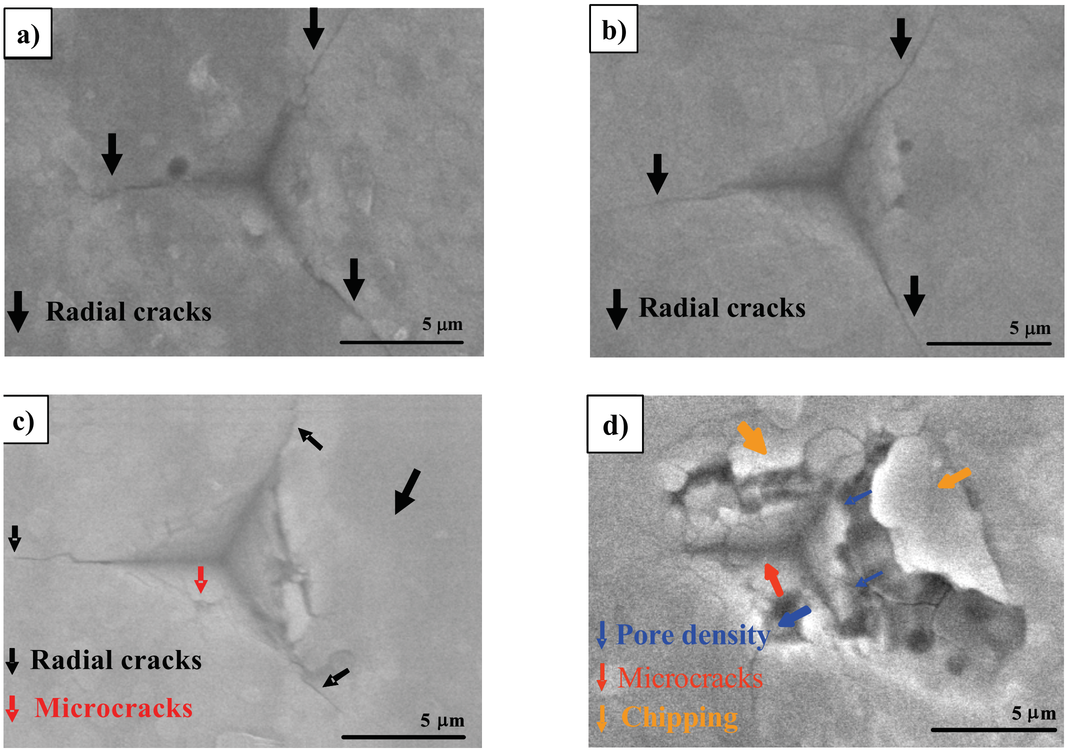

Fig. 9.6. Nanoindentation imprints in welded samples observed by FE-SEM showing different fracture effects. a) Reference bulk sample, b) high-quality θ=0° weld, at grain region, and c) at boundary region, d) θ=14° weld at boundary region.

9.4. Coated conductors

One of the most important requirements for this type of structured materials is that they must not present any delamination fracture between layers, as this phenomenon could produce a reduction of the mechanical stability. For this reason, in this Thesis we have studied the mechanical properties (*H* and *E*) of several CeO_2/Ni-5%W with and without doping agents (Ta and Zr) in order to better understand they behaviour under uniaxial pressure. The mechanical properties have been obtained in an easy way, using the 10% rule for the *H* value, and the Bec and Rar models for *E*.

In the case of hardness, we can extract a substrate-independent value when the applied load was lower to 0.9 mN. In this case, the radius of plastic deformation field is lower than the thickness of the layer. In order to verify this, the plastic radius has been obtained using the Lawn's equation[16], for each sample, and in all cases present a radii lower than the thickness of the layer, see *table 5 chapter 8* (*page 143*). In this case, the better studied layer was CeO_2 doped with Zr, which presents the highest *H* value

($H_{CeO2\text{-}Z\ r}$= 2.75 ± 0.25 GPa). As can be seen in *Table 9.2,* all the different samples present a similar value.

In relation to the E value, we cannot extract it directly using the 10% as the radius of the elastic deformation range is much greater than that of the plastic range. For this reason, Bec *et al.*[17] and Rar *et al.*[18] models have been employed, in order to isolate the substrate contribution. The sample presenting a higher E value is the CeO_2 doped with Zr (E_{Bec} = 249 GPa and E_{Rar} = 235 GPa). Sikimachi *et al.*[19] reported an E value of 140 GPa for samples of CeO_2 deposited by pulsed laser deposition (PLD). This value is very similar to those found in this work for films of undoped-CeO_2 and CeO_2 doped with Ta obtained by PED.

If we compare the different models employed to extract the E value, we can observe that Bec model is more permissive than Rar model. The main problem with these models is the contact point between the indenter and the sample. When the applied load is too low (lower than 0.9 mN), we can make a significant error when we correct this parameter, yielding to E values far from those reported in the literature. In other words, we should work under a methodological way in order to reduce this error. Sometimes, it is a bit difficult to be reduced because we are working in the range of the equipment's sensitivity, and in this case, we produce the same error for each sample.

The Bec *et al.*[17] model is easier than Rar *et al.*[18] as this last depends on the Poisson's ratio of the substrate, and sometimes this value is unknown. If the substrate layer is ceramic, we can consider that this parameter is equal to 0.3, but it could not be correct and thus yielding to a considerable error. In the case that this value is unknown, I recommend to employ the Bec model, as it is very robust and more easy.

One of the important requirements to use these type of buffer layers is that the coating (in this case CeO_2-undoped and doped) presents similar H and E values than YBCO. In this case, no delamination will occur after YBCO deposition. In this study, we observed that H values for each sample are around 6 GPa lower than for YBCO bulk samples. However, E value for the CeO_2 layer doped with Zr is higher than E for YBCO samples. The different samples studied present good out-of-plane orientation degrees, dielectric strength and mismatch with Ni-W substrate to be employed as a coated conductors. However, we believe that they can experience delamination. As a future work, we consider the study of other bi- and trylayers systems (i.e. YBCO/LAO, YBCO/LZO/Ni-5%W and YBCO/CeO_2/YSZ) and perform a trench with FIB under the imprint in order to observe the possible fracture mechanisms produced during the indentation process.

Finally, we would like to discuss the different fracture mechanisms observed by FE-SEM for each studied sample, see *figure 6 chapter 8* (*page 142*). These images provide a quality value for the strength of the material when it is penetrated by a Berkovich indenter. The thin layer doped with Zr presented a smaller contact area. Therefore, this material is harder than the other ones. For the undoped sample, we observed a microcracks network inside the indented region, and radial cracks at the corners of the imprints. We observed that a brittle thin film was produced when CeO_2 was doped with Ta. The residual nanoindentations exhibit microcracks inside of the imprint, which produce a considerable reduction of the mechanical properties of the thin film. There were formed by stress and extended downwards into the specimen, but were usually quite shallow. The residual nanoimprints on the samples doped with Zr did not present radial cracks at the corners nor microcracks inside of the imprint. This phenomenon indicates that the mechanical properties for this sample were better than those of the other samples.

9.4. References

[1] S. Basu, M. W. Barsoum; *J. Mater. Res.* 22 **(2007)** 2470.

[2] I. N. Sneddon; *Int. J. Engineering Science* 3 **(1965)** 47.

[3] W. J. Galler, T. K. Worthington, T. R. Dinger, F. Holtzberg, D. L. Kaiser, R. L. Sandstrom; *Physica B* 148 **(1987)** 221.

[4] J. Rabier, P. D. Tall, M. F. Denanot; *Philosophical Magazine A* 67 **(1993)** 1021.

[5] P. D. Tall, C. Coupeau, J. Rabier; *Scripta Materialia* 49 **(2003)** 903.

[6] W. C. Oliver, G. M. Pharr; *J. Mater. Res.* 7 **(1992)** 1564.

[7] Y. Y. Lim, M. M. Chaudhri; *J. Phys. A : Appl. Phys.* 34 **(2001)** L70.

[8] Ya. M. Soifer, A. Verdyan, J. Azoulay, M. Kazakevich, E. Rabkin; *Physica C* 402 **(2004)** 80.

[9] R. F. Cook, T. R. Dinger, D. R. Clarke; *Appl. Phys. Lett.* 51 **(1987)** 454.

[10] A. Verdyan, Y. M. Soifer, J. Azoulay, E. Rabkin, M. Kazakevich; *IEEE Trans. Appl. Supercond.* 15 **(2000)** 3585.

[11] T. H. Johansen; *Superconductor. Sci. Technol.* 13 **(2001)** R121.

[12] N. Sakai, F. Murakama, P. Diko, S. Takebashi, S. I. Yoo, M. Murakami; *Adv. Supercond. X* 11 **(1997)** 645.

[13] N. M. Alford, J. D. Birchall, W. J. Clegg, M. A. Harmer, K. Kendall, D. H. Jones; *J. Mater. Sci.* 23 **(1988)** 761.

[14] J. Joo, S. B. Jung, W. Nah, J. Y. Kim, T. S. Kim; *Cryogenics* 39 **(1999)** 107.

[15] Y. Gaillard, E. Jiménez-Piqué, F. Soldera, F. Mücklich, M. Anglada; *Acta Mater.* 56 **(2008)** 4206.

[16] B. R. Lawn, A. G. Evans, D. B. Marshall; *J. Am.Ceram. Soc.* 63 **(1980)** 574.

[17] S. Bec, A. Tondk, J. L. Lobet; *Philos. Mag.* 86 **(2006)** 5347.

[18] R. Andrei, H. Song, G. M. Pharr; *Mater. Res. Soc. Symp. Proc.* 695 **(2002)** 431.

[19] K. Shikimachi, N. Kashima, S. Nagaya, T. Muroga, S- Miyata, T. Watanabe, Y. Yamada, T- Izumi, Y. Shiohara; *IEEE Trans. Appl. Supercond.* 15 **(2005)** 3548.

10

CONCLUSIONS

When you cease to strive to
understand, then you will know
without understanding

Chinese Proverb

- Nanoindentation technique is an essential tool in the characterization of the mechanical properties of small volumes, thin films, bulk materials and advanced materials, and the characterization of the second phases, for applications where hardness and stiffness are important.

- Nanohardness and Young's modulus for each phase present in the YBCO compound textured by Bridgman and TSMG techniques (Y-123 and Y-211) can be isolated for applied loads lower or equal to 10 mN, because the residual nanoindentation imprint is lower than the size of the heterogeneous inclusions present in the Y-123 matrix. In this case, the Y-211 nanohardness is nearly twice that for the Y-123 ($H_{Y\text{-}211} \sim 2H_{Y\text{-}123}$) for both texturing techniques studied.

- H and E for samples textured by TSMG are lower than the samples manufactured by Bridgman technique. This decrease could be attributed to the different density of microstructural defects originated during the oxygenation process, which produce a fragilization of the TSMG sample.

- *E* for YBCO material obtained by spherical indentation and the Hertzian equations, has a value of 123.5 ± 3.4 GPa. This is in agreement with previous results of the literature using sharp indentations.

- The elasto-to-plastic transition for YBCO samples textured by Bridgman technique takes place at mean a contact pressure of 3.5 GPa (giving us a plastic deformation around 150 nm of penetration depth), which implies that the indentation yield strength is around 3.2 GPa. Moreover, TSMG technique takes place at a mean contact pressure of 3.9 GPa, which implies that the indentations yield strength is around 3.5 GPa.

- With a cross-section, and using FIB technique, we have determined that the samples present a heterogeneous distribution of Y-211 particles imbedded in the Y-123 matrix. No generation of porosity or microcracking have been observed, so the deformation mechanisms can be attributed to dislocations movement and twin generation in the [001]-planes and [110]-axis, respectively.

- AFM technique allows to study the different plastic deformation mechanisms activated during the indentation process in ceramic materials. Several slip lines have been visualized in the vicinity of the residual imprints performed by Berkovich and spherical tip indenter. TSMG samples, also present an activation of the different twins at 75º of the slip lines. The direction of the slip lines presents a high dependence with the crystallographic orientation for Bridgman samples. The field stress generated by spherical indentation produces a nucleation of slip lines and cross-slip movement inside the contact radius. The different load-displacement curves (5 cycles) using spherical tip, present an open loop. Therefore, an energy dissipation mechanism takes place.

- We determined the variation of the nanohardness and Young's modulus across the *ab*-plane of YBCO silver-welds of different (001) misorientation angles. A reduction of 30% in the value of the grain nanohardness is measured as the sample is oxygenated and passes from tetragonal to the orthorhombic phase.

- For misoriented welds the nanohardness is reduced in a 50 μm width welding path along the boundary due to the absence of the harder Y-211 phase. The oxygenation process induces in some cases micro- and macrocracks arising from the weld, which decrease the nanohardness in a broader area ranging between 100 μm to 3 mm, respectively.

- Mechanical properties (hardness) measured at room temperature have been correlated to superconducting properties (that is critical current density) of YBCO measured at cryogenic temperature, 77K.

- High quality zero-angle welds could be fabricated without degradation of either their mechanical or magnetic properties across the joint. This represents an important step forward towards the implementation of welds in bulk, large scale systems.

- Zr-doped CeO_2 employed as coated conductor showed better mechanical properties among the studied samples, with E higher than the undoped or Ta-doped samples. Furthermore, this layer did not present any cracks or fracture within the indented region. Thus, this material is an ideal candidate as a reliable and efficient buffer layer in HTSC-cc or, in general, in thin film applications where good mechanical properties like H, K_{IC}, and E are required. The results obtained on different CeO_2 based film grown by PED are similar to the ones reported for CeO_2 layers deposited by PLD.

11

FUTURE WORK

A champion of the working man
has never yet been known to die
of overwork

Robert Frost (1875-1963)
American Poet

During the development of the work that led to this Thesis, it was tried to perform a comprehensive analysis of the micro/nanomechanical properties on HTSC ceramic materials, with the special focus on YBCO bulk materials. As the time to perform this Thesis is limited, we propose several lines of research in order to better understand the mechanical behaviour at similar working conditions, and also know more things about the degradation and oxygenation process of this type of materials:

- Study the crystallographic orientation of the different YBCO grains by EBSD, obtain the Burgers vector and the slip line activated during the indentation process, to better understand the plastic deformation mechanism.

- Determination of the oxygenation kinetics of YBCO ceramic materials using nanoindentation technique at different times and temperatures of oxygenation in order to obtain the energy of activation.

- Determination of the degradation kinetics of YBCO ceramics materials at wet atmosphere.

- Study the mechanical properties and the fracture mechanism under the imprints of multilayered epitaxial YBCO thin films and coated conductors.

Appendix Section

Character is like a tree and reputation like its shadow. The shadow is what we think o fit; the tree is the real thing.

Abraham Lincoln (1809-1865)
President of the United States

Appendix A

RESUM EN CATALÀ

Un home intel·ligent és aquell que
sap ser tant intel·ligent com per
contractar gent més intel·ligent
que ell.

John Fitzgerald Kennedy (1917-1963)
Polític americà

A.1. Introducció

El present treball neix de la necessitat de conèixer el comportament mecànic d'uns materials superconductors que poden transportar el corrent d'una forma més neta i eficient, per tal de satisfer les necessitats energètiques de la nostra societat. En l'actualitat, els materials superconductors d'YBCO presenten unes molt bones propietats magnètiques i de transport de corrent, però, per contra, existeix un ampli desconeixement del seu comportament mecànic. Per tant, el principal objectiu d'aquest treball és fer un estudi bàsic de les diferents propietats mecàniques, així com dels diferents mecanismes activats durant el procés d'indentació, emprant la tècnica de nanoindentació (per a la caracterització del camp de deformació elàstic, plàstic i la transició elasto-plàstica).

A.1.1. Propietats mecàniques, Nanoindentació

En enginyeria, el coneixement de les propietats mecàniques permet un correcte disseny per a una futura aplicació. També cal tenir en compte el comportament que pot tenir un material en els diferents processos de mecanitzat als que es pugui sotmetre. Entre aquestes característiques mecàniques i tecnològiques destaquen:

- Resistència a esforços de tracció, compressió, flexió i torsió, així com desgast i fatiga, duresa, resiliència, elasticitat, tenacitat, fragilitat, cohesió, plasticitat, ductilitat, mal·leabilitat, porositat, les facilitats que tingui el material per a ser soldat, mecanitzat, tractat tèrmicament, així com la resistència que tingui als processos d'oxidació i corrosió. Així mateix, és interessant conèixer la conductivitat elèctrica i tèrmica que tingui i les facilitats per a formar aliatges.
- Per part de les propietats tecnològiques cal destacar com es tria un material per a un comportament determinat, la densitat d'aquest, el color, el punt de fusió, la disponibilitat i el preu.

A causa de que cada material presenta un comportament diferent, és necessari analitzar el seu comportament mitjançant proves experimentals. Entres les propietats mecàniques més comunes que es mesuren en els materials es troben la resistència a tracció, a compressió, la deformació, el coeficient de Poisson i el mòdul d'elasticitat o mòdul de Young. En aquesta Tesi, ens centrarem en l'estudi de les propietats mecàniques de materials ceràmics d'YBCO. Els materials ceràmics són generalment fràgils. Gairebé sempre es fracturen davant esforços de tensió i presenten poca elasticitat. Els porus i altres imperfeccions microscòpiques actuen com entalles o concentradores d'esforç, reduint la resistència als esforços esmentats.

La tècnica d'indentació va ser implementada per Brinell cap al 1900. Actualment, els assajos d'indentació, es poden classificar en funció de la càrrega aplicada (P):

- ***Assajos de macroindentació:*** $P > 10$ N
- ***Assajos de microindentació:*** $10 \text{ N} > P > 10$ mN
- ***Assajos de nanoindentació:*** $P < 10$ mN

L'assaig d'indentació, consisteix en pressionar un indentador contra el material d'estudi i es procedeix a mesurar el tamany de l'empremta residual tal i com es mostra en la *Fig. A.1*.

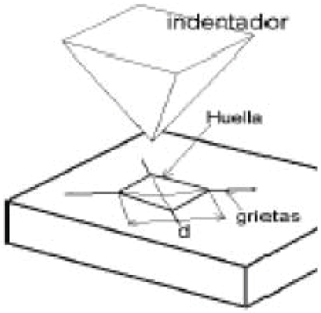

Fig. A.1. Empremta residual en forma piramidal generada en aplicar una càrrega sobre un material fràgil mitjançant un indentador tipus Vickers.

La tècnica de nanoindentació permet emprar diferents tipus d'indentadors segons l'estudi a realitzar;

- ***Indentador Berkovich:*** estudi de la zona plàstica. Ens permet obtenir els valors de duresa (*H*) i del mòdul de Young (*E*), veure *Fig. A.2a*.
- ***Indentador Cube Corner y Knoop:*** ens permet realitzar un estudi de la tenacitat de fractura (K_{IC}). Aquests tipus d'indentadors són semblants a l'indentador tipus Vickers, emprat en microindentació. Permeten realitzar assajos comparatius entre nanoindentació i microindentació.
- ***Indentador esfèric:*** emprat per a realitzar un estudi del camp de deformació elàstic, així com un estudi més acurat de la transició elasto-plàstica. Aquest tipus d'indentador ens permet obtenir la corba tensió (σ)-deformació (ε), així com l'extracció del límit elàstic (σ_e) i la tensió màxima a cisalla (τ_{max}) (veure *Fig. A.2b*).

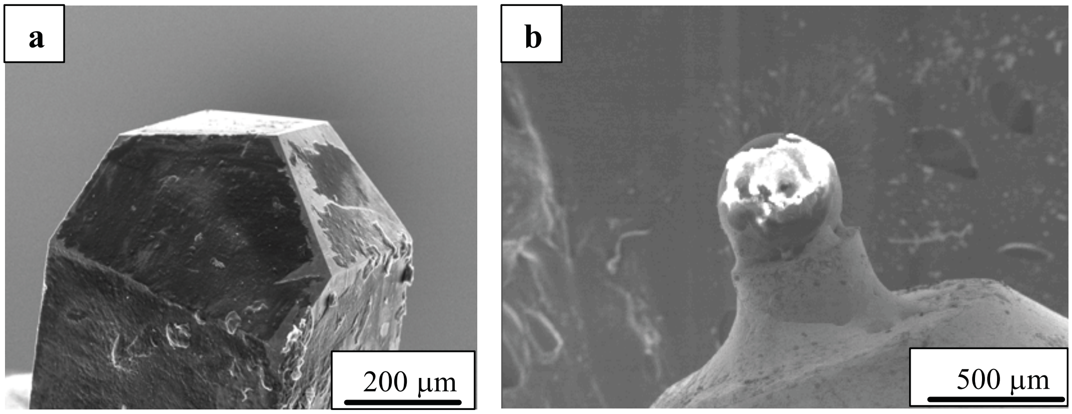

Fig. A.2. Imatge de microscòpia electrònica d'escombrat de diferents tipus de nanoindentadors. a) Indentador de diamant tipus Berkovich. b) Indentador de Zafir tipus esfèric.

Alguns equips per a la mesura de la H permeten enregistrar valors molt petits de força i desplaçament durant el procés de càrrega i descàrrega. Aquest tipus d'assaig es coneix com assaig de duresa instrumentada o nanoindentació. Les càrregues de treball oscil·len entre 50 nN i els 500 mN. La resolució teòrica en desplaçament de l'equip de treball és inferior als 0,01 nm, i la resolució teòrica de càrrega és aproximadament de 50 nN.

Els assajos de duresa instrumentada van ser desenvolupats per evitar mesurar l'àrea de contacte $[A(h_c)]$ ja que degut a la càrrega aplicada es fa difícil la mesura de les diagonals de cadascuna de les empremtes. Els primers treballs experimentals realitzats de manera sistemàtica es van fer cap a finals dels anys 70 i durant l'inici de la dècada dels 80. L'any 1986, Doener & Nix van realitzar un treball més acurat sobre aquesta tècnica. Però no va ser fins l'any 1992 quan Oliver & Pharr el van millorar i van desenvolupar un mètode per tal d'interpretar de manera sistemàtica els diferents resultats obtinguts mitjançant un nanoindentador. Actualment, aquest és el mètode més emprat.

Aquesta tècnica presenta una sèrie d'avantatges, així com d'inconvenients, si la comparem amb les tècniques convencionals:

- ***Avantatges:*** instrument robust i versàtil; ens permet avaluar les propietats mecàniques dels diferents materials a partir d'anàlisis elàstiques i elasto-plàstiques a partir de les corbes càrrega-desplaçament (P-h), sense la necessitat de visualitzar l'empremta residual; tècnica no destructiva; permet realitzar matrius d'indentacions; tècnica selectiva i econòmica.

- ***Inconvenients:*** necessitat d'un bon acabat superficial (ASTM E-3 80); necessitat del coneixement del coeficient de Poisson del material d'estudi; incertesa en la determinació del punt de contacte indentador-mostra i deriva tèrmica.

A.1.1.1. Mecanismes de contacte

Normalment existeixen dos tipus de mecanismes de contacte: elàstic i elasto-plàstic. Aquests dos mecanismes es troben descrits a la *Fig. A.3*.

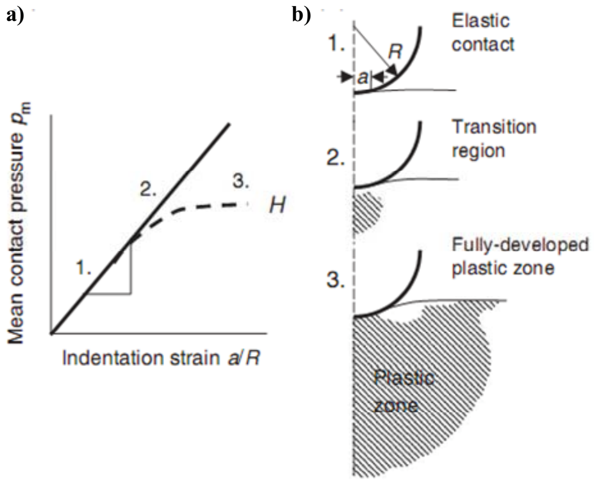

Fig. A.3. Mecanismes de contacte indentador-mostra.

- *Elàstic:* un camp de deformació elàstica és aquell que no presenta empremta residual després de que el material ha estat sotmès a un determinat esforç inferior al seu límit elàstic. La tècnica de nanoindentació permet fer un estudi bastant acurat del camp de deformació elàstica emprant un indentador esfèric i les equacions de Hertz.

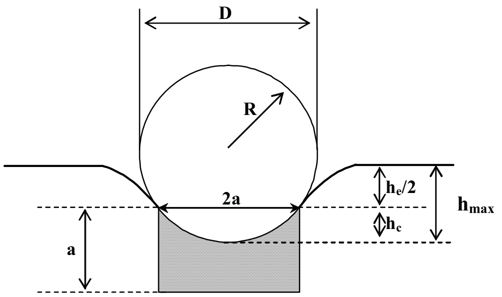

Fig. A.4. Esquema del procès d'indentació esfèrica.

La teoria de Hertz va ser desenvolupada al voltant del 1881. Aquest model descriu un comportament totalment elàstic si les corbes de càrrega-descàrrega s'ajusten a la següent expressió:

$$P = \left(\frac{3}{4} E_{eff} R^{1/2} \right) h_e^{3/2} \qquad \textbf{eq. A.1}$$

on R es el radi de l'indentador, h_e és la deformació elàstica produïda i E_{eff} es el mòdul de Young efectiu o reduït, que es pot obtenir mitjançant la següent expressió:

$$\frac{1}{E_{eff}} = \frac{1-\nu^2}{E} + \frac{1-\nu_i^2}{E_i} \qquad \textbf{eq. A.2}$$

on ν és el coeficient de Poisson del material d'estudi. El subíndex *i* fa referència a les propietats de l'indentador. En aquest estudi s'ha emprat un indentador de diamant, que presenta els següents valors: E_i = 1141 GPa i ν = 0,07.

- *Elasto-Plàstic:* en aquest camp de deformació coincideix la transició entre una deformació totalment elàstica i una plàstica. Està governat per una enorme recuperació elàstica. Aquesta transició s'estudia a partir de la corba σ–ε obtinguda mitjançant un indentador esfèric i les següents expressions per al límit elàstic (σ_e):

$$p_m = 1{,}1\sigma_e \qquad \textbf{eq. A.3}$$

i per la tensió màxima a cisalla (τ_{max}):

$$\tau_{\max} = 0{,}46 p_m \qquad \textbf{eq. A.4}$$

on p_m es la pressió mitja de contacte indentador-mostra.

El camp de deformació plàstica està governat per la corba de càrrega. Per poder estudiar aquest camp de deformació, normalment s'empra un indentador tipus Berkovich i el model d'Oliver i Pharr, veure *Fig. A.5*.

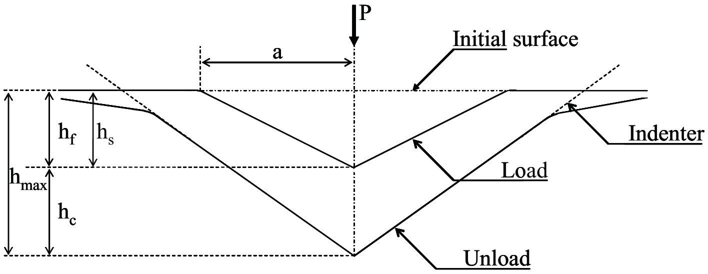

Fig. A.5. Esquema de procés de càrrega i descàrrega emprant un indentador tipus Berkovich.

Les dues propietats més importants que s'extreuen són la *H* i el *E*, a partir de les següents expressions:

$$H = \frac{P_{\max}}{A(h_c)} = \frac{P_{\max}}{24.56 h_c^2} \qquad \textbf{eq. A.5}$$

$$E_{eff} = \frac{1}{\beta}\frac{\sqrt{\pi}}{2}\frac{S}{\sqrt{A(h_c)}} \qquad \textbf{eq. A.6}$$

on β és igual a 1,034 per a un indentador tipus Berkovich, *S* és la rigidesa del material obtinguda a partir del tram lineal de la corba de descàrrega, $A(h_c)$ és l'àrea de contacte entre l'indentador i la mostra d'estudi, i h_c fa referència a la profunditat de penetració de contacte. Aquest últim paràmetre s'obté a partir de la següent expressió:

$$h_c = h_{\max} - \varepsilon \frac{P}{S} \qquad \textbf{eq. A.7}$$

on ε és igual a 0,75 per a indentadors tipus Berkovich.

A.1.1.2. Estudi de capes primes

Per poder caracteritzar capes primes, primer s'ha d'entendre bé la diferència entre un camp de deformació elàstica i un de plàstica. En la *Fig. A.6* es pot observar un esquema general dels camps de deformació induïts per una indentació. A càrregues grans, el camp de deformació elàstica i plàstica són majors i poden interactuar amb el substrat.

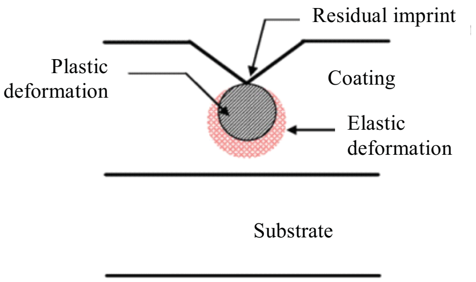

Fig. A.6. Esquema general dels camps de deformació induïts per la indentació.

En la *Fig.* A.7 s'observa l'evolució de *H* i *E* a diferents profunditats de penetració.

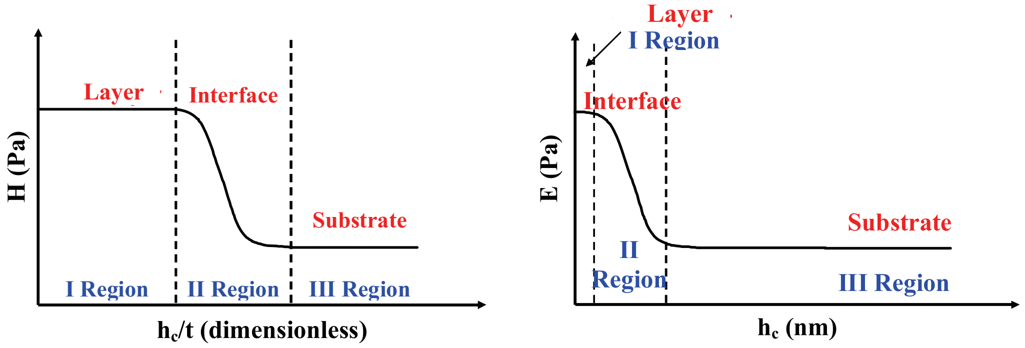

Fig. A.7. Evolució de la *H* i *E* *vs. h*.

Controlant les condicions d'operació, podem extreure els valors de *H* de la capa sense interacció amb el substrat. Per contra, degut a que el camp de deformació elàstica és molt més gran que el plàstic no es pot extreure el valor de *E* de manera directa i, per tant, s'han d'emprar diferents models, com el de Bec i Rar *et al*.

A.1.2. Materials superconductors

El fenomen de la superconductivitat va ser descobert al 1911 pel físic holandès Heike Kamerlingh Onnes a l' Universitat de Leiden. Aquest descobriment, que va ser fortuït, es va produir en estudiar la resistivitat dels metalls purs a baixa temperatura. D'ençà d'aquest descobriment, la comunitat científica ha dedicat molts esforços a descobrir els mecanismes de la superconductivitat i desenvolupar aplicacions dels materials superconductors. L'estudi dels superconductors va patir una gran revolució al 1986, en ser descoberta la superconductivitat del material $La_{1.85}Ba_{0.15}CuO_4$ a una temperatura aproximada de 35 K als laboratoris IBM a Zurich per en J. G. Bednorz i en K. A. Müller. A banda de l'increment en la temperatura del fenomen (fins aquell moment la temperatura crítica més elevada era de l'ordre de 20 K), l'estudi dels materials superconductors s'havia centrat en metalls i aliatges metàl·lics, i aquest, en canvi, era un material ceràmic. Aquesta nova línia d'investigació va portar a un increment continu de la temperatura crítica dels materials descoberts fins que al 1987 es va arribar a 92 K amb el compost $YBa_2Cu_3O_{7-\delta}$ (Y-123), a la Universitat de Houston. Malauradament, no s'ha arribat a aconseguir una temperatura crítica per sobre de la temperatura ambient i actualment el llindar s'ha establert en 138K amb un compost de mercuri ($Hg_{0.8}Tl_{0.2}Ba_2Ca_2Cu_3O_{8.33}$).

En un principi, es va creure que els materials superconductors entrarien a les nostres vides en infinitat d'aplicacions, i fins i tot, van arribar a ser portada a la revista *Times* al Maig del 1987. Malauradament, aquests tipus de materials només s'estan desenvolupant en aplicacions on no es poden emprar materials convencionals.

A.1.2.1. Classificació dels materials superconductors

Superconductor de tipus I: és aquell que expulsa el camp magnètic del seu interior fins a un valor del camp anomenat camp crític (H_c), a partir del qual el material perd les severs propietats superconductores. Aquest comportament de diamagnètic perfecte, que es pot observar a la *Fig. A.8*, és anomenat efecte Meissner.

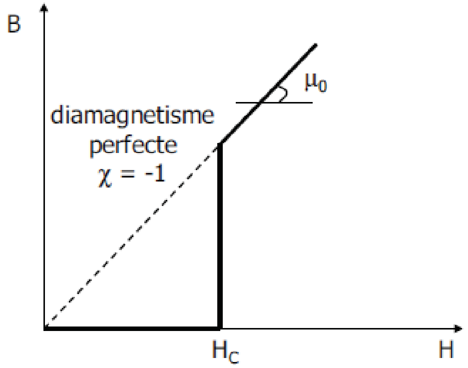

Fig. A.8. Corba B(H) per un material superconductor de tipus I.

Superconductor de tipus II: aquest superconductor presenta el mateix comportament que el de *tipus I* per sota del camp crític inferior, H_{c1}. Ara bé, entre el H_{c1} i el camp crític superior H_{c2} el diamagnetisme deixa de ser perfecte, l'expulsió del camp en l'interior del material és parcial i es coneix com estat mixt (veure *Fig. A.9*). Aquest estat mixt, permet penetrar el camp magnètic dins del material en forma de petits nanotubs anomenats vòrtex.

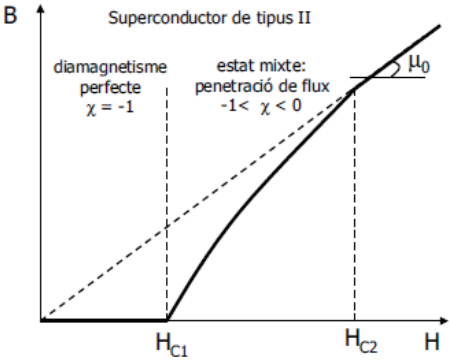

Fig. A.9. Corba B(H) per un superconductor de tipus II.

A.1.2.2. L' $YBa_2Cu_3O_{7-\delta}$

L'$YBa_2Cu_3O_{7-\delta}$ (Y-123 o YBCO) va ser descobert al 1987 per *P. Chu* i té una temperatura crítica de l'ordre de 92 K. El seu descobriment va suposar un gran impacte tecnològic ja que la temperatura de treball era superior a la temperatura d'ebullició del nitrogen líquid, obrint les portes a noves aplicacions ja que els superconductors que hi havia fins el moment únicament podien ser refrigerats amb heli líquid.

Estructura cristal·logràfica i anisotropia: L'estructura cristal·logràfica del Y-123 va ser estudiada a partir de l'any del seu descobriment per nombrosos grups. A la *Fig. A.10* es pot veure la seva estructura cristal·logràfica tipus perovskita, on es distingeixen els plans *ab* de CuO_2 separats per cadenes metàl·liques de $CuO_{1-\delta}$. Aquesta és una important característica d'aquest compost, a diferencia dels altres òxids superconductors d'alta temperatura crítica.

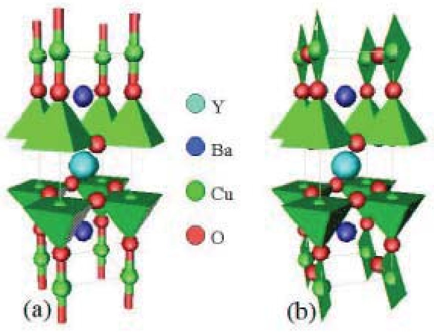

Fig. A.10. Representació de l'estructura cristal·logràfica pel compost amb a) δ=1 i b) δ=0.

Donat el caràcter anisotròpic de l'estructura, les propietats de transport en l'estat normal i el superconductor es troben fortament influenciades per la seva orientació cristal·logràfica.

Efecte del contingut d'oxigen: L'estructura cristal·logràfica del Y-123 varia depenent del contingut d'oxigen, de l'ordre de $\delta \sim$ 0,5. Hi ha una transició estructural de tetragonal a ortoròmbica, que es la fase superconductora com es pot veure a la *Fig. A.11*. La diferència entre les dues xarxes cristal·lines es pot observar a la *Fig. A.10*, on es veu una representació de les cel·les unitat pel compost Y-123 amb $\delta = 0$ i $\delta = 1$.

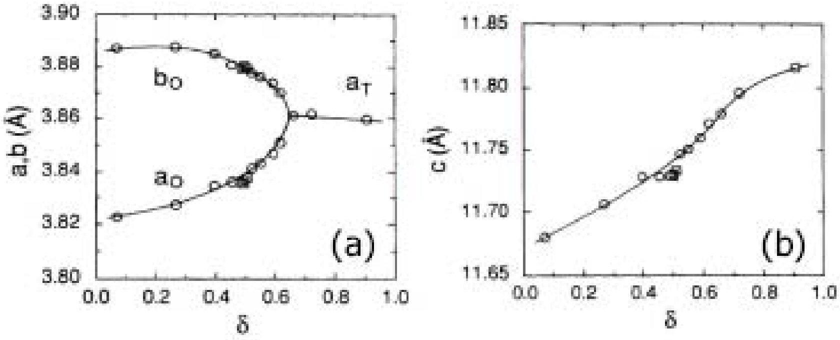

Fig. A.11. Paràmetres de xarxa a) *a* i *b*, b) *c* per Y-123 en funció de δ.

Diagrama de fases: El diagrama de fases del YBCO ens proporciona informació sobre les diferents reaccions de fusió i solidificació depenent de la composició inicial. El sistema d'estudi té una reacció peritèctica a ~ 1015ºC tal com es pot observar a la *Fig. A.12.* La fase Y-123 és la fase superconductora i la fase Y_2BaCuO_5 (Y-211) és no superconductora o aïllant. La reacció peritèctica correspon a la formació de la fase Y-123 segons la següent reacció:

$$\text{Y-211}_s + L \rightarrow \text{Y-123}_s \qquad \mathbf{\mathit{1015^{o}C < T < 1200^{o}C}} \qquad \mathbf{\mathit{(reac.\ 1)}}$$

Com es pot veure en la *Fig. A.12* i en la *reac. 1*, per sobre la temperatura peritèctica (T_p) tenim un líquid de composició Ba-Cu-O deficient en *Y* i Y-211. En disminuir la temperatura per sota de la T_p comença el procés de nucleació i creixement del Y-123.

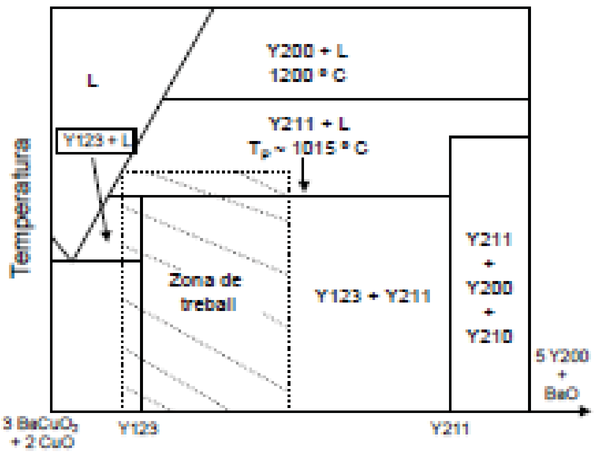

Fig. A.12. Diagrama de fases pseudo-binari pel sistema Y-Ba-Cu-O.

Model de creixement de la fase Y-123: Com es pot observar a la *Fig. A.13*, el gradient de concentració de Y actua de força motriu pel creixement de la interfase. El valor $C_{L,Y\text{-}211}$ és més alt que el $C_{L,Y\text{-}123}$; aquesta diferència provoca un transport de Y cap al front de creixement. El líquid al front del creixement es satura en Y, on es produeix la nova nucleació d'un cristall de Y-123 per tornar a l'equilibri $C_{L,Y\text{-}123}$. Aleshores, $C_{L,Y\text{-}211}$ baixa degut al transport de Y cap al front de creixement. Per tornar a la composició metastable $C_{L,Y\text{-}211}$; les partícules de Y-211 es dissolen al líquid i suposen una nova aportació de Y cap al front de creixement. Si es du a terme un sotarefredament adient es pot aconseguir un front de creixement pla, i no una nucleació heterogènia en tota la mostra. En aquestes condicions de treball, els nous cristalls de Y-123 que nucleen del líquid en el front de creixement ho fan de manera epitaxial amb els que ja han nucleat i d'aquesta manera s'obté una mostra amb una única orientació cristal·lina (monodomini).

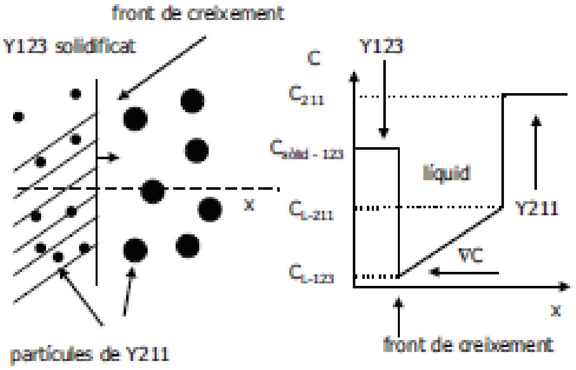

Fig. A.13. La figura de l'esquerra mostra un esquema del front de creixement. La de la dreta mostra el perfil de concentració de Y des del front de creixement fins a prop d'una partícula de Y-211

Les partícules de Y-211 continuen dissolent-se fins que són atrapades pel front de creixement. En aquest moment, el front de creixement les empenyerà si la seva mida és inferior a l'anomena't radi crític o bé quedaran incloses a la matriu de Y-123 si és superior.

A.2. Resum de les publicacions presentades

A.2.1. *Duresa i mòdul de Young del Y-123, Y-211 i de l'interfase Y-123/Y-211*

Les propietats mecàniques (*H* i *E*) a escala nanomètrica i temperatura ambient de la fase ortoròmbica del YBCO, tant per mostres texturades amb la tècnica Bridgman com la de creixement induït per llavor a temperatura ambient, han estat obtingudes a diferents càrregues aplicades (5, 10, 30 i 100 mN) en el pla *ab* utilitzant la tècnica de nanoindentació i les equacions d'Oliver i Pharr. Els valors de *H* i *E* per a cadascuna de les fases i càrregues aplicades es poden observar en la *Taula A.1*.

Taula A.1. Taula resum de les diferents propietats mecàniques (*H* i *E*) d'elements superconductors d'YBaCuO emprant la tècnica de nanoindentació.

Propietats mecàniques	Fase	Càrrega, mN	Bridgman	TSMG
H	*Y-123*	5	10,4 ± 0.5	11,0 ± 0,5
	Y-211		19,1 ± 0.8	15,2 ± 0,9
	Y-123/Y-211$_{interfase}$		14,8 ± 0.5	14,9 ± 1,0
	Y-123	10	11,2 ± 0,4	10,3 ± 0,9
	Y-211		16,9 ± 0,5	17,0 ± 0,6
	Y-123/Y-211$_{interfase}$		15,1 ± 0,3	14,8 ± 0,9
	Y-123/Y-211$_{interfase}$	30	11,1 ± 0,3	8,5 ± 0,9
	Y-123/Y-211$_{interfase}$	100	8,9 ± 0.2	7,9 ± 0.8
E	*Y-123*	5	197 ± 7	176 ± 15
	Y-211		194 ± 9	224 ± 18
	Y-123/Y-211$_{interfase}$		201 ± 7	208 ± 21
	Y-123	10	189 ± 4	174 ± 17
	Y-211		206 ± 4	207 ± 11
	Y-123/Y-211$_{interfase}$		204 ± 6	190 ± 16
	Y-123/Y-211$_{interfase}$	30	180 ± 5	140 ± 14
	Y-123/Y-211$_{interfase}$	100	173 ± 3	129 ± 6

Tal i com es pot observar en la *Taula A.1*, els valors de duresa per a les mostres texturades mitjançat la tècnica Bridgman presenten un valor de *H* superior a les obtingudes mitjançant la tècnica TSMG; aquest fenomen s'atribueix a la diferent densitat d'esquerdes introduïda en el material per cada tècnica de creixement. En el cas de TSMG, el conformat provoca un major nombre de defectes que fan que el valor de duresa del material disminueixi, veure *Fig. A.14*.

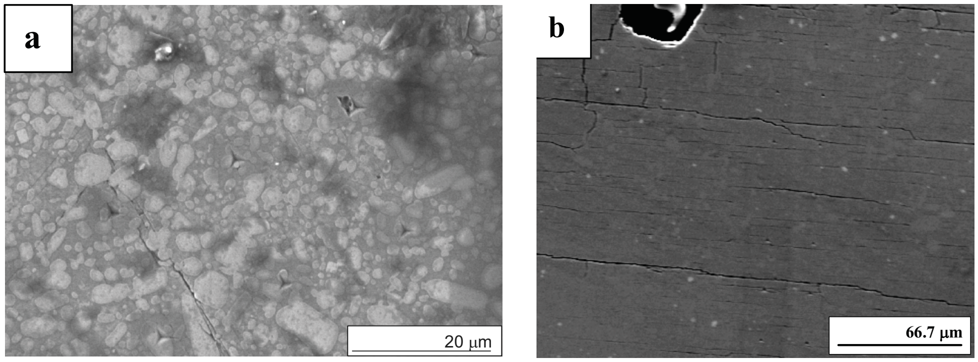

Fig. A.14. Imatge de microscòpia electrònica d'escombrat d'alta resolució on es poden observar els defectes superficials de l'eix *c* de mostres texturades per a) tècnica Bridgman, i b) TSMG.

Tal i com es pot observar en la *Taula A.1*, quan la càrrega aplicada es inferior o igual a 10 mN s'ha pogut aïllar els valors de *H* i *E* per a cadascuna de les fases presents, ja que la mida residual de l'empremta és inferior a la dels precipitats de Y-211, veure *Fig.A.15* per a les mostres Bridgman i *Fig. A.16* per a les mostres TSMG.

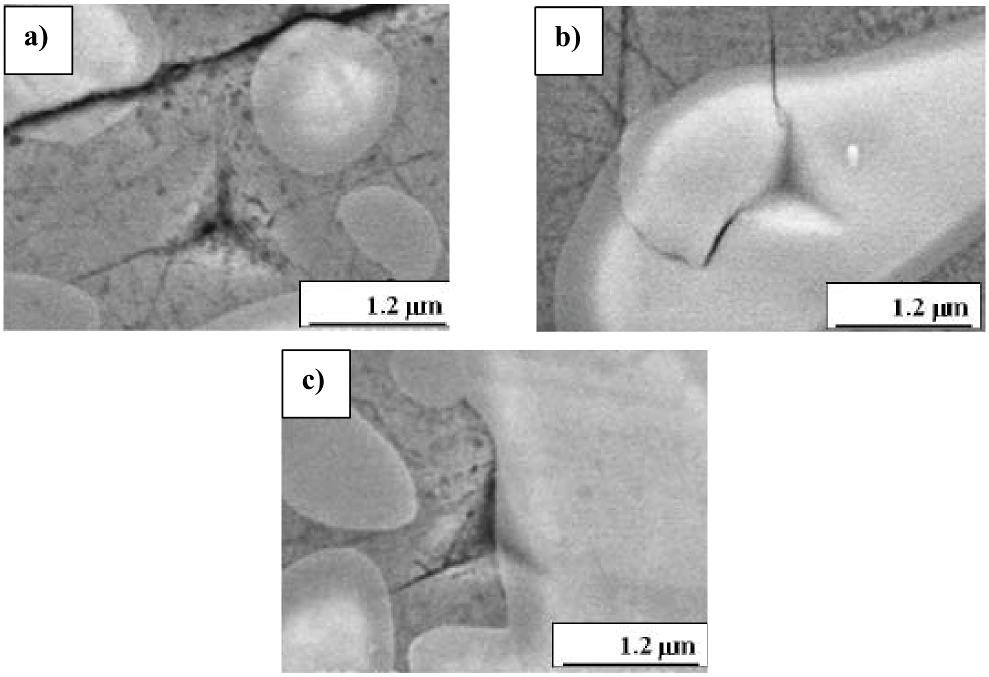

Fig.A.15. Empremtes residuals realitzades a 10 mN de càrrega aplicada per a cadascuna de les fases observades per microscòpia electrònica d'alta resolució per a mostres texturades amb la tècnica Bridgman. a) Y-123, b) Y-211 i c) Y-123/Y-211interfase.

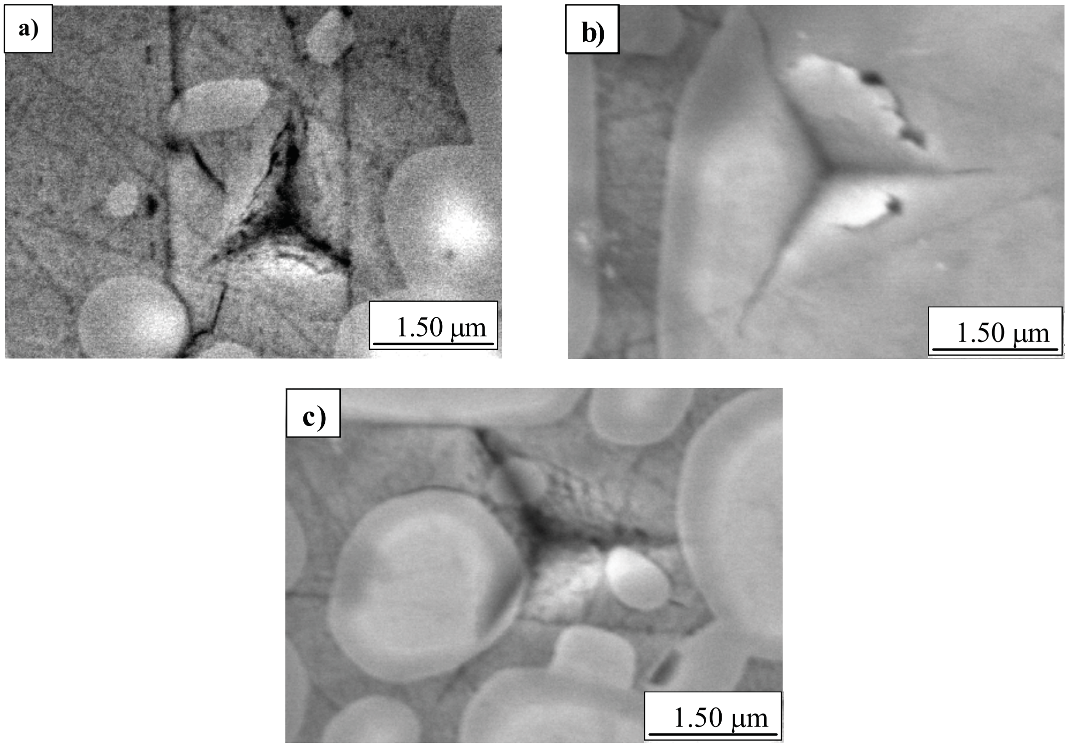

Fig. A.16. Empremtes residuals realitzades a 10 mN de carrega aplicada per a cadascuna de les fases observades per microscòpia electrònica d’alta resolució per a mostres texturades amb la tècnica TSMG. a) Y-123, b) Y-211 i c) Y-123/Y-211interfase.

Val a dir que les empremtes per als precipitats presents en les *Fig.A.15b* i *Fig. A.16b* es troben just al límit de fase. Per tant, els valor de H i E es trobaran fortament influenciats per la matriu, Y-123. El valor del E obtingut per a les partícules de Y-211 és més gran que per la matriu de Y-123, degut a que l’enllaç iònic del precipitats és superior al de la matriu.

A.2.2. Corba σ–ε

En aquesta secció, es presenten les diferents corbes enginyerils (veure *Fig. A.17*) per a elements d’YBCO obtinguts mitjançant la tècnica Bridgman i TSMG, obtingudes per indentació esfèrica.

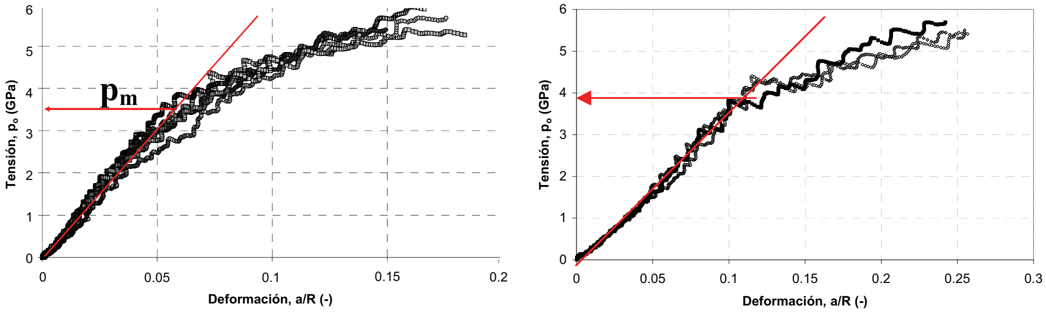

a) b)

Fig. A.17. Corba σ–ε. a) mostres Bridgman, b) mostres TSMG.

A partir de la corba σ–ε, s'extreu el valor de la pressió mitja de contacte (p_m), i d'aquí, emprant les *Eq. A.3* i *A.4*, s'obté el límit elàstic i la tensió màxima a cisalla, respectivament. Tal com es pot observar en la *Fig. A.17*, la corba enginyeril ens dóna informació sobre el punt de contacte indentador-mostra. En aquesta gràfica es distingeixen tres zones clarament diferenciades. Inicialment, un tram lineal que correspon a la deformació elàstica del material. En segon lloc, a una pressió mitja de contacte (p_m), hi ha la transició entre la deformació elàstica i plàstica, i finalment, per sobre de la p_m, ens trobem en el rang de deformació totalment plàstic, produint una deformació remanent.

Taula A.2. Taula resum de les diferents propietats mecàniques obtingudes mitjançant indentació esfèrica.

Propietat mecànica	**Fase**	**Indentador**	**Bridgman**	**TSMG**
p_m **(GPa)**	*YBCO*	Esfèric	3,5 ± 0,2	3,9 ± 0,2
σ_e **(GPa)**			3,2 ± 0,2	3,6 ± 0,1
τ_{max} **(GPa)**			1,6 ± 0,1	1,8 ± 0,1

Tal i com s'observa en la *Taula A.2*, les diferents propietats mecàniques obtingudes a partir de la corba enginyeril són molt semblants, tant per les mostres d'YBCO obtingudes mitjançant la tècnica Bridgman com les obtingudes per TSMG. En altres paraules, el tram lineal de la corba enginyeril subministra les propietats intrínseques del material, per aquest motiu les propietats obtingudes de la *Taula A.2* són invariants amb la tècnica de conformació emprada.

A.2.3. Mecanismes de deformació plàstica

En aquesta secció, ens centrem en l'estudi dels diferents mecanismes de deformació plàstica (com per exemple el moviment de dislocacions, macles, etc.) activats mitjançant nanoindentació Berkovich i esfèrica, i observats mitjançant microscòpia de forces atòmiques, AFM.

Mostres TSMG: Emprant l'indentador tipus Berkovich, s'ha observat mitjançant AFM l'activació de línies de dislocacions en la zona col·lindant a l'empremta residual (veure *Fig. A.18*). Val a dir que aquest estudi s'ha realitzat en una zona d'un monodomini de Y-123 lliure de precipitats que interfereixin amb els mecanismes de deformació plástica.

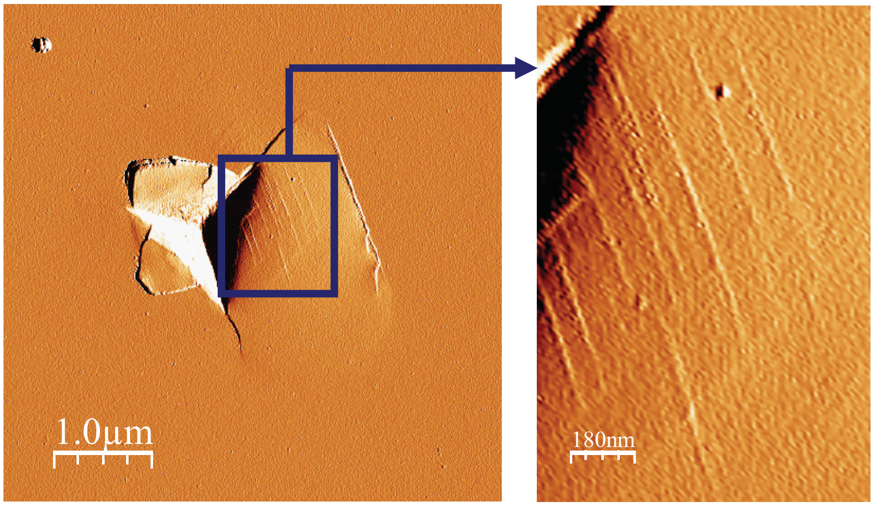

Fig. A.18. Imatge d'error d'una empremta residual on s'aprecien línies de dislocacions en la zona col·lindant a l'empremta de nanoindentació.

A més a més, la *Fig. A.18* mostra un mecanisme de fractura característic per als materials ceràmics conegut amb el nom d'escrostonament. Com es pot observar en la imatge anterior, les línies de dislocacions es troben incloses en l'interior de la zona de fractura. A més, s'ha activat el maclatge, veure *Fig. A.19*. En aquesta imatge (*Fig. A.19a*), es pot observar la imatge d'error, on s'observen esquerdes radials al vèrtex de la nanoindentació, així com macles a 75º de les línies de dislocacions. La *Fig. A.19b* ens mostra la imatge de la mateixa empremta, però en 3D, on s'aprecien les diferent macles activades.

Fig. A.19. a) Imatge d'error d'una empremta residual on s'aprecien macles i línies de dislocacions. b) Imatge 3D on s'aprecien amb més detall les macles.

Una vegada descrits alguns dels mecanismes de deformació plàstica activats mitjançant indentació tipus Berkovich, s'estudien possibles mecanismes de deformació emprant un indentador esfèric ($R \approx 9{,}5$ μm). Degut a que aquest indentador presenta una major superfície de contacte, s'espera l'activació d'altres mecanismes de deformació. La *Fig. A.20* ens mostra les corbes característiques per a una càrrega aplicada de 25 mN (1 cicle) i 50 mN (5 cicles), sobre el pla basal del YBCO.

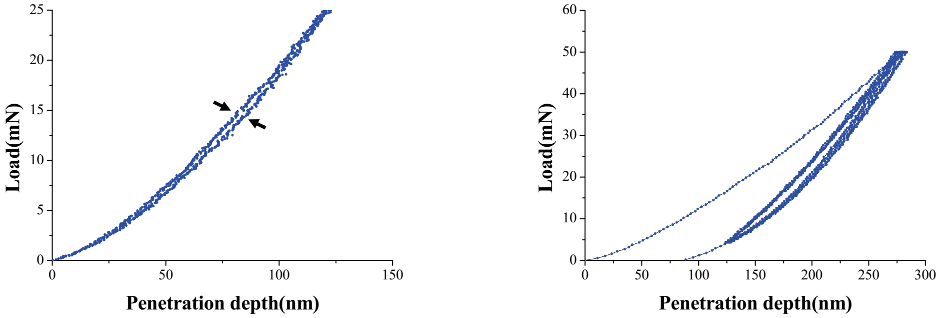

a) **b)**

Fig. A.20. Corba *P-h* realitzada sobre el pla basal (001). a) 1 cicle a 25 mN de càrrega aplicada, b) 5 cicles a 50 mN de càrrega aplicada.

La *Fig. A.20a,* mostra un cicle obert en la part central de la corba *P-h* (la corba de càrrega i descàrrega no van pel mateix lloc) produint-se una deformació totalment elàstica. Per contra, en augmentar la càrrega aplicada, existeix una deformació plàstica remanent encara que té lloc el mateix mecanisme. Aquest efecte s'atribueix al fenomen d'activació i aniquilació de dislocacions, conegut amb el nom "*d'Incipient Kink Bands,* *IKB"*; aquest fenomen normalment es produeix en materials nanolaminats, com és el cas de les fases MAX, el grafit, el YBCO, etc.

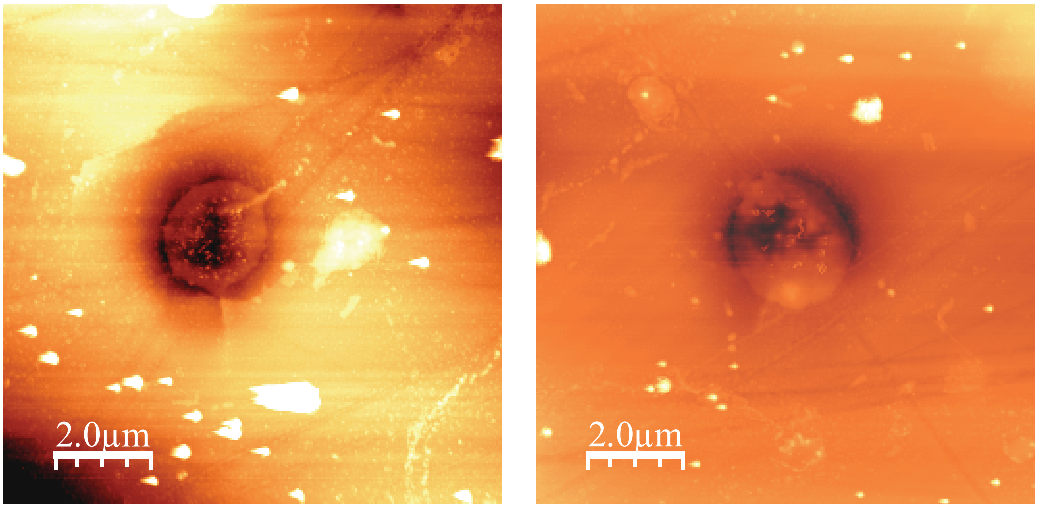

a) **b)**

Fig. A.21. Micrografies de microscopia de forces atòmiques d'empremtes esfèriques residuals. a) 50 mN de càrrega, 1 cicle. b) 50 mN de càrrega, 5 cicles.

Les imatges de topografia que es presenten a la *Fig. A.21*, mostren una capa de brutícia en l'interior del cercle de contacte, produint un emmascarament dels diferents mecanismes activats durant aquest procés. Degut a aquest fenomen, no es pot assegurar amb certesa l'activació de les *IKB* en aquests tipus de materials. La *Fig. A.21a*, mostra fractura en forma d'esquerda des de l'interior de l'empremta cap a l'exterior. Per contra, la *Fig. A.21b* no mostra cap indici de fractura en la zona col·lindant a la indentació.

Mostres Bridgman policristal·lines: Emprant un indentador tipus Berkovich s'ha observat l'activació de línies de deslliçament en les zones col·lindants a l'empremta. En aquest tipus de mostres, no s'ha observat l'activació de les macles, tot i que no es descarta que en altres plans puguin ser generades, veure *Fig. A.22*. En aquesta figura, es pot observar que, depenent de l'orientació cristal·lina del gra, s'activen uns o altres plans de lliscament. Per tant, els mecanismes de deformació plàstica estan fortament relacionats amb l'orientació cristal·lina del gra en estudi.

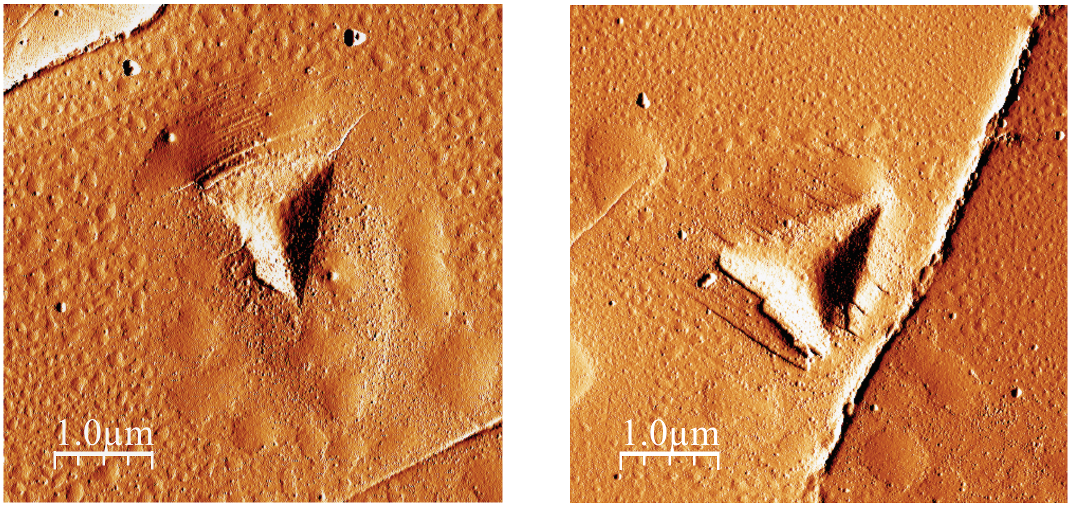

Fig. A.22. Imatges d'error d'empremtes residuals en diferents grans produïdes a 45º del pla basal mitjançant indentació Berkovich.

Es pot observar en la *Fig. A.23* una indentació realitzada en el límit de gra. En aquest cas, cap mecanisme de deformació ha estat activat degut a que el camp de deformació plàstica generat per l'assaig d'indentació produeix un tancament del límit de fase, el qual actua com a esquerda.

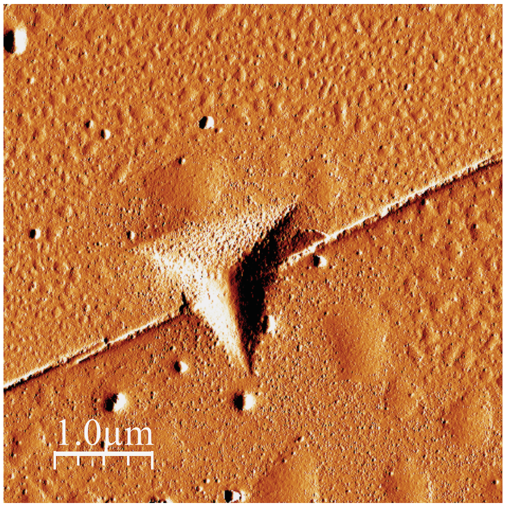

Fig. A.23. Imatge d'error d'una empremta residual produïda a 45ºdel pla basal.

La *Fig. A.24* mostra els diferents mecanismes activats mitjançant indentació esfèrica per a una càrrega màxima aplicada de 50 mN amb un (*Fig. A.24a*) i cinc cicles (*Fig. A.24b*). A diferència de les mostres texturades mitjançant la tècnica TSMG, les corbes *P-h* obtingudes per a les mostres Bridgman no presenten un cicle obert, no es produeix dissipació d'energia i, per tant, no es compleix el model de les *IKB*. Aquestes corbes de *P-h* no han estat presentades ja que no aporten informació complementaria a l'estudi.

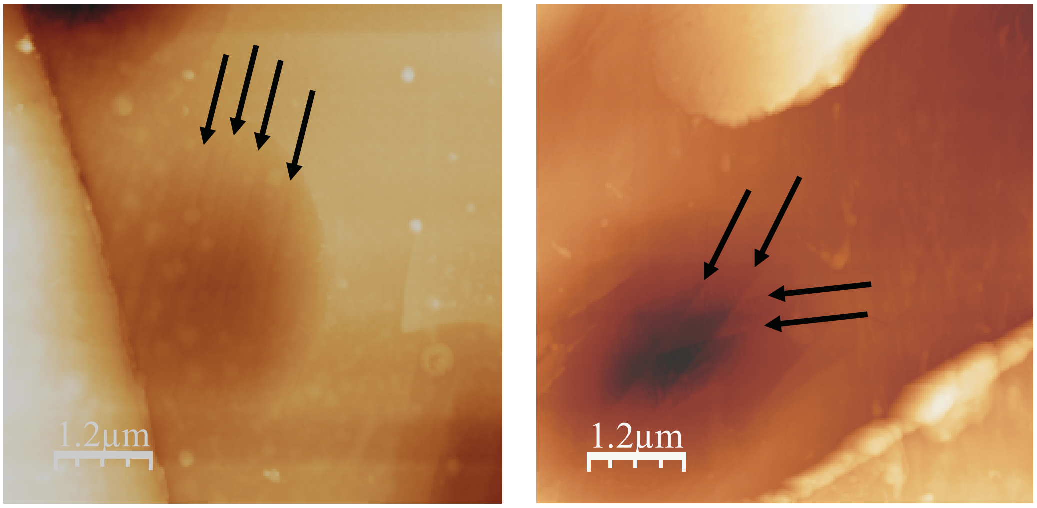

a) b)

Fig. A.24. Imatges de topografia d'empremtes residuals on es poden observar els diferents mecanismes de deformació plàstica. a) 50 mN, 1 cicle. b) 50 mN, 5 cicles.

La *Fig. A.24a* mostra que dins del cercle de contacte es produeix el moviment de dislocacions en una mateixa direcció. Per contra, a la *Fig. A.24b* s'observa que es produeix un fenomen de moviment creuat de dislocacions. Aquest efecte es pot veure millor a la *Fig. A.25*, on es presenta la imatge de topografia i la d'error. En aquestes imatges es pot observar que en interaccionar dues dislocacions es produeix una petita distorsió; aquest efecte s'atribueix a l'orientació cristal·lina.

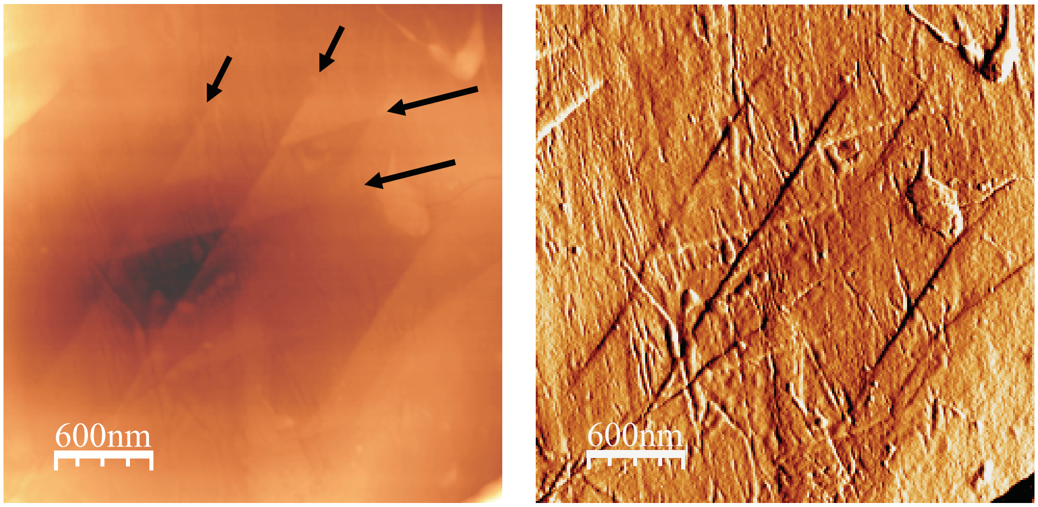

Fig. A.25. Ampliació dels moviment creuats de dislocacions (*Fig. A.24b*).

A.2.4. Correlació entre propietats mecàniques i superconductores

Durant l'última dècada, s'han focalitzat els esforços per poder realitzar soldadures de materials ceràmics d'YBCO emprant una làmina de *Ag* i d'aquesta manera obtenir materials màssics de llargues dimensions. La *Fig. A.26* mostra l'evolució de la *H* en la zona de soldadura tant per mostres sense oxigenar (*fase tetragonal*) com oxigenades (*fase ortorómbica*). A més a més, es pot observar el mateix estudi per unes mostres patró, sense soldar.

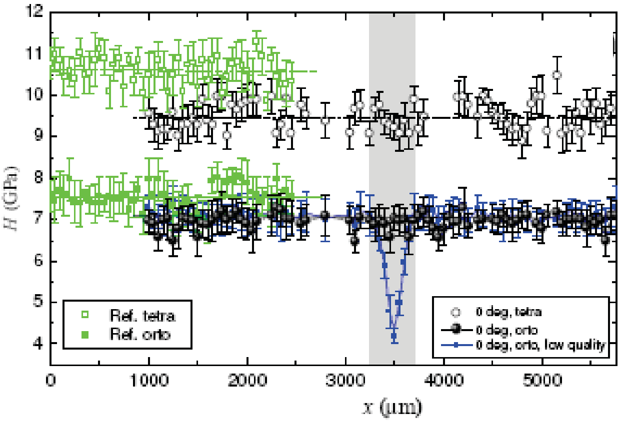

Fig. A.26. Estudi de l'estabilitat mecànica en la zona de soldadura per a mostres amb una desorientació de 0º en fase tetragonal i ortorròmbica. Evolució de la *H* per les mostres de referència (sense soldar).

A la *Fig. A.26* es pot observar que els valors de *H* per a la fase ortoròmbica són inferiors que per la tetragonal, degut a les diferents microesquerdes originades durant el procés d'oxigenació (veure *Fig. A.14*). Com es pot observar, aquesta tècnica ens pot permetre realitzar l'estudi de la qualitat de la soldadura. L'objectiu principal d'aquest estudi és determinar si existeix una correlació entre les propietats mecàniques obtingudes a temperatura ambient i una propietat superconductora (la densitat de corrent) obtinguda a la temperatura del nitrogen líquid, veure *Fig. A.27*.

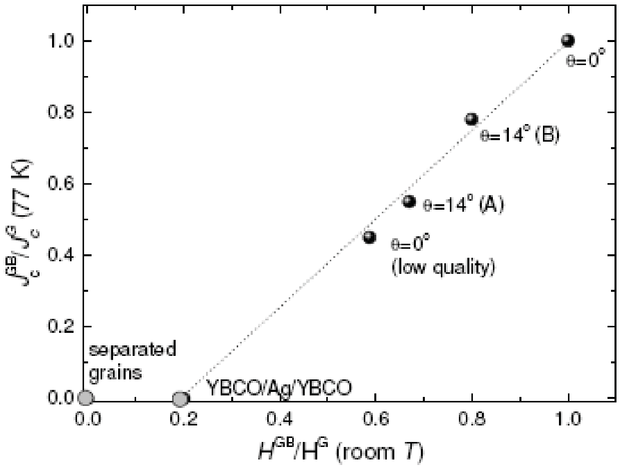

Fig. A.27. Correlació entre les propietats mecàniques i superconductores.

Tal i com s'observa en la *Fig. A.27,* existeix una relació lineal entre les propietats mecàniques obtingudes a temperatura ambient i les superconductores a temperatura criogènica. Per tant, és possible correlacionar una mesura de duresa a temperatura ambient que no destruïm ni modifiquem les propietats intrínseques del material, amb una mesura de propietats elèctriques, en condicions d'operació (en aquest cas superconductores).

A.2.5. Estudi de les propietats mecàniques de capes fines

En aquesta secció, s'estudien les propietats mecàniques (*H* i *E*) de capes de CeO_2 dopat utilitzades com a capes tampó per a la producció de cables superconductors. Per poder obtenir el valor de *H* s'ha treballat amb càrregues inferiors a 1 mN ja que, com hem comprovat, per sota d'aquest llindar el valor de *H* és constant i no està influenciat pel substrat. Per contra, el *E* es troba fortament influenciat pel camp de deformació elàstic i no es manté constant a càrregues inferiors a 0,9 mN. Per poder aïllar el valor de *E* s'ha emprat els models de Bec *et al.* i el de Rar *et al.* La *Taula A.3* mostra les diferents propietats de *H* i *E* per a cadascuna de les capes primes estudiades.

Taula A.3. Taula resum de les diferents propietats mecàniques de capes tampó emprades per a la producció de cables superconductors d'YBCO.

Mostra	**Indetador**	**$H_{10\%}$ (GPa)**	**E_{Bec} (GPa)**	**E_{Rar} (GPa)**
Undoped-CeO_2	Berkovich	2.28 ± 0.20	150	145
10%Ta-CeO_2		2.32 ± 0.14	152	136
15%Zr-CeO_2		2.75 ± 0.25	249	235

Tal com s'observa en la *Taula A.3*, la capa de CeO_2 dopada amb un 15% de Zr presenta unes propietats mecàniques, tant de *H* com de *E*, més elevades que les altres mostres estudiades. Aquest fenomen s'atribueix a l'addició de Zr dins de la capa de CeO_2, que produeix un augment de la tenacitat de la capa prima.

A.3. Conclusions

La tècnica de nanoindentació o indentació instrumentada és una tècnica molt versàtil que ens permet determinar propietats mecàniques tals com la duresa, el mòdul de Young, etc. Aquesta tècnica ens ajuda a aïllar les propietats de precipitats, inclusions en l'interior d'una matriu, etc. Aquesta tècnica s'ha emprat per tal de caracteritzar materials heterogenis i capes primes. Les conclusions obtingudes a partir d'aquesta tesis es mostren a continuació:

La duresa i el mòdul de Young per cadascuna de les fases presents en els compostos d'YBCO obtinguts mitjançant la tècnica Bridgman i TSMG poden ser aïllades quan la càrrega aplicada es inferior o igual a 10 mN, ja que l'empremta residual es inferior a la mida dels precipitats distribuïts heterogèniament en l'interior de la matriu. En aquest cas, la duresa del Y-211 és aproximadament el doble que per la matriu Y-123. Per ambdós processos de texturació.

El valor de *H* i *E* per a les mostres TSMG és inferior que per les mostres obtingudes mitjançant la tècnica Bridgman. Aquesta reducció s'atribueix a la diferent densitat de defectes microestructurals generats durant el procés de texturació i oxigenació, els quals fragilitzen les mostres obtingudes per TSMG.
El valor del *E* obtingut mitjançant indentació esfèrica i les equacions de Hertz, està al voltant de 123,5 ± 3,4 GPa. Aquest resultat està en concordança amb els valors de *E* reportats a la bibliografia.

La transició elasto-plàstica per les mostres d'YBCO obtingudes per la tècnica Bridgman, es pot dur a terme quan la pressió mitja de contacte indentador-mostra es de 3,5 GPa, produint una profunditat de penetració de 150 nm i obtenint un límit elàstic de 3,2 GPa. Pel que fa les mostres obtingudes mitjançant la tècnica TSMG, la pressió mitja de contacte és de 3,9 GPa, obtenint un valor de límit elàstic de 3,5 GPa.

Mitjançant un tall transversal al centre de la indentació, s'ha pogut observar que la mostra en estudi presenta una estructura altament heterogenea pel que fa a la distribució de partícules de Y-211 en l'interior de la matriu. També s'ha observat que no existeixen microesquerdes activades durant el procés d'indentació. Per tant, els mecanismes de deformació activats mitjançant l'assaig d'indentació s'atribueixen a la generació de dislocacions i al procés de maclat.

La microscopia de forces atòmiques ens permet estudiar els diferents mecanismes de deformació plàstica activats durant el procés d'indentació en materials ceràmics. Diferents línies de lliscament han estat observades al contorn de l'indentació. En les mostres obtingudes per la tècnica TSMG s'han activat línies de dislocacions i macles, formant un angle entre elles de 75º. Per contra, a les mostres Bridgman únicament s'ha pogut observar la generació de línies de lliscament, les quals es troben íntimament relaciones amb l'orientació cristal·lina del gra. Emprant un indentador esfèric, per les mostres Bridgman s'han activat línies de lliscament i lliscament creuat dins del radi de contacte del indentador. Per contra, a les mostres TSMG no s'ha pogut observar el mecanisme de deformació, ja que a les empremtes residuals s'hi ha dipositat contaminació.

S'ha determinat l'evolució de la duresa en la zona de soldadura de mostres d'YBCO/Ag/YBCO en el pla (001). La tècnica de nanoindentació presenta una elevada sensitivitat ja que permet observar l'evolució de la duresa en la zona de la soldadura i zones col·lindants a l'indentació. S'ha obtingut una correlació lineal entre les propietats superconductores obtingudes a temperatures criogèniques i les propietats mecàniques obtingudes a temperatura ambient.

Les capes primes de CeO_2 dopades amb *Zr* presenten unes millors propietats mecàniques que les mostres sense dopar o dopades amb *Ta*. Per tant, aquest material es un òptim candidat per ser emprat com a capa tampó per a dipositar capes primes d'YBCO.

Appendix B

PUBLICATIONS AND MEETINGS

> ***Whatever your life's work is, do it well. A man should do his job so well that the living, the dead, and the unborn could do it no better.***
>
> *Martin Luther King Jr. (1929-1968)*
> *American black leader*

B.1. Published articles

1. E. Bartolomé, J. J. Roa, B. Bozzo, M. Segarra, X. Granados. Nanoindentation of melt-textured $YBa_2Cu_3O_{7-x}$ silver welds. S*uperconductor Science and Technology* **23** (2010) 045013/1.

2. M. Morales, J. J. Roa, X. G. Capdevila, M. Segarra, S. Piñol. Mechanical properties at nanometric scale of GDC and YSZ used as electrolytes for SOFCs, *Acta Materialia* **58** (2010) 2504.

3. J. J. Roa, E. Jiménez-Piqué, X. G. Capdevila, M. Segarra. Nanoindentation with spherical tips of single crystals of YBCO textured by Bridgman technique: Determination of indentation stress-strain curves. *Journal of the European Ceramic Society* **30** (2010) 1477.

4. J. C. Ruiz-Morales, D. Marrero-López, J. Peña-Martín, J. Canales-Vázquez, J. J. Roa, M. Segarra, S. N. Savvin, P. Núñez. Fabrication of a Novel Type of Electrolyte-Supported Solid Oxide Fuel Cell with Honeycomb Structure. *Journal of Power Sources* **195** (2010) 516.

5. J. J. Roa, M. Morales, X. G. Capdevila, M. Segarra. Mecanismos de fractura de electrolitos soportados de YSZ y GDC inducidos mediante ensayos de indentación instrumentada. *Boletín Sociedad Española de Cerámica y Vidrio* **49** (2010) 35.

6. M. Morales, J. J. Roa, X. G. Capdevila, M. Segarra, S. Piñol. Pilas de combustible basadas en electrolitos de ceria dopada con gadolinia operadas con metano y propano. *Boletín Sociedad Española de Cerámica y Vidrio* **49** (2010) 67.

7. M. Morales, J. J. Roa, X. G. Capdevila, M. Segarra, S. Piñol. Effect of sintering temperature on the Mechanical properties of film $Gd_{0.2}Ce_{0.8}O_{1.9}$ Electrolyte for SOFCs using Nanoindentation. *Journal of New Materials for Electrochemical Systems* **12** (2009) 187.

8. J. J. Roa, E. Gilioli, F. Bissoli, F. Pattini, S. Rampino, X. G. Capdevila, M. Segarra. Study of the mechanical properties of CeO_2 layers with Nanoindentation technique. *Thin Solid Films* **518** (2009) 227.

9. J. J. Roa, X. G. Capdevila, M. Martínez, F. Espiell, M. Segarra. Nanohardness and Young's modulus of YBCO samples textured by the Bridgman technique. *Nanotechnology* **18** (2007) 385701.

B.2. Submitted articles

1. J. J. Roa, M. Martínez, F. T. Dias, M. Segarra. Determination of the oxygenation kinetics in TSMG-YBCO sample. *Submitted* **(2010)**.

2. J. J. Roa, M. Morales, A. Magrasó, P. Núñez, M. Segarra. Mechanical properties of lanthanum tungstate at micro/nanometric scale. *Submitted* **(2010)**.

3. J. J. Roa, J. C. Ruiz-Morales, J. Canales-Vázquez, M. Morales, X. G. Capdevila, P. Núñez, M. Segarra. Mechanical characterization at nanometric scale of a new design of SOFC. *Submitted* **(2010)**.

4. M. Morales, J. J. Roa, X. G. Capdevila, M. Segarra, S. Piñol. Anode supported SOFCs operated at intermediate temperatures under single chamber conditions. *Submitted* **(2010)**.

5. J. J. Roa, M. Morales, X. G. Capdevila, M. Segarra. Residual tensile stress in the interphase Ni-YSZ/YSZ induced by Nanoindentation. *Submitted* **(2010)**.

6. J. J. Roa, G. Oncins, F. Teixeira Dias, X. G. Capdevila, V. Neves Vieira, J. Schaf, M. Segarra. AFM as an alternative for Young's modulus determination in ceramic materials at elastic deformation regime. *Submitted* **(2009)**.

7. J.J. Roa, E. Jiménez-Piqué, X. G. Capdevila, T. Puig, X. Obradors, M. Segarra. Nanoindentation of multilayered epitaxial $YBa_2Cu_3O_{7-\delta}$ thin films and coated conductors. *Submitted* **(2009)**.

8. J. J. Roa, M. Morales, X. G. Capdevila, M. Segarra. Mechanical properties and plastic behaviour mechanism induced by Nanoindentation technique of YSZ and GDC materials used as electrolytes in Fuel Cells devices. *Submitted* **(2009)**.

9. J. J. Roa, E. Bartolomé, B. Bozzo, X. G. Capdevila, X. Granados, M. Segarra. Brittle phenomena activated by nanoindentation in melt-textured $YBa_2Cu_3O_{7-\delta}$ silver welds. *Submitted* **(2009)**.

B.3. Review Article

1. J. J. Roa, G. Oncins, J. Díaz, X. G. Capdevila, F. Sanz, M. Segarra. Study of the Friction, Adhesion and mechanical properties of Ceramic by AFM. *Submitted.* **(2010)**.

B.4. Chapter of Book

1. J. J. Roa, X. G. Capdevila, M. Segarra. Mechanical Characterization at Nanometric Scale of Ceramic Superconductor Composites. *Nanotechnology: Nanofabrication, Patterning, and Self Assembly-NOVA SCIENCE PUBLISHERS.* **(2009)**. I.S.B.N.: 978-1-60692-162-3.

B.5. Proceedings

1. J. J. Roa, E. Batolomé, B. Bozzo, X. G. Capdevila, X. Granados, M. Segarra. Nanomechanical properties of silver-welded YBCO bulk boundaries. *Accepted to Journal of Physics: Conference Series* **(2010)**.

2. J. C. Ruiz-Morales, S. N. Savvin, P. Núñez, J. Peña-Martínez, J. Canales-Vázquez, D. Marrero-López, J. J. Roa, M. Segarra. Novel Procedures for the Microstructural Design of SOFC Materials. *ECS Transaction, The Electrochemical Society* **25** pages 567-576 (2009) I.S.S.N.: 978-1-56677-739.

3. J. J. Roa, F. T. Dias, V. N. Vieira, G. Oncins, J. Dias, J. Schaf, X. G. Capdevila, M. Segarra. Caracterización mecánica a escala picométrica de $YBa_{1,75}Sr_{0,25}Cu_3O_{7-\delta}$ monocristalino mediante la técnica de autoflujo. *Anales de la Mecánica de la Fractura* 26 **Vol. 2** pág. 489 (2009). I.S.S.N.: 0213-3725.

4. J. J. Roa, M. Morales, M. Martínez, X. G. Capdevila, M. Segarra. Curva tensión-deformación mediante indentación esférica para materiales cerámicos superconductores de YBCO-TSMG. *Anales de la Mecánica de la Fractura* 26 **Vol. 2** pág. 495 (2009). I.S.S.N.: 0213-3725.

5. M. Morales, J. J. Roa, M. Martínez, X. G. Capdevila, M. Segarra, S. Piñol. Propiedades mecánicas a escala nanométrica de YSZ y GDC usados como electrolitos en pilas de combustible de óxido sólido. *Anales de la Mecánica de la Fractura* 26 **Vol. 2** pág. 543 (2009). I.S.S.N.: 0213-3725.

6. J. J. Roa, M. Martínez, A. I. Fernández, X. G. Capdevila, M. Segarra. Estudio de las propiedades mecánicas del YBCO mediante la ley de las mezclas y las relaciones de Kerner. *X Congreso Nacional de Materiales* 1 **Vol. 2** pág. 653 (2008). I.S.S.N.: 978-84-608-0768-1.

7. J. J. Roa, X. G. Capdevila, M. Segarra. Estudio de los mecanismos de Fractura durante la oxigenación del YBCO. *Anales de la Mecánica de la Fractura* 25 **Vol. 1** pág. 55 (2008). I.S.N.N.: 0213-3725.

8. J. J. Roa, E. Jiménez-Piqué, X. G. Capdevila, M. Segarra. Yield Strength, Shear Stress and Toughness of YBCO simples textured by Bridgman technique. *Journal of Physics: Conference Series*. **Vol. 97** pp. 012116 (2008).

B.6. Invited communication

1. J. J. Roa. Mechanical properties of High Temperature Superconductors at nano/micrometric scale. Seminar in the Laboratoire de Physique des Matériaux UMR 6630, PHYMAT **(2009)**.

2. M. Segarra, J. J. Roa, X. G. Capdevila, M. Morales. Caracterización de propiedades mecánicas a nivel nanométrico. Jornada IN^{2}UB. Col·legi Oficial de Metges de Barcelona. Barcelona **(2009)**.

3. J. J. Roa. Caracterización mecánica a escala nanométrica/picométrica de materiales superconductores de YBCO. Seminarios de Fronteras de la Ciencia de Materiales-Universidad Politécnica de Madrid. Madrid **(2009)**.

B.7. Oral presentations

1. J. J. Roa, C. Tromas, X. G. Capdevila, M. Segarra. Plastic deformation mechanisms nucleated during the nanoindentation process in YBCO. *Reunión de Nanomecánica y Nanoindentación, NANOMEC*. Barcelona, España **(2010)**

2. J. J. Roa, M. Morales, X. G. Capdevila, J. C. Ruiz-Morales, J. Canales-Vázquez, P. Núñez, M. Segarra. Mechanical characterization at nanometric scale of a new design of anode and electrolyte for electrolyte-supported SOFCs. *Workshop on Solid Oxide Fuel Cells: Materials and Technology*. Albacete, España **(2009)**.

3. M. Morales, J. J. Roa, X. G. Capdevila, M. Segarra, S. Piñol. Single chamber SOFCs based on gadolinia doped ceria electrolyte operated on methane and propane. *Workshop on Solid Oxide Fuel Cells: Materials and Technology*. Albacete, España **(2009)**.

4. K. Konstanopoulou, J. Y. Pastor, J. J. Roa, M. Segarra. Comportamiento mecánico a 300 k y 77 k de materiales masivos superconductores de YbaCuO. *49th Congreso Español de Cerámica y Vidrio.* Linares (Jaén), España **(2009)**.

5. J. J. Roa, E. Bartolomé, B. Bozzo, X. G. Capdevila, X. Granados, M. Segarra. Nano-mechanical properties of silver-welded YBCO bulks. *9th European Conference on Applied Superconductivity*. Dresden, Alemania **(2009)**.

6. J. J. Roa, M. Morales, X. G. Capdevila, M. Segarra. Nanoindentación y Picoindentación como herramientas complementarias para la caracterización mecánica de electrolitos en SOFC. *IX Reunión de Electrocerámica*. Leganés, España **(2009)**.

7. M. Morales, J. J. Roa, X. G. Capdevila, M. Segarra, S. Piñol. Sofás basadas en electrolitos de ceria dopada con gadolinia operadas con metano en una sola cámara. *IX Reunión de Electrocerámica.* Leganés, España **(2009)**.

8. J. J. Roa, M. Morales, M. Martínez, X. G. Capdevila, M. Segarra. Curva tensión-deformación mediante indentación esférica para materiales cerámicos superconductores de YBCO-TSMG. *XXVI Encuentro del Grupo Español de Fractura*. Santander, España **(2009)**.

9. M. Morales, J. J. Roa, M. Martínez, X. G. Capdevila, M. Segarra, S. Piñol. Propiedades mecánicas a escala nanométrica de YSZ y GDC usados como electrolitos en Pilas de Combustible de Óxido Sólido. *XXVI Encuentro del Grupo Español de Fractura*. Santander, España **(2009)**.

10. J. J. Roa, E. Gilioli, F. Bissoli, F. Patín, S. Rampino, X. G. Capdevila, M. Segarra. Mechanical properties at nanometric scale of CeO_2 layers. *Challenges in Materials for Energy 2008.* Barcelona, España **(2008)**.

11. J. J. Roa, X. G. Capdevila, M. Segarra. Indentación Instrumentada de capas delgadas de CeO_2 dopadas com Zr. *Reunión de Nanomecánica y Nanoindentación; NANOMEC*. Barcelona, España **(2008)**.

12. J. J. Roa, X. G. Capdevila, M. Segarra. Estudio de los mecanismos de fractura durante el proceso de oxigenación del $YBa_2Cu_3O_{7-\delta}$ (YBCO). *XXV Encuentro del Grupo Español de Fractura*. Sigüenza, España **(2008)**.

13. J. J. Roa, X. G. Capdevila, M. Segarra. Mechanical properties of TSMG-YBaCuO bulk superconductors with spherical tipped nanoindenter. *Energy Challenges 2007*. Barcelona, España **(2007)**.

14. J. J. Roa, M. Segarra. Study of the mechanical properties of Copper and YBCO by nanoindentation. *EXPLORING NANOMECHANICS, MTS Nano User's Meeting*. Madrid, España **(2007)**.

15. J. J. Roa, M. Segarra. Determinación de Propiedades Mecánicas de Materiales Superconductores (YBCO) mediante Nanoindentación. *Energy Challenges 2006.* Barcelona, España **(2006)**.

B.8. Poster presentations

1. J. J. Roa, F. Espiell, M. Segarra, E. Gilioli, F. Bissoli, F. Pattini, S. Rampino. Mechanical stability of CeO2 buffer layers for coated conductors. *International Workshop on Coated conductors for applications 2009*. Barcelona, España **(2009)**.

2. M. Morales, J. J. Roa, X. G. Capdevila, M. Segarra, S. Piñol. Mechanical characterization at nanometric scale of anode-supported thin film ceria electrolytes for IT-SOFCs. *Workshop on Solid Oxide Fuel Cells: Materials and Technology*. Albacete, España **(2009)**.

3. J. J. Roa, J. C. Ruiz-Morales, M. Morales, P. Núñez, J. Canales-Vázquez, X. G. Capdevila, M. Segarra. Young's modulus determination at picometric scale of a new design of electrolyte-supported SOFCs. *Workshop on Solid Oxide Fuel Cells: Materials and Technology*. Albacete, España **(2009)**.

4. J. C. Ruiz-Morales, S. N. Savvin, P. Núñez, J. Peña-Martínez, J. Canales-Vázquez, D. Marrero-López, J. J. Roa, M. Segarra. Novel Procedures for the Microstructural Design of SOFC Materials. *SOFC XI. 216th ECS Meeting*. Vienna, Austria **(2009)**.

5. J. J. Roa, F. T. Dias, V. N. Vieira, A. Ghosh, X. Obradors, M. Segarra, F. Wolf-Fabris. Pseudoap regime in YBaCuO simples studied by transport measurements. *9th European Conference on Applied Superconductivity*. Dresden, Alemania **(2009)**.

6. J. J. Roa, V. N. Vieira, F. T. Dias, J. SCAF, F. Wolf-Fabris, M. Segarra. Critical currents and flux pinning in chemically doped YBaCuO. *9th European Conference on Applied Superconductivity*. Dresden, Alemania **(2009)**.

7. J. J. Roa, M. Morales, X. G. Capdevila, M. Segarra. Estudio de las propiedades mecánicas a escala nanométrica de materiales cerámicos avanzados para la energía. Jornada IN^{2}UB. Barcelona, España **(2009)**.

8. M. Morales, J. J. Roa, X. G. Capdevila, M. Segarra, S. Piñol. Caracterización mecánica mediante nanoindentación de YSZ y GDC usados como electrolitos en las Sofás. *IX Reunión de Electrocerámica*. Leganés, España **(2009)**.

9. E. Bartolomé, J. J. Roa, B. Bozzo, M. Segarra, and X. G. Granados. Nanoindentation and magnetic properties of $YBa_2Cu_3O_{7-x}$ bulk boundaries. *Workshop Escola Universitària Salaciana de Sarrià*. Barcelona, España **(2009)**.

10. V. N. Vieira, F. T. Dias, J. Schaf, J. J. Roa, M. Segarra. Critical currents and flux pinning in chemically doped YBaCuO. *Workshop on Routes to Superconductivity at Ambient Conditions.* Brasil **(2009)**.

11. F. T. Dias, V. N. Vieira, J. J. Roa, M. Segarra. Pseudogap regime in YBaCuO samples. *Workshop on Routes to Superconductivity at Ambient Conditions*. Brasil **(2009)**.

12. J. J. Roa, F. T. Dias, V. N. Vieira, G. Oncins, J. Schaf, X. G. Capdevila, M. Segarra. Mechanical characterization at picometric scale of superconductor ceramics, YCaBaCuO. *Nanotech Insight conference*. Barcelona, España **(2009)**.

13. J. J. Roa, F. T. Dias, V. N. Vieira, G. Oncins, J. Diaz, J. Schaf, X. G. Capdevila, M. Segarra. Caracterización mecánica a escala picométrica de $YBa_{1,75}Sr_{0,25}Cu_3O_{7-\delta}$ monocristalino mediante la técnica de Autoflujo. *XXVI Encuentro del Grupo Español de Fractura*. Santander, España **(2009)**.

14. J. J. Roa, X. G. Capdevila, M. Segarra. Nanohardness and Young's modulus of YBCO samples textured by Top-Seeded-Melt-Growth technique at different crystallographic planes. *11th Mediterranean Congress of Chemical Engineering. Chemical Engineering in the Frontiers of knowledge.* Barcelona, España **(2008)**.

15. J. J. Roa, M. Martínez, A. I. Fernández, X. G. Capdevila, M. Segarra. Estudio de las propiedades mecánicas del YBCO mediante la ley de las mezclas y las relaciones de Kerner. *X Congreso Nacional de Materiales*. Donostia-San Sebastián, España **(2008)**.

16. J. J. Roa, X. G. Capdevila, M. Segarra. Determianció de les propietats mecàniques a escala nanomètrica d'elements superconductors d'YBCO texturats mitjançant la tècnica Bridgman. *Masterquímica IV*. Barcelona, España **(2008)**.

17. J. J. Roa, E. Jiménez-Piqué, X. G. Capdevila, M. Martínez, M. Segarra. Yield Strength, Shear Stress and Thoughness of YBCO samples textured by Bridgman technique. *8th European Conference on Applied Superconductivity*. Brussels, Bélgica **(2007)**.

18. J. J. Roa, X. G. Capdevila, M. Martínez, F. Espiell, M. Segarra. Synthesis, texture and mechanical properties of the tetragonal phase of YBCO at room temperature. *7th SCENET School of Superconducting Materials and Applications.* Camerino, Italia **(2006)**.